

LEVERAGING MULTI-MESSENGER ASTROPHYSICS FOR DARK MATTER SEARCHES

By

Daniel Nicholas Salazar-Gallegos

A DISSERTATION

Submitted to  
Michigan State University  
in partial fulfillment of the requirements  
for the degree of

Physics—Doctor of Philosophy  
Computational Mathematics in Science and Engineering—Dual Major

Today

## **ABSTRACT**

I did Dark Matter with HAWC and IceCube. I also used Graph Neural Networks

## **ACKNOWLEDGMENTS**

I love my friends. Thanks to everyone that helped me figure this out. Amazing thanks to the people at LANL who supported me. Eames, etc Dinner Parties Jenny and her child Kaydince Kirsten, Pat, Andrea Family. You're so far but so critical to my formation. Unconditional love. Roommate

## TABLE OF CONTENTS

LIST OF TABLES . . . . .	vi
LIST OF FIGURES . . . . .	viii
CHAPTER 1 DARK MATTER IN THE COSMOS . . . . .	1
1.1 Introduction . . . . .	1
1.2 Dark Matter Basics . . . . .	2
1.3 Evidence for Dark Matter . . . . .	3
1.4 Searching for Dark Matter: Particle DM . . . . .	10
1.5 Sources for Indirect Dark Matter Searches . . . . .	15
1.6 Multi-Messenger Dark Matter . . . . .	17
CHAPTER 2 HIGH ALTITUDE WATER CHERENKOV (HAWC) OBSERVATORY . . . . .	20
2.1 The Detector . . . . .	20
2.2 Event Reconstruction . . . . .	25
2.3 Background Estimation: Direct Integration . . . . .	33
CHAPTER 3 GLORY DUCK: MULTI-WAVELENGTH SEARCH FOR DARK MATTER ANNIHILATION TOWARDS DWARF SPHEROIDAL GALAXIES . . . . .	35
3.1 Introduction . . . . .	35
3.2 Dataset and Background . . . . .	37
3.3 Analysis . . . . .	39
3.4 Likelihood Methods . . . . .	43
3.5 HAWC Results . . . . .	50
3.6 Glory Duck Combined Results . . . . .	52
3.7 HAWC Systematics . . . . .	57
3.8 $J$ -factor distributions . . . . .	59
3.9 Discussion and Conclusions . . . . .	65
CHAPTER 4 MULTITHREADING HAWC ANALYSES FOR DARK MATTER SEARCHES . . . . .	69
4.1 Introduction . . . . .	69
4.2 Dataset and Background . . . . .	69
4.3 Analysis . . . . .	71
4.4 Likelihood Methods . . . . .	75
4.5 Computational Methods: Multithreading . . . . .	75
4.6 Analysis Results . . . . .	81
4.7 Systematics . . . . .	86
4.8 Conclusion and Discussion . . . . .	86
CHAPTER 5 ICECUBE NEUTRINO OBSERVATORY . . . . .	88
5.1 The Detector . . . . .	89
5.2 Event Reconstruction . . . . .	93

5.3	Background . . . . .	99
<b>CHAPTER 6</b>	<b>HEAVY DARK MATTER ANNIHILATION SEARCH WITH ICE-CUBE'S NORTH SKY TRACK DATA . . . . .</b>	<b>100</b>
6.1	Introduction . . . . .	100
6.2	Dataset and Background . . . . .	100
6.3	Analysis . . . . .	102
6.4	Likelihood Methods . . . . .	111
6.5	Background Simulation . . . . .	111
6.6	Signal Recovery . . . . .	129
6.7	Systematics . . . . .	132
6.8	Conclusions . . . . .	135
<b>CHAPTER 7</b>	<b>NU DUCK: CONCLUSIONS AND FUTURE DIRECTIONS . . . . .</b>	<b>137</b>
7.1	Conclusions . . . . .	137
7.2	Future Directions: Multi-Messenger Dark Matter Search . . . . .	138
<b>APPENDIX A</b>	<b>MULTI-EXPERIMENT SUPPLEMENTARY FIGURES . . . . .</b>	<b>140</b>
<b>APPENDIX B</b>	<b>MULTITHREADING DARK MATTER ANALYSES SUPPLEMENTARY MATERIAL . . . . .</b>	<b>141</b>
B.1	Remaining Spectral Models . . . . .	141
B.2	<code>mpu_analysis.py</code> . . . . .	142
B.3	Comparison with Glory Duck . . . . .	151
<b>APPENDIX C</b>	<b>ICECUBE HEAVY DARK MATTER ANALYSIS SUPPLEMENTARY MATERIAL . . . . .</b>	<b>154</b>
C.1	Docker Image for Oscillating Neutrino Spectra . . . . .	154
C.2	Spline Fitting Statuses . . . . .	157
C.3	Neutrino Composite Spectra . . . . .	158
C.4	Segue 1 And Ursa Major II Signal Recovery . . . . .	159
C.5	$n_s$ Sensitivities . . . . .	165
<b>BIBLIOGRAPHY . . . . .</b>		<b>167</b>

## LIST OF TABLES

<p>Table 2.1 Definitions of <math>f_{\text{hit}}</math> energy estimator bins. Bins are defined by the fraction of available PMTs that are triggered during an air shower event. The angular resolution, <math>\Theta_{68}</math>, is the bin containing 68% of events [34]. . . . .</p> <p>Table 3.1 Summary of the relevant properties of the dSphs used in the present work. Column 1 lists the dSphs. Columns 2 and 3 present their heliocentric distance and galactic coordinates, respectively. Columns 4 and 5 report the <math>J</math>-factors of each source given from the <math>\mathcal{GS}</math> and <math>\mathcal{B}</math> independent studies and their estimated <math>\pm 1\sigma</math> uncertainties. The values <math>\log_{10} J</math> (<math>\mathcal{GS}</math> set) [59] correspond to the mean <math>J</math>-factor values for a source extension truncated at the outermost observed star. The values <math>\log_{10} J</math> (<math>\mathcal{B}</math> set) [63] are provided for a source extension at the tidal radius of each dSph. <b>Bolded sources are within HAWC's field of view and provided to the Glory Duck analysis.</b> . . . . .</p> <p>Table 3.2 Summary of dSph observations by each experiment used in this work. A ‘-’ indicates the experiment did not observe the dSph for this study. For Fermi-LAT, the exposure at 1 GeV is given. For HAWC, <math> \Delta\theta </math> is the absolute difference between the source declination and HAWC latitude. HAWC is more sensitive to sources with smaller <math> \Delta\theta </math>. For IACTs, we show the zenith angle range, the total exposure, the energy range, the angular radius <math>\theta</math> of the signal or ON region, the ratio of exposures between the background-control (OFF) and signal (ON) regions (<math>\tau</math>), and the significance of gamma-ray excess in standard deviations, <math>\sigma</math>. . . . .</p> <p>Table 4.1 Summary of the relevant properties of the dSphs used in the present work. Column 1 lists the dSphs. Columns 2 and 3 present their heliocentric distance and galactic coordinates, respectively. Column 4 reports the <math>J</math>-factors of each source given from the <math>\mathcal{LS}</math> studies and estimated <math>\pm 1\sigma</math> uncertainties. The values <math>\log_{10} J</math> (<math>\mathcal{LS}</math> set) [80] correspond to the mean <math>J</math>-factor values for a source extension truncated at <math>0.5^\circ</math>. . . . .</p> <p>Table 4.2 Timing summaries for analyses for serial and multithreaded processes. <math>M</math> tasks is the number of functional-parallel tasks ran for the computation. <math>T_{p,c}</math> is a single run time in hours:minutes:seconds for runs utilizing <math>p</math> nodes and <math>c</math> threads. Runs are run interactively on the same computer to maximize consistency. Empty entries are indicated with ‘-’. <math>(\cdot)</math> entries are estimated entries extrapolated from data earlier in the column. . . . .</p> <p>Table 4.3 Speed up summaries for analyses for serial and multithreaded processes. <math>M</math> tasks is the number of functional-parallel tasks ran for the computation. <math>S_{p,c}</math> is a single speedup comparison for runs utilizing <math>p</math> nodes and <math>c</math> threads. <math>[\cdot]</math> are the estimated speedups calculated from Tab. 4.2, Eq. (4.7), and Eq. (4.4). Empty entries are indicated with ‘-’. . . . .</p>	<p>29</p> <p>44</p> <p>45</p> <p>74</p> <p>80</p> <p>81</p>
---	---

Table 6.1 Spline err tolerances used for input in particle physics component to Eq. (3.1). Column 1 is the DM annihilation channel being fit. Columns 2, 3, and 4 are the tolerances for "GOOD" (pass), "OK" requires inspection, and "FAIL" (tune and refit) respectively. Column 5 has the X ranges over which the error is evaluated. MAX/MIN [·,·] takes the maximum or minimum of the two enclosed values. . . . .	108
--	-----

## LIST OF FIGURES

<p>Figure 1.1 Rotation curve fit to NGC 6503 from [7]. Dashed line is the contribution from visible matter. Dotted curves are from gas. Dash-dot curves are from dark matter (DM). Solid line is the composite contribution from all matter and DM sources. Data are indicated with bold dots with error bars. Data agree strongly with a matter + DM composite prediction. . . . .</p> <p>Figure 1.2 Light from distant galaxy is bent in unique ways depending on the distribution of mass between the galaxy and Earth. Yellow dashed lines indicate where the light would have gone if the matter were not present [8]. . . . .</p> <p>Figure 1.3 (left) Optical image of galactic cluster 1E0657-558. (right) X-ray image of the cluster with redder meaning hotter and higher baryon density. (both) Green contours are reconstruction of gravity contours from weak lensing. White rings are the best fit mass maxima at 68.3%, 95.5%, and 99.7% confidence. The matter maxima of the clusters are clearly separated from x-ray maxima. [9]</p> <p>Figure 1.4 Plank CMB sky. Sky map features small variations in temperature in primordial light. These anisotropies are used to make inferences about the universe's energy budget and developmental history. [10] . . . . .</p> <p>Figure 1.5 Observed Cosmic Microwave Background power spectrum as a function of multipole moment from Plank [10]. Blue line is best fit model from <math>\Lambda</math>CDM. Red points and lines are data and error, respectively. . . . .</p> <p>Figure 1.6 Predicted power spectra of CMB for different <math>\Omega_m h^2</math> values for fixed baryon density from [11]. (left) Low <math>\Omega_m h^2</math> increases the prominence of first and second peaks. (middle) <math>\Omega_m h^2</math> is most similar to the observed power spectrum. The second and third peaks are similar in height. (right) <math>\Omega_m h^2</math> is large which suppresses the first peak and raises the prominence of the third peak. . . . .</p> <p>Figure 1.7 The Standard Model (SM) of particle physics. Figure taken from <a href="http://www.quantumdiaries.org/2014/03/14/the-standard-model-a-beautiful-but-flawed-theory/">http://www.quantumdiaries.org/2014/03/14/the-standard-model-a-beautiful-but-flawed-theory/</a> . . . . .</p> <p>Figure 1.8 Simplified Feynman diagram demonstrating with different ways DM can interact with SM particles. The 'X's refer to the DM particles whereas the SM refer to fundamental particles in the SM. The large circle in the center indicates the vertex of interaction and is purposely left vague. The colored arrows refer to different directions of time as well as their respective labels. The arrows indicate the initial and final state of the DM -SM interaction in time.</p>	<p>4</p> <p>6</p> <p>7</p> <p>8</p> <p>9</p> <p>9</p> <p>11</p> <p>12</p>
--	---

Figure 1.9 A single jet event in ATLAS detector from 2017 [16]. Jet momentum was observed to be 1.9 TeV. Missing transverse momentum was observed to be 1.9 TeV compared to the initial transverse momentum of the event was 0. Implied MET is traced by a red dashed line in event display. . . . .	13
Figure 1.10 More detailed pseudo-Feynman diagram of particle cascade from dark matter annihilation into 2 quarks. The quarks hadronize and down to stable particles like $\gamma$ or the anti-proton ( $p^-$ ). Diagram pulled from ICRC 2021 presentation on DM annihilation search [17]. . . . .	14
Figure 1.11 Dark Matter (DM) decay spectrum for $b\bar{b}$ initial state and $\gamma$ final state. Redder spectra are for larger DM masses. Bluer spectra are light DM masses. $x$ is a unitless factor defined as the ratio of the mass of DM, $m_\chi$ , and the final state particle energy $E_\gamma$ . Figure from [19]. . . . .	16
Figure 1.12 Different dark matter density profiles compared. Some models produce exceptionally large densities at small $r$ [20]. . . . .	17
Figure 1.13 The Milky Way Galaxy in photons ( $\gamma$ ) and neutrinos ( $\nu$ ) [22]. The Galactic center is at $l=0^\circ$ and is the brightest region in all panels. (top) An Optical color image of the Milky Way galaxy seen from Earth. Clouds of gas and dust obscure some light from stars. (2nd down) Integrated flux of $\gamma$ -rays observed by the Fermi-LAT telescope [23]. (middle) Expected neutrino emission that corresponds with Fermi-LAT observations. (2nd up) Expected neutrino emission profile after considering detector systematics of IceCube. (bottom) Observed neutrino emission from region of the galactic plane. Substantial neutrino emission was detected. . . . .	18
Figure 1.14 Dark Matter annihilation spectra for different final state particle and standard model annihilation channels [24]. Photons (red), $e^\pm$ (green), $\bar{p}$ (blue), $\nu$ (black). . . . .	19
Figure 2.1 Photo of the HAWC detector that I took on May 17, 2023. Main array is centered in the photo and comprised of the larger tanks. Outriggers are the smaller tanks around the main array. . . . .	20
Figure 2.2 A particle physics illustration of high energy particle showers. Left shower is an electromagnetic shower from a high energy gamma-ray. Most particles in the shower will be a combination of photons and charged leptons, in this case electrons ( $e$ ). Right figure shows a cosmic ray particle shower. The cosmic ray will produce many more types of particles including pions ( $\pi$ ), neutrinos, and charged leptons. Figure pulled from [26]. . . . .	21
Figure 2.3 The WCDs. Left image features several WCDs looking from within the main array of HAWC. Right image shows a schematic of a WCD pulled from [25]. . . . .	22

Figure 2.4	Overview of HAWC control and data electronics. The LoToT and HiToT threshold signals are discussed in Section 2.1.2. Figure from [27] . . . . .	23
Figure 2.5	Schematic of data flow in HAWC data acquisition and online processing system. Pulled from [29]. . . . .	24
Figure 2.6	How HAWC FEB intially processes analog PMT signals. Signals are split through an amplifier and discriminator circuit. Each path is designated for either the HIGH or LOW threshold for the signal. The 2-edge event corresponds to LOW, while the 4 edge corresponds to HIGH. . . . .	24
Figure 2.7	An particle shower incident on WCDs. Secondary particles of an air shower travel in a cone centered on primary incident particle. Reconstruction of the initial angle is possible with arrival time of hits in PMTs inside WCDs. Figure from [33]. . . . .	26
Figure 2.8	Charge deposition in each PMT for a reconstructed gamma-ray event. WCDs are outlined in black surrounding the 4 smaller circles that represent PMTs. The color scale indicates the charge deposition in each PMT. The best shower core fit from SFCF is noted with a red star in the center of the dashed circle [34].	27
Figure 2.9	Simulated normalized energy distribution of each $f_{\text{hit}}$ bin defined in Tab. 2.1. Monte Carlo simulation of gamma-rays with $E^{-2.63}$ spectral shape and simulated source at 20° declination. Figure from [34]. . . . .	29
Figure 2.10	Neural Network energy estimator performance compared to true energy. The dotted line is the identity line where the estimator and injection agree. Gamma/hadron separation cuts were applied with the energy estimation. Figure pulled from [37] . . . . .	31
Figure 2.11	Lateral distribution functions (LDFs) for cosmic ray (left) and a photon candidate from the Crab Nebula (right). Cosmic ray LDF has clearly isolated hits far from the reconstructed shower core. Gamma-ray shower shows a more cuspy event [34]. . . . .	32

Figure 3.1	Sensitivities of five gamma-ray experiments compared to percentages of the Crab nebula's emission and dark matter annihilation. Solid lines present estimated sensitivities to power law spectra [FACT CHECK THIS]for each experiment. Green lines are Fermi-LAT sensitivities where lighter green is the sensitivity to the galactic center and dark green is its sensitivity to higher declinations. Orange, red, and purple solid lines represent the MAGIC, HESS, and VERITAS 50 hour sensitivities respectively. The maroon and brown lines are the HAWC 1 year and 5 year sensitivities. Across four decades of gamma-ray energy, these experiments have similar sensitivities on the order $10^{-12}$ erg cm $^{-2}$ s $^{-1}$ . The dotted lines are estimated dark matter fluxes assuming $m_\chi = 5$ TeV DM annihilating to bottom quarks (red), tau leptons (blue), and W bosons (green). Faded gray lines outline percentage flux of the Crab nebula. Figure is an augmented version of [40] . . . . .	36
Figure 3.2	Effect of Electroweak (EW) corrections on expected DM annihilation spectrum for $\chi\chi \rightarrow W^-W^+$ . Solid lines are spectral models that consider EW corrections. Dash-dot lines are spectral models without EW corrections. Red lines are models for $M_\chi = 1$ TeV. Blue lines represent models for $M_\chi = 100$ TeV. All models are sourced from the PPPC4DMID [58]. . . . .	40
Figure 3.3	$\frac{dJ}{d\Omega}$ maps for Segue1 (top) and Coma Berenices (bottom). Origin is centered on the specific dwarf spheroidal galaxies (dSph). X and Y axes are the angular separation from the center of the dwarf. Profile is truncated at the scale radius. Plots of the remaining 11 dSph HAWC studied are linked in Fig. A.1. . . . .	42
Figure 3.4	Illustration of the combination technique showing a comparison between $-2 \ln \lambda$ provided by four instruments (colored lines) from the observation of the same dSph without any $J$ nuisance and their sum, <i>i.e.</i> the resulting combined likelihood (thin black line). According to the test statistics of Equation (3.7), the intersection of the likelihood profiles with the line $-2 \ln \lambda = 2.71$ indicates the 95% C.L. upper limit on $\langle \sigma v \rangle$ . The combined likelihood (thin black line) shows a smaller value of upper limit on $\langle \sigma v \rangle$ than those derived by individual instruments. We also show how the uncertainties on the $J$ factor effects the combined likelihood and degrade the upper limit on $\langle \sigma v \rangle$ (thick black line). All likelihood profiles are normalized so that the global minimum $\widehat{\langle \sigma v \rangle}$ is 0. We note that each profile depends on the observational conditions in which a target object was observed. The sensitivity of a given instrument can be degraded and the upper limits less constraining if the observations are performed in non-optimal conditions such as a high zenith angle or a short exposure time. . . . .	48
Figure 3.5	. . . . .	51

Figure 3.6 HAWC TS values for best fit $\langle\sigma v\rangle$ versus $m_\chi$ for seven SM annihilation channels with $J$ factors from $\mathcal{GS}$ . The solid black line shows the combined best fit TS values. The colored, dashed lines are the TS values for each of the 13 sources HAWC studied. . . . .	52
Figure 3.7 HAWC Brazil bands at 95% confidence level on $\langle\sigma v\rangle$ versus DM mass for seven annihilation channels with $J$ -factors from $\mathcal{GS}$ [69]. The solid line represents the combined limit from 13 dSphs. The dashed line is the expected limit. The green band is the 68% containment. The yellow band is the 95% containment. . . . .	53
Figure 3.8 Upper limits at 95% confidence level on $\langle\sigma v\rangle$ in function of the DM mass for eight annihilation channels, using the set of $J$ factors from Ref. [69] ( $\mathcal{GS}$ set in Table 3.1). The black solid line represents the observed combined limit, the black dashed line is the median of the null hypothesis corresponding to the expected limit, while the green and yellow bands show the 68% and 95% containment bands. Combined upper limits for each individual detector are also indicated as solid, colored lines. The value of the thermal relic cross-section in function of the DM mass is given as the red dotted-dashed line [70]. . . . .	54
Figure 3.9 Same as Fig. 3.8, using the set of $J$ factors from Ref. [63, 71] ( $\mathcal{B}$ set in Table 3.1). . . . .	55
Figure 3.10 Comparisons of the combined limits at 95% confidence level for each of the eight annihilation channels when using the $J$ factors from Ref. [69] ( $\mathcal{GS}$ set in Table 3.1), plain lines, and the $J$ factor from Ref. [63, 71] ( $\mathcal{B}$ set in Table 3.1), dashed lines. The cross-section given by the thermal relic is also indicated [70]. . . . .	57
Figure 3.11 Comparisons of the combined limits at 95% confidence level for a point source analysis and extended source using [69] $\mathcal{GS}$ J-factor distributions and PPPC [58] annihilation spectra. Shown are the limits for Segue1 which will have the most significant impact on the combined limit. 6 of the 7 DM annihilation channels are shown. Solid lines are extended source studies. Dashed lines are point source studies. Overall, the extended source analysis improves the limit by a factor of 2. . . . .	59
Figure 3.12 Same as Fig. 3.11 on Coma Berenices. This dSph also contributes significantly to the limit. The limits are identical in this case. . . . .	60
Figure 3.13 Comparison of combined limits when correcting for HAWC's pointing systematic. All DM annihilation channels are shown. The solid black line is the ratio between published limit to the declination corrected limit. The blue solid line or "Combined_og" represented the limits computed for Glory Duck. The solid orange line or "Combined_ad" represented the limits computed after correcting for the pointing systematic. . . . .	61

Figure 3.14 Differential map of  $dJ/\Omega$  from model built in Section 3.8.1 and profiles provided directly from authors. (Top) Differential from Segue1. (bottom) Differential from Coma Berenices. Note that their scales are not the same. Segue1 shows the deepest discrepancies which is congruent with its large uncertainties. Both models show anuli where unique models become apparent. . . . . 62

Figure 3.15 HAWC limits for Coma Berenices (top) and Segue1 (bottom) for two different map sets. Blue lines are limits calculated on maps with poor model representation. Orange lines are limits calculated on spatial profiles provided by the authors of [59]. Black line is the ratio of the poor spatial model limits to the corrected spatial models. The left y-axis measures  $\langle\sigma v\rangle$  for the blue and orange lines. The right y-axis measures the ratio and is unitless. . . . . 63

Figure 3.16 Comparisons between the  $J$ -factors versus the angular radius for the computation of  $J$  factors from Ref. [69] ( $\mathcal{GS}$  set in Table 3.1) in blue and for the computation from Ref. [63, 71] ( $\mathcal{B}$  set in Tab. 3.1) in orange. The solid lines represent the central value of the  $J$ -factors while the shaded regions correspond to the  $1\sigma$  standard deviation. . . . . 65

Figure 3.17 Comparisons between the  $J$ -factors versus the angular radius for the computation of  $J$  factors from Ref. [69] ( $\mathcal{GS}$  set in Tab. 3.1) in blue and for the computation from Ref. [63, 71] ( $\mathcal{B}$  set in Tab. 3.1) in orange. The solid lines represent the central value of the  $J$ -factors while the shaded regions correspond to the  $1\sigma$  standard deviation. . . . . 66

Figure 4.1 Spectral hypotheses from PPPC [58] and HDM [79] for DM annihilation:  $\chi\chi \rightarrow W^-W^+$ . Solid lines are spectral models with EW corrections from the PPPC. Dash-dot lines are spectral models from HDM. Red lines are models for  $M_\chi = 1$  TeV. Blue lines represent models for  $M_\chi = 100$  TeV. . . . . 72

Figure 4.2 Photon spectra for  $\chi\chi \rightarrow \gamma\gamma$  (left) and  $\chi\chi \rightarrow ZZ$  (right) after Gaussian convolution of line features. Both spectra have  $\delta$ -features at photon energies equal to the DM mass. Bluer lines are annihilation spectra with lower DM mass. Redder lines are spectra from larger DM mass. All spectral models are sourced from the Heavy Dark Matter models [79]. Axes are drawn roughly according to the energy sensitivity of HAWC. . . . . 73

Figure 4.3  $\frac{dJ}{d\Omega}$  maps for Coma Berenices, Segue1, and Sextans. Columns are divided for the  $\pm 1\sigma$  uncertainties in  $dJ/d\Omega$  around the mean value from  $\mathcal{LS}$  [80]. Origin is centered on the specific dwarf spheroidal galaxies (dSph).  $\theta$  and  $\phi$  axes are the angular separation from the center of the dwarf. Profiles are truncated at  $1^\circ$  and flattened beyond. . . . . 74

Figure 4.4	Infographic on how jobs and DM computation was organized in Section 3.3. Jobs were built for each permutation of CHANS and SOURCES shown by the left block in the figure. Each job, which took on the order 2 hrs to compute, had the following work flow: 1. Import HAWC analysis software, 2 min to run. 2. Load HAWC count maps, 5 min to run. 3. Load HAWC energy and spatial resolutions, 4 min. 5. Load DM spatial source templates and spectral models, less than 1 s. 6. Perform likelihood fit on data and model, about 8 min per DM mass. 7. Write results to file, less than 1s. . . . .	76
Figure 4.5	Graphic of Gustafson parallel coding pattern. $f_s$ is the fraction of a program, in time, spent on serial computation. $f_p$ is the fraction of computing time that is parallelizable. $T_p$ is the total time for a parallel program to run. $T_1$ is the total time for a parallel program to run if only 1 processor is allocated. $P_N$ is the $N$ -th processor where it's row is the computation the processor performs. The Gustafson pattern is most similar to what is implemented for this analysis. Figure is pulled from [82]. . . . .	78
Figure 4.6	Task chart for one multithreaded job developed for this project. Green blocks indicate a shared resource across the threads AND computation performed serially. Red blocks indicate functional parallel processing within each thread. 3 threads are represented here, yet many more can be employed during the full analysis. Jobs are defined by the SOURCE as these require unique maps to be loaded into the likelihood estimator. The $m_\chi$ , CHAN, and $\langle\sigma v\rangle$ variables are entered into the thread pool and allocated as evenly as possible across the threads. . . . .	79
Figure 4.7	HAWC upper limits at 95% confidence level on $\langle\sigma v\rangle$ versus $m_\chi$ for $\chi\chi \rightarrow b\bar{b}$ , $t\bar{t}$ , $u\bar{u}$ , $d\bar{d}$ , $s\bar{s}$ , $c\bar{c}$ , $gg$ , $W^+W^-$ , and $hh$ . Limits are with $\mathcal{LS}$ J-factors [80]. The solid line represents the observed combined limit. Dashed lines represent limits from individual dSphs. . . . .	82
Figure 4.8	HAWC upper limits at 95% confidence level on $\langle\sigma v\rangle$ versus $m_\chi$ for $\chi\chi \rightarrow \nu_e\bar{\nu}_e$ , $\nu_\mu\bar{\nu}_\mu$ , $\nu_\tau\bar{\nu}_\tau$ , $e\bar{e}$ , $\mu\bar{\mu}$ , $\tau\bar{\tau}$ , $\gamma\gamma$ and $ZZ$ . Limits use $\mathcal{LS}$ J-factors [80]. The solid line represents the observed combined limit. Dashed lines represent limits from individual dSphs. . . . .	83
Figure 4.9	HAWC TS values for best fit $\langle\sigma v\rangle$ versus $m_\chi$ for SM annihilation channels: $\chi\chi \rightarrow b\bar{b}$ , $t\bar{t}$ , $u\bar{u}$ , $d\bar{d}$ , $s\bar{s}$ , $c\bar{c}$ , $gg$ , $W^+W^-$ , and $hh$ . Limits use $\mathcal{LS}$ J-factors. The solid black line shows the combined best fit TS values. The colored, dashed lines are the TS values from each dSph. . . . .	84
Figure 4.10	HAWC TS values for best fit $\langle\sigma v\rangle$ versus $m_\chi$ for SM annihilation channels: $\chi\chi \rightarrow \nu_e\bar{\nu}_e$ , $\nu_\mu\bar{\nu}_\mu$ , $\nu_\tau\bar{\nu}_\tau$ , $e\bar{e}$ , $\mu\bar{\mu}$ , $\tau\bar{\tau}$ , $\gamma\gamma$ and $ZZ$ . Limits use $\mathcal{LS}$ J-factors. The solid black line shows the combined best fit TS values. The colored, dashed lines are the TS values from each dSph. . . . .	85

Figure 4.11 Comparison of HAWC limits from this analysis to Glory Duck (Fig. 3.5) for 3 dSphs and 3 DM annihilation channels: $b\bar{b}$ , $\tau\bar{\tau}$ , and $e\bar{e}$ . Each sector shows the 95% confidence limit from Glory Duck (blue line) and this analysis (orange line) in the top plot. The lower plot features the ratio in log scale of Glory Duck to this analysis in a red solid line. Horizontal dashed lines are for ratios of 1.0 (black) and $\sqrt{2}$ (blue). Ratios larger than 1.0 are for limits smaller, or stricter, than Glory Duck. Ratios larger than $\sqrt{2}$ indicates limits are stricter than a simple doubling of the Glory Duck data. . . . .	87
Figure 5.1 IceCube Neutrino observatory and science center at the South Pole. Detector volume is beneath glacial ice. Image from [83]. . . . .	88
Figure 5.2 IceCube Laboratory (ICL) that houses the data acquisition systems. Picture from [83]. . . . .	89
Figure 5.3 Composition of the Digital Optical Module (DOM). Left image is an illustration of the mechanical layout. Right is a flow chart of functional connections. Figure from [84] . . . . .	90
Figure 5.4 Graphic of the full IceCube Neutrino Observatory. In-ice array is made up of 86 strings with a total of 5160 optical sensors. Deepcore is a denser arrangement of optical sensors for sensitivity to lower energy neutrinos. Figure from [83]. . . . .	91
Figure 5.5 Data flow chart PMT waveforms from the DOMs. "Hit Records" are sent to the surface DAQ computers in ICL. Full waveform data, represented with dashed arrows, are included when neighboring DOMs are hit in coincidence above the SPE discriminator threshold. . . . .	92
Figure 5.6 Feynman diagrams for W (a/b) and Z (c/d) boson mediated interactions between neutrinos and light quarks. Charged current (CC) interactions are shown in panels a and b. Neutral current (NC) interactions are shown in panels c and d. NC interactions occur between neutrinos and quarks within atomic nuclei in the ice. CC interactions will exchange W bosons and produce a lepton corresponding to the neutrino flavor and a hadronic cascade. NC interactions will exchange a Z boson and produce a hadronic cascades. Figure from [85]. . . . .	94
Figure 5.7 Event topologies for high energy NC and CC neutrino interactions with ice. Signatures can be split as either: hadronic and electromagnetic cascades; Cherenkov radiation from a charged, long-lived particle. Cascades from $\tau$ decays will depend on its decay products. For energies below 1 PeV the double bang of the $\nu_\tau$ signature overlap and are indistinguishable. Figure from [86]. . . . .	95

Figure 5.8	A simulation of a track-like event in IceCube. Redder bubbles indicate earlier photon arrival times. Greener bubbles occur later. The size of the DOM bubble illustrate the charge deposition in the DOM. For this event, the CC neutrino interaction occurred by the red hits. There is then a long muon track going to the left. Figure taken from [87]. . . . .	96
Figure 5.9	Same as Fig. 5.8 but for a cascade-like event. Figure taken from [87]. . . . .	97
Figure 5.10	Same as Fig. 5.8 but for a double-bang event. Two distinct cascades are visible if the initial neutrino is very high energy. Figure taken from [87]. . . . .	97
Figure 6.1	Neutrino spectra at production (left panels) and after oscillation at Earth (right panels). Blue, orange, and green lines are the $\nu_e$ , $\nu_\mu$ , and $\nu_\tau$ spectra respectively. Top panels show the spectra in $\frac{dN}{dE}$ . Lower panels plot the flavor ratio to $\nu_e + \nu_\mu + \nu_\tau$ . SM annihilation channels $b\bar{b}$ , $\tau\bar{\tau}$ , and $\nu_\mu\bar{\nu}_\mu$ are shown for $M_\chi = 1$ PeV, TeV, and EeV. . . . .	104
Figure 6.2	Signal recovery for 100 TeV DM annihilation into $\nu_\mu\bar{\nu}_\mu$ for a source at Dec = $16.06^\circ$ . $n_{\text{inj}}$ is the number of injected signal events in simulation. $n_s$ is the number of reconstructed signal events from the simulation data. Although the uncertainties are small and tight, the reconstructed $n_s$ are systematically underestimated. . . . .	105
Figure 6.3	Left panel shows the two kernels overlaying the original spectrum from $\chi$ aronv after propagation to Earth [95]. The vertical red line indicates where the original neutrino line is maximized. Blue line is the output from $\chi$ aronv. Green line is the spectrum after convolution with a flat kernel. Orange line is the spectrum after Gaussian convolution. Right panel shows the signal recovery of the spectral model using the Gaussian kernel with parameters enumerated above. . . . .	106
Figure 6.4	Example spline that failed the fit. Failed splined are corrected on a case by case basis unless the SM channel has a systematic problem fitting the splines. In this case, I made a bookkeeping error and loaded the incorrect spectral model	108
Figure 6.5	Summary of input spectral models that were smoothed with Gaussian kernels. Spectral models are for $\chi\chi \rightarrow e\bar{e}$ , $\mu\bar{\mu}$ , $\tau\bar{\tau}$ , $\nu_e\bar{\nu}_e$ , $\nu_\mu\bar{\nu}_\mu$ , and $\nu_\tau\bar{\nu}_\tau$ . These spectra are the composite ( $\nu_\mu + \nu_\tau$ ) of neutrino flavors. Every spectral model used for this analysis is featured as a colored solid line. Bluer lines are for low $m_\chi$ models. $m_\chi$ ranges from 681 GeV to 100 PeV. HDM [79], $\chi$ arov [95], and Photospline [99] are used to generate these spectra. Energy (x-axis) was chosen to roughly represent the energy sensitivity of NST. . . . .	109

Figure 6.6 Test statistic (TS) distributions for Segue 1 and $\chi\chi \rightarrow b\bar{b}$ . Each subplot, except the final, is the TS distribution for a specific DM mass listed in the subplot. Orange dashed lines are the traces for a $\chi^2$ distribution with 1 degree of freedom. $\epsilon[\cdot]$ is the fraction of trials smaller than the bracketed value. The final subplot features the all DM spectral models, similar to Fig. 6.5, used as input for the TS distributions.	112
Figure 6.7 Same as Fig. 6.6 for Segue 1 $\chi\chi \rightarrow \tau\bar{\tau}$	113
Figure 6.8 Same as Fig. 6.6 for Segue 1 $\chi\chi \rightarrow \nu_\mu\bar{\nu}_\mu$	114
Figure 6.9 Same as Fig. 6.6 for Ursa Major II 1 $\chi\chi \rightarrow b\bar{b}$	115
Figure 6.10 Same as Fig. 6.6 for Ursa Major II 1 $\chi\chi \rightarrow \tau\bar{\tau}$	116
Figure 6.11 Same as Fig. 6.6 for Ursa Major II 1 $\chi\chi \rightarrow \nu_\mu\bar{\nu}_\mu$	117
Figure 6.12 Same as Fig. 6.6 for 15, GS $J$ -factor, stacked sources and $\chi\chi \rightarrow b\bar{b}$	118
Figure 6.13 Same as Fig. 6.6 for 15, GS $J$ -factor, stacked sources and $\chi\chi \rightarrow t\bar{t}$	119
Figure 6.14 Same as Fig. 6.6 for 15, GS $J$ -factor, stacked sources and $\chi\chi \rightarrow u\bar{u}$	120
Figure 6.15 Same as Fig. 6.6 for 15, GS $J$ -factor, stacked sources and $\chi\chi \rightarrow d\bar{d}$	121
Figure 6.16 Same as Fig. 6.6 for 15, GS $J$ -factor, stacked sources and $\chi\chi \rightarrow e\bar{e}$	122
Figure 6.17 Same as Fig. 6.6 for 15, GS $J$ -factor, stacked sources and $\chi\chi \rightarrow \mu\bar{\mu}$	123
Figure 6.18 Same as Fig. 6.6 for 15, GS $J$ -factor, stacked sources and $\chi\chi \rightarrow \tau\bar{\tau}$	124
Figure 6.19 Same as Fig. 6.6 for 15, GS $J$ -factor, stacked sources and $\chi\chi \rightarrow W^+W^-$	125
Figure 6.20 Same as Fig. 6.6 for 15, GS $J$ -factor, stacked sources and $\chi\chi \rightarrow ZZ$	126
Figure 6.21 Same as Fig. 6.6 for 15, GS $J$ -factor, stacked sources and $\chi\chi \rightarrow \nu_e\bar{\nu}_e$	127
Figure 6.22 Same as Fig. 6.6 for 15, GS $J$ -factor, stacked sources and $\chi\chi \rightarrow \nu_\mu\bar{\nu}_\mu$	128

Figure 6.23 Signal Recovery study for an analysis with 15 stacked sources using the $\mathcal{GS}$ $J$ -factors [59]. Above shows 14 studies for DM mass ranging between 1 TeV and 20 PeV for $\chi\chi \rightarrow \mu_\mu\overline{\mu_\mu}$ . The bottom right subplot features every spectral model used as input for the remaining subplots. The remaining subplots show $n_{\text{inj}}$ as the number of signal events injected into background simulation. Whereas, $n_s$ is the number of signal events recovered from analyzing the injected simulation. Blue line represents the median values of 100 simulations. Light blue bands show the $1\sigma$ statistical uncertainty around the median. . . . .	130
Figure 6.24 Same as Fig. 6.23 but for $\chi\chi \rightarrow t\bar{t}$ (top) and $b\bar{b}$ (bottom). . . . .	131
Figure 6.25 IceCube North Sky Track Sensitivities. Each panel shows sensitivity curves for various DM annihilation channels. Sensitivities are for the velocity-weighted cross-section $\langle\sigma v\rangle$ versus $m_\chi$ . Dotted, colored lines are sensitivities for individual sources. Solid white lines are for the combined sensitivity of all 15 $\mathcal{GS}$ sources used in this study. . . . .	133
Figure 6.26 Same as Fig. 6.25 for three additional DM annihilation channels. . . . .	134
Figure 6.27 Panel A: Neutrino's from the Northern sky and incident on the IceCube detector will travel through the Earth. How much of the Earth these neutrinos travels is a function of zenith from the vertical axis. Panel B: SM prediction of neutrino transmission probabilities for neutrinos arriving at $90^\circ - 180^\circ$ zenith and with 100 GeV to 100 PeV energies. High-energy neutrinos traversing the whole Earth are completely absorbed, whereas low-energy neutrinos pass through unimpeded. Neutrinos coming from above the horizon will arrive unimpeded for all neutrino energies. Figure pulled from [102]. . . . .	135
Figure 6.28 $\langle\sigma v\rangle$ sensitivities for 5 imaginary sources with $\log_{10} J = 19.42 \log_{10}(\text{GeV}^2\text{cm}^{-5})$ . Each imaginary source shares a declination with a source in Tab. 3.1 . . . . .	136
Figure 7.1 The prompt electron neutrino and photon spectrum resulting from the decay of a 2EeV DM particle to $\nu_e\overline{\nu}_e$ , as currently being searched for at IceCube [5]. Solid curves represent the results of this work, and predict orders of magnitude more flux at certain energies than the dashed results of Pythia 8.2, one of the only existing methods to generate spectra at these masses. In both cases energy conservation is satisfied: there is a considerable contribution to a $\delta$ -function at $x = 1$ , associated with events where an initial W or Z was never emitted and thus no subsequent shower developed. Large disagreements are generically observed at these masses for electroweak dominated channels, while the agreement is better for colored initial SM states. . . . .	138
Figure 7.2 TODO: neutrino and bb plot with nu Sensitivities[NEEDS A SOURCE][FACT CHECK THIS] . . . . .	139

Figure A.1 Sister figure to Figure 3.3. Sources in the first row from left to right: Bootes I, Canes Venatici I, II. In second row: Draco, Hercules, Leo I. In the first row: Leo II, Leo IV, Sextans. In the final row: Ursa Major I, Ursa Major II. . . . .	140
Figure B.1 Sister figure to Figure 4.2 for remaining SM primary annihilation channels studied for this thesis. These did not require any post generation smoothing and so are directly pulled from [79] with a binning scheme most helpful for a HAWC analysis. . . . .	141
Figure B.2 Comparison of HAWC limits from this analysis to Glory Duck (Fig. 3.5) for Coma Berenices and 7 DM annihilation channels. . . . .	151
Figure B.3 Same as Fig. B.2 but for Segue 1. . . . .	152
Figure B.4 Same as Fig. B.2 but for Sextans. . . . .	153
Figure C.1 Current status of spline tables according to constraints defined by Tab. 6.1. Green splines are splines that passed under the GOOD tolerance. Yellow are splines that are OK. Red are splines that FAIL. All yellow splines were inspected individually before running the analysis. Splines were made for the $\mu$ (PID 14; top panel) flavor and $\tau$ (PID 16; bottom panel) neutrino flavors. . . . .	157
Figure C.2 Sister figure to Fig. 6.5 for annihilation channels that did not require kernel smoothing. These spectra are the composite ( $\nu_\mu + \nu_\tau$ ) of neutrino flavors. Every spectral model used for this analysis is featured as a colored solid line. Bluer lines are for lower DM mass spectral models. DM masses range from 681 GeV to 100 PeV. . . . .	158
Figure C.3 Same as Fig. 6.23 but for Segue 1 and $\chi\chi \rightarrow b\bar{b}$ . . . . .	159
Figure C.4 Same as Fig. 6.23 but for Segue 1 and $\chi\chi \rightarrow t\bar{t}$ . . . . .	160
Figure C.5 Same as Fig. 6.23 but for Segue 1 and $\chi\chi \rightarrow \nu_\mu\bar{\nu}_\mu$ . . . . .	161
Figure C.6 Same as Fig. 6.23 but for Ursa Major II and $\chi\chi \rightarrow b\bar{b}$ . . . . .	162
Figure C.7 Same as Fig. 6.23 but for Ursa Major II and $\chi\chi \rightarrow t\bar{t}$ . . . . .	163
Figure C.8 Same as Fig. 6.23 but for Ursa Major II and $\chi\chi \rightarrow \nu_\mu\bar{\nu}_\mu$ . . . . .	164
Figure C.9 IceCube North Sky Track Sensitivities for $n_s/\langle N \rangle$ . $n_s$ values are the counts fed into Eq. (6.8) to produce Fig. 6.26 and Fig. 6.25. . . . .	165
Figure C.10 Same as Fig. C.9 for three additional DM annihilation channels. . . . .	166

# **CHAPTER 1**

## **DARK MATTER IN THE COSMOS**

### **1.1 Introduction**

The dark matter problem can be summarized in part by the following thought experiment.

Let us say you are the teacher for an elementary school classroom. You take them on a field trip to your local science museum and among the exhibits is one for mass and weight. The exhibit has a gigantic scale, and you come up with a fun problem for your class.

You ask your class, "What is the total weight of the classroom? Give your best estimation to me in 30 minutes, and then we'll check your guess on the scale. If your guess is within 10% of the right answer, we will stop for ice cream on the way back."

The students are ecstatic to hear this, and they get to work. The solution is some variation of the following strategy. The students should give each other their weight or best guess if they do not know. Then, all they must do is add each student's weight and get a grand total for the class. The measurement on the giant scale should show the true weight of the class. When comparing the measured weight to your estimation, multiply the measurement by  $1.0 \pm 0.1$  to get the  $\pm 10\%$  tolerances for your estimation.

Two of your students, Sandra and Mario, return to you with a solution.

They say, "We weren't sure of everyone's weight. We used 65 lbs. for the people we didn't know and added everyone who does know. There are 30 of us, and we got 2,000 lbs.! That's a ton!"

You estimated 1,900 lbs. assuming the average weight of a student in your class was 60 lbs. So, you are pleased with Sandra's and Mario's answer. You instruct your students to all gather on the giant scale and read off the weight together. To all your surprise, the scale reads *10,000 lbs!* 10,000 is significantly more than a 10% error from 2,000. In fact, it is approximately 5 times more massive than either your or your students' estimates. You think to yourself and conclude there must be something wrong with the scale. You ask an employee to check the scale and verify it is well calibrated. They confirm that the scale is in working order. You weigh a couple of students individually to assess that the scale is well calibrated. Sandra weighs 59 lbs., and Mario weighs

62 lbs., typical weights for their age. You then weigh each student individually and see that their weights individually do not deviate greatly from 60 lbs. So, where does all the extra weight come from?

This thought experiment serves as an analogy to the Dark Matter problem. The important substitution to make however is to replace the students with stars and the classroom with a galaxy, say the Milky Way. Individually the mass of stars is well measured and defined with the Sun as our nearest test case. However, when we set out to measure the mass of a collection of stars as large as galaxies, our well-motivated estimation is wildly incorrect. There simply is no way to account for this discrepancy except without some unseen, or dark, contribution to mass and matter in galaxies. I set out in my thesis to narrow the possibilities of what this Dark Matter could be.

This chapter is organized like the following... **TODO: Text should look like ... Chapter x has blah blah blah.**

## 1.2 Dark Matter Basics

Presently, a more compelling theory of cosmology that includes Dark Matter (DM) in order to explain a variety of observations is  $\Lambda$  Cold Dark Matter, or  $\Lambda$ CDM. I present the evidence supporting  $\Lambda$ CDM in Section 1.3 yet discuss the conclusions of the  $\Lambda$ CDM model here. According to  $\Lambda$ CDM fit to observations on the Cosmic Microwave Background (CMB), DM is 26.8% of the universe's current energy budget. Baryonic matter, stuff like atoms, gas, and stars, contributes to 4.9% of the universe's current energy budget [1, 2, 3].

DM is dark; it does not interact readily with light at any wavelength. DM also does not interact noticeably with the other standard model forces (Strong and Weak) at a rate that is readily observed [3]. DM is cold, which is to say that the average velocity of DM is below relativistic speeds [1]. 'Hot' DM would not likely manifest the dense structures we observe like galaxies, and instead would produce much more diffuse galaxies than what is observed [3, 1]. DM is old; it played a critical role in the formation of the universe and the structures within it [1, 2].

Observations of DM have so far been only gravitational. The parameter space available to what DM could be therefore is extremely broad. The broad DM parameter space is iteratively tested in

DM searches by supposing a hypothesis that has not yet been ruled out and performing observations to test them. When the observations yield a null result, the parameter space is constrained further. I present some approaches for DM searches in Section 1.4.

### 1.3 Evidence for Dark Matter

Dark Matter (DM) has been a looming problem in physics for almost 100 years. Anomalies have been observed by astrophysicists in galactic dynamics as early as 1933 when Fritz Zwicky noticed unusually large velocity dispersion in the Coma cluster. Zwicky's measurement was the first recorded to use the Virial theorem to measure the mass fraction of visible and invisible matter in celestial bodies [4]. From Zwicky in [5], "*If this would be confirmed, we would get the surprising result that dark matter is present in much greater amount than luminous matter.*" Zwicky's and others' observation did not instigate a crisis in astrophysics because the measurements did not entirely conflict with their understanding of galaxies [4]. In 1978, Rubin, Ford, and Norbert measured rotation curves for ten spiral galaxies [6]. Rubin et al.'s 1978 publication presented a major challenge to the conventional understanding of galaxies that could no longer be dismissed by measurement uncertainties. Evidence has been mounting ever since for this exotic form of matter. The following subsections provide three compelling pieces of evidence in support of the existence of DM.

#### 1.3.1 First Clues: Stellar Velocities

Zwicky, and later Rubin, measured the stellar velocities of various galaxies to estimate their virial mass. The Virial Theorem upon which these observations are interpreted is written as

$$2T + V = 0. \quad (1.1)$$

Where  $T$  is the kinetic energy and  $V$  is the potential energy in a self-gravitating system. The classical Newton's law of gravity from stars and gas was used for gravitational potential modeled in the observed galaxies:

$$V = -\frac{1}{2} \sum_i \sum_{j \neq i} \frac{m_i m_j}{r_{ij}}. \quad (1.2)$$

Zwicky et al. measured just the velocities of stars apparent in optical wavelengths [5]. Rubin et al. added by measuring the velocity of the hydrogen gas via the 21 cm emission line of Hydrogen [6]. The velocities of the stars and gas are used to infer the total mass of galaxies and galaxy clusters via Equation (1.1). An inferred mass is obtained from the luminosity of the selected sources. The two inferences are compared to each other as a luminosity to mass ratio which typically yielded [1]

$$\frac{M}{L} \sim 400 \frac{M_{\odot}}{L_{\odot}} \quad (1.3)$$

$M_{\odot}$  and  $L_{\odot}$  referring to stellar mass and stellar luminosity, respectively. These ratios clearly indicate a discrepancy in apparent light and mass from stars and gas and their velocities.

Rubin et al. [6] demonstrated that the discrepancy was unlikely to be an underestimation of the mass of the stars and gas. The inferred "dark" mass was up to 5 times more than the luminous mass. This dark mass also needed to extend well beyond the extent of the luminous matter.

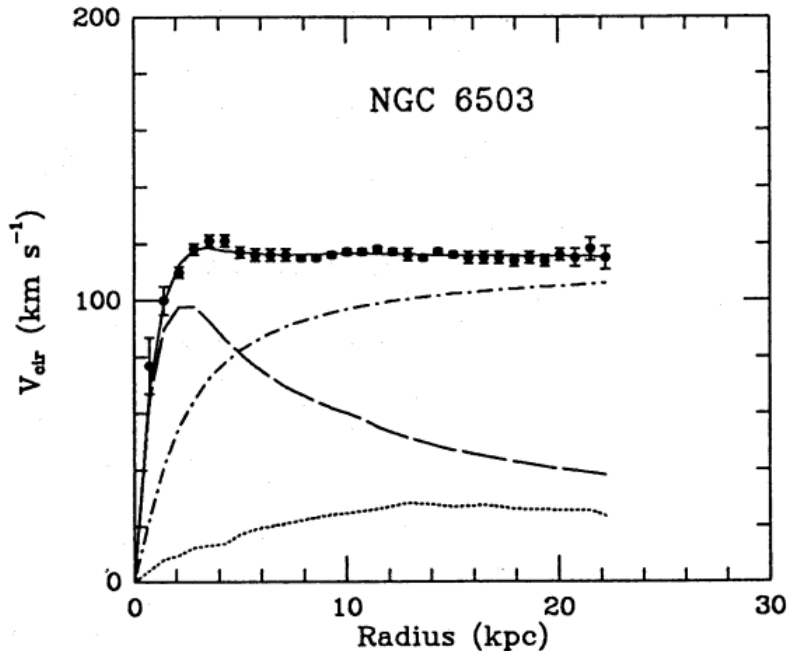


Figure 1.1 Rotation curve fit to NGC 6503 from [7]. Dashed line is the contribution from visible matter. Dotted curves are from gas. Dash-dot curves are from dark matter (DM). Solid line is the composite contribution from all matter and DM sources. Data are indicated with bold dots with error bars. Data agree strongly with a matter + DM composite prediction.

Figure 1.1 features one of many rotation curves plotted from the stellar velocities within galaxies.

The measured rotation curves mostly feature a flattening of velocities at higher radius which is not expected if the gravity was only coming from gas and luminous matter. The extension of the flat velocity region also indicates that the DM is distributed far from the center of the galaxy. Modern velocity measurements include significantly larger objects, galactic clusters, and smaller objects, dwarf galaxies. Yet, measurements along this regime are leveraging the Virial theorem with Newtonian potential energies. We know Newtonian gravity is not a comprehensive description of gravity. New observational techniques have been developed since 1978, and those are discussed in the following sections.

### 1.3.2 Evidence for Dark Matter: Gravitational Lensing

Modern evidence for dark matter comes from new avenues beyond stellar velocities. Gravitational lensing from DM is a new channel from general relativity. General relativity predicts aberrations in light caused by massive objects. In recent decades we have been able to measure the lensing effects from compact objects and DM halos. Figure 1.2 shows how different massive objects change the final image of a faraway galaxy resulting from gravitational lensing. Gravitational lensing developed our understanding of dark matter in two important ways.

Gravitational lensing provides additional compelling evidence for DM. The observation of two merging galactic clusters in 2006, shown in Figure 1.3, provided a compelling argument for DM outside the Standard Model. These clusters merged recently in astrophysical time scales. Galaxies and star cluster have mostly passed by each other as the likelihood of their collision is low. Therefore, these massive objects will mostly track the highest mass, dark and/or baryonic, density. Yet, the intergalactic gas is responsible for the majority of the baryonic mass in the systems [4]. These gas bodies will not phase through and will heat up as they collide together. The hot gas is located via x-ray emission from the cluster. Two observations of the clusters were performed independently of each other.

The first was the lensing of light around the galaxies due to their gravitational influences. When celestial bodies are large enough, the gravity they exert bends space and time itself. The warped space-time lenses light and will deflect in an analogous way to how glass lenses will bend

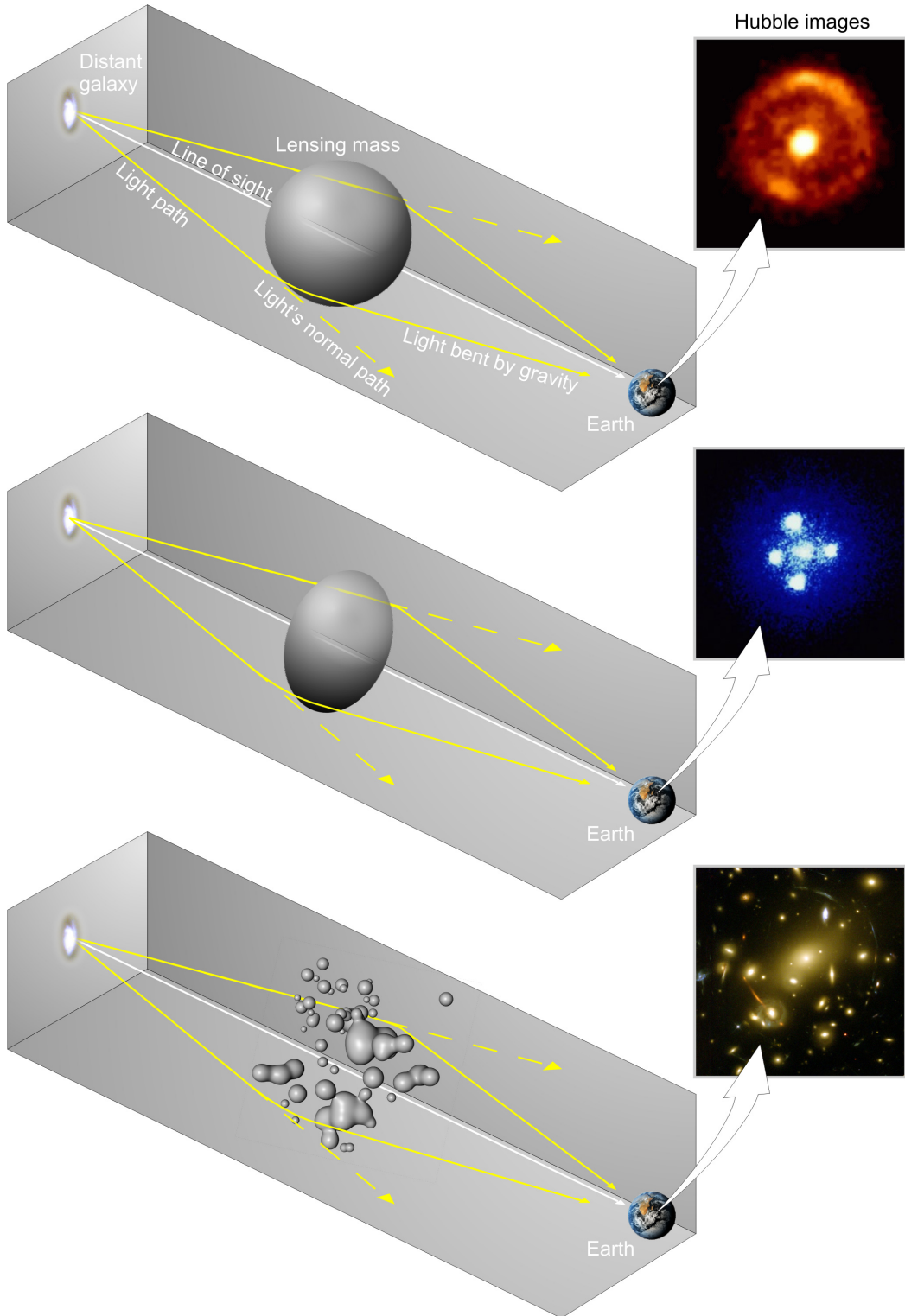


Figure 1.2 Light from distant galaxy is bent in unique ways depending on the distribution of mass between the galaxy and Earth. Yellow dashed lines indicate where the light would have gone if the matter were not present [8].

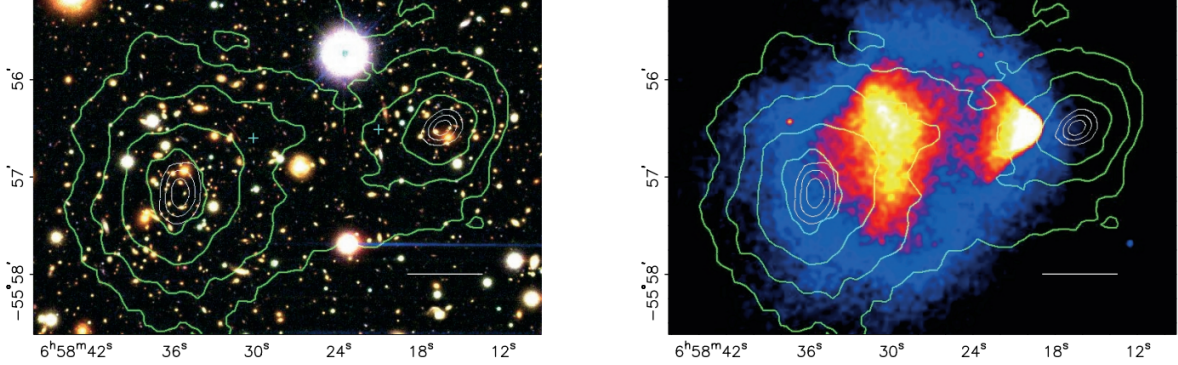


Figure 1.3 (left) Optical image of galactic cluster 1E0657-558. (right) X-ray image of the cluster with redder meaning hotter and higher baryon density. (both) Green contours are reconstruction of gravity contours from weak lensing. White rings are the best fit mass maxima at 68.3%, 95.5%, and 99.7% confidence. The matter maxima of the clusters are clearly separated from x-ray maxima. [9]

light, see Figure 1.2. With a sufficient understanding of light sources behind a massive object, we can reconstruct the contours of the gravitational lenses. The gradient of the contours shown in Figure 1.3 then indicates how dense the matter is and where it is.

The x-ray emission can then be observed from the clusters. Since these galaxies are mostly gas and are merging, then the gas should be getting hotter. If they are merging, the x-ray emissions should be the strongest where the gas is mostly moving through each other. Hence, X-ray emission maps out where the gas is in the merging galaxy cluster.

The lensing and x-ray observations were done on the Bullet cluster featured on Figure 1.3. The x-ray emissions do not align with the gravitational contours from lensing. The incongruence in mass density and baryon density suggests that there is a lot of matter somewhere that does not interact with light. Moreover, this dark matter cannot be baryonic [9]. The Bullet Cluster measurement did not really tell us what DM is exactly, but it did give the clue that DM also does not interact with itself very strongly. If DM did interact strongly with itself, then it would have been more aligned with the x-ray emission [9]. There have been follow-up studies of galaxy clusters with similar results. The Bullet Cluster and others like it provide a persuasive case against something possibly amiss in our gravitational theories.

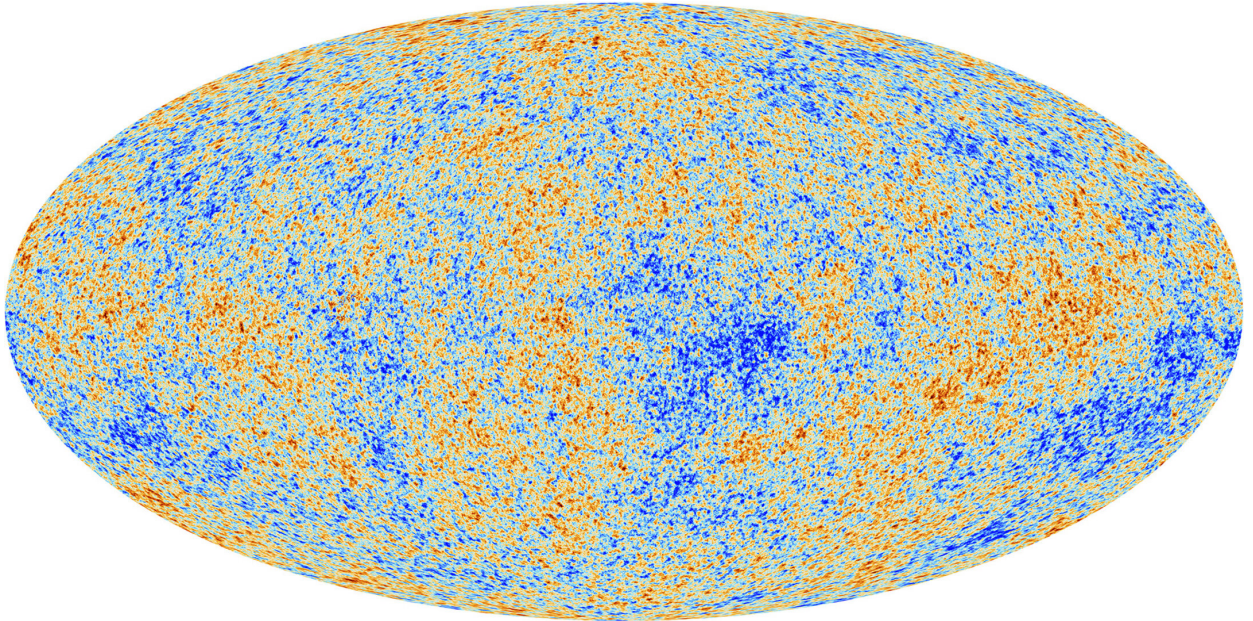


Figure 1.4 Plank CMB sky. Sky map features small variations in temperature in primordial light. These anisotropies are used to make inferences about the universe’s energy budget and developmental history. [10]

### 1.3.3 Evidence for Dark Matter: Cosmic Microwave Background

The Cosmic Microwave Background (CMB) is the primordial light from the early universe when Hydrogen atoms formed from the free electron and proton soup in the early universe. The CMB is the earliest light we can observe; released when the universe was about 380,000 years old. Then we look at how the simulated universes look like compared to what we see. Figure 1.4 is the most recent CMB image from the Plank satellite after subtracting the average value and masking the galactic plane [10]. Redder regions indicate a slightly hotter region in the CMB, and blue indicates colder. The intensity variations are on the order of 1 in 1000 with respect to the average value.

The Cosmic Microwave Background shows that the universe had DM in it from an incredibly early stage. To measure the DM, Dark Energy, and matter fractions of the universe from the CMB, the image is analyzed into a power spectrum, which shows the amplitude of the fluctuations as a function of spherical multipole moments.  $\Lambda$ CDM provides the best fit to the power spectra of the CMB as shown in Figure 1.5. The CMB power spectrum is quite sensitive to the fraction of each energy contribution in the early universe. Low  $l$  modes are dominated by variations in gravitational potential. Intermediate  $l$  emerge from oscillations in photon-baryon fluid from

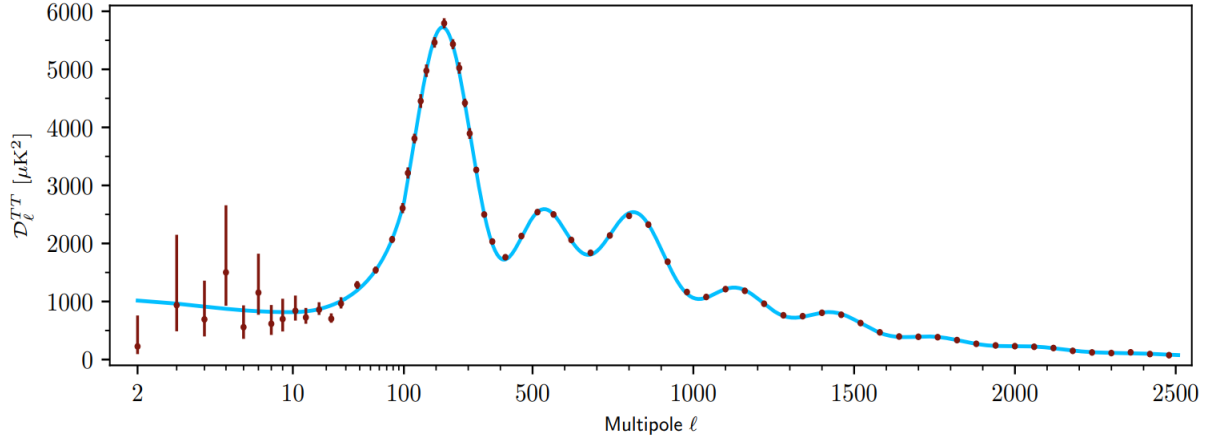


Figure 1.5 Observed Cosmic Microwave Background power spectrum as a function of multipole moment from Plank [10]. Blue line is best fit model from  $\Lambda$ CDM. Red points and lines are data and error, respectively.

competing baryon pressures and gravity. High  $l$  is a damped region from the diffusion of photons during electron-proton recombination. [1]

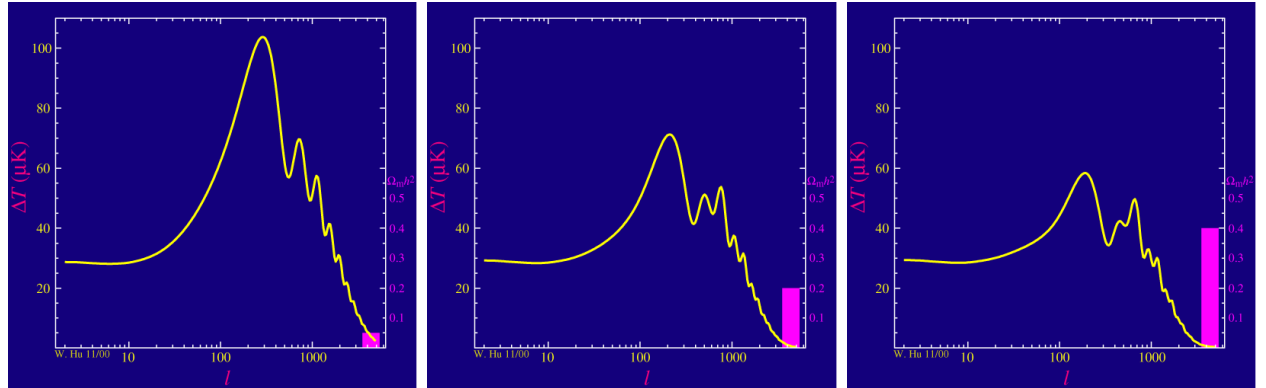


Figure 1.6 Predicted power spectra of CMB for different  $\Omega_m h^2$  values for fixed baryon density from [11]. (left) Low  $\Omega_m h^2$  increases the prominence of first and second peaks. (middle)  $\Omega_m h^2$  is most similar to the observed power spectrum. The second and third peaks are similar in height. (right)  $\Omega_m h^2$  is large which suppresses the first peak and raises the prominence of the third peak.

The harmonics would look quite different for a universe with less DM. Figure 1.6 demonstrates the effect  $\Omega_m h^2$  has on the expected power spectrum for fixed baryon matter density. [11] Sweeping  $\Omega_m h^2$  in this way clearly shows the effect dark matter has on the CMB power spectrum. The observations fit well with the  $\Lambda$ CDM model, and the derived fractions are as follows. The matter fraction:  $\Omega_m = 0.3153$ ; and the baryon fraction:  $\Omega_b = 0.04936$  [10]. Plank's observations also provide a measure of the Hubble constant,  $H_0$ .  $H_0$  especially has seen a growing tension in the

past decade that continues to deepen with observations from instruments like the James Webb Telescope [12, 13]. As Hubble tensions deepen, we may find that perhaps  $\Lambda$ **CDM**, despite its successes, is missing some critical physics.

Overall, the Newtonian motion of stars in galaxies, weak lensing from galactic clusters, and power spectra from primordial light form a compelling body of research in favor of dark matter. It takes another leap of theory and experimentation to make observations of DM that are non-gravitational in nature. In Section 1.3, the evidence for DM implies strongly that the DM is matter and not a lost parameter in the gravitational fields between massive objects. Finally, if we take one axiom: that this matter has quantum behavior, such as being described by some Bohr wavelength and abiding by some fermion or boson statistics; then we arrive at particle dark matter. One particle DM hypothesis is the Weakly Interacting Massive Particle (WIMP). This DM candidate theory is discussed further in the next section and is the focus of this thesis.

#### 1.4 Searching for Dark Matter: Particle DM

Section 1.4 shows the Standard Model of particle physics and is currently the most accurate model for the dynamics of fundamental particles like electrons and photons. The current status of the SM does not have a viable DM candidate. When looking at the standard model, we can immediately exclude any charged particle because charged particles interact strongly with light. Specifically, this will rule out the following charged, fundamental particles:  $e, \mu, \tau, W, u, d, s, c, t, b$  and their corresponding antiparticles. Recalling from Section 1.2 that DM must be long-lived and stable over the age of the universe which excludes all SM particles with decay half-lives at or shorter than the age of the universe. The lifetime constraint additionally eliminates the  $Z$  and  $H$  bosons. Finally, the candidate DM needs to be somewhat massive. Recall from Section 1.2 that DM is cold or not relativistic through the universe. This eliminates the remaining SM particles:  $\nu_{e,\mu,\tau}, g, \gamma$  as DM candidates. Because there are no DM candidates within the SM, the DM problem strongly hints to physics beyond the SM (BSM).

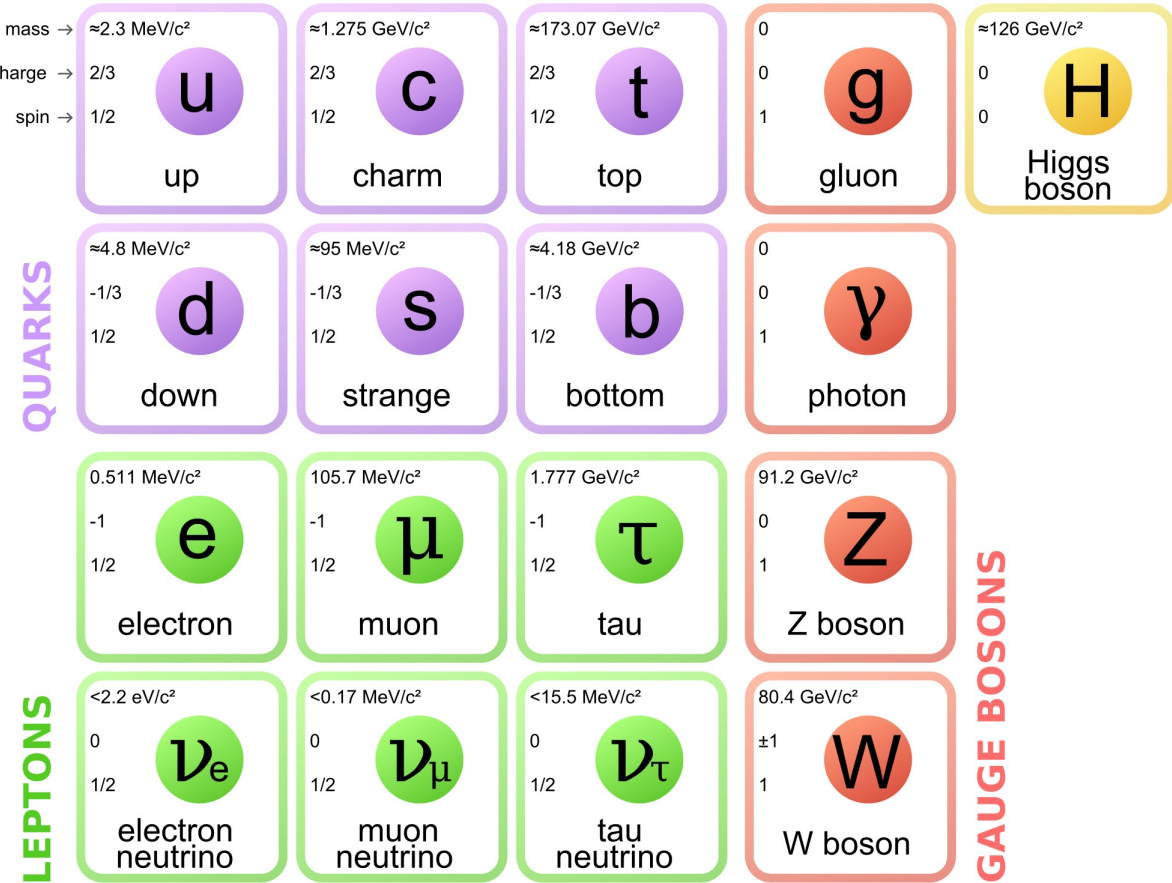


Figure 1.7 The Standard Model (SM) of particle physics. Figure taken from <http://www.quantumdiaries.org/2014/03/14/the-standard-model-a-beautiful-but-flawed-theory/>

### 1.4.1 Shake it, Break it, Make it

When considering DM that couples in some way with the SM, the interactions are roughly demonstrated by interaction demonstrated in Figure 1.8. The figure is a simplified Feynman diagram where the arrow of time represents the interaction modes of: **Shake it, Break it, Make it.**

**Shake it** refers to the direct detection of dark matter. Direct detection interactions start with a free DM particle and an SM particle. The DM and SM interact via elastic or inelastic collision and recoil away from each other. The DM remains in the dark sector and imparts some momentum onto the SM particle. The hope is that the momentum imparted onto the SM particle is sufficiently high enough to pick up with extremely sensitive instruments. Because we cannot create the DM in the lab, a direct detection experiment must wait until DM is incident on the detector. Most direct detection experiments are therefore placed in low-background environments with inert detection

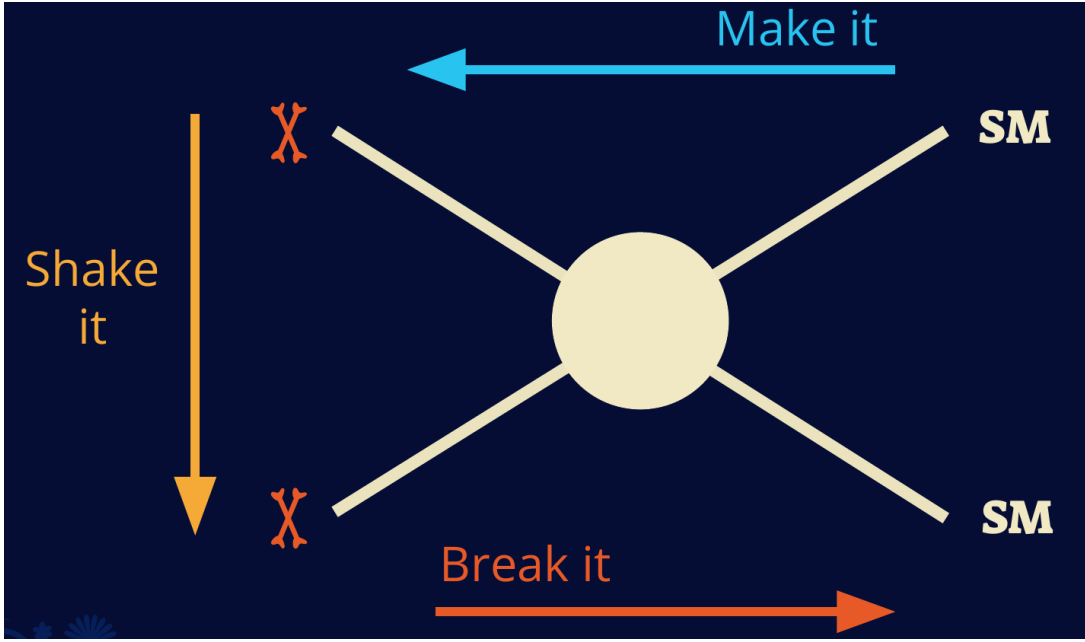


Figure 1.8 Simplified Feynman diagram demonstrating different ways DM can interact with SM particles. The 'X's refer to the DM particles whereas the SM refer to fundamental particles in the SM. The large circle in the center indicates the vertex of interaction and is purposely left vague. The colored arrows refer to different directions of time as well as their respective labels. The arrows indicate the initial and final state of the DM -SM interaction in time.

media like the noble gas Xenon. [14]

**Make it** refers to the production of DM from SM initial states. The experiment starts with particles in the SM. These SM particles are accelerated to incredibly high energies and then collide with each other. In the confluence of energy, DM hopefully emerges as a byproduct of the SM annihilation. Often it is the collider experiments that are energetic enough to hypothetically produce DM. These experiments include the world-wide collaborations ATLAS and CMS at CERN where protons collide together at extreme energies. The DM searches, however, are complex. DM likely does not interact with the detectors and lives long enough to escape the detection apparatus of CERN's colliders. This means any DM production experiment searches for an excess of events with missing momentum or energy in the events. An example event with missing transverse momentum is shown in Figure 1.9. The missing momentum with no particle tracks implies a neutral particle carried the energy out of the detector. However, there are other neutral particles in the SM, like neutrons or neutrinos, so any analysis has to account for SM signatures of missing

momentum. [15]

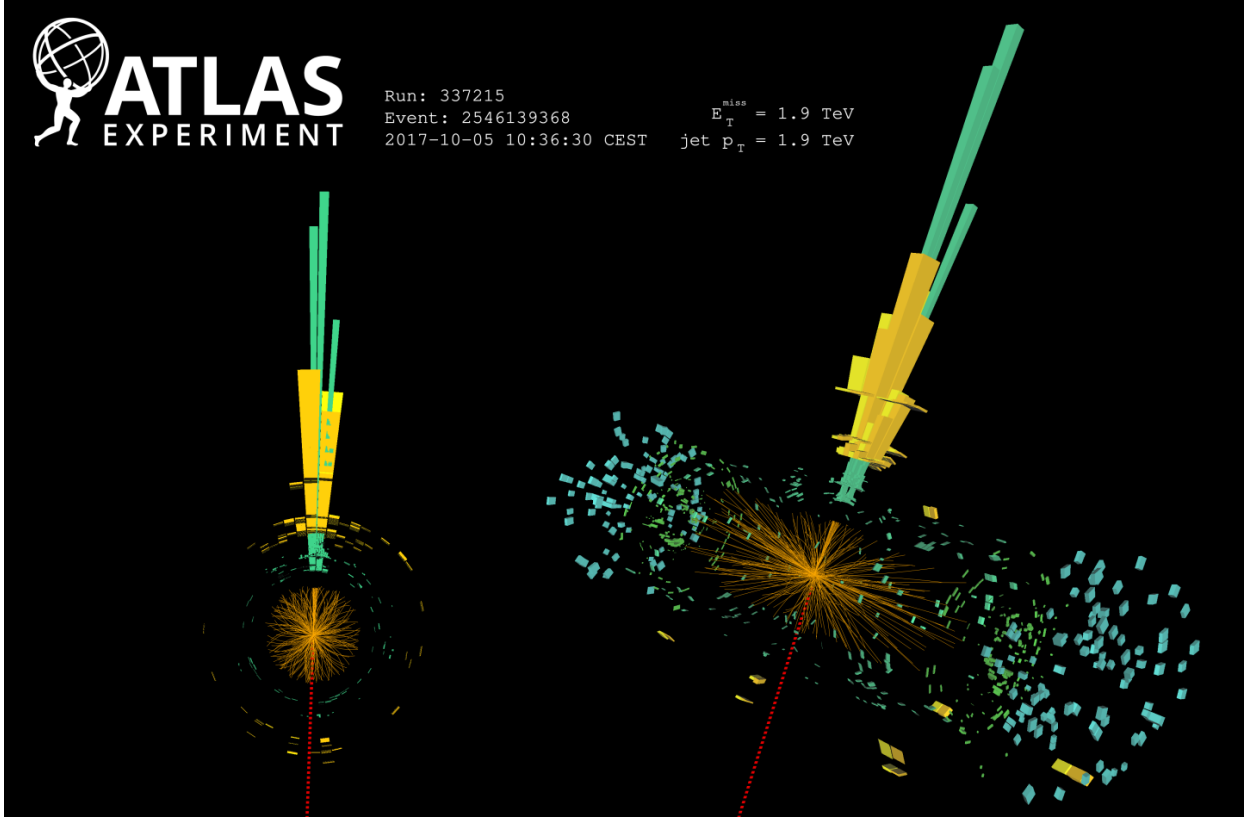


Figure 1.9 A single jet event in ATLAS detector from 2017 [16]. Jet momentum was observed to be 1.9 TeV. Missing transverse momentum was observed to be 1.9 TeV compared to the initial transverse momentum of the event was 0. Implied MET is traced by a red dashed line in event display.

#### 1.4.2 Break it: Standard Model Signatures of Dark Matter through Indirect Searches

**Break it** refers to the creation of SM particles from the dark sector, and it is the primary focus of this thesis. The interaction begins with DM or in the dark sector. The hypothesis is that this DM will either annihilate with itself or decay and produce an SM byproduct. This method is often referred to as the Indirect Detection of DM because we have no lab to directly control or manipulate the DM. Therefore, most indirect DM searches are performed using observations of known DM densities among the astrophysical sources. The strength is that we have the whole of the universe and its 13.6-billion-year lifespan to use as a detector and particle accelerator. Additionally, locations of dark matter are well cataloged since it was astrophysical observations that presented

the problem of DM in the first place.

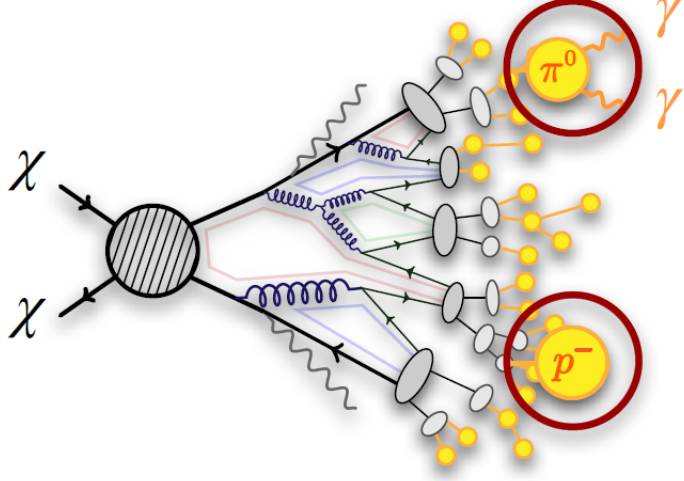


Figure 1.10 More detailed pseudo-Feynman diagram of particle cascade from dark matter annihilation into 2 quarks. The quarks hadronize and down to stable particles like  $\gamma$  or the anti-proton ( $p^-$ ). Diagram pulled from ICRC 2021 presentation on DM annihilation search [17].

However, anything can happen in the universe. There are many difficult to deconvolve backgrounds when searching for DM. One prominent example is the galactic center. We know the galactic center has a large DM content because of stellar kinematics in our Milky Way and DM halo simulations. Yet, any signal from the galactic center is challenging to parse apart from the extreme environment of our supermassive black hole, unresolved sources, and diffuse emission from the interstellar medium [18]. Despite the challenges, any DM model that yields evidence in the other two observation methods, **Shake it or Make it** must be corroborated with indirect observations of the known DM sources. Without corroborating evidence, DM observation in the lab is hard-pressed to demonstrate that it is the model contributing to the DM seen at the universal scale.

In the case of WIMP DM, signals are described in terms of primary SM particles produced from DM decay or annihilation. The SM initial state particles are then simulated down to stable final states such as the  $\gamma$ ,  $\nu$ ,  $p$ , or  $e$  which can traverse galactic lengths to reach Earth.

Figure 1.10 shows the quagmire of SM particles that emerges from SM initial states that are not stable [17]. There are many SM particles with varying energies that can be produced in such an

interaction. For any arbitrary DM source and stable SM particle, the SM flux from DM annihilating to a neutral particle in the SM,  $\phi$ , from a region in the sky is described by the following.

$$\frac{d\Phi_\gamma}{dE_\gamma} = \frac{\langle\sigma v\rangle}{8\pi m_\chi^2} \frac{dN_\gamma}{dE_\gamma} \times \int_{\text{source}} d\Omega \int_{l.o.s} \rho_\chi^2 dl(r, \theta') \quad (1.4)$$

In Equation (3.1),  $\langle\sigma v\rangle$  is the velocity-weighted annihilation cross-section of DM to the SM.  $m_\chi$  refers to the mass of DM, noted with Greek letter  $\chi$ .  $\frac{dN_\phi}{dE_\phi}$  is the N particle flux weighted by the particle energy. An example is provided in Figure 1.11 for the  $\gamma$  final state. The integrated terms are performed over the solid angle,  $d\Omega$ , and line of sight, l.o.s.  $\rho$  is the density of DM for a location  $(r, \theta')$  in the sky. The terms left of the ' $\times$ ' are often referred to as the particle physics component. The terms on the right are referred to as the astrophysical component. For decaying DM, the equation changes to...

$$\frac{d\Phi_\phi}{dE_\phi} = \frac{1}{4\pi\tau m_\chi} \frac{dN_\phi}{dE_\phi} \times \int_{\text{source}} d\Omega \int_{l.o.s} \rho_\chi dl(r, \theta') \quad (1.5)$$

In Equation (1.5),  $\tau$  is the decay lifetime of the DM. Just as in Equation (3.1), the left and right terms are the particle physics and the astrophysical components respectively. The integrated astrophysical component of Equation (3.1) is often called the J-Factor. Whereas the integrated astrophysical component of Equation (1.5) is often called the D-Factor.

Exact DM  $\text{DM} \rightarrow \text{SM SM}$  branching ratios are not known, so it is usually assumed to go 100% into an SM particle/anti-particle. Additionally, when a DM annihilation or decay produces one of the neutral, long-lived SM particles ( $\nu$  or  $\gamma$ ), the particle is traced back to a DM source. For DM above GeV energies, there are very few SM processes that can produce particles with such a high energy. Seeing such a signal would almost certainly be an indication of the presence of dark matter. Fortunately, the universe provides us with the largest volume and lifetime ever for a particle physics experiment.

## 1.5 Sources for Indirect Dark Matter Searches

The first detection of DM relied on optical observations. Since then, we have developed new techniques to find DM dense regions. As described in Section 1.3.1, many DM dense regions were found through observing galactic rotation curves. Our Milky Way galaxy is among DM dense regions

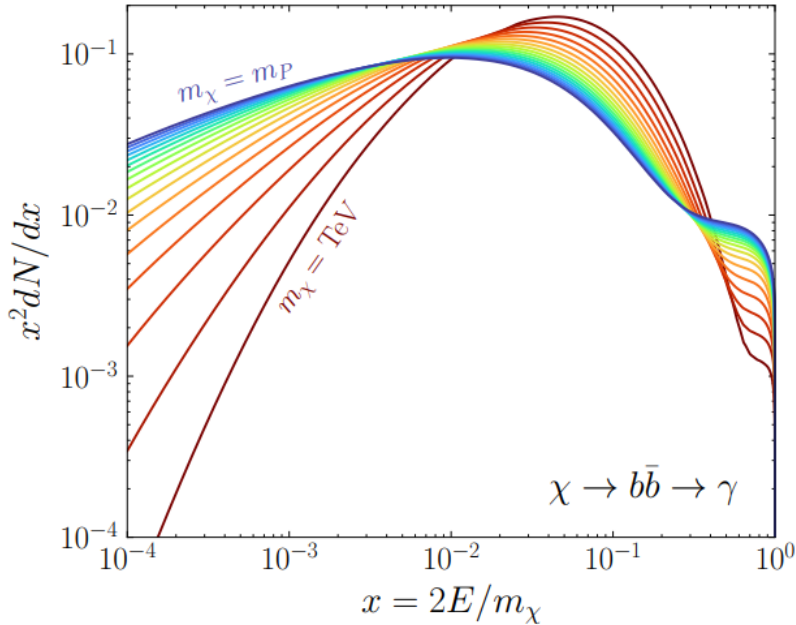


Figure 1.11 Dark Matter (DM) decay spectrum for  $b\bar{b}$  initial state and  $\gamma$  final state. Redder spectra are for larger DM masses. Bluer spectra are light DM masses.  $x$  is a unitless factor defined as the ratio of the mass of DM,  $m_\chi$ , and the final state particle energy  $E_\gamma$ . Figure from [19].

discovered, and it is the largest nearby DM dense region to look at. Additionally, the DM halo surrounding the Milky Way is clumpy [18]. There are regions in the DM halo of the Milky Way that have more DM than others that have captured gas over time. These sub-halos were dense enough collapse gas and form stars. These apparent sub galaxies are known as dwarf spheroidal galaxies and are the main sources studied in this thesis. Each source type comes with different trade-offs. Galactic Center studies will be very sensitive to the assumed distribution of DM. The central DM density can vary substantially as demonstrated in Figure 1.12. At distances close to the center of the galaxy, or small  $r$ , the differences in DM densities can be 3-4 orders of magnitude. Searches toward the galactic center will therefore be quite sensitive to the assumed DM distribution.

Searches toward Dwarf Spheroidal Galaxies (dSph's) suffer from uncertainties in the DM density less than the galactic center studies. This is mostly from their diminutive size being smaller than the angular resolution of most  $\gamma$ -ray observatories [18]. The DM content dSph's are typically determined with the Virial theorem, Equation (1.1), and are usually majority DM [18] in mass. DSph's tend to be ideal sources to look at for DM searches. Their environments are quiet with little

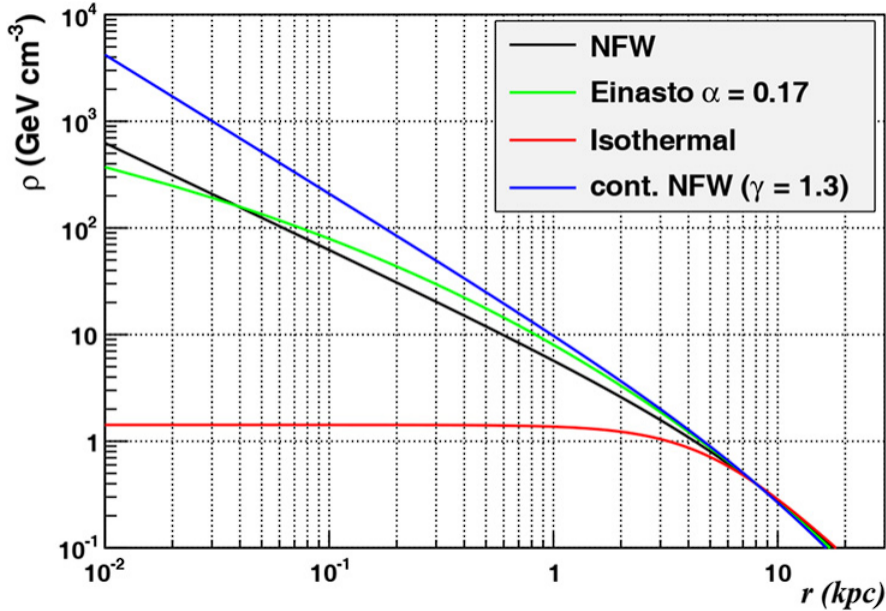


Figure 1.12 Different dark matter density profiles compared. Some models produce exceptionally large densities at small  $r$  [20].

astrophysical background. Unlike the galactic center, the most active components of dSph's are the stars within them versus a violent accretion disc around a black hole. All this together means that dSph's are among the best sources to look at for indirect DM searches. dSph's are the targets of focus for this thesis.

## 1.6 Multi-Messenger Dark Matter

Astrophysics entered a new phase in the past few decades that leverages our increasing sensitivity to SM channels and general relativity (GR). Up until the 21st century, astrophysical observations were performed with photons ( $\gamma$ ) only. Astrophysics with this 'messenger' is fairly mature now. Novel observations of the universe have since only adjusted the sensitivity of the wavelength of light that is observed except at MeV energies. Gems like the CMB [10], and more have ultimately been observations of different wavelengths of light. Multi-messenger astrophysics proposes using other SM particles such as the  $p^{+/-}$ , or  $\nu$  or gravitation waves predicted by general relativity.

The experiment LIGO had a revolutionary discovery in 2016 with the first detection of a binary black hole merger [21]. This opened the collective imagination to observing the universe through gravitational waves. There has also been a surge of interest in the neutrino ( $\nu$ ) sector. IceCube

demonstrated that we are sensitive to neutrinos in regions that correlate with significant photon emission like the galactic plane [22]. Neutrinos, like gravitational waves and light, travel mostly unimpeded from their source to our observatories. This makes pointing to the originating source of these messengers much easier than it is for cosmic rays which are deflected from their source by magnetic fields.

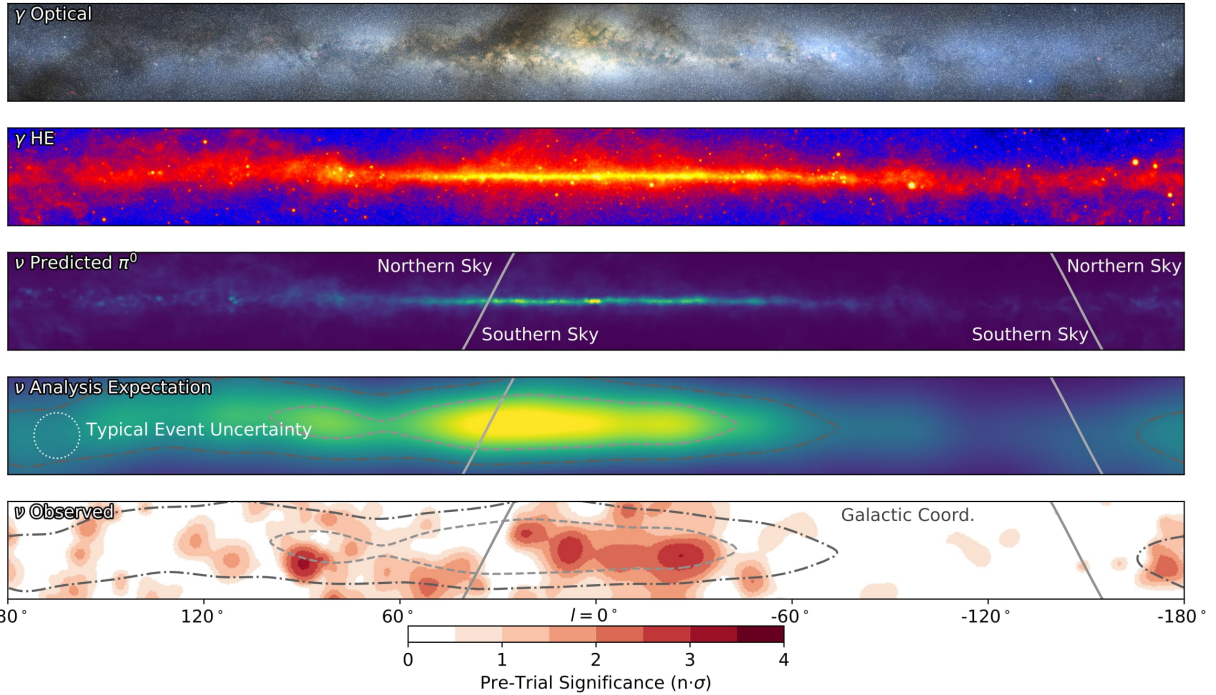


Figure 1.13 The Milky Way Galaxy in photons ( $\gamma$ ) and neutrinos ( $\nu$ ) [22]. The Galactic center is at  $l=0^\circ$  and is the brightest region in all panels. (top) An Optical color image of the Milky Way galaxy seen from Earth. Clouds of gas and dust obscure some light from stars. (2nd down) Integrated flux of  $\gamma$ -rays observed by the Fermi-LAT telescope [23]. (middle) Expected neutrino emission that corresponds with Fermi-LAT observations. (2nd up) Expected neutrino emission profile after considering detector systematics of IceCube. (bottom) Observed neutrino emission from region of the galactic plane. Substantial neutrino emission was detected.

The IceCube collaboration recently published a groundbreaking result of the Milky Way in neutrinos. The recent result from IceCube, shown in Figure 1.13, proves that we can make observations under different messenger regimes. The top two panels show the appearance of the galactic plane to different wavelengths of light. Some sources are more apparent in some panels, while others are not. This new channel is powerful because neutrinos are readily able to penetrate through gas and dust in the Milky Way. This new image also refines our understanding of how high

energy particles are produced. For example, the fit to IceCube data prefers neutrino production from the decay of  $\pi^0$  [22].

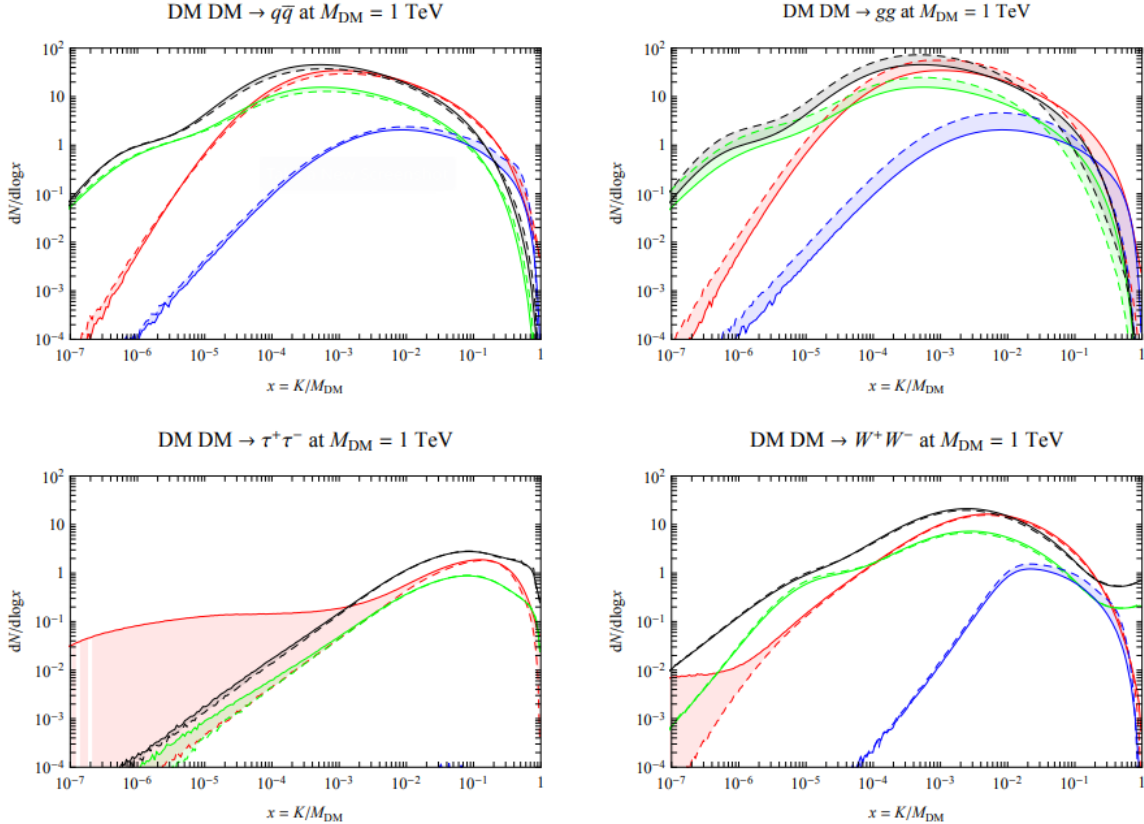


Figure 1.14 Dark Matter annihilation spectra for different final state particle and standard model annihilation channels [24]. Photons (red),  $e^\pm$  (green),  $\bar{p}$  (blue),  $\nu$  (black).

Exposing our observations to more cosmic messengers greatly increases our sensitivity to rare processes. In the case of DM, Figure 1.14, there are many SM particles produced in DM annihilation. Among the final state fluxes are gammas and neutrinos. Charged particles are also produced however they would not likely make it to Earth since they will be deflected by magnetic fields between the source and Earth. This means observatories that can see the neutral messengers are especially good for DM searches and for combining data for a multi-messenger DM search.

## CHAPTER 2

### HIGH ALTITUDE WATER CHERENKOV (HAWC) OBSERVATORY

#### 2.1 The Detector



Figure 2.1 Photo of the HAWC detector that I took on May 17, 2023. Main array is centered in the photo and comprised of the larger tanks. Outriggers are the smaller tanks around the main array.

The High Altitude Water Cherenkov (HAWC) Observatory is a specialized instrument designed for the observation of high energy gamma-rays and cosmic rays [25]. Located on the Sierra Negra volcano in Mexico, HAWC observes gamma rays and cosmic rays in the energy range of approximately 100 GeV to 100's of TeV. HAWC is strategically situated to maximize observational efficiency due to its high altitude. At an elevation of 4,100 meters, it monitors about two-thirds of the sky every day with an uptime above 90%. This capability is essential for studying high-energy astrophysical phenomena.

HAWC consists of 300 water Cherenkov detectors (WCDs) spread over  $22,000 \text{ m}^2$ . Each main array detector is filled with purified water and equipped with four, upward-facing photomultiplier tubes (PMTs). See Fig. 2.3 for schematic of WCDs. These PMTs detect Cherenkov radiation from charged particles passing through the tanks. These charged particles are generated when a high

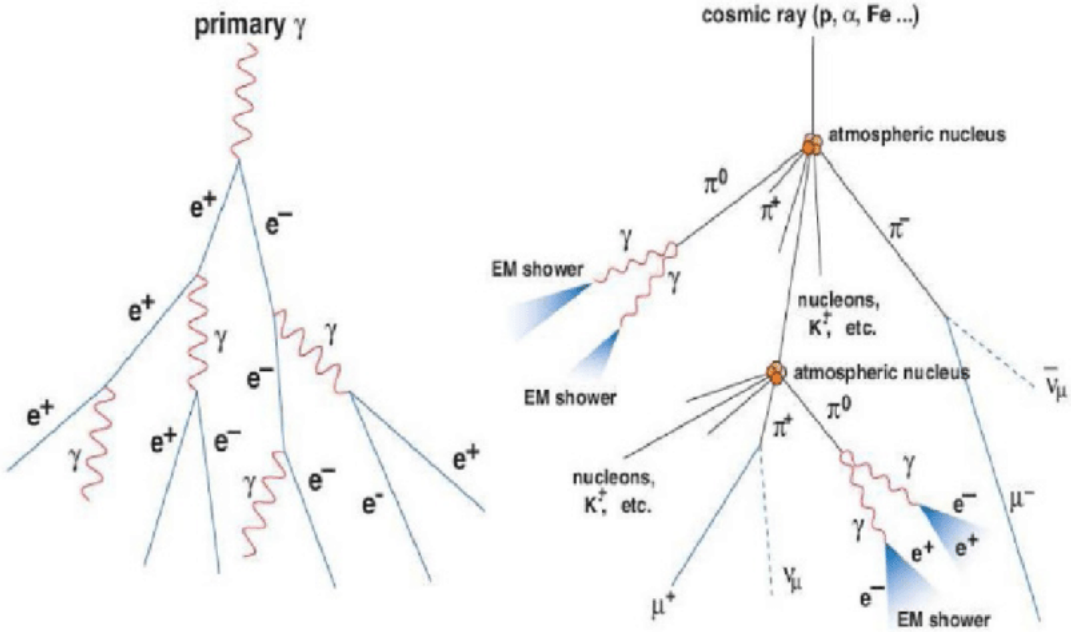


Figure 2.2 A particle physics illustration of high energy particle showers. Left shower is an electromagnetic shower from a high energy gamma-ray. Most particles in the shower will be a combination of photons and charged leptons, in this case electrons ( $e$ ). Right figure shows a cosmic ray particle shower. The cosmic ray will produce many more types of particles including pions ( $\pi$ ), neutrinos, and charged leptons. Figured pulled from [26].

energy gamma or cosmic ray collides with gas in the atmosphere to create a charged particle shower, see Fig. 2.2. The observatory includes a separate tank configuration which are referred to as the outriggers. They are a secondary array of 345 smaller WCD's. Surrounding the main array, each outrigger tank measures 1.55 meters in diameter and height and contain a single upward-facing eight-inch PMT. This add-on increases the instrumented footprint fourfold. The outriggers are meant to improve the reconstruction of showers extending beyond the main array, especially for events above 10 TeV. However, at the time of writing this thesis, the outriggers have not been fully integrated into HAWC's reconstruction software.

### 2.1.1 Construction and Hardware

Each main array WCD, see Fig. 2.3, is a cylindrical tank with dimensions of 7.3 m in diameter and 5.4 m in height and filled with 180,000 L of water [25]. The metal shell of these tanks is made from bolted together, corrugated, galvanized steel panels. The tanks are placed into 0.6 m deep

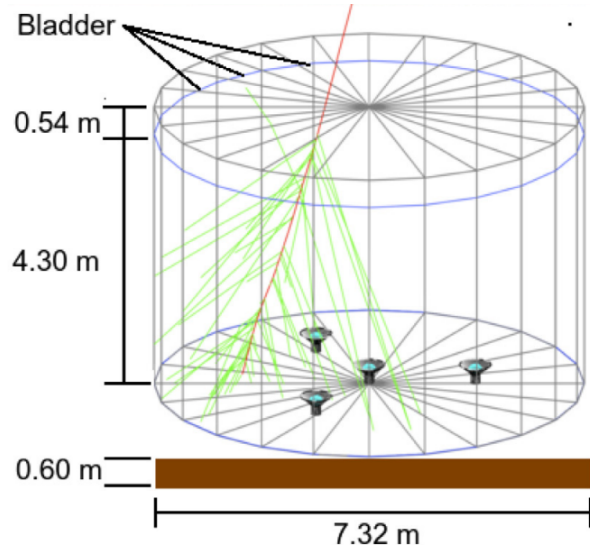


Figure 2.3 The WCDs. Left image features several WCDs looking from within the main array of HAWC. Right image shows a schematic of a WCD pulled from [25].

trenches filled with rammed earth to secure it against seismic activity [27]. The interior of each tank is lined with a black, low-density polyethylene bladder, designed to be impermeable to external light and to prevent reflection of Cherenkov light within the tank. This bladder is approximately 0.4 mm thick and composed of two layers of three-substrate film. To further minimize light penetration, a black agricultural foil covers the bladder. The ground and walls inside the tank are protected with felt and sand to safeguard against punctures. The tanks are filled 4.5 m deep of purified water, achieving a photon attenuation length for Cherenkov photons that exceeds the tank's dimensions [27]. This purification level ensures the optimal detection environment for the photons generated by traversing charged particles.

At the base of each tank, four photomultiplier tubes (PMTs) are installed to detect the Cherenkov radiation emitted by charged particles in water. Three 8-inch diameter PMTs surround a larger 10 inch PMT from Hamamatsu [28]. The variation in PMT response is carefully accounted for in event reconstruction algorithms. Signals from the PMTs traverse 610 ft cables to the counting house, where they are processed by Front-End Boards (FEBs), see Figs. 2.4 and 2.5. These FEBs, along with Time to Digital Converters (TDCs), digitize the signals and manage the high voltage supply to the PMTs.

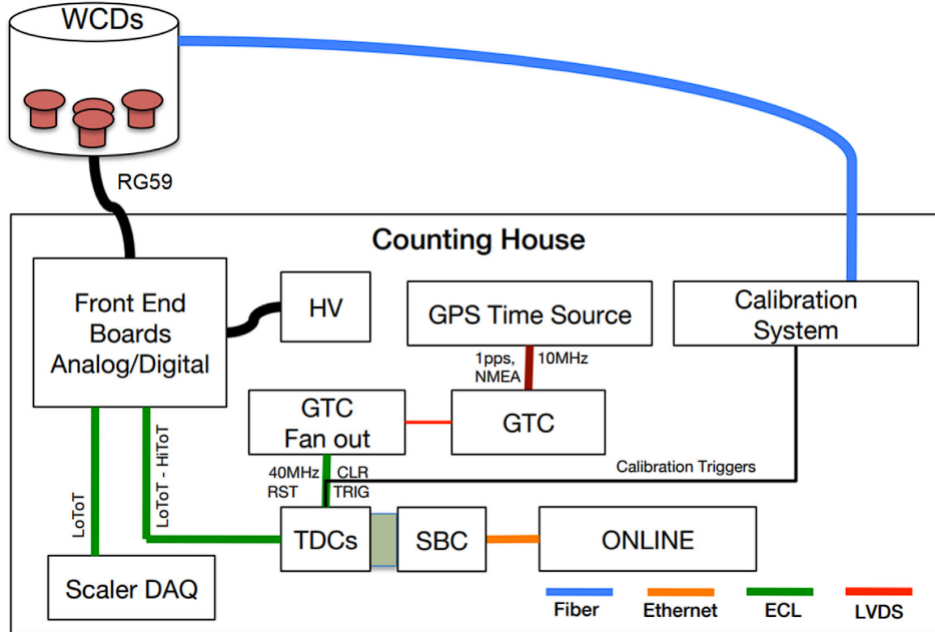


Figure 2.4 Overview of HAWC control and data electronics. The LoToT and HiToT threshold signals are discussed in Section 2.1.2. Figure from [27]

## 2.1.2 Data Acquisition and Signal Processing

The HAWC data acquisition (DAQ) and signal processing systems convert the physical detection of particles into analyzable data. This process involves a series of steps from initial signal detection by PMTs to digital conversion and preliminary analysis, see Figs. 2.5 and 2.6.

Once the signal from the PMTs arrive at the counting house, they enter the Front-End Boards (FEBs). The FEBs are responsible for the initial processing of these signals, which includes amplification and integration [30]. Each PMT signal is compared against preset LOW/HIGH voltage thresholds in the FEBs, see Fig. 2.6, identifying signals that correspond to about 1/4 and 4 photoelectrons, respectively. This differentiation allows the system to gauge the strength of the detected Cherenkov radiation. The processed signals are then digitized by Time to Digital Converters (TDCs). These converters measure the time over threshold (ToT) for each signal, a parameter that reflects both the duration and amplitude of the signal. This digitization facilitates reconstruction of the original event for translating the physical interactions within the detectors into data [27, 29, 30].

Synchronization across the HAWC observatory is maintained by a central GPS Timing and

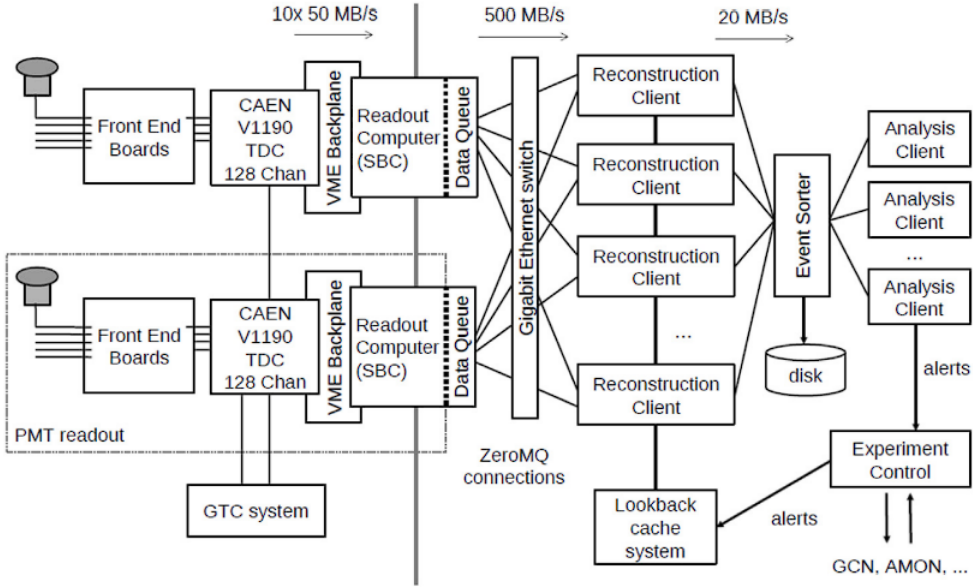


Figure 2.5 Schematic of data flow in HAWC data acquisition and online processing system. Pulled from [29].

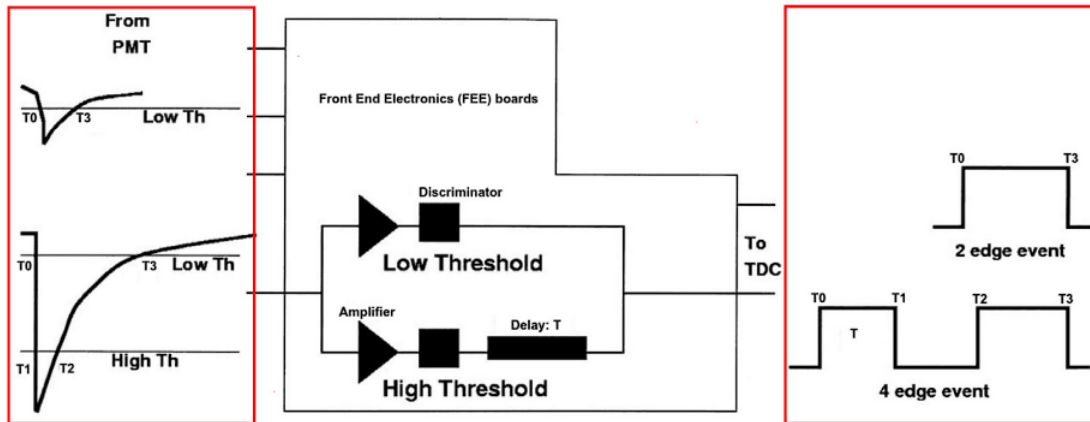


Figure 2.6 How HAWC FEB intially processes analog PMT signals. Signals are split through an amplifier and discriminator circuit. Each path is designated for either the HIGH or LOW threshold for the signal. The 2-edge event corresponds to LOW, while the 4 edge corresponds to HIGH.

Control (GTC) system, which achieves a timing resolution of 98 ps. This high-resolution timing is vital for accurately reconstructing the timing and location of air showers initiated by cosmic and gamma rays. The GTC system ensures that all components of the DAQ operate in unison to preserve the temporal integrity of the detected events [27, 31].

Once digitized, the data are transferred to an online event reconstruction system. This system runs the Reconstruction Client, which utilizes the raw PMT data to reconstruct the characteristics of the air showers, such as their direction and energy [29]. The capacity for real-time analysis allows HAWC to promptly respond to astrophysical phenomena like Gamma Ray Bursts (GRBs) and to participate in multi-messenger astronomy by following up on alerts from other observatories. This real-time processing system is designed to handle high data throughput, using ZeroMQ [32] for efficient data transfer between software components. Analysis Clients perform specific online analyses that require immediate data, including monitoring for GRBs, solar flare activity, and participation in global efforts to track gravitational waves and neutrinos [27].

The DAQ system is overseen by an Experiment Control system and crew that manage the operational aspects of data collection. This includes initiating and terminating data collection runs and monitoring the experiment for errors. In the event of a system crash, often caused by environmental factors such as lightning, the Experiment Control system is designed to automatically restart the experiment and minimize downtime [27, 29].

## 2.2 Event Reconstruction

Event reconstruction at the HAWC Observatory is a critical procedure that converts the raw data from the observatory’s WCDs into a coherent framework for understanding cosmic and gamma-ray events. This process includes several distinct steps. Core Fitting determines the geometric center of the air shower on the detector plane. Angle Reconstruction assesses the trajectory of the incoming particle, revealing its origin in the sky. Energy Estimation is performed using both *f*-hit and Neural Network (NN) methods to quantify the energy of the detected events. Gamma/Hadron discrimination differentiates between gamma-ray and hadronic cosmic ray initiated showers, a vital step for astrophysical interpretations. Each of these steps is integral to the observatory’s objective

of investigating the high-energy universe and enable the transformation of signals into detailed insights about high energy cosmic phenomena.

### 2.2.1 Core Fitting

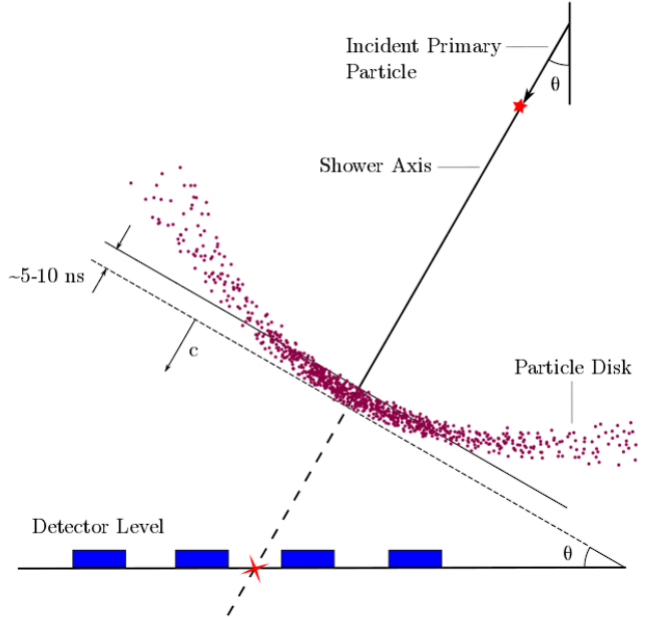


Figure 2.7 An air shower incident on WCDs. Secondary particles of an air shower travel in a cone centered on primary incident particle. Reconstruction of the initial angle is possible with arrival time of hits in PMTs inside WCDs. Figure from [33].

In the study of air showers, accurately determining the location of the air shower core on the ground is crucial for reconstructing the direction of the originating primary particle. An illustration of this can be seen in a HAWC event plot, Figs. 2.2 and 2.11, where the lateral charge distribution across the array is displayed. The core is identified and marked with a red star, reconstructed using a predetermined functional form, Eq. (2.1).

We model signal  $S_i$  from the  $i$ th PMT is given by the following equation:

$$S_i = S(A, \tilde{x}, \tilde{x}_i) = A \left( \frac{1}{2\pi\sigma^2} e^{-\frac{|\vec{x}_i - \vec{x}|^2}{2\sigma^2}} + \frac{N}{(0.5 + |\vec{x}_i - \vec{x}|/R_m)^3} \right) \quad (2.1)$$

In this model,  $\tilde{x}$  represents the core location and  $\tilde{x}_i$  is the position of the  $i$ th PMT.  $R_m$  stands for the Molière radius, which is approximately 120 meters at the altitude of HAWC.  $\sigma$  is the standard deviation of the Gaussian distribution.  $N$  is the normalization factor for the tail of the distribution.

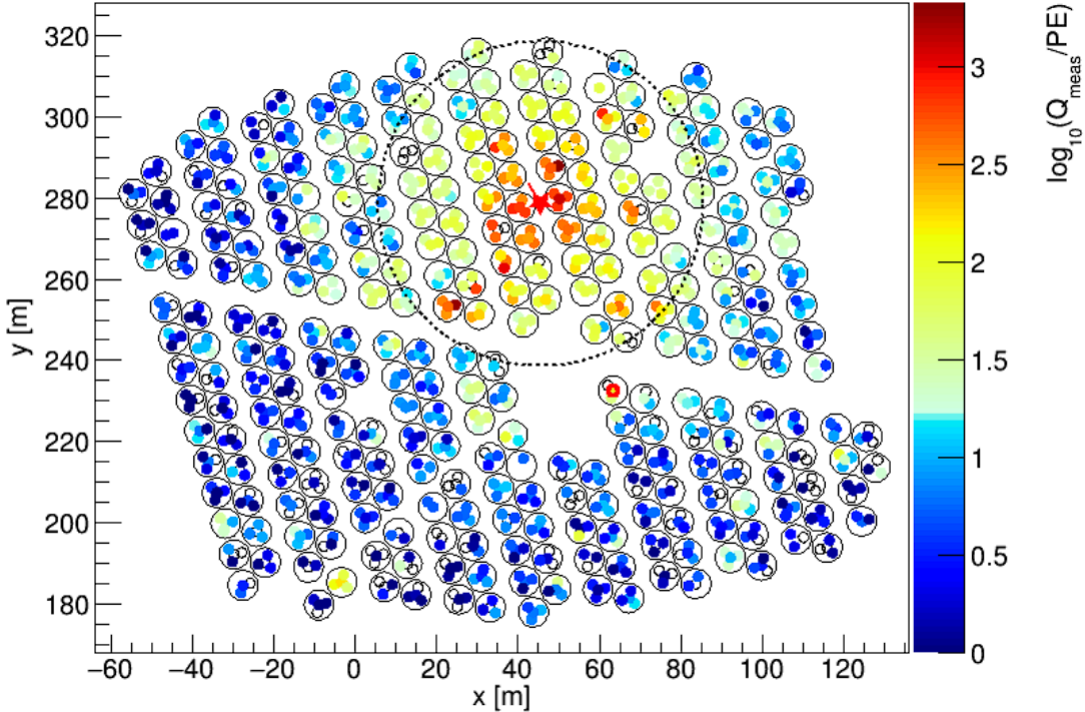


Figure 2.8 Charge deposition in each PMT for a reconstructed gamma-ray event. WCDs are outlined in black surrounding the 4 smaller circles that represent PMTs. The color scale indicates the charge deposition in each PMT. The best shower core fit from SFCF is noted with a red star in the center of the dashed circle [34].

The equation incorporates fixed values of  $\sigma = 10$  m and  $N = 5 \cdot 10^{-5}$ . This leaves the core location and overall amplitude  $A$  as the free parameters to be determined during fitting.

The chosen functional form for the Super Fast Core Fit (SFCF) algorithm is a simplified version of a modified Nishimura-Kamata-Greisen (NKG) function [35], selected for its computational efficiency which is essential for rapid fitting of air shower cores. The SFCF form allows numerical minimization to converge more quickly due to the function's simplicity, the analytical computation of its derivatives, and the absence of a pole at the core location [34]. Figure 2.8 provides a visualization of a recorded event, with the plot depicting the charge recorded by each PMT as a function of the distance to the reconstructed shower core. Through the application of the SFCF, core locations can be identified with a median error of approximately 2 m for large events and about 4 m for smaller ones, assuming the gamma-ray event core impacts directly upon the HAWC detector array [34]. It is noted that as the core's distance from the main array increases, the precision in

locating the core diminishes [34], highlighting the importance of proximity in the accuracy of core reconstruction.

### 2.2.2 Angle Reconstruction

After establishing the core position, the next step is angle reconstruction. This process determines the primary particle's trajectory. The angle of arrival is indicative of the originating gamma ray's direction. It correlates to the cosmic source of the gamma-ray. We deduce this angle using the timing of PMT hits [34].

The air shower's front is conically shaped, not flat. This shape arises from the travel patterns of secondary particles. An event example is illustrated in Fig. 2.7. Far from the core, secondary particles undergo multiple scattering. They also travel longer distances [36]. Particle sampling decreases with distance from the core. This decrease results in measurable delays in arrival times [36, 34]. Simulations provide a corrective measure for these effects. The correction is a function of shower parameters [34]. It adjusts both curvature and sampling. The distance from the shower core and the charge recorded by PMTs are crucial to this correction. A function based on simulation and Crab Nebula observations is used for this purpose [34]. This curvature correction allows us to fit the particle front as a plane wave.

Corrections lead to the  $\chi^2$  minimization step. This technique fits a plane to the timing data of the PMTs. It then calculates the shower's angle of arrival. The zenith and azimuth angles are the results of this fit [36]. The local angles are converted to celestial coordinates. These coordinates allow correlation with gamma-ray sources. Right ascension (RA) and declination (Dec) are used for this purpose. RA is akin to longitude, and Dec to latitude.

The reconstructed angle's resolution ranges from  $0.1^\circ$  to  $1^\circ$ . This range depends on the incoming particle's energy and zenith angle [36]. The analysis uses a curvature/sampling correction. This correction applies a quadratic function based on distance from the core [34]. The adjustment improves angular resolution. However, discrepancies between simulation and observation persist. These discrepancies introduce systematic errors into HAWC analyses [34].

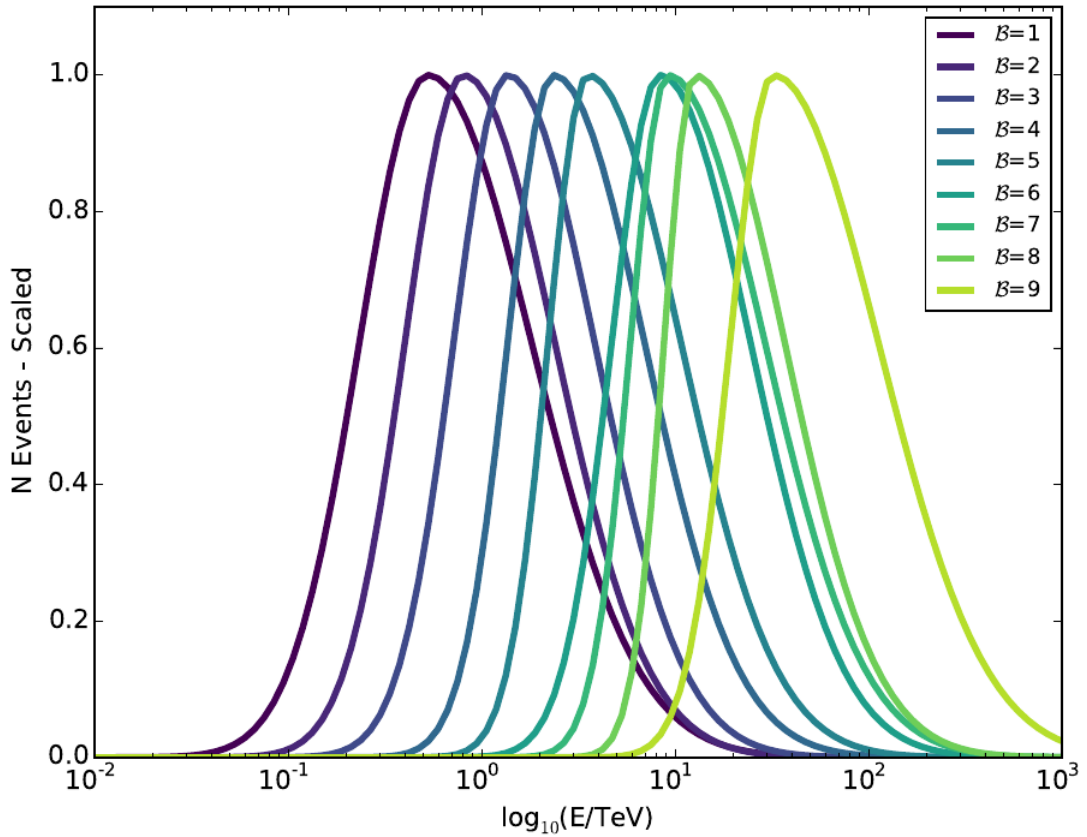


Figure 2.9 Simulated normalized energy distribution of each  $f_{\text{hit}}$  bin defined in Tab. 2.1. Monte Carlo simulation of gamma-rays with  $E^{-2.63}$  spectral shape and simulated source at  $20^\circ$  declination. Figure from [34].

Bin	Lower Edge %	Upper Edge %	$\Theta_{68}$ ( $^\circ$ )
1	6.7	10.5	1.05
2	10.5	16.2	0.69
3	16.2	24.7	0.50
4	24.7	35.6	0.39
5	35.6	48.5	0.30
6	48.5	61.8	0.28
7	61.8	74.0	0.22
8	74.0	84.0	0.20
9	84.0	100	0.17

Table 2.1 Definitions of  $f_{\text{hit}}$  energy estimator bins. Bins are defined by the fraction of available PMTs that are triggered during an air shower event. The angular resolution,  $\Theta_{68}$ , is the bin containing 68% of events [34].

### 2.2.3 $f_{\text{hit}}$ Energy Estimation

The HAWC Observatory quantifies the primary particle energy of air showers using a metric known as  $f_{\text{hit}}$ . This ratio compares the count of PMTs involved in the event reconstruction to the total number of functional PMTs at the time [34]. The main array consists of about 1200 PMTs, but the count may vary due to maintenance or other operational factors.

Events are stratified into several  $f_{\text{hit}}$  bins. Each bin corresponds to a specific range of angular resolutions, enabling a structured approach to event analysis based on the extent of the shower footprint, see Tab. 2.1. The  $f_{\text{hit}}$  metric, while effective, has several limitations. It is dependent on the zenith angle and the spectral characteristics presumed for the observed source. The variable also reaches a saturation point around 10 TeV, after which the detector's ability to discriminate between higher energy levels diminishes [34]. Furthermore, the energy distribution for each  $f_{\text{hit}}$  bin is notably broad, see Fig. 2.9. In response to these limitations, HAWC has developed more intricate algorithms for energy estimation. These algorithms incorporate the zenith angle and the distribution of charge around the shower core for a more accurate assessment of the primary particle's energy, particularly at energies surpassing 10 TeV [36].

The relationship between  $f_{\text{hit}}$  and primary energy is complex. Atmospheric attenuation can cause high-energy showers to present a smaller footprint, misrepresenting their energy in the  $f_{\text{hit}}$  metric. This effect is captured in simulations that chart the actual energy distribution across  $f_{\text{hit}}$  categories [36]. Such distributions vary with the declination of the source and the theoretical energy spectrum used in the model.

### 2.2.4 Neural Network Energy Estimation

The energy estimation for photon events at the HAWC Observatory is refined through an artificial neural network (NN) algorithm. This method, based on the Toolkit for Multivariate Analysis NN, adopts a multilayer-perceptron model with logistic activation functions across its layers. The structure includes two hidden layers, the first with 15 nodes and the second with 14, designed to process input variables through a neural network optimized to estimate primary particle energies [38].

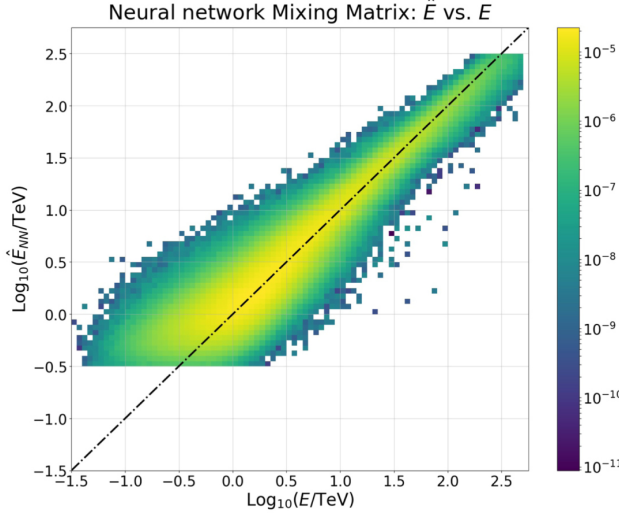


Figure 2.10 Neural Network energy estimator performance compared to true energy. The dotted line is the identity line where the estimator and injection agree. Gamma/hadron separation cuts were applied with the energy estimation. Figure pulled from [37]

The NN is trained to minimize a specific error function that measures discrepancies between the NN’s energy predictions and the actual energies from Monte Carlo simulations. This minimization targets an error function that incorporates the relative importance of each event, weighting more the importance to mimic an  $E^{-2}$  power law spectrum. This approach helps achieve a uniform error rate across energies ranging from 1 to 100 TeV. The optimization process leverages the Broyden-Fletcher-Goldfarb-Shanno algorithm that calibrates the NN’s 479 weights [37].

The spectral analysis employs a binned likelihood method, using a forward-folding technique to accommodate the energy estimate’s bias and resolution [37]. This establishes a 2D binning scheme that categorizes events by both their  $f_{\text{hit}}$  value and estimated energy. The decision to use this scheme over a simple energy-based binning lies in the correlation between gamma/hadron separation parameters and the angular resolution with both the size and energy of the event. The spectrum of interest is partitioned into nine  $f_{\text{hit}}$  bins, each further divided into 12 energy bins, spanning from 0.316 TeV to 316 TeV, encompassing a total of 108 bins [37]. However, not all bins contribute to the final estimate. Bins with low event populations or insufficient Monte Carlo simulation are excluded. This approach focuses on the central 99% of events by estimated energy within each  $f_{\text{hit}}$  bin, effectively removing outliers [37].

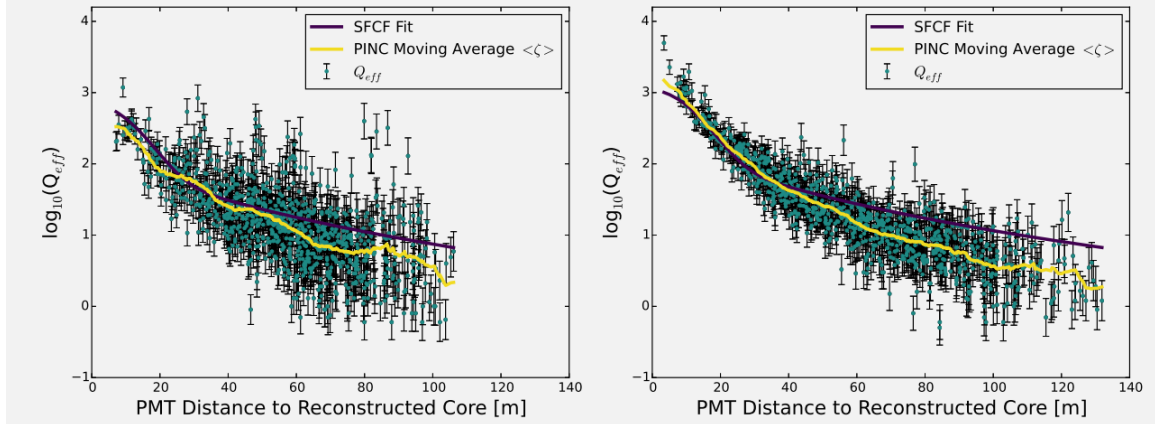


Figure 2.11 Lateral distribution functions (LDFs) for cosmic ray (left) and a photon candidate from the Crab Nebula (right). Cosmic ray LDF has clearly isolated hits far from the reconstructed shower core. Gamma-ray shower shows a more cuspy event [34].

Input variables for the NN are selected to capture key characteristics of the air shower: energy deposition, containment, and atmospheric attenuation. The algorithm calculates energy deposition using the fraction of PMTs and tanks activated, alongside the logarithm of the normalization from the lateral distribution fit. Containment is inferred from the distance between the shower core and the array's center, while atmospheric attenuation is evaluated using the reconstructed zenith angle and a detailed analysis of the shower's lateral charge distribution [38, 37].

This refined NN energy estimation methodology is an integral component of HAWC's toolkit, enabling precise analysis of high-energy gamma-ray events. It represents a significant advancement in the field by more accurately mapping observed shower characteristics to primary particle energies.

## 2.2.5 G/H Discrimination

At the HAWC Observatory, distinguishing between air showers initiated by gamma rays and those by hadronic cosmic rays is fundamental for astrophysical data purity. The separation process leverages differences in shower characteristics: electromagnetic showers from gamma rays typically display fewer muons and a smoother lateral distribution, whereas hadronic showers are more chaotic due to the abundance of muons and hadronic sub-showers.

Two primary parameters facilitate the identification of cosmic-ray events [34]:

**Compactness (C):** This parameter evaluates the charge captured by PMTs, particularly focusing on the PMT with the highest effective charge beyond a 40-meter radius from the shower core.

Compactness is inversely proportional to this effective charge, as higher charges at extended distances from the core are indicative of hadronic showers. It is mathematically expressed as:

$$C = \frac{N_{\text{hit}}}{CxPE_{40}} \quad (2.2)$$

where  $N_{\text{hit}}$  is the number of PMTs hit and  $CxPE_{40}$  is the effective charge measured outside a 40 m radius from the shower cores [34].

PINCness (P): PINCness quantifies the "clumpiness" of a shower using the charges recorded by PMTs and is short for Parameter for Identifying Nuclear Cosmic Rays. It is computed from the logarithm of the effective charge,  $Q_{\text{eff},i}$ , of each PMT hit,  $i$ , compared to an expected average for that annular region. A higher PINCness suggests a less smooth distribution, typical of hadronic showers. The formula is:

$$P = \frac{1}{N} \sum_{i=0}^N \frac{(\zeta_i - \langle \zeta \rangle)^2}{\sigma_{\zeta_i}^2} \quad (2.3)$$

where  $\zeta_i = \log_{10}(Q_{\text{eff},i})$ . The average,  $\langle \zeta \rangle$  is the average over an annular region surrounding the shower core. The errors,  $\sigma_{\zeta_i}$ , are computed and allocated from gamma-ray candidates close to the Crab.

These parameters are tested and modeled in simulations and with observational data near the Crab Nebula. Figure 2.11 illustrating the lateral distributions for representative cosmic-ray and photon candidate showers, as well as the distribution of these discrimination parameters, affirm their efficacy [34].

The discrimination technique has remained consistent, but cut values have been reoptimized for the 2D bins based on  $f_{\text{hit}}$  and NN estimated energy. This refinement enhances the selection of high-energy events. Each bin ensures at least 50% efficiency for gamma-ray detection, with efficiencies extending up to nearly 100% in certain bins [34, 37].

### 2.3 Background Estimation: Direct Integration

The ratio of cosmic rays to gamma rays can be as high as 10,000 to 1, depending on the energy. At HAWC, we confront a significant challenge even after gamma/hadron cuts: our gamma-ray data is still inundated with cosmic-ray events. To tackle this, we rely on the direct integration method

developed by Milagro [39]. This method capitalizes on the cosmic rays' isotropic nature resulting from their deflection by interstellar magnetic fields.

The direct integration method estimates background events by integrating over a stable two-hour period of detector operation. The expected number of background events at a particular sky coordinate  $(\phi, \theta)$  is determined by integrating the normalized detector's efficiency with the all-sky event rate:

$$N_{\text{exp}}(\phi, \theta) = \int \int E(\text{ha}, \theta) \cdot R(t) dt \quad (2.4)$$

Here,  $E(\text{ha}, \theta)$ , represents the detector's efficiency, which varies with local coordinates (hour angle and declination).  $R(t)$  is the event rate as a function of time [39].

Our background estimation is expected to falter in high-energy ranges where cosmic-ray events are less frequent due to enhanced gamma/hadron discrimination. Sparsity in our background and data also arise at the limits of HAWC's sensitivity and during short-term analyses of transient events. HAWC addresses these issues by using a pixel size of  $0.5^\circ$  in our direct integration to maintain robustness in our estimation [34, 36]. In constructing the background model, it's crucial to exclude areas of the sky with known gamma-ray sources. Regions containing the Crab Nebula, Mrk 421, Mrk 501, and the Galactic Plane are masked to prevent their significant gamma-ray signals from biasing our background estimate [34].

## CHAPTER 3

### GLORY DUCK: MULTI-WAVELENGTH SEARCH FOR DARK MATTTER ANNIHILATION TOWARDS DWARF SPHEROIDAL GALAXIES

#### 3.1 Introduction

The field of astrophysics now has several instruments and observatories sensitive to high energy gamma-rays. The energy sensitivity for the modern gamma-ray program spans many orders of magnitude. Figure 3.1 demonstrates these comparable sensitivities across energies for the five experiments: Fermi-LAT, HAWC, HESS, MAGIC, and VERITAS.

Each of the five experiments featured in Figure 3.1 have independently searched for DM annihilation from dwarf spheroidal galaxies (dSph) and set limits on annihilation cross-section of WIMPs. Intriguingly, there are regions of substantial overlap in their energy sensitivities. This clearly motivates an analysis that combines data from these five. Each experiment has unique gamma-ray detection methods and their weaknesses and strengths can be leveraged with each other. The HAWC gamma-ray observatory is extensively introduced in chapter 2, so it is not introduced here. A brief description of the remaining experiments are in the following paragraphs.

The Large Area Telescope (LAT) is a pair conversion telescope mounted on the NASA Fermi satellite in orbit  $\sim$ 550 km above the Earth [41]. LAT's field of view covers about 20% of the whole sky, and it sweeps the whole sky approximately every 3 hours. LAT's gamma-ray energy sensitivity ranges from 20 MeV up to 1 TeV. Previous DM searches towards dSphs using Fermi-LAT are published in [42] and [43].

The High Energy Spectroscopic System (HESS), Major Atmospheric Gamma Imaging Cherenkov (MAGIC), and Very Energetic Radiation Imaging Telescope Array System (VERITAS) are arrays of Imaging Atmospheric Cherenkov Telescopes (IACT). These telescopes observe the Cherenkov light emitted from gamma-ray showers in the Earth's atmosphere. The field of view for these telescopes is no larger than  $5^\circ$  with energy sensitivities ranging from 30 GeV up to 100 TeV [44, 45, 46]. IACTs are able to make precise observations in selected regions of the sky, however can only be operated in ideal dark conditions. HESS's observations of the dwarves

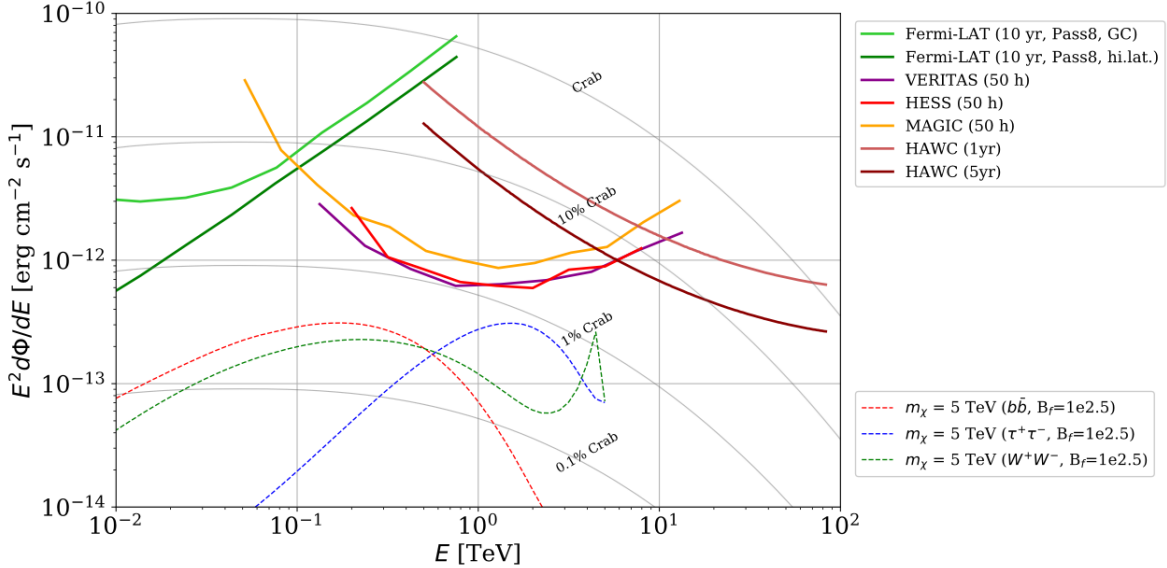


Figure 3.1 Sensitivities of five gamma-ray experiments compared to percentages of the Crab nebula’s emission and dark matter annihilation. Solid lines present estimated sensitivities to power law spectra [FACT CHECK THIS] for each experiment. Green lines are Fermi-LAT sensitivities where lighter green is the sensitivity to the galactic center and dark green is its sensitivity to higher declinations. Orange, red, and purple solid lines represent the MAGIC, HESS, and VERITAS 50 hour sensitivities respectively. The maroon and brown lines are the HAWC 1 year and 5 year sensitivities. Across four decades of gamma-ray energy, these experiments have similar sensitivities on the order  $10^{-12}$  erg  $\text{cm}^{-2}\text{s}^{-1}$ . The dotted lines are estimated dark matter fluxes assuming  $m_\chi = 5$  TeV DM annihilating to bottom quarks (red), tau leptons (blue), and W bosons (green). Faded gray lines outline percentage flux of the Crab nebula. Figure is an augmented version of [40]

Sculptor and Carina were between January 2008 and December 2009. HESS’s observations of Coma Berenices were taken from 2010 to 2013, and Fornax was observed in 2010 [47, 48, 49]. MAGIC provided deep observations of Segue1 between 2011 and 2013 [50]. MAGIC also provides data for three additional dwarves: Coma Berenices, Draco, and Ursa Major II where observations were made in: January - June 2019 [51], March - September 2018 [51], and 2014 - 2016 [52] respectively. VERITAS provided data for Boötes I, Draco, Segue 1, and Ursa Minor from 2009 to 2016 [53].

This chapter presents the Glory Duck analysis, the name given for the search for dark matter annihilation from dSph by combining data from the five gamma-ray observatories: Fermi-LAT, HAWC, HESS, MAGIC, and VERITAS. Specifically, the methods in analysis and modeling are presented for the HAWC gamma-ray observatory. This work will be published in the Journal of

Cosmology and Astroparticle Physics and presented at the International Cosmic Ray Conference in 2019, 2021, and 2023 [54, 55, 56] and others.

## 3.2 Dataset and Background

This section enumerates the data analysis and background estimation methods used for HAWC’s study of dSphs. Section 3.2.1 and Section 3.2.2 are most useful for fellow HAWC collaborators looking to replicate the Glory Duck analysis.

### 3.2.1 Itemized HAWC files

These files are only available withing HAWC’s internal documentation and collaborators. They are not meant for public access, and are presented here so that HAWC collaborators can reproduce results accurately.

- Detector Response: `response_aerie_svn_27754_systematics_best_mc_test_nobranepulse\_10pctlogchargesmearing_0.63qe_25kHzNoise_run5481_curvature0_index3.root`
- Data Map: `maps-20180119/liff/maptree_1024.root`
- Spectral Dictionary: `DM_CirrelliSpectrum_dict_gammas.npy`
- Analysis wiki: [https://private.hawc-observatory.org/wiki/index.php/Glory\\_Duck\\_Multi-Experiment\\_Dark\\_Matter\\_Search](https://private.hawc-observatory.org/wiki/index.php/Glory_Duck_Multi-Experiment_Dark_Matter_Search)

### 3.2.2 Software Tools and Development

This analysis was performed using HAL and 3ML [34, 57] in Python version 2. I built software to implement the *A Poor Particle Physicist Cookbook for Dark Matter Indirect Detection* (PPPC) [58] DM spectral model and dSphs spatial model from [59] for HAWC analysis. A NumPy version of this dictionary was made for both Py2 and Py3. The code base for creating this dictionary is linked on my GitLab sandbox:

- Py2: [Dictionary Generator \(Deprecated\)](#)

- Py3: [PPPC2Dict](#)

The analysis was performed using the  $f_{hit}$  framework as used and described in the HAWC Crab paper [34]. The Python2 NumPy dictionary file for gamma-ray final states is `dmCirSpecDict.npy`. The corresponding Python3 file is `DM_CirrelliSpectrum_dict_gammas.npy`. These files can also be used for decay channels and the PPPC describes how [58]. All other software used for data analysis, DM profile generation, and job submission to SLURM are also kept in my sandbox for [the Glory Duck](#) project.

### 3.2.3 Data Set and Background Description

The HAWC data maps used for this analysis contain 1017 days of data between runs 2104 (2014-11-26) and 7476 (2017-12-20). They were generated from pass 4.0 reconstruction. The analysis is performed using the  $f_{hit}$  energy binning scheme with bins (1-9) similar to what was done for the Crab and previous HAWC dSph analysis [34, 60]. Bin 0 was excluded as it has substantial hadronic contamination and poor angular resolution.

This analysis was done on dSphs because of their large DM mass content relative to baryonic mass. We consider the following to estimate the background to this study.

- The dSphs' angular extent are small relative to HAWC's spatial resolution, so the analysis is not sensitive to large or small scale anisotropies.
- The dSphs used in this analysis are off the galactic plane and therefore not contaminated by diffuse emission from the galaxy.
- The dSphs are baryonically faint relative to their expected dark matter content and are not expected to contain high energy gamma-ray sources.

Therefor we make no additional assumptions on the background from our sources and use HAWC's standard direct integration method for background estimation [34]. The largest background under this consideration is from an isotropic flux of cosmic rays. The contamination of this hadronic flux is worse at lower energies where HAWC's gamma/hadron discrimination worse. It is possible

for gamma rays from DM annihilation to scatter in transit to HAWC via Inverse Compton Scattering (ICS). This was investigated and its impact on the flux is negligible. Supporting information on this is in Section 3.7.1

### 3.3 Analysis

The expected differential photon flux from DM-DM annihilation to standard model particles,  $d\Phi_\gamma/dE_\gamma$ , over solid angle,  $\Omega$ , is described by the familiar equation.

$$\frac{d\Phi_\gamma}{dE_\gamma} = \frac{\langle\sigma v\rangle}{8\pi m_\chi^2} \frac{dN_\gamma}{dE_\gamma} \times \int_{\text{source}} d\Omega \int_{l.o.s} dl(r, \theta') \rho_\chi^2 J(r, \theta') \quad (3.1)$$

Where  $\langle\sigma v\rangle$  is the velocity weighted annihilation cross-section.  $\frac{dN}{dE}$  is the expected differential number of photons produced at each energy per annihilation.  $m_\chi$  is the rest mass of the supposed DM particle.  $\rho_\chi$  is the DM density.  $J$  is the astrophysical J-factor and is defined as

$$J = \int d\Omega \int_{l.o.s} dl \rho_\chi^2(r, \theta') \quad (3.2)$$

$l$  is the distance to the source from Earth.  $r$  is the radial distance from the center of the source.  $\theta'$  is the half angle defining a cone containing the DM source. How each component is synthesized and considered for HAWC's analysis is presented in the following sections. Section 3.3.1 presents the particle physics model for DM annihilation. Section 3.3.2 presents the spatial distributions built for each dSph.

#### 3.3.1 $\frac{dN_\gamma}{dE_\gamma}$ - Particle Physics Component

For these spectra, we import the PPPC with Electroweak (EW) corrections [58]. Public versions of the imported tables are provided by the [authors online](#). The spectrum is implemented as a model script in astromodels for 3ML. The EW corrections were previously not considered for HAWC and are significant for DM annihilating to EW coupled SM particles such as all leptons, and the  $\gamma$ ,  $Z$ , and  $W$  bosons [60]. Figure 3.2 demonstrates the significance of EW corrections for W boson annihilation. Across EW SM channels, the gamma-ray spectra become harder than spectra without EW corrections. Tables from the PPPC were reformatted into Python NumPy dictionaries for collaboration-wide use. A class in astromodels was developed to include the EW correction from the PPPC and is aptly named `PPPCSpectra` within `DM_models.py`.

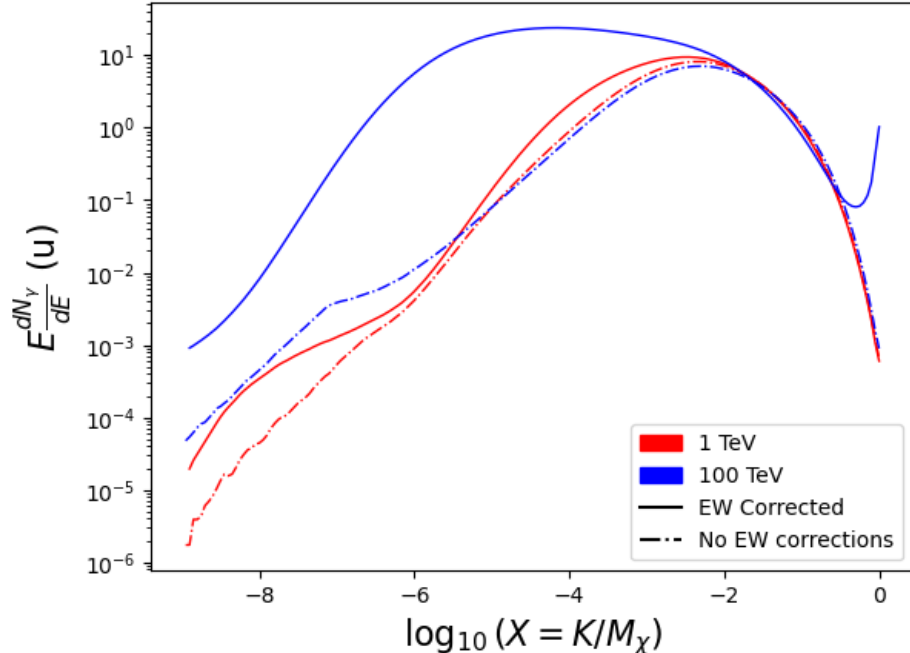


Figure 3.2 Effect of Electroweak (EW) corrections on expected DM annihilation spectrum for  $\chi\chi \rightarrow W^-W^+$ . Solid lines are spectral models that consider EW corrections. Dash-dot lines are spectral models without EW corrections. Red lines are models for  $M_\chi = 1$  TeV. Blue lines represent models for  $M_\chi = 100$  TeV. All models are sourced from the PPPC4DMID [58].

### 3.3.2 J- Astrophysical Component

The J-factor profiles for each source are imported from Geringer-Sameth (referred to with  $\mathcal{GS}$ ) [59].  $\mathcal{GS}$  fits the Zhao DM profile to the dSphs which has a DM density described as [61]

$$\rho(r) = \frac{\rho_0}{(r/R_s)^\gamma (1 + (r/R_s)^\alpha)^{(\beta-\gamma)}}. \quad (3.3)$$

$R_s$  is the scale radius and free parameter in the model.  $\gamma$  is the logarithmic slope in the region  $r \ll R_s$ .  $\beta$  is the logarithmic slope in the region  $r \gg R_s$ .  $\alpha$  is known as the sharpness of transition where  $r \approx R_s$ . The classic Navarro-Frenk-White [62] (NFW) can be retrieved from Zhao by fixing  $(\alpha, \beta, \gamma) = (1, 3, 1)$ .

$\mathcal{GS}$  best fits were pulled from the publication as  $J(\theta)$ , where  $\theta$  is the angular separation from the center of the source. HAWC requires maps in terms of  $\frac{dJ}{d\Omega}$ , so the conversion from the maps was done in the following way...

First, convert the angular distances to solid angles

$$\Omega = 2 \cdot \pi(1 - \cos(\theta)) \quad (3.4)$$

which reduces with a small angle approximation to  $\pi\theta^2$ . Next, the central difference for both the  $\Delta J$  and  $\Delta\Omega$  value were calculated from the discretized  $J(\theta)$  with the central difference stencil:

$$\Delta\phi_i = \phi_{i+1} - \phi_{i-1} \quad (3.5)$$

Where  $\phi$  is either  $\Omega$  or  $J$ . These were done separately in case the grid spacing in  $\theta$  was not uniform. Finally, these lists are divided so that we are left with an approximation of the  $dJ/d\Omega$  profile that is a function of  $\theta$ . Admittedly, this is an approximation method for the map which introduces small errors compared to the true profile estimate. This was checked as a systematic against the author's profiling of the spatial distribution and is documented in Section 3.8.1.

With  $\frac{dJ}{d\Omega}(\theta)$ , a map is generated, first by filling in the north-east quadrant of the map. This quadrant is then reflected twice, vertically then horizontally, to fill the full map. Maps are then normalized by dividing the discrete 2D integral of the map. The 2D integral was a simple height of bins, Newton's integral:

$$p^2 \cdot \sum_{i,j=0}^{N,M} \frac{dJ}{d\Omega}(\theta_{i,j}, \phi_{i,j}) \quad (3.6)$$

These maps are HEALpix maps with NSIDE 16384 and saved in the .fits format. The hyper fine resolution was selected to better preserve the total expected counts after integrating Eq. (3.1) with the detector response.

Another DM spatial distribution model from Bonnivard ( $\mathcal{B}$ ) [63] was used for the Glory Duck study. However, to save computational time, limits from  $\mathcal{GS}$  were scaled to  $\mathcal{B}$  instead of each experiment performing a full study a second time. How these models compare is demonstrated for each dSph in Figure 3.16 and Figure 3.17 Plots of these maps are provided for each source in chapter A Examples of the two most impactful dSphs derived from  $\mathcal{GS}$ , Segue1 and Coma Berenices are featured in Figure 3.3

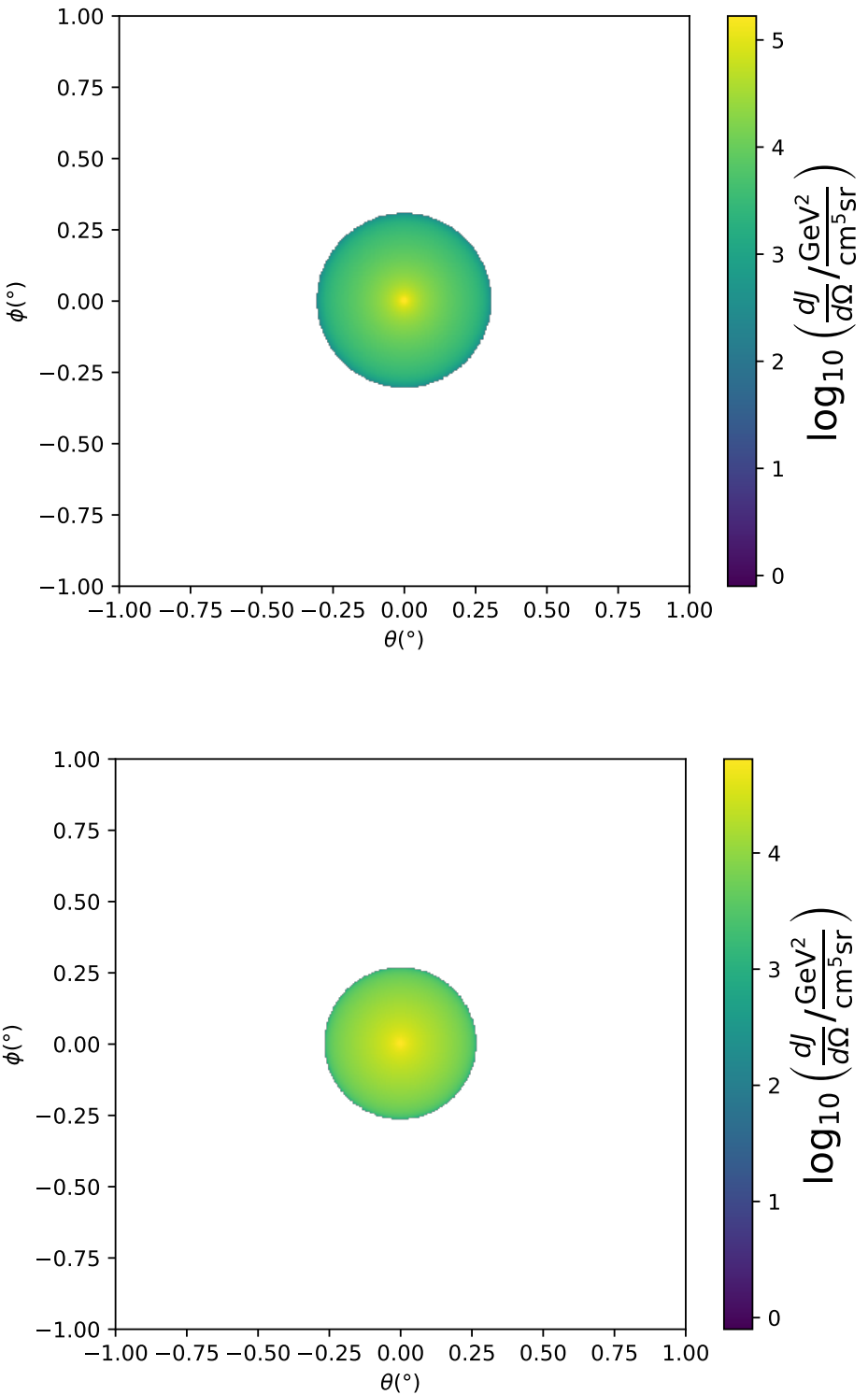


Figure 3.3  $\frac{dJ}{d\Omega}$  maps for Segue1 (top) and Coma Berenices (bottom). Origin is centered on the specific dwarf spheroidal galaxies (dSph). X and Y axes are the angular separation from the center of the dwarf. Profile is truncated at the scale radius. Plots of the remaining 11 dSph HAWC studied are linked in Fig. A.1.

### 3.3.3 Source Selection and Annihilation Channels

We use many of the dSphs presented in HAWC’s previous dSph DM search [60]. HAWC’s sources for Glory Duck include Boötes I, Coma Berenices, Canes Venatici I + II, Draco, Hercules, Leo I, II, + IV, Segue 1, Sextans, and Ursa Major I + II. A full description of all sources used in Glory Duck is found in Table 3.1. Triangulum II was excluded from the Glory Duck analysis because of large uncertainties in its  $J$  factor. Ursa Minor was excluded from HAWC’s contribution to the combination because the source extension model extended Ursa Minor beyond HAWC’s field of view. Ursa Minor was not expected to contribute significantly to the combined limit, so work was not invested in a solution to include Ursa Minor.

This analysis improves on the previous HAWC dSph paper [60] in the following ways. Previously, the dSphs were treated and implemented as point sources. For this analysis, dSphs are modeled and treated as extended source. The impact of this change with respect to the upper limit is source dependent and is explored in Section 3.7.2. Previously, the particle physics model used for gamma-ray spectra from DM annihilation did not have EW corrections where the PPPC includes them. Finally, the gamma-ray ray dataset is much larger. The study performed here analyzes over 1000 days of data compared to 507.

The SM annihilation channels probed for the Glory Duck combination include  $b\bar{b}$ ,  $e\bar{e}$ ,  $\mu\bar{\mu}$ ,  $\tau\bar{\tau}$ ,  $t\bar{t}$ ,  $W^+W^-$ , and  $ZZ$ . A summary of all sources, with a description of each experiments’ sensitivity to the source, is provided in Table 3.2.

## 3.4 Likelihood Methods

### 3.4.1 HAWC Likelihood

For every analysis bin in energy,  $f_{hit}$  bins (1-9), and location, we can expect  $N$  signal events and  $B$  background events. The expected number of excess signal events from dark matter annihilation,  $S$ , is estimated by convolving Equation (3.1) with HAWC’s energy response and pixel point spread functions. I then compute the test statistic (TS) with the log-likelihood ratio test,

$$TS_{\max} = -2 \ln \left( \frac{\mathcal{L}_0}{\mathcal{L}^{\max}} \right) \quad (3.7)$$

Table 3.1 Summary of the relevant properties of the dSphs used in the present work. Column 1 lists the dSphs. Columns 2 and 3 present their heliocentric distance and galactic coordinates, respectively. Columns 4 and 5 report the  $J$ -factors of each source given from the  $\mathcal{GS}$  and  $\mathcal{B}$  independent studies and their estimated  $\pm 1\sigma$  uncertainties. The values  $\log_{10} J$  ( $\mathcal{GS}$  set) [59] correspond to the mean  $J$ -factor values for a source extension truncated at the outermost observed star. The values  $\log_{10} J$  ( $\mathcal{B}$  set) [63] are provided for a source extension at the tidal radius of each dSph. **Bolded sources are within HAWC's field of view and provided to the Glory Duck analysis.**

Name	Distance (kpc)	$l, b$ ( $^{\circ}$ )	$\log_{10} J$ ( $\mathcal{GS}$ set) $\log_{10}(\text{GeV}^2\text{cm}^{-5}\text{sr})$	$\log_{10} J$ ( $\mathcal{B}$ set) $\log_{10}(\text{GeV}^2\text{cm}^{-5}\text{sr})$
<b>Boötes I</b>	66	358.08, 69.62	$18.24^{+0.40}_{-0.37}$	$18.85^{+1.10}_{-0.61}$
<b>Canes Venatici I</b>	218	74.31, 79.82	$17.44^{+0.37}_{-0.28}$	$17.63^{+0.50}_{-0.20}$
<b>Canes Venatici II</b>	160	113.58, 82.70	$17.65^{+0.45}_{-0.43}$	$18.67^{+1.54}_{-0.97}$
Carina	105	260.11, -22.22	$17.92^{+0.19}_{-0.11}$	$18.02^{+0.36}_{-0.15}$
<b>Coma Berenices</b>	44	241.89, 83.61	$19.02^{+0.37}_{-0.41}$	$20.13^{+1.56}_{-1.08}$
<b>Draco</b>	76	86.37, 34.72	$19.05^{+0.22}_{-0.21}$	$19.42^{+0.92}_{-0.47}$
Fornax	147	237.10, -65.65	$17.84^{+0.11}_{-0.06}$	$17.85^{+0.11}_{-0.08}$
<b>Hercules</b>	132	28.73, 36.87	$16.86^{+0.74}_{-0.68}$	$17.70^{+1.08}_{-0.73}$
<b>Leo I</b>	254	225.99, 49.11	$17.84^{+0.20}_{-0.16}$	$17.93^{+0.65}_{-0.25}$
<b>Leo II</b>	233	220.17, 67.23	$17.97^{+0.20}_{-0.18}$	$18.11^{+0.71}_{-0.25}$
<b>Leo IV</b>	154	265.44, 56.51	$16.32^{+1.06}_{-1.70}$	$16.36^{+1.44}_{-1.65}$
Leo V	178	261.86, 58.54	$16.37^{+0.94}_{-0.87}$	$16.30^{+1.33}_{-1.16}$
Leo T	417	214.85, 43.66	$17.11^{+0.44}_{-0.39}$	$17.67^{+1.01}_{-0.56}$
Sculptor	86	287.53, -83.16	$18.57^{+0.07}_{-0.05}$	$18.63^{+0.14}_{-0.08}$
<b>Segue I</b>	23	220.48, 50.43	$19.36^{+0.32}_{-0.35}$	$17.52^{+2.54}_{-2.65}$
Segue II	35	149.43, -38.14	$16.21^{+1.06}_{-0.98}$	$19.50^{+1.82}_{-1.48}$
<b>Sextans</b>	86	243.50, 42.27	$17.92^{+0.35}_{-0.29}$	$18.04^{+0.50}_{-0.28}$
<b>Ursa Major I</b>	97	159.43, 54.41	$17.87^{+0.56}_{-0.33}$	$18.84^{+0.97}_{-0.43}$
<b>Ursa Major II</b>	32	152.46, 37.44	$19.42^{+0.44}_{-0.42}$	$20.60^{+1.46}_{-0.95}$
Ursa Minor	76	104.97, 44.80	$18.95^{+0.26}_{-0.18}$	$19.08^{+0.21}_{-0.13}$

Table 3.2 Summary of dSph observations by each experiment used in this work. A ‘-’ indicates the experiment did not observe the dSph for this study. For Fermi-LAT, the exposure at 1 GeV is given. For HAWC,  $|\Delta\theta|$  is the absolute difference between the source declination and HAWC latitude. HAWC is more sensitive to sources with smaller  $|\Delta\theta|$ . For IACTs, we show the zenith angle range, the total exposure, the energy range, the angular radius  $\theta$  of the signal or ON region, the ratio of exposures between the background-control (OFF) and signal (ON) regions ( $\tau$ ), and the significance of gamma-ray excess in standard deviations,  $\sigma$ .

Source name	Fermi-LAT	HAWC	H.E.S.S, MAGIC, VERITAS						
	Exposure ( $10^{11}$ s m $^2$ )	$ \Delta\theta $ ( $^\circ$ )	IACT	Zenith ( $^\circ$ )	Exposure (h)	Energy range (GeV)	$\theta$ ( $^\circ$ )	$\tau$	$S$ ( $\sigma$ )
Boötes I	2.6	4.5	VERITAS	15 – 30	14.0	100–41000	0.10	8.6	-1.0
Canes Venatici I	2.9	14.6	–	–	–	–	–	–	–
Canes Venatici II	2.9	15.3	–	–	–	–	–	–	–
Carina	3.1	–	H.E.S.S.	27 – 46	23.7	310 – 70000	0.10	18.0	-0.3
Coma Berenices	2.7	4.9	H.E.S.S.	47 – 49	11.4	550 – 70000	0.10	14.4	-0.4
Draco	3.8	38.1	MAGIC	5 – 37	49.5	60 – 10000	0.17	1.0	–
			MAGIC	29 – 45	52.1	70 – 10000	0.22	1.0	–
			VERITAS	25 – 40	49.8	120 – 70000	0.10	9.0	-1.0
Fornax	2.7	–	H.E.S.S.	11 – 25	6.8	230 – 70000	0.10	45.5	-1.5
Hercules	2.8	6.3	–	–	–	–	–	–	–
Leo I	2.5	6.7	–	–	–	–	–	–	–
Leo II	2.6	3.1	–	–	–	–	–	–	–
Leo IV	2.4	19.5	–	–	–	–	–	–	–
Leo V	2.4	–	–	–	–	–	–	–	–
Leo T	2.6	–	–	–	–	–	–	–	–
Sculptor	2.7	–	H.E.S.S.	10 – 46	11.8	200 – 70000	0.10	19.8	-2.2
Segue I	2.5	2.9	MAGIC	13 – 37	158.0	60 – 10000	0.12	1.0	-0.5
			VERITAS	15 – 35	92.0	80 – 50000	0.10	7.6	0.7
Segue II	2.7	–	–	–	–	–	–	–	–
Sextans	2.4	20.6	–	–	–	–	–	–	–
Ursa Major I	3.4	32.9	–	–	–	–	–	–	–
Ursa Major II	4.0	44.1	MAGIC	35 – 45	94.8	120 – 10000	0.30	1.0	-2.1
Ursa Minor	4.1	–	VERITAS	35 – 45	60.4	160 – 93000	0.10	8.4	-0.1

where  $\mathcal{L}_0$  is the null hypothesis, or no DM emission, likelihood.  $\mathcal{L}^{\max}$  is the best fit signal hypothesis where  $\langle\sigma v\rangle$  maximizes the likelihood. We calculate the likelihood of each source and model, assuming events are Poisson distributed, with

$$\mathcal{L} = \prod_i \frac{(B_i + S_i)^{N_i} e^{-(B_i + S_i)}}{N_i!} \quad (3.8)$$

where  $S_i$  is the sum of expected number of signal counts.  $B_i$  is the number of background counts observed.  $N_i$  is the total number of counts.

I also calculate an upper limit on  $\langle\sigma v\rangle$  by calculating the 95% confidence level (CL). For the CL, we define a parameter,  $TS_{95}$ , as

$$TS_{95} \equiv \sum_{\text{bins}} \left[ 2N \ln \left( 1 + \frac{\epsilon S_{\text{ref}}}{B} \right) - 2\epsilon S_{\text{ref}} \right] \quad (3.9)$$

where the expected signal counts from a dSph is scaled by  $\epsilon$ .  $S_{\text{ref}}$  is the expected number of excess counts in a bin from DM emission from a dSph with a corresponding annihilation cross-section,  $\langle\sigma v\rangle$ . We scan  $\epsilon$  such that

$$2.71 = TS_{\max} - TS_{95} \quad (3.10)$$

HAWC's exclusive results are provided in Section 3.5.

### 3.4.2 Glory Duck Joint Likelihood

The joint likelihood for the 5-experiment combination was done similarly as Section 3.4.1. We calculate upper limits on  $\langle\sigma v\rangle$  from the TS, Eq. (3.7), and define the likelihood ratio more generally

$$\lambda(\langle\sigma v\rangle | \mathcal{D}_{\text{dSphs}}) = \frac{\mathcal{L}(\langle\sigma v\rangle; \hat{\nu} | \mathcal{D}_{\text{dSphs}})}{\mathcal{L}(\widehat{\langle\sigma v\rangle}; \hat{\nu} | \mathcal{D}_{\text{dSphs}})} \quad (3.11)$$

$\mathcal{D}_{\text{dSphs}}$  is the totality of observations across experiments and dSphs.  $\nu$  are the nuisance parameters which are the  $J$  factors in this study.  $\widehat{\langle\sigma v\rangle}$  and  $\hat{\nu}$  are the respective estimate that maximize  $\mathcal{L}$  globally. Finally,  $\hat{\nu}$  is the set of nuisance parameters that maximize  $\mathcal{L}$  for a fixed value of  $\langle\sigma v\rangle$ .

The *complete* joint likelihood,  $\mathcal{L}$  that encompasses all observations from all instruments and dSphs can be factorized into *partial* functions for each dSph  $l$  (with  $\mathcal{L}_{\text{dSph},l}$ ) and its  $J$  factor ( $\mathcal{J}_l$ ):

$$\mathcal{L}(\langle\sigma v\rangle; \nu | \mathcal{D}_{\text{dSphs}}) = \prod_{l=1}^{N_{\text{dSphs}}} \mathcal{L}_{\text{dSph},l}(\langle\sigma v\rangle; J_l, \nu_l | \mathcal{D}_l) \times \mathcal{J}_l(J_l | J_{l,\text{obs}}, \sigma_{\log J_l}). \quad (3.12)$$

For this study,  $N_{\text{dSphs}} = 20$  is the number of dSphs studied.  $\mathcal{D}_l$  are the gamma-ray observations of dSph,  $l$ .  $\nu_l$  are the nuisance parameters modifying the gamma-ray observations of dSph,  $l$ , but excludes  $\mathcal{J}_l$ .  $\mathcal{J}_l$  is the  $J$  factor for dSph,  $l$ , as defined in Equation (3.2), and it is a nuisance parameter whose value is unknown.  $\log_{10} J_{l,\text{obs}}$  and  $\sigma_{\log J_l}$  are obtained by fitting a log-normal function of  $J_{l,\text{obs}}$  to the posterior distribution of  $J_l$  [64].  $\log_{10} J_{l,\text{obs}}$  and  $\sigma_{\log J_l}$  values are provided in Table 3.1. The term  $\mathcal{J}_l$  constraining  $J_l$  is written as:

$$\mathcal{J}_l(J_l | J_{l,\text{obs}}, \sigma_{\log J_l}) = \frac{1}{\ln(10)J_{l,\text{obs}}\sqrt{2\pi}\sigma_{\log J_l}} \exp\left(-\frac{(\log_{10} J_l - \log_{10} J_{l,\text{obs}})^2}{2\sigma_{\log J_l}^2}\right). \quad (3.13)$$

Both the  $\mathcal{GS}$  and  $\mathcal{B}$ , displayed in Table 3.1, sets of  $J$  factors are used in this analysis. Equation (3.13) is also normalized, so it can also be interpreted as a probability density function (PDF) for  $J_{l,\text{obs}}$ . From Equation (3.1), we can also see that  $\langle\sigma v\rangle$  and  $J_l$  are degenerate when computing  $\mathcal{L}_{\text{dSph},l}$ . Therefore, as noted in [65], it is sufficient to compute  $\mathcal{L}_{\text{dSph},l}$  versus  $\langle\sigma v\rangle$  for a fixed value of  $J_l$ . We used  $J_{l,\text{obs}}(\mathcal{GS})$  reported in Tab. 3.1, in order to perform the profile of  $\mathcal{L}$  with respect to  $J_l$ . The degeneracy implies that for any  $J'_l \neq J_{l,\text{obs}}$  (in practice in our case we used  $J'_l = J_{l,\text{obs}}(\mathcal{B})$  to compute results from a different set of  $J$  factors):

$$\mathcal{L}_{\text{dSph},l}(\langle\sigma v\rangle; J'_l, \nu_l | \mathcal{D}_l) = \mathcal{L}_{\text{dSph},l}\left(\frac{J'_l}{J_{l,\text{obs}}} \langle\sigma v\rangle; J_{l,\text{obs}}, \nu_l | \mathcal{D}_l\right), \quad (3.14)$$

which is a straightforward rescaling operation that reduces the computational needs of the profiling operation since:

$$\mathcal{L}(\langle\sigma v\rangle; \hat{\nu} | \mathcal{D}_{\text{dSphs}}) = \prod_{l=1}^{N_{\text{dSphs}}} \max_{J_l} \left[ \mathcal{L}_{\text{dSph},l}(\langle\sigma v\rangle; J_l, \hat{\nu}_l | \mathcal{D}_l) \times \mathcal{J}_l(J_l | J_{l,\text{obs}}, \sigma_{\log J_l}) \right]. \quad (3.15)$$

In addition, Eq. (3.14) enables the combination of data from different gamma-ray instruments and observed dSphs via tabulated values of  $\mathcal{L}_{\text{dSph},l}$ , or equivalently of  $\lambda$  from Eq. (3.11) as was done in this work, versus  $\langle\sigma v\rangle$ .  $\mathcal{L}_{\text{dSph},l}$  is computed for a fixed value of  $J_l$  and profiled with respect to all instrumental nuisance parameters  $\nu_l$ , these nuisance parameters are discussed in more detail below. These values are produced by each detector independently and therefore there is no need to share sensitive low-level information used to produce them, such as event lists. Figure 3.4 illustrates the multi-instrument combination technique used in this study with a comparison of the upper limit

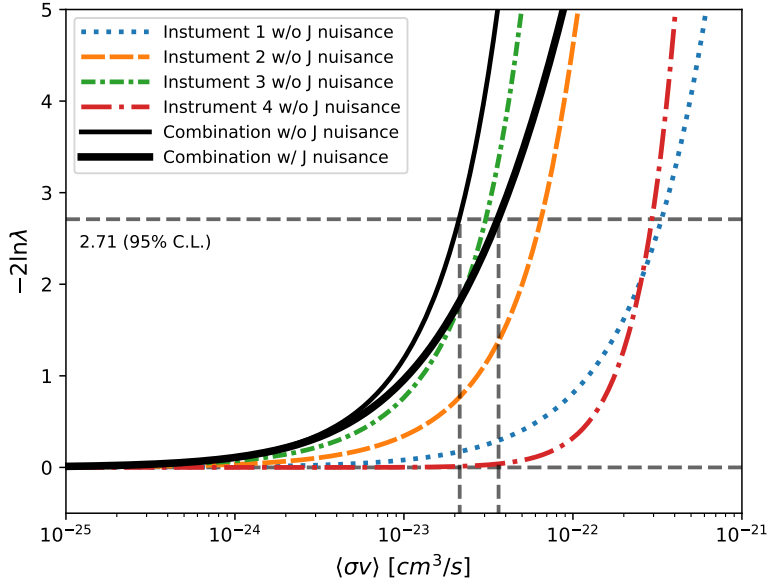


Figure 3.4 Illustration of the combination technique showing a comparison between  $-2 \ln \lambda$  provided by four instruments (colored lines) from the observation of the same dSph without any  $J$  nuisance and their sum, *i.e.* the resulting combined likelihood (thin black line). According to the test statistics of Equation (3.7), the intersection of the likelihood profiles with the line  $-2 \ln \lambda = 2.71$  indicates the 95% C.L. upper limit on  $\langle\sigma v\rangle$ . The combined likelihood (thin black line) shows a smaller value of upper limit on  $\langle\sigma v\rangle$  than those derived by individual instruments. We also show how the uncertainties on the  $J$  factor effects the combined likelihood and degrade the upper limit on  $\langle\sigma v\rangle$  (thick black line). All likelihood profiles are normalized so that the global minimum  $\widehat{\langle\sigma v\rangle}$  is 0. We note that each profile depends on the observational conditions in which a target object was observed. The sensitivity of a given instrument can be degraded and the upper limits less constraining if the observations are performed in non-optimal conditions such as a high zenith angle or a short exposure time.

on  $\langle\sigma v\rangle$  obtained from the combination of the observations of four experiments towards one dSph versus the upper limit from individual instruments. It also shows graphically the effect of the  $J$ -factor uncertainty on the combined observations.

The *partial* joint likelihood function for gamma-ray observations of each dSph ( $\mathcal{L}_{\text{dSph},l}$ ) is written as the product of the likelihood terms describing the  $N_{\text{exp},l}$  observations performed with any of our observatories:

$$\mathcal{L}_{\text{dSph},l} (\langle\sigma v\rangle; J_l, \nu_l | \mathcal{D}_l) = \prod_{k=1}^{N_{\text{exp},l}} \mathcal{L}_{lk} (\langle\sigma v\rangle; J_l, \nu_{lk} | \mathcal{D}_{lk}), \quad (3.16)$$

where each  $\mathcal{L}_{lk}$  term refers to an observation of the  $l$ -th dSph with associated  $k$ -th instrument

responses.  $N_{\text{exp},l}$  varies from dSph to dSph and can be inferred from Table 3.2.

Each collaboration separately analyzes their data for  $\mathcal{D}_{lk}$  corresponding to dSph  $l$  and gamma-ray detector  $k$ , using as many common assumptions as possible in the analysis. HAWC's treatment was described earlier in Section 3.4.1 whereas the specifics of the remaining experiments is left to the publication. We compute the values for the likelihood functions  $\mathcal{L}_{lk}$  (see Eq. (3.16)) for a fixed value of  $J_l$  and profile over the rest of the nuisance parameters  $\nu_{lk}$ . Then, values of  $\lambda$  from Eq. (3.11) are computed as a function of  $\langle \sigma v \rangle$ , and shared using a common format. Results are computed for seven annihilation channels,  $W^+W^-$ ,  $ZZ$ ,  $b\bar{b}$ ,  $t\bar{t}$ ,  $e^+e^-$ ,  $\mu^+\mu^-$ , and  $\tau^+\tau^-$  over 62  $m_\chi$  values between 5 GeV and 100 TeV provided in [58]. The  $\langle \sigma v \rangle$  range is defined between  $10^{-28}$  and  $10^{-18} \text{ cm}^3 \cdot \text{s}^{-1}$ , with 1001 logarithmically spaced values. The likelihood combination, i.e. Equation (3.12), and profile over the  $J$ -factor to compute the profile likelihood ratio  $\lambda$ , Equation (3.11), are carried out with two different public analysis software packages, namely `gLike` [66] and `LklCom` [67], that provide the same results [68].

As mentioned previously, each experiment computes the  $\mathcal{L}_{lk}$  from Equation (3.11) differently. The remainder of this section highlights the differences in this calculation across the experiments. Four experiments, namely *Fermi*-LAT, H.E.S.S., HAWC and MAGIC, use a binned likelihood to compute the  $\mathcal{L}_{lk}$ . For these experiments, for each observation  $\mathcal{D}_{lk}$  of a given dSph  $l$  carried out using a given gamma-ray detector  $k$ , the binned likelihood function is:

$$\mathcal{L}_{lk} (\langle \sigma v \rangle; J_l, \nu_{lk} | \mathcal{D}_{lk}) = \prod_{i=1}^{N_E} \prod_{j=1}^{N_P} \left[ \mathcal{P}(s_{lk,ij}(\langle \sigma v \rangle, J_l, \nu_{lk}) + b_{lk,ij}(\nu_{lk}) | N_{lk,ij}) \right] \times \mathcal{L}_{lk,\nu} (\nu_{lk} | \mathcal{D}_{\nu_{lk}}) \quad (3.17)$$

where  $N_E$  and  $N_P$  are the number of considered bins in reconstructed energy and arrival direction, respectively;  $\mathcal{P}$  represents a Poisson PDF for the number of gamma-ray candidate events  $N_{lk,ij}$  observed in the  $i$ -th bin in energy and  $j$ -th bin in arrival direction, when the expected number is the sum of the expected mean number of signal events  $s_{ij}$  (produced by DM annihilation) and of background events  $b_{ij}$ ;  $\mathcal{L}_{lk,\nu}$  is the likelihood term for the extra  $\nu_{lk}$  nuisance parameters that vary from one instrument  $k$  to another. The expected counts for signal events  $s_{ij}$  for a given dSph  $l$  and

detector  $k$  is given by:

$$s_{ij}(\langle\sigma\nu\rangle, J) = \int_{E'_{\min,i}}^{E'_{\max,i}} dE' \int_{P'_{\min,j}}^{P'_{\max,j}} d\Omega' \int_0^\infty dE \int_{\Delta\Omega_{tot}} d\Omega \int_0^{T_{\text{obs}}} dt \frac{d^2\Phi(\langle\sigma\nu\rangle, J)}{dEd\Omega} \text{IRF}(E', P' | E, P, t) \quad (3.18)$$

where  $E'$  and  $E$  are the reconstructed and true energies,  $P'$  and  $P$  the reconstructed and true arrival directions;  $E'_{\min,i}$ ,  $P'_{\min,j}$ ,  $E'_{\max,i}$ , and  $P'_{\max,j}$  are their lower and upper limits of the  $i$ -th energy bin and the  $j$ -th arrival direction bin;  $T_{\text{obs}}$  is the (dead-time corrected) total observation time;  $t$  is the time along the observations;  $d^2\Phi/dEd\Omega$  is the DM flux in the source region (see Equation (3.1)); and  $\text{IRF}(E', P' | E, P, t)$  is the IRF, which can be factorized as the product of the effective collection area of the detector  $A_{\text{eff}}(E, P, t)$ , the PDFs for the energy estimator  $f_E(E' | E, t)$ , and arrival direction  $f_P(P' | E, P, t)$  estimators. Note that for Fermi-LAT, HAWC, MAGIC, and VERITAS the effect of the finite angular resolution is taken into account through the convolution of  $d\Phi/dEd\Omega$  with  $f_P$  in Equation (3.18), whereas in the cases of H.E.S.S.  $f_P$  is approximated by a delta function. This approximation has been made in order to maintain compatibility of the result with what has been previously published. The difference introduced by this approximation is  $< 5\%$  for all considered dSphs. A more comprehensive review of the differences between the analyses of different instruments can be found in [40].

### 3.5 HAWC Results

13 of the 20 dSphs considered for the Glory Duck analysis are within HAWC's field of view. These dSph are analyzed for emission from DM annihilation according to the likelihood method described in Section 3.4. The 13 likelihood profiles are then stacked to synthesize a combined limit on the dark matter cross-section,  $\langle\sigma\nu\rangle$ . This combination is done for the 7 SM annihilation channels used in the Glory Duck analysis. Figure 3.5 shows the combined limit for all annihilation channels with HAWC only observations. We also perform 300 studies of Poisson trials on the background. These trials are used to produce HAWC sensitivities with  $\pm 1\sigma$  and  $\pm 2\sigma$  uncertainty bands which were shared with the other collaborators for combination. The results on fitting to HAWC's Poisson trials of the DM hypothesis is shown in Figure 3.7 for all the DM annihilation channels studied for Glory Duck.

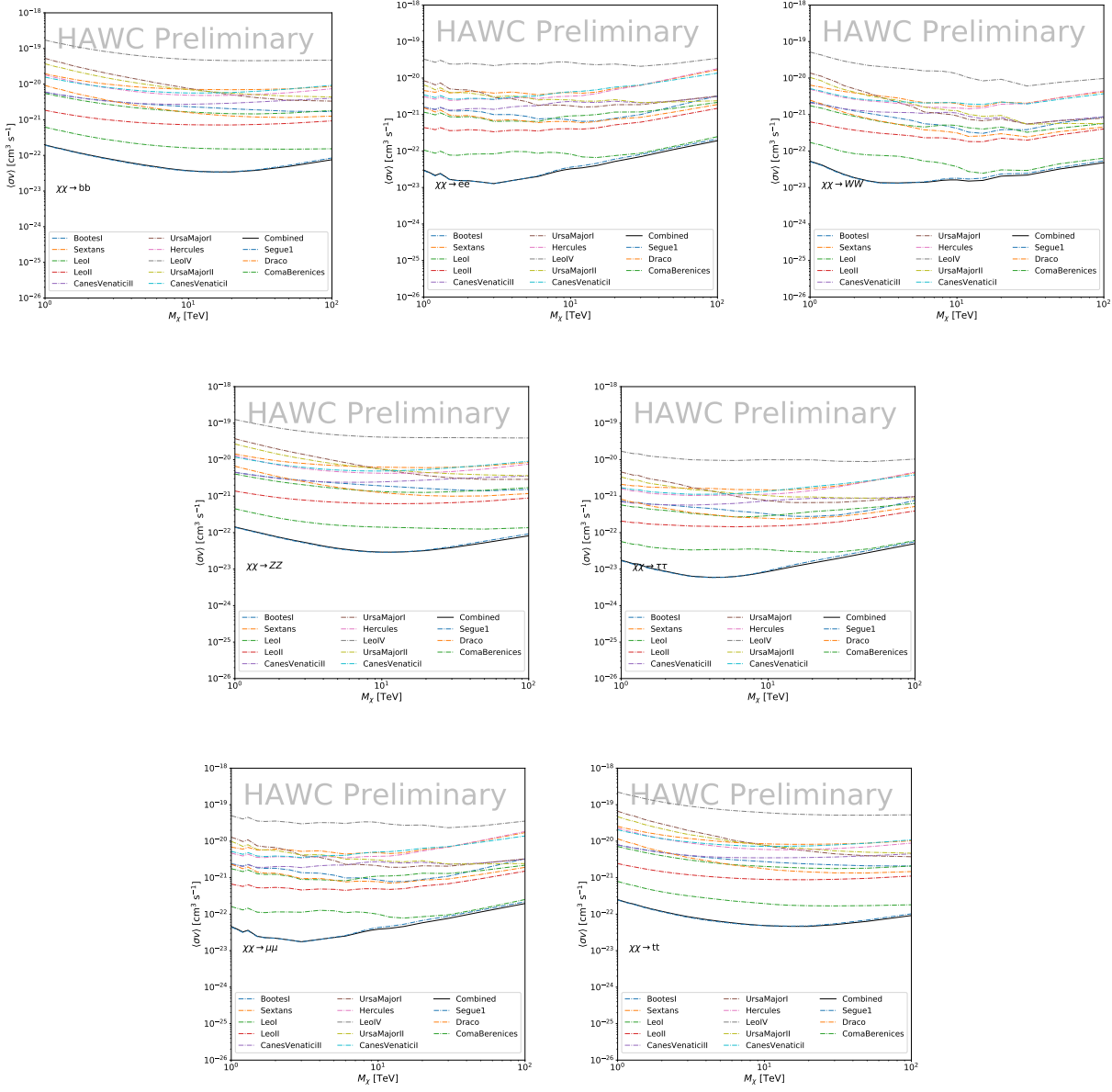


Figure 3.5

No DM was found in HAWC observations. HAWC's limits are dominated by the dSphs Segue1 and Coma Berenices. The remaining 11 dSphs do not contribute significantly to the limit because they are at high zenith and/or have much smaller  $J$  factors. Even though some remaining dSphs have large  $J$  factors, they are towards the edge of HAWC's field of view where HAWC analysis is less sensitive.

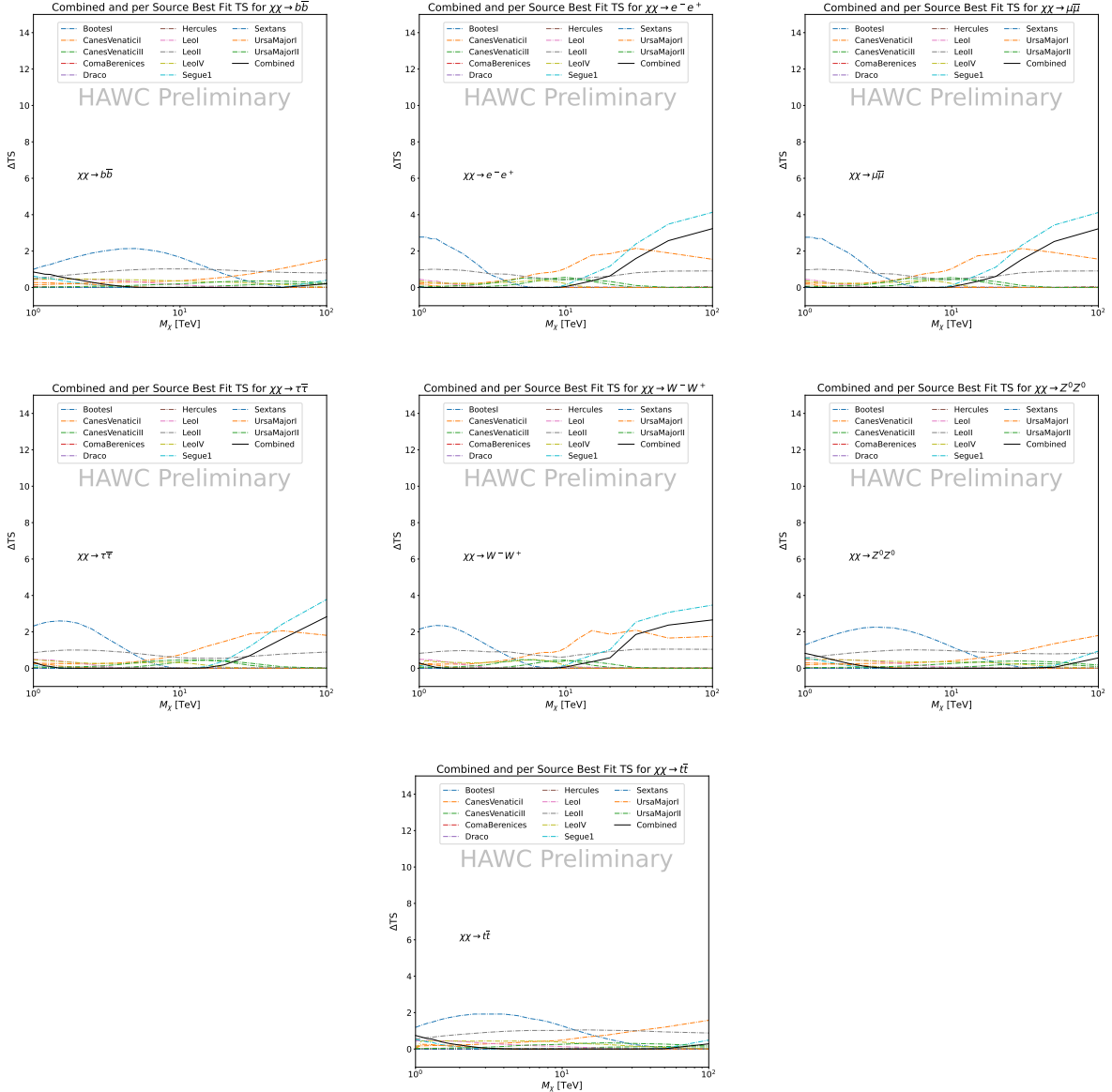


Figure 3.6 HAWC TS values for best fit  $\langle\sigma v\rangle$  versus  $m_\chi$  for seven SM annihilation channels with  $J$  factors from  $\mathcal{GS}$ . The solid black line shows the combined best fit TS values. The colored, dashed lines are the TS values for each of the 13 sources HAWC studied.

### 3.6 Glory Duck Combined Results

The crux of this analysis is that HAWC's results are combined with 4 other gamma-ray observatories: Fermi-LAT, H.E.S.S., MAGIC, and VERITAS. No significant DM emission was observed by any of the five instruments. We present the upper limits on  $\langle\sigma v\rangle$  assuming seven independent DM self annihilation channels, namely  $W^+W^-$ ,  $Z^+Z^-$ ,  $b\bar{b}$ ,  $t\bar{t}$ ,  $e^+e^-$ ,  $\mu^+\mu^-$ , and  $\tau^+\tau^-$ . The 68%

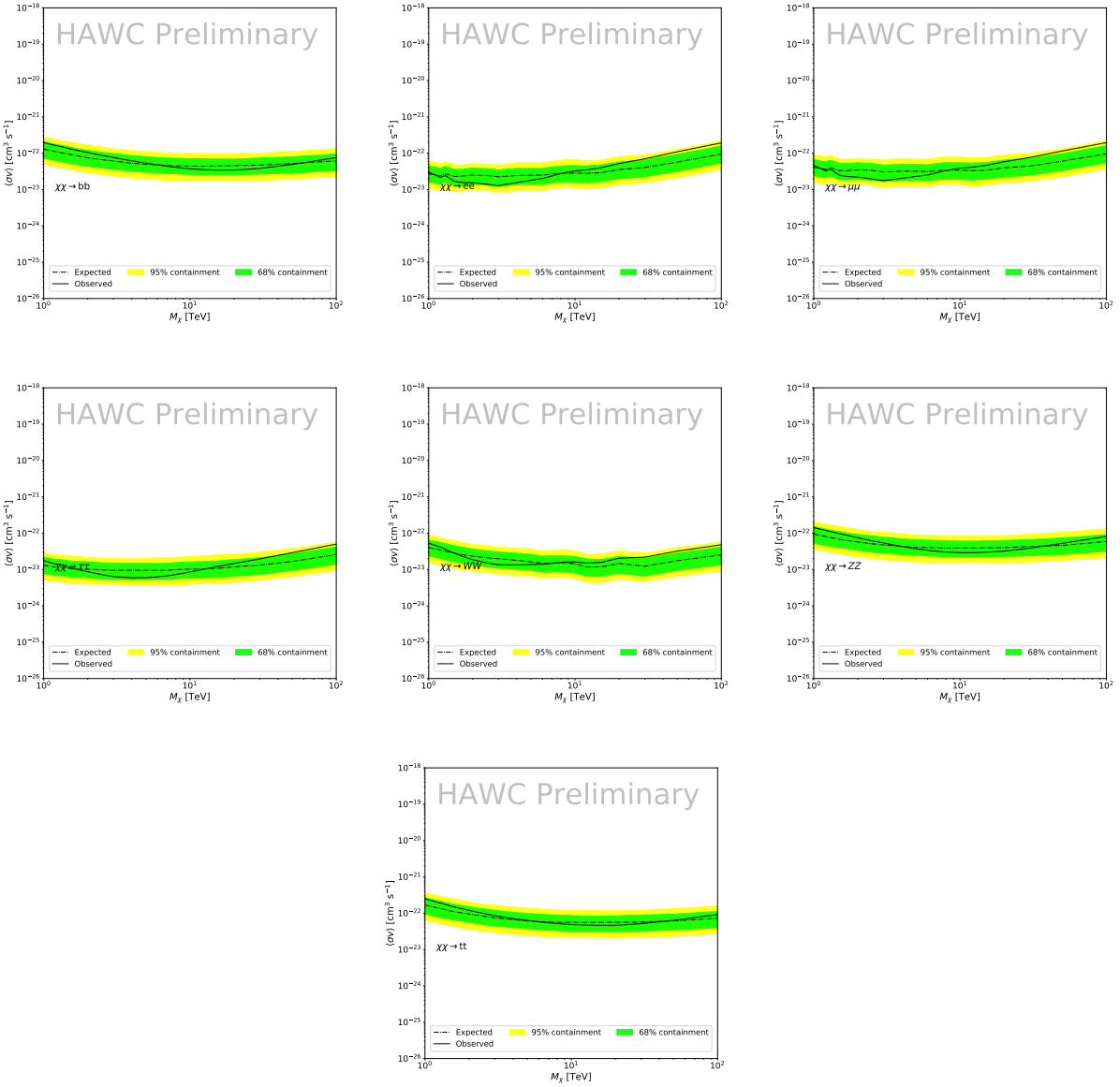


Figure 3.7 HAWC Brazil bands at 95% confidence level on  $\langle\sigma v\rangle$  versus DM mass for seven annihilation channels with  $J$ -factors from  $\mathcal{GS}$  [69]. The solid line represents the combined limit from 13 dSphs. The dashed line is the expected limit. The green band is the 68% containment. The yellow band is the 95% containment.

and 95% containment bands are produced from 300 Poisson realizations of the null hypothesis corresponding to each of the combined datasets. These 300 realizations are combined identically to dSph observations. The containment bands and the median are extracted from the distribution of resulting limits on the null hypothesis. These 300 realizations are obtained either by fast simulations of the OFF observations, for H.E.S.S., MAGIC, VERITAS, and HAWC, or taken from real

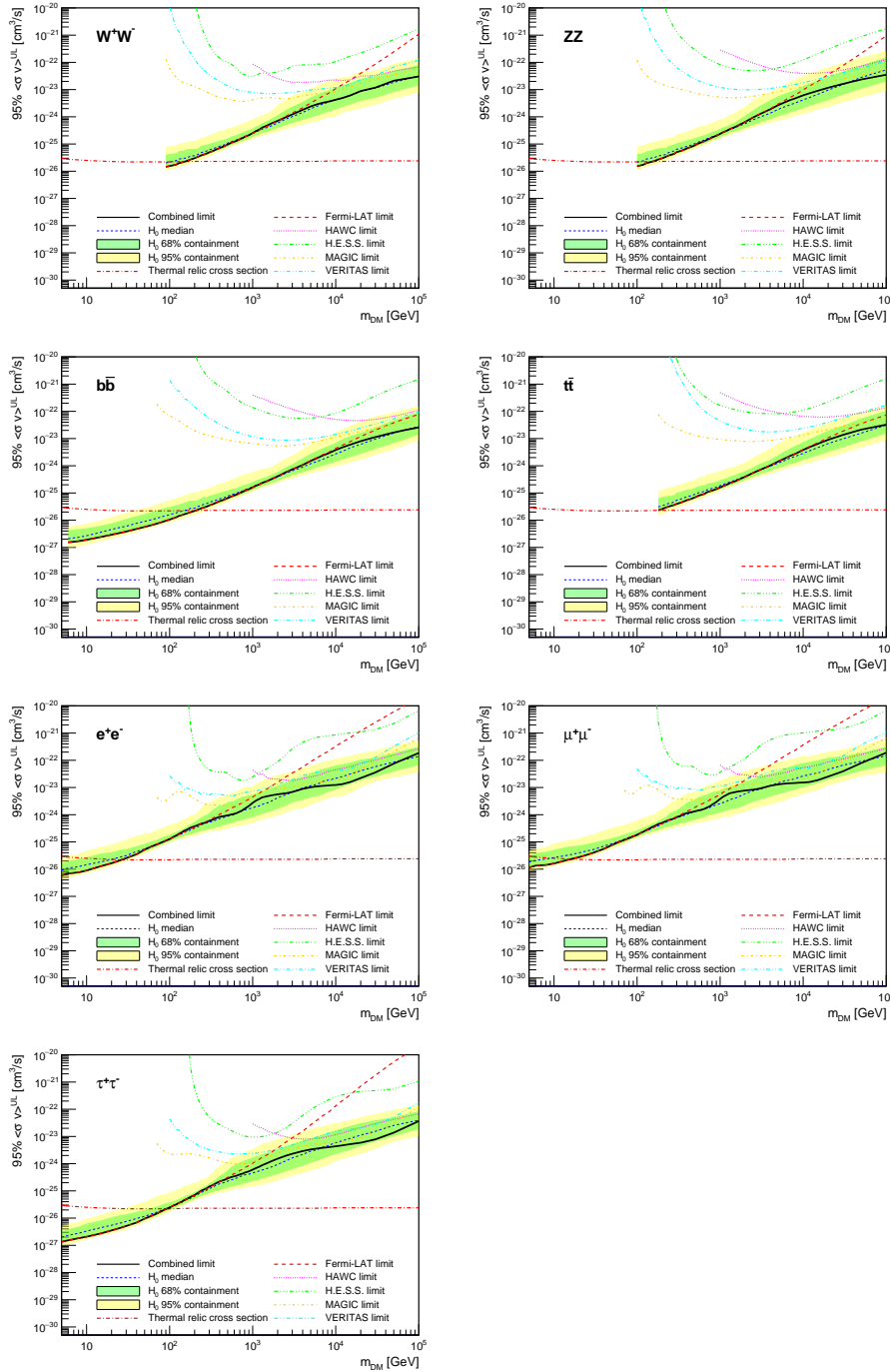


Figure 3.8 Upper limits at 95% confidence level on  $\langle\sigma v\rangle$  in function of the DM mass for eight annihilation channels, using the set of  $J$  factors from Ref. [69] ( $\mathcal{GS}$  set in Table 3.1). The black solid line represents the observed combined limit, the black dashed line is the median of the null hypothesis corresponding to the expected limit, while the green and yellow bands show the 68% and 95% containment bands. Combined upper limits for each individual detector are also indicated as solid, colored lines. The value of the thermal relic cross-section in function of the DM mass is given as the red dotted-dashed line [70].

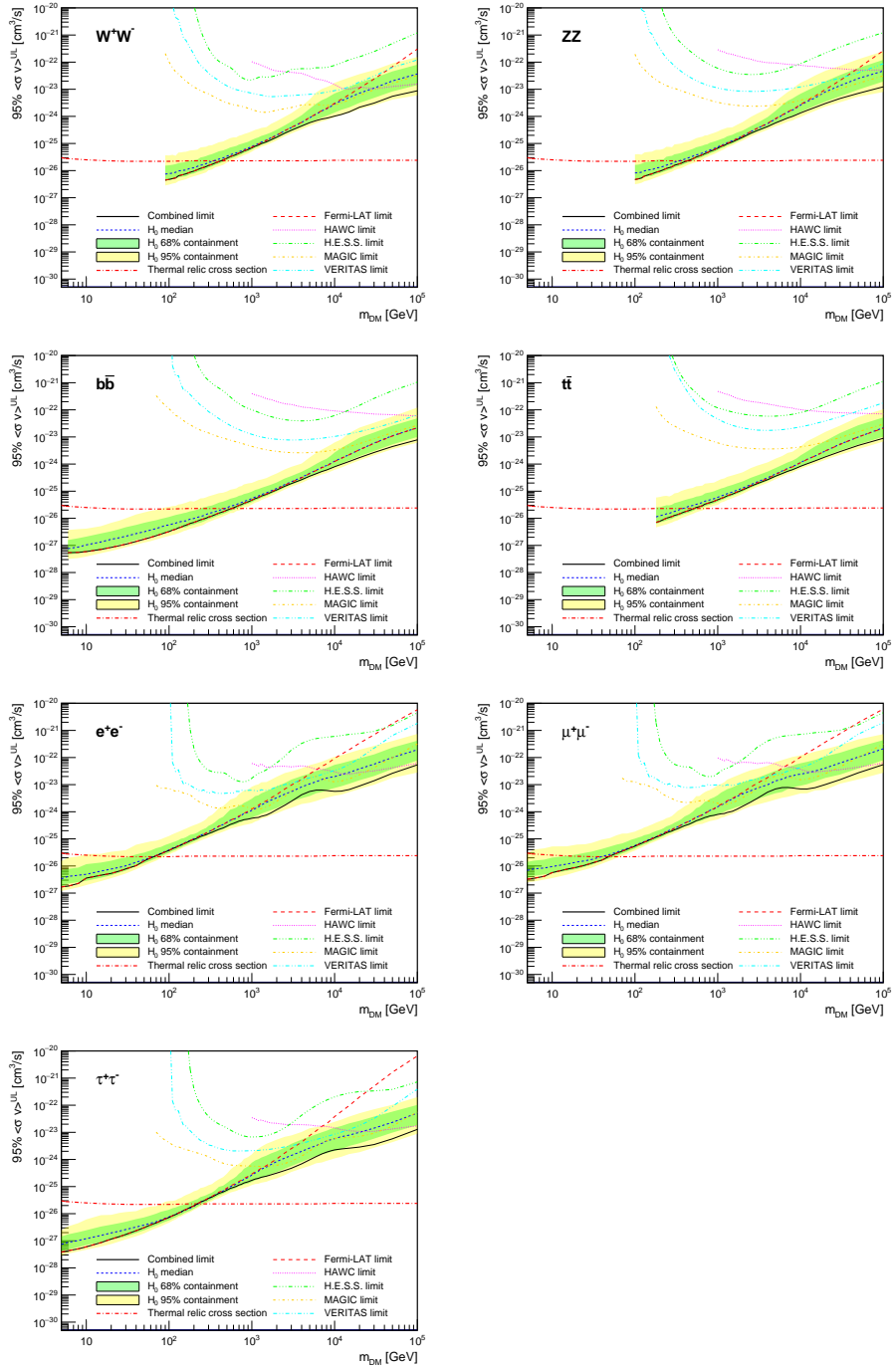


Figure 3.9 Same as Fig. 3.8, using the set of  $J$  factors from Ref. [63, 71] ( $\mathcal{B}$  set in Table 3.1).

observations of empty fields of view in the case of Fermi-LAT [64, 72, 73].

The obtained limits are shown in Figure 3.8 for the  $\mathcal{G}\mathcal{S}$  set of  $J$ -factors [69] and in Figure 3.9 for the  $\mathcal{B}$  set of  $J$ -factors [63, 71]. The combined limits are presented with their 68% and 95% containment bands, and are expected to be close to the median limit when no signal is present.

We observe agreement with the null hypothesis for all channels, within  $2\sigma$  standard deviations, between the observed limits and the expectations given by the median limits. Limits obtained from each detector are also indicated in the figures, where limits for all dSphs observed by the specific instrument have been combined.

Below  $\sim 300$  GeV, the *Fermi*-LAT dominates the DM limits for all annihilation channels. From  $\sim 300$  GeV to  $\sim 2$  TeV, *Fermi*-LAT continues to dominate for the hadronic and bosonic DM channels, yet the IACTs (H.E.S.S., MAGIC, and VERITAS) and *Fermi*-LAT all contribute to the limit for leptonic DM channels. For DM masses between  $\sim 2$  TeV to  $\sim 10$  TeV, the IACTs dominate leptonic DM annihilation channels, whereas both the *Fermi*-LAT and the IACTs dominate bosonic and hadronic DM annihilation channels. From  $\sim 10$  TeV to  $\sim 100$  TeV, both the IACTs and HAWC contribute significantly to the leptonic DM limit. For hadronic and bosonic DM, the IACTs and *Fermi*-LAT both contribute strongly.

We notice that the limits computed using the  $\mathcal{B}$  set of  $J$ -factor are always better compared to the ones calculated with the  $\mathcal{GS}$  set. For the  $W^+W^-$ ,  $Z^+Z^-$ ,  $b\bar{b}$ , and  $t\bar{t}$  channels, the ratio between the limits computed with the two sets of  $J$ -factor is varying between a factor of  $\sim 3$  and  $\sim 5$  depending on the energy, with the largest ratio around 10 TeV. For the channels  $e^+e^-$ ,  $\mu^+\mu^-$ , and  $\tau^+\tau^-$ , the ratio lies between  $\sim 2$  to  $\sim 6$ , being maximum around 1 TeV. Examining Figure 3.16 and Figure 3.17 in Section 3.8, these differences are explained by the fact that the  $\mathcal{B}$  set provides higher  $J$ -factors for the majority of the studied dSphs, with the notable exception of Segue I. The variation on the ratio of the limits for the two sets is due to different dSph dominating the limits depending on the energy. One set,  $\mathcal{B}$ , pushes the range of which thermal cross-section which can be excluded to higher mass. This comparison demonstrates the magnitude of systematic uncertainties associated with the choice of the  $J$ -factor calculation. The  $\mathcal{GS}$  and  $\mathcal{B}$  sets present a difference in the limits for all channels of about This difference is explained, see Figure 3.16 and Figure 3.17, by the fact that the  $\mathcal{B}$  set provides higher  $J$ -factors for all dSph except for Segue I.

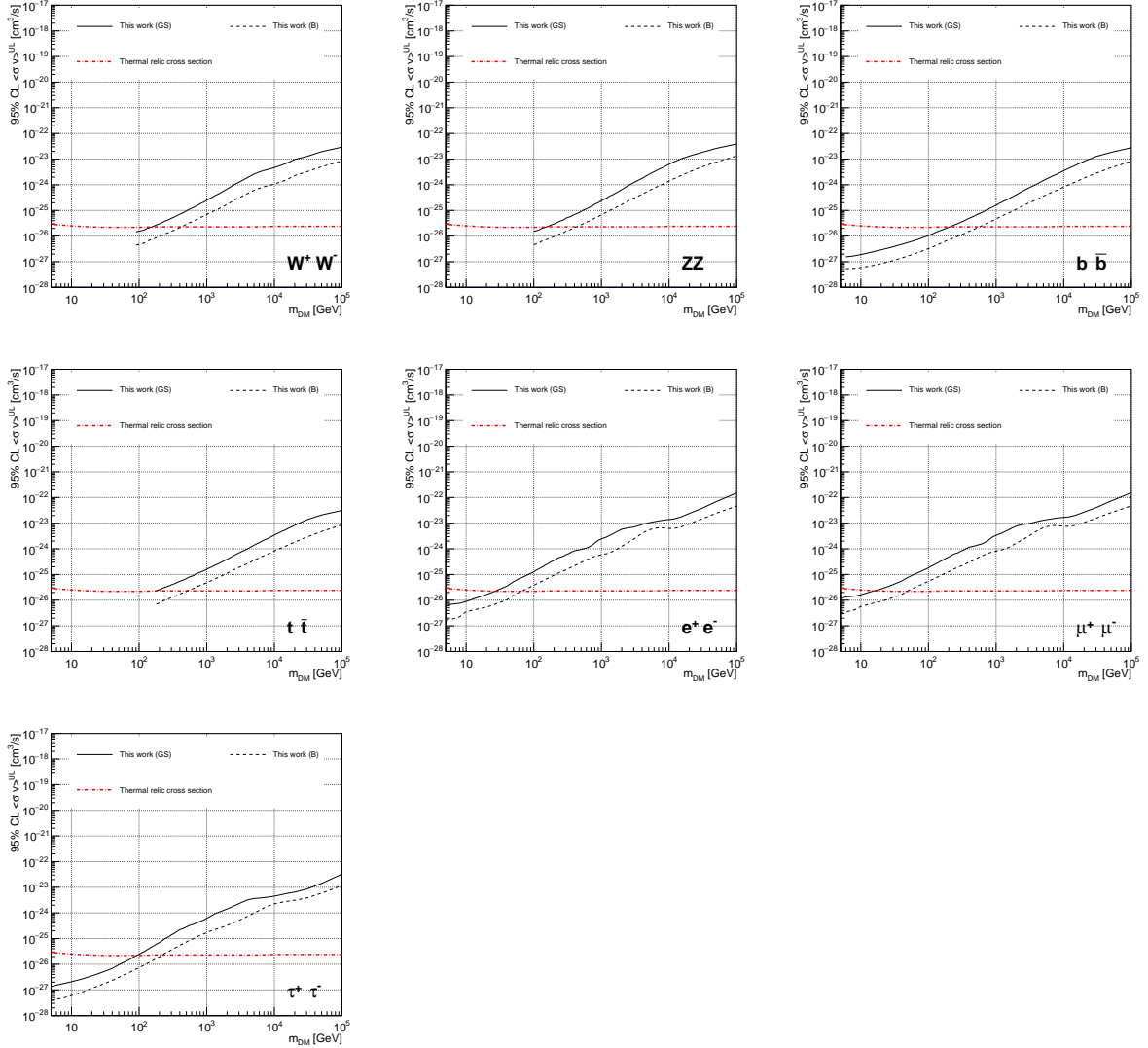


Figure 3.10 Comparisons of the combined limits at 95% confidence level for each of the eight annihilation channels when using the  $J$  factors from Ref. [69] ( $\mathcal{GS}$  set in Table 3.1), plain lines, and the  $J$  factor from Ref. [63, 71] ( $\mathcal{B}$  set in Table 3.1), dashed lines. The cross-section given by the thermal relic is also indicated [70].

### 3.7 HAWC Systematics

#### 3.7.1 Inverse Compton Scattering

The DM-DM annihilation channels produce many high energy electrons regardless of the primary annihilation channel. These high energy electrons can produce high energy gamma-rays through Inverse Compton Scattering (ICS). If this effect is strong, it would change the morphology of the source and increase the total expected gamma-ray counts from any source. The PPPC [58]

provides tools in Mathematica for calculating the impact of ICS for an arbitrary location in the sky for a specified annihilation channel. We calculated the change in gamma-ray counts for DM annihilation to primary  $e\bar{e}$  for RA and Dec corresponding to Segue1 and Coma Berenices. These dSphs were chosen because they are the strongest contributors to the limit.  $e\bar{e}$  was selected because it would have the largest number of high energy electrons. The effect was found to be on the order of  $10^{-7}$  on the gamma-ray spectrum. As a result, this systematic is not considered in our analysis.

### 3.7.2 Point Source Versus Extended Source Limits

The previous DM search toward dSph approximated the dSphs as point sources [60]. In this analysis, the dSphs are implemented as extended with J-factor distributions following those produced by [69]. The resolution of the cited map is much finer than HAWC’s angular resolution. The vast majority of the J-factor distribution is represented on the central HAWC pixel of the dSph spatial map. However, the neighboring 8 pixels are not negligible and contribute to our limit.

Figure 3.11 shows a substantial improvement to the limit for Segue1. Fig. 3.12 however showed identical limits. These disparities are best explained by the relative difference in their J-Factors. Both dSphs pass almost overhead the HAWC detector, however Segue1 has the larger J-Factor between the two. Adjacent pixels to the central pixel will therefore contribute to the limits. This is the case for other dSph that are closer to the zenith of the HAWC detector.

Comparison plots for all sources and the combined limit can be found in the sandbox for the Glory Duck project.

### 3.7.3 Impact of Pointing Systematic

During the analysis it was discovered that directional reconstruction of gamma-rays had a systematic bias at large zenith angles. Slides describing this systematic can be found [here](#). Shown on the presentation is dependence on the pointing systematic on declination. New spatial profiles were generated for every dSph and limits were computed for the adjusted declination.

Section 3.7.3 demonstrates the impact of this systematic for all DM annihilation channels studied by HAWC. The impact is a tiny improvement, yet mostly identical, to the combined limits.

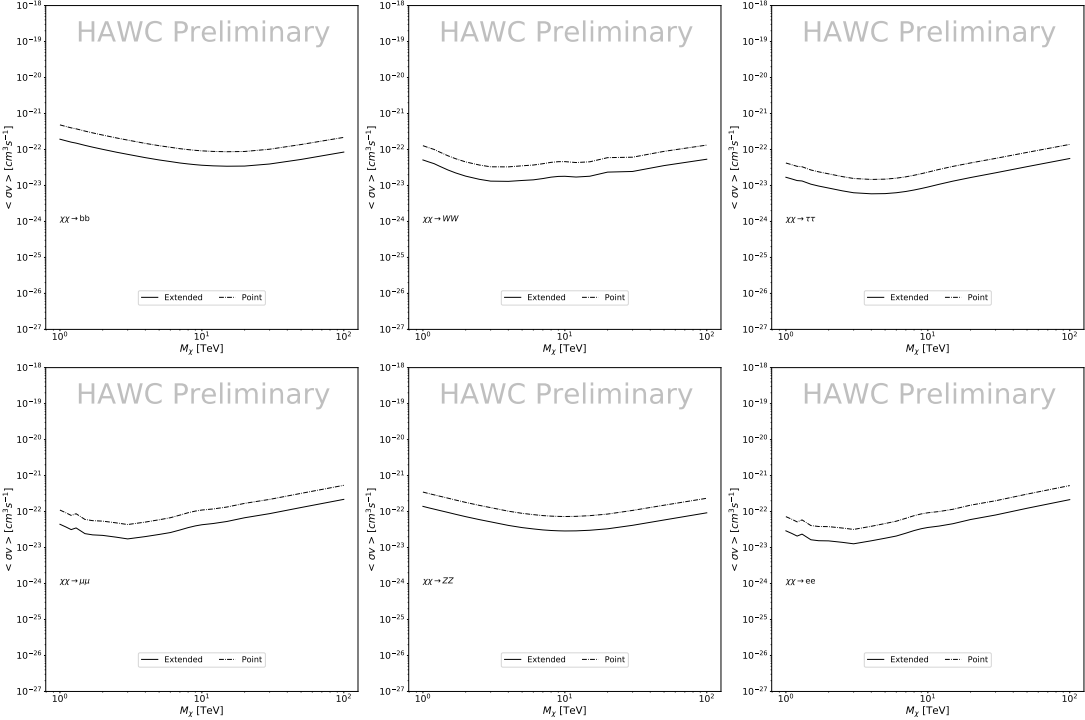


Figure 3.11 Comparisons of the combined limits at 95% confidence level for a point source analysis and extended source using [69]  $\mathcal{GS}$  J-factor distributions and PPPC [58] annihilation spectra. Shown are the limits for Segue1 which will have the most significant impact on the combined limit. 6 of the 7 DM annihilation channels are shown. Solid lines are extended source studies. Dashed lines are point source studies. Overall, the extended source analysis improves the limit by a factor of 2.

### 3.8 J-factor distributions

#### 3.8.1 Numerical integration of $\mathcal{GS}$ maps

It was discovered well after the HAWC analysis was completed that the published tables from  $\mathcal{GS}$  [59] quoted median  $J$ -factors were computed in a non-trivial manner. The assumption myself and collaborators had been that the published tables represented the  $J$ -factor as a function of  $\theta$  for the best global fit model on a per-source basis. However, this is not the case. Instead, what is published are the best fit model for each dwarf that only considers stars up to the angular separation  $\theta$ . Therefore, the model is changing for each value of  $\theta$  for each dwarf. Yet, the introduced features from unique models at each  $\theta$  are much smaller than the angular resolution of HAWC. It is not expected for these effects to impact the limits and TS greatly as a result.

Median  $J$ -factor model profiles were provided by the authors. New maps were generated

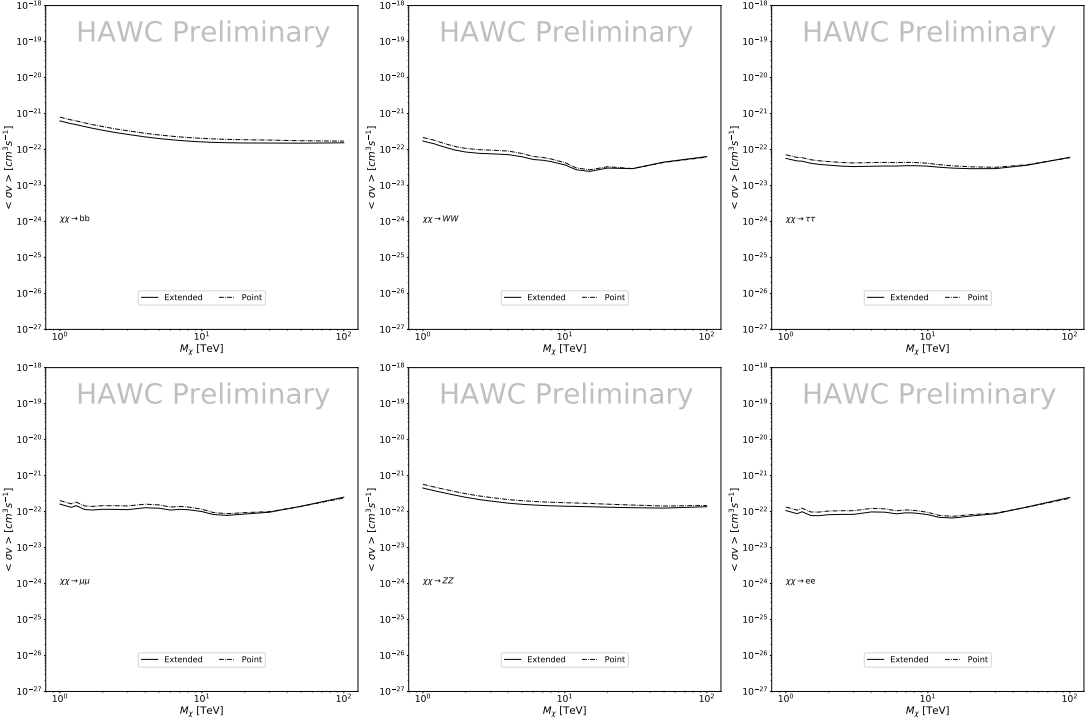


Figure 3.12 Same as Fig. 3.11 on Coma Berenices. This dSph also contributes significantly to the limit. The limits are identical in this case.

and analyzed for Segue1 and Coma Berenices. Figure 3.14 shows the differential between maps generated with the method from Section 3.8.1 and from the authors of [59]. These maps were reanalyzed for all SM DM annihilation channels. Upper limits for these channels are shown in Figure 3.15

From Figure 3.15, we can see that the impact of these model difference was no substantial. The observed impact was a fractional effect which is much smaller than the impact from selecting another DM spatial distribution model as was shown in Figure 3.10.

### 3.8.2 $\mathcal{GS}$ Versus $\mathcal{B}$ spatial models

We show in this appendix a comparison between the  $J$ -factors computed by Geringer-Sameth *et al.* [69] (the  $\mathcal{GS}$  set) and the ones computed by Bonnivard *et al.* [63, 71] (the  $\mathcal{B}$  set). The  $\mathcal{GS}$   $J$ -factors are computed through a Jeans analysis of the kinematic stellar data of the selected dSphs, assuming a dynamic equilibrium and a spherical symmetry for the dSphs. They adopted the generalized DM density distribution, known as Zhao-Hernquist, introduced by [61], carrying

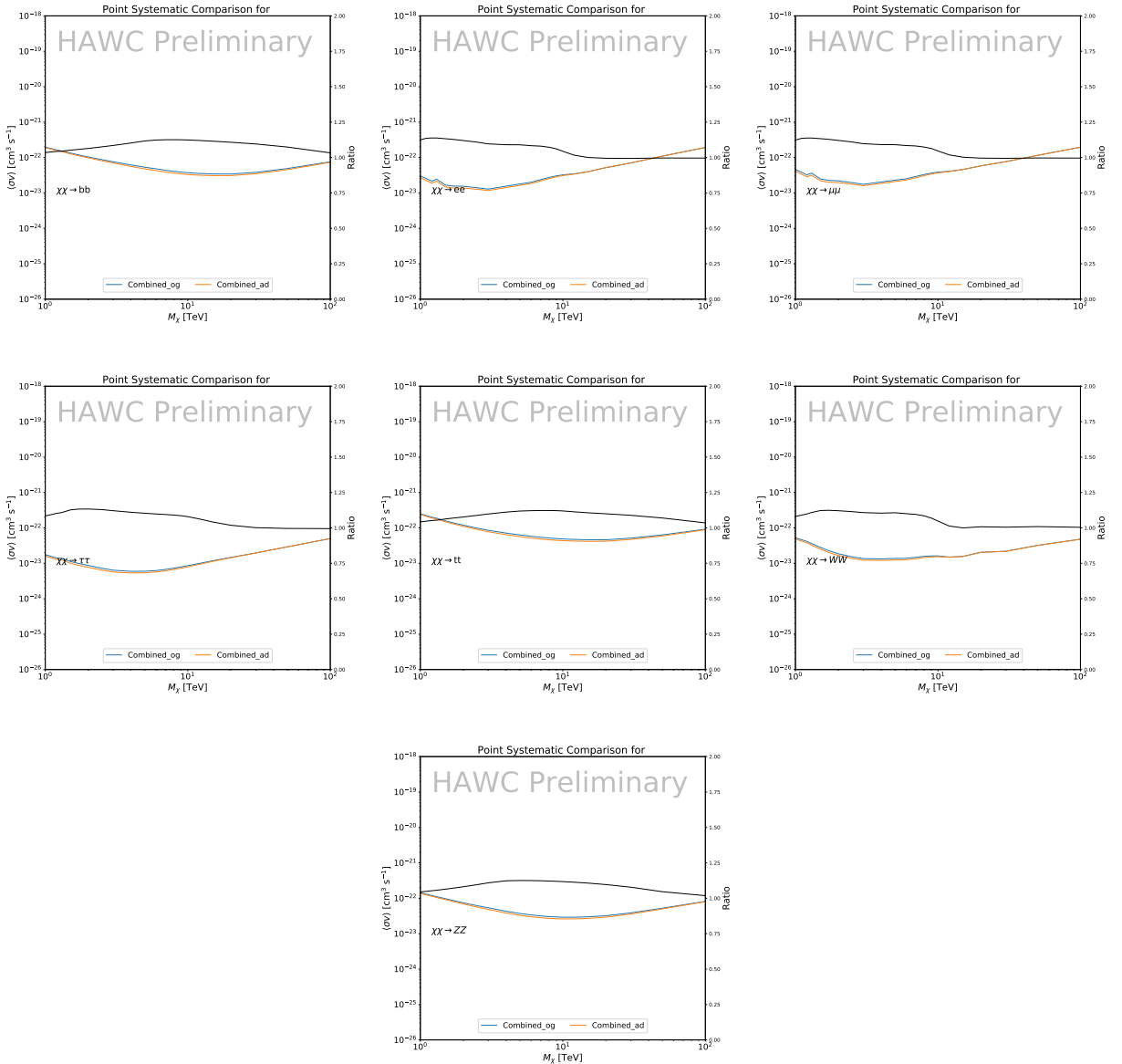


Figure 3.13 Comparison of combined limits when correcting for HAWC's pointing systematic. All DM annihilation channels are shown. The solid black line is the ratio between published limit to the declination corrected limit. The blue solid line or "Combined\_og" represented the limits computed for Glory Duck. The solid orange line or "Combined\_ad" represented the limits computed after correcting for the pointing systematic.

three additional index parameters to describe the inner and outer slopes, and the break of the density profile. Such a profile parametrization allows the reduction of the theoretical bias from the choice of a specific radial dependency on the kinematic data. In other words, the increase of free parameters with the use of the Zhao-Hernquist profile allows a better description of the mass

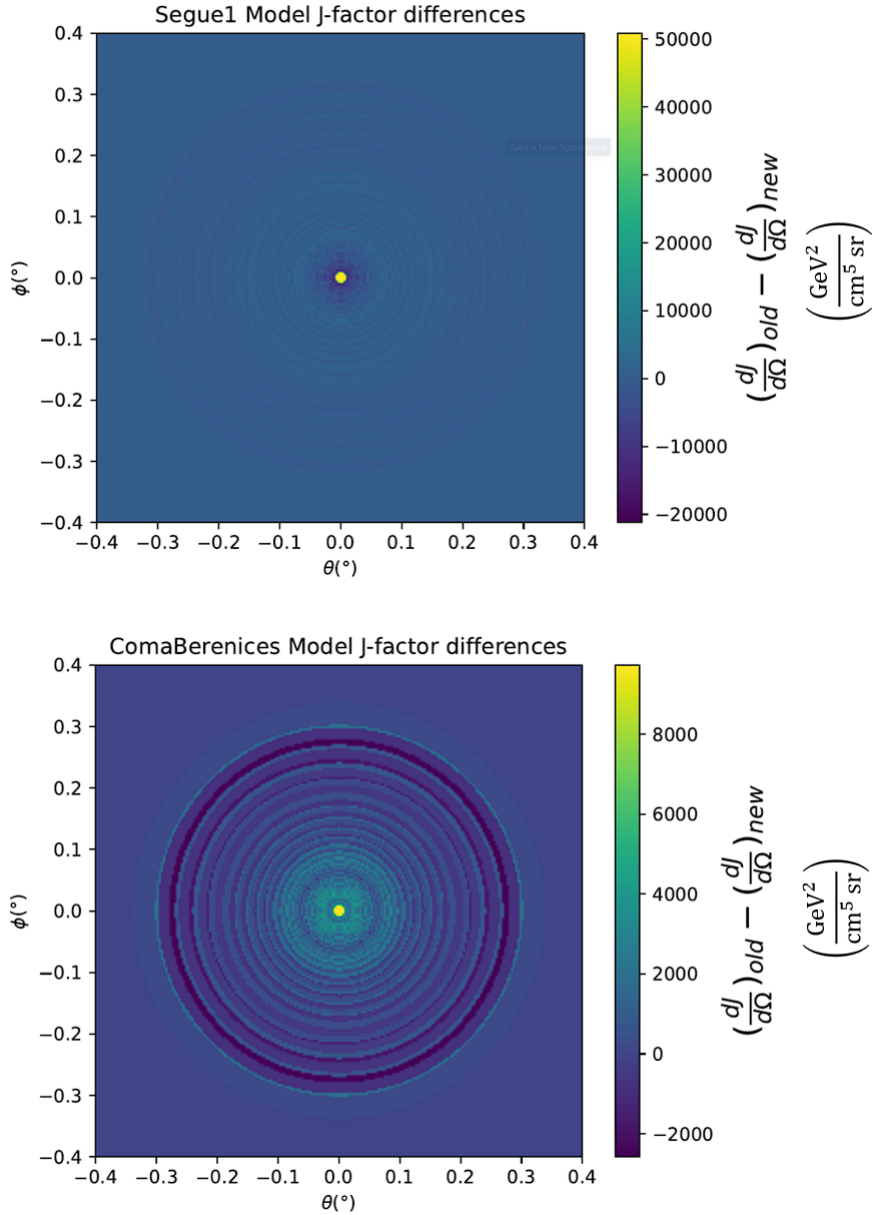


Figure 3.14 Differential map of  $dJ/\Omega$  from model built in Section 3.8.1 and profiles provided directly from authors. (Top) Differential from Segue1. (bottom) Differential from Coma Berenices. Note that their scales are not the same. Segue1 shows the deepest discrepancies which is congruent with its large uncertainties. Both models show anuli where unique models become apparent.

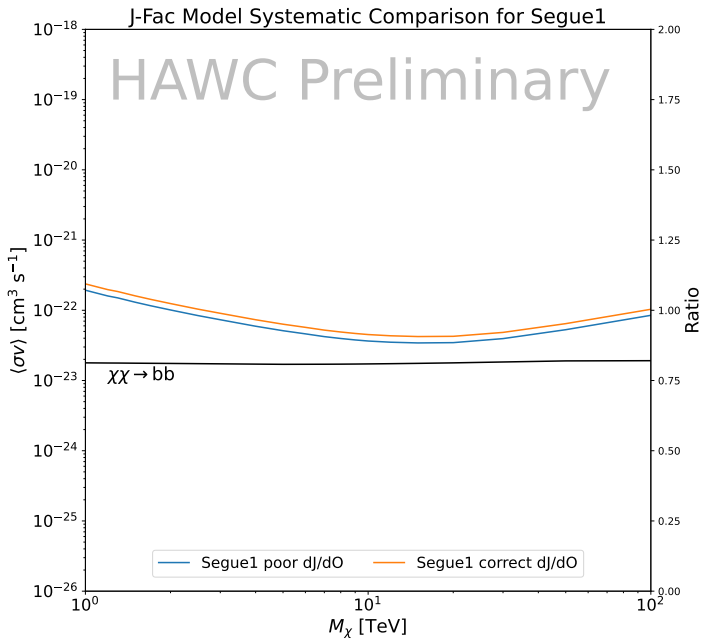
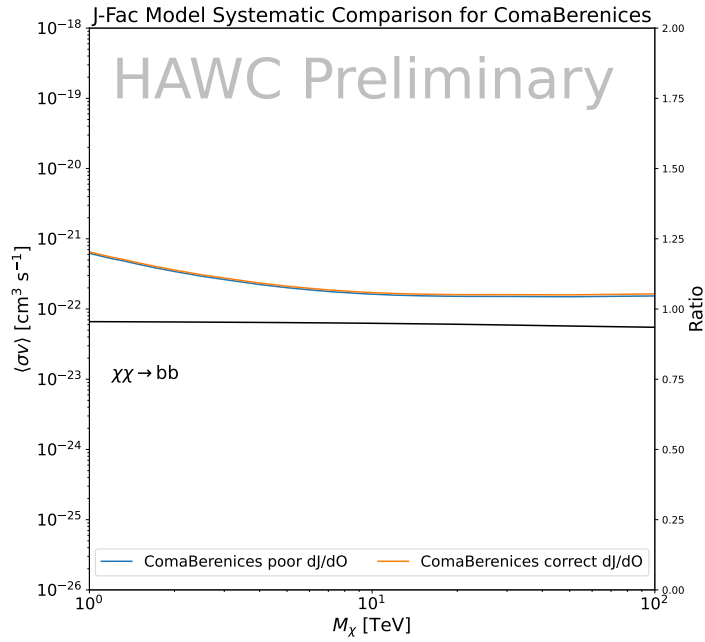


Figure 3.15 HAWC limits for Coma Berenices (top) and Segue1 (bottom) for two different map sets. Blue lines are limits calculated on maps with poor model representation. Orange lines are limits calculated on spatial profiles provided by the authors of [59]. Black line is the ratio of the poor spatial model limits to the corrected spatial models. The left y-axis measures  $\langle\sigma v\rangle$  for the blue and orange lines. The right y-axis measures the ratio and is unitless.

density distribution of dark matter.

In addition, a constant velocity anisotropy profile and a Plummer light profile [74] for the stellar distribution were assumed. The velocity anisotropy profile depends on the radial and tangential velocity dispersion. However, its determination remains challenging since only the line-of-sight velocity dispersion can be derived from velocity measurements. Therefore, the parametrization of the anisotropy profile is obtained from simulated halos (see [75] for more details). They provide the values of the  $J$ -factors of regions extending to various angular radius up to the outermost member star.

The  $\mathcal{B}$   $J$ -factors were computed through a Jeans analysis taking into account the systematic uncertainties induced by the DM profile parametrization, the radial velocity anisotropy profile, and the triaxiality of the halo of the dwarf galaxies. They performed a more complete study of the dSph kinematics and dynamics than  $\mathcal{GS}$  for the determination of the  $J$ -factor. Conservative values of the  $J$ -factors where obtained using an Einasto DM density profile [76], a realistic anisotropy profile known as the Baes & Van Hese profile [77] which takes into account that the inner regions can be significantly non-isotropic, and a Zhao-Hernquist light profile [61].

For both sets,  $J$ -factor values are provided for all dSphs as a function of the radius of the integration region [69, 63, 71]. Table 3.1 shows the heliocentric distance and Galactic coordinates of the twenty dSphs, together with the two sets of  $J$ -factor values integrated up to the outermost observed star for  $\mathcal{GS}$  and the tidal radius for  $\mathcal{B}$ . Both  $J$ -factor sets were derived through a Jeans analysis based on the same kinematic data, except for Draco where the measurements of [78] have been adopted in the computation of the  $\mathcal{B}$  value. The computations for producing the  $\mathcal{GS}$  and  $\mathcal{B}$  samples differ in the choice of the DM density, velocity anisotropy, and light profiles, for which the set  $\mathcal{B}$  takes into account some sources of systematic uncertainties.

Figure 3.16 and Figure 3.17 show the comparisons for the  $J$ -factor versus the angular radius for each of the 20 dSphs used in this study. The uncertainties provided by the authors are also indicated in the figures. For the  $\mathcal{GS}$  set, the computation stops at the angular radius corresponding to the outermost observed star, while for the  $\mathcal{B}$  set, the computation stops at the angular radius

corresponding to the tidal radius.

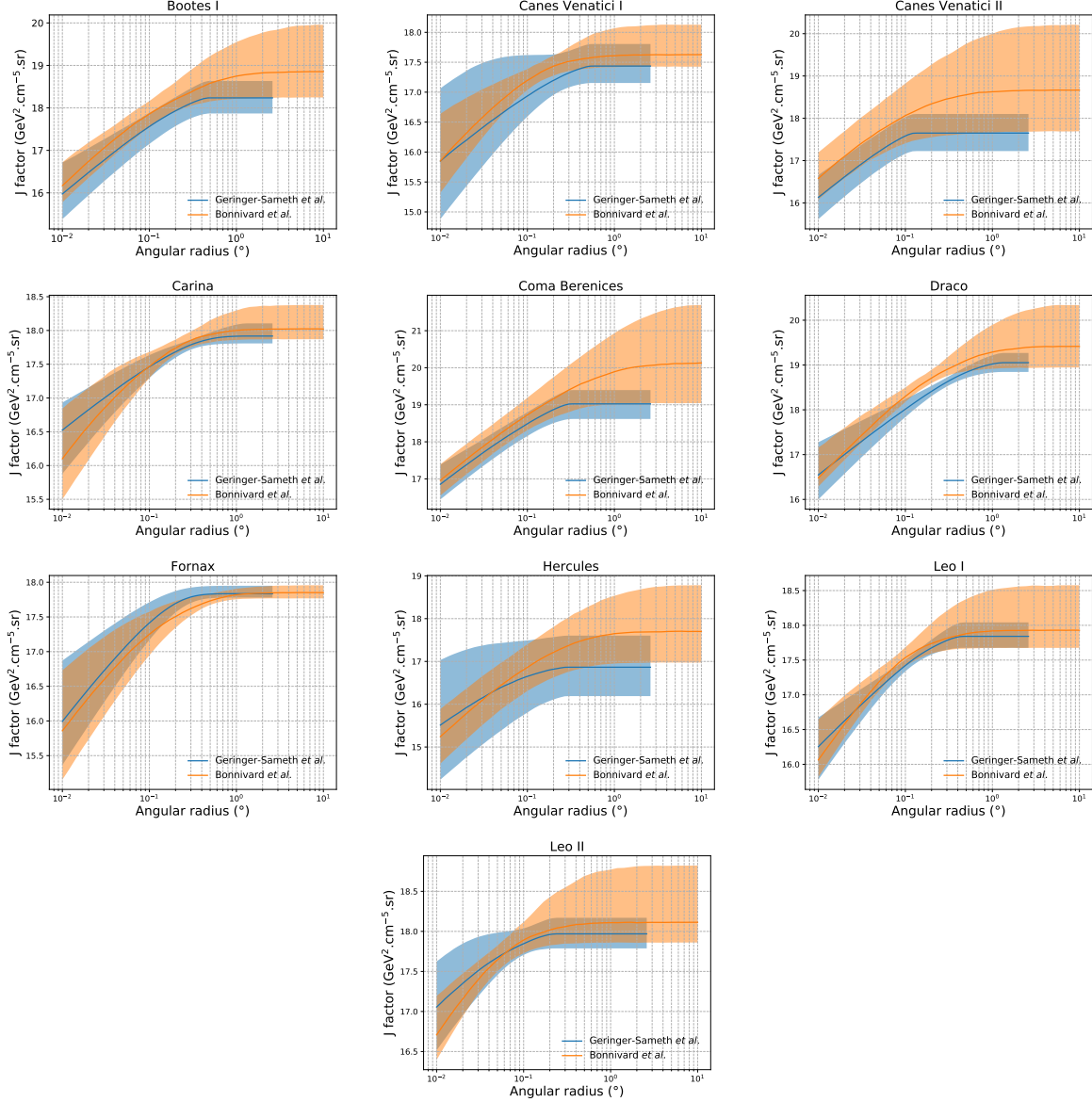


Figure 3.16 Comparisons between the  $J$ -factors versus the angular radius for the computation of  $J$  factors from Ref. [69] ( $\mathcal{GS}$  set in Table 3.1) in blue and for the computation from Ref. [63, 71] ( $\mathcal{B}$  set in Tab. 3.1) in orange. The solid lines represent the central value of the  $J$ -factors while the shaded regions correspond to the  $1\sigma$  standard deviation.

### 3.9 Discussion and Conclusions

In this multi-instrument analysis, we have used observations of 20 dSphs from the gamma-ray telescopes Fermi-LAT, H.E.S.S., MAGIC, VERITAS, and HAWC to perform a collective DM search annihilation signals. The data were combined across sources and detectors to significantly

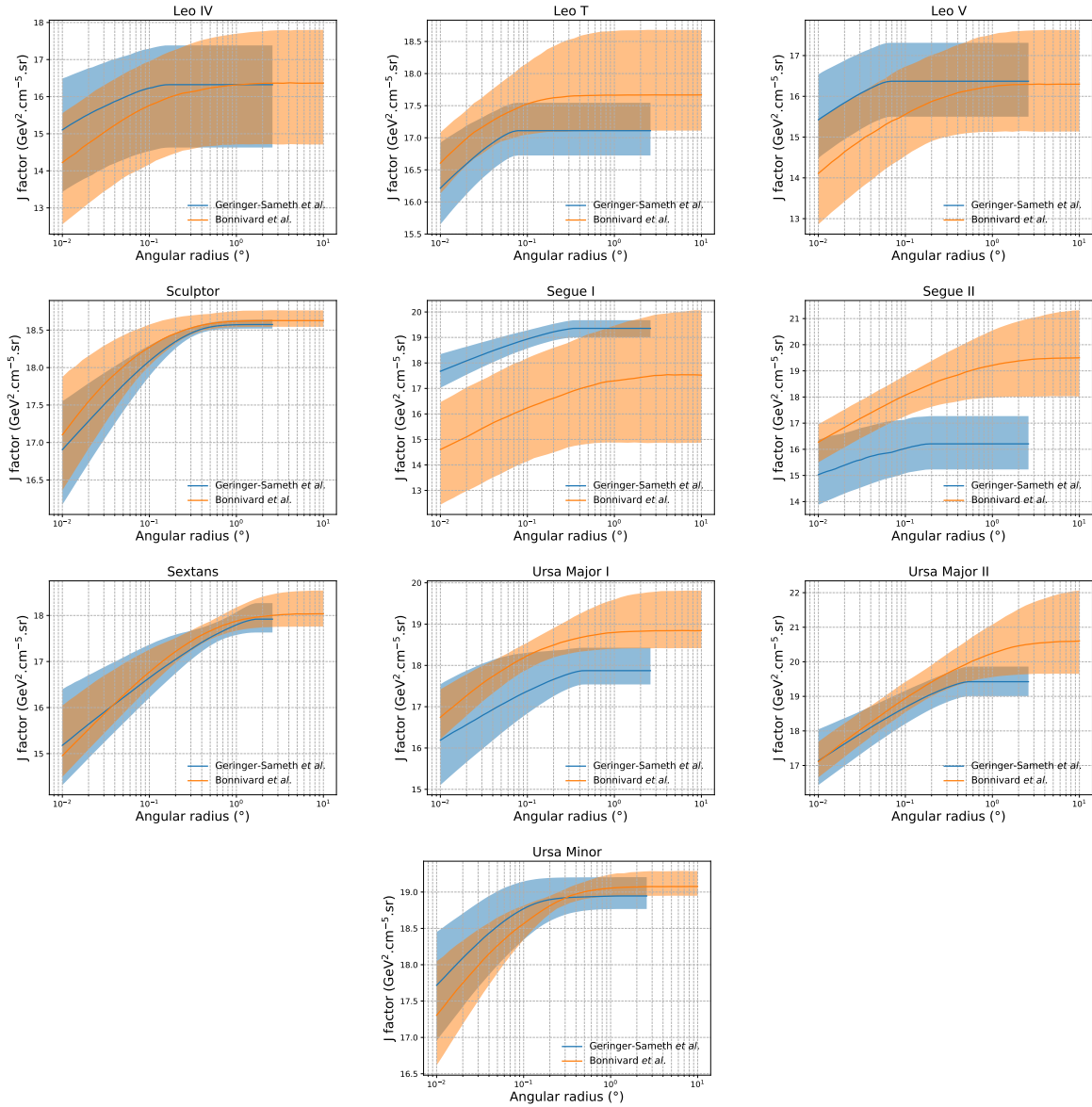


Figure 3.17 Comparisons between the  $J$ -factors versus the angular radius for the computation of  $J$  factors from Ref. [69] ( $\mathcal{GS}$  set in Tab. 3.1) in blue and for the computation from Ref. [63, 71] ( $\mathcal{B}$  set in Tab. 3.1) in orange. The solid lines represent the central value of the  $J$ -factors while the shaded regions correspond to the  $1\sigma$  standard deviation.

increase the sensitivity of the search. We have observed no significant deviation from the null, no DM hypothesis, and so present our results in terms of upper limits on the annihilation cross-section for seven potential DM annihilation channels.

Fermi-LAT brings the most stringent constraints for continuum channels below approximately 1 TeV. The remaining detectors dominate at higher energies. Overall, for multi-TeV DM mass,

the combined DM constraints from all five telescopes are 2-3 times stronger than any individual telescope for multi-TeV DM.

Derived from observations of many dSphs, our results produce robust limits given the DM content of the dSphs is relatively well constrained. The obtained limits span the largest mass range of any WIMP DM search. Our combined analysis improves the sensitivity over previously published results from each detector which produces the most stringent limits on DM annihilation from dSphs. These results are based on deep exposures of the most promising known dSphs with the currently most sensitive gamma-ray instruments. Therefore, our results constitute a legacy of a generation of gamma-ray instruments on WIMP DM searches towards dSphs. Our results will remain the reference in the field until a new generation of more sensitive gamma-ray instruments begin operations, or until new dSphs with higher  $J$ -factors are discovered.

This analysis serves as a proof of concept for future multi-instrument and multi-messenger combination analyses. With this collaborative effort, we have managed to sample over four orders in magnitude in gamma-ray energies with distinct observational techniques. Determining the nature of DM continues to be an elusive and difficult problem. Larger datasets with diverse measurement techniques could be essential to tackling the DM problem. A future collaboration using similar techniques as the ones described in this paper could grow even beyond gamma rays. The models we used for this study include annihilation channels with neutrinos in the final state. Advanced studies could aim to merge our results with those from neutrino observatories with large data sets. Efforts are already underway to add data from the IceCube, ANTARES, and KM3NeT observatories to these gamma-ray results.

From this work, a selection of the best candidates for observations, according to the latest knowledge on stellar dynamics and modelling techniques for the derivation of the  $J$ -factors on the potential dSphs targets, is highly desirable at the time that new experiments are starting their dark matter programs using dSphs. Given the systematic uncertainty inherent to the derivation of the  $J$ -factors, an informed observational strategy would be to select both objects with the highest  $J$ -factors that could lead to DM signal detection, and objects with robust  $J$ -factor predictions, i.e.

with kinematic measurements on many bright stars, which would strengthen the DM interpretation reliability of the observation outcome.

This analysis combines data from multiple telescopes to produce strong constraints on astrophysical objects. From this perspective, these methods can be applied beyond just DM searches. Almost every astrophysical study can benefit from multi-telescope, multi-wavelength gamma-ray studies. We have enabled these telescopes to study the cosmos with greater precision and detail. Many astrophysical searches can benefit from multi-instrument gamma-ray studies, for which our analysis lays the foundation.

## CHAPTER 4

### MULTITHREADING HAWC ANALYSES FOR DARK MATTER SEARCHES

#### 4.1 Introduction

HAWC’s current software suite, plugins to 3ML and HAL [68, 34], do not fully utilize computational advancements of recent decades. Said advancements include the proliferation of Graphical Processing Units (GPUs), and multithreading on multicore processors. The analysis described in chapter 3 took up to 3 months of wall time waiting for the full gambit of data analysis and simulation of background to compute. Additionally, with the updated 2D energy binning scheme split by  $f_{\text{hit}}$  and estimated energy from our Neural Network (NN) method, the time needed to compute was expected to grow. Although excessive computing time was, in part, from an intense use of a shared computing cluster, it was evident that there was room for improvement. In HAWC’s next generation dSph DM search, I decided to develop codes that would utilize the multicore processors on modern high performance computing clusters. The results of this work are featured in this chapter and brought a human timing improvement to computation that scales approximately as  $1/N$  where  $N$  is the number of threads.

#### 4.2 Dataset and Background

This section describes the data and background methods used for HAWC’s multithreaded study of dSphs. Section 4.2.1 and Section 4.2.2 are most useful for fellow HAWC collaborators looking to replicate a multithreaded dSph DM search.

##### 4.2.1 Itemized HAWC files

These files are only available within HAWC’s internal documentation and collaborators. They are not meant for public access, and are presented here so that HAWC collaborators can reproduce results accurately.

- Detector Resolution: `refit-Pass5-Final-NN-detRes-zenith-dependent.root`
- Data Map: `Pass5-Final-NN-maptree-ch103-ch1349-zenith-dependent.root`

- Spectral Dictionary: `HDMspectra_dict_gamma.npy`

### 4.2.2 Software Tools and Development

This analysis was performed using HAL and 3ML [34, 57] in Python3. I built software in collaboration with Michael Martin and Letrell Harris to implement the *Dark Matter Spectra from the Electroweak to the Planck Scale* (HDM) [79] and dSphs spatial model from [80] for HAWC analysis. A NumPy dictionary of HDM, `HDMspectra_dict_gamma.npy`, was made for portability within the collaboration. These dictionaries were generated from the [git repository](#) [79]. The analysis was performed using the Neural Network energy estimator for Pass 5.F. A description of this estimator was provided in chapter 2. [TODO: Define a subsection when it's written](#), and its key, relevant improvements are an improved energy estimation and improved sensitivities at higher zenith angles. All other software used for data analysis, DM profile generation, and job submission to SLURM are also kept in my sandbox in the [Dark Matter HAWC](#) project. The above repository also incorporates the model inputs used previously in Glory Duck, described in chapter 3, so Glory Duck remains compatible with modern software.

### 4.2.3 Data Set and Background Description

The HAWC data maps used for this analysis contain 2565 days of data between runs 2104 and 7476. They were generated from pass 5.f reconstruction. The analysis is performed using the NN energy estimator with nominal bin list:

```
B1C0Ea, B1C0Eb, B1C0Ec, B1C0Ed, B1C0Ee, B2C0Ea, B2C0Eb, B2C0Ec, B2C0Ed, B2C0Ee,
B3C0Ea, B3C0Eb, B3C0Ec, B3C0Ed, B3C0Ee, B3C0Ef, B4C0Eb, B4C0Ec, B4C0Ed, B4C0Ee,
B4C0Ef, B5C0Ec, B5C0Ed, B5C0Ee, B5C0Ef, B5C0Eg, B6C0Ed, B6C0Ee, B6C0Ef, B6C0Eg,
B6C0Eh, B7C0Ee, B7C0Ef, B7C0Eg, B7C0Eh, B7C0Ei, B8C0Ee, B8C0Ef, B8C0Eg, B8C0Eh,
B8C0Ei, B8C0Ej, B9C0Ef, B9C0Eg, B9C0Eh, B9C0Ei, B9C0Ej, B10C0Eg, B10C0Eh,
B10C0Ei, B10C0Ej, B10C0Ek, B10C0El
```

Bin 0 was excluded as it has substantial hadronic contamination and poor angular resolution. This

list was cut down depending on the declination of the source because the PSF of these bins were too large, or the statistics were too low.

Background considerations and source selection was identical to Section 3.2.3, and no additional arguments are provided here. Many of the HAWC systematics explored in Section 3.7 also apply for this DM search and are not added upon here.

### 4.3 Analysis

The analysis and its systematics are almost identical to Section 3.3. Importantly, we use the same Equation (3.1) and Equation (3.2) for estimating the gamma-ray flux at HAWC from our sources.

#### 4.3.1 $\frac{dN_\gamma}{dE_\gamma}$ - Particle Physics Component

For these spectra, we import HDM with Electroweak (EW) corrections and additional corrections for neutrinos above the EW scale [79]. The spectra are implemented as a model script in astromodels for 3ML. A comprehensive description of EW corrections and neutrino considerations are provided later in Sec. 7.

Figure 4.1 demonstrates the impact of changes implemented in HDM on DM annihilation to W bosons. A class in astromodels was developed to include HDM and is aptly named `HDMspectra` within `DM_models.py`. The SM DM annihilation channels studied here are  $\chi\chi \rightarrow:$

$$e^+e^-, \mu^+\mu^-, \tau^+\tau^-, b\bar{b}, t\bar{t}, gg, W^+W^-, ZZ, c\bar{c}, u\bar{u}, d\bar{d}, s\bar{s}, \nu_e\overline{\nu_e}, \nu_\mu\overline{\nu_\mu}, \nu_\tau\overline{\nu_\tau}, \gamma\gamma, hh.$$

For  $\gamma\gamma$  and  $ZZ$ , a substantial fraction of the signal photons are expected to have  $E_\gamma = m_\chi$  [79]. This introduces a  $\delta$ -function in the tested spectra, referred to as a spectral line, that is much narrower than the energy resolution of the HAWC detector. To ensure that this feature is not lost in the likelihood fits, the ‘line’ feature is convolved with a Gaussian kernel with a  $1\sigma$  width of  $0.05 \cdot m_\chi$  and total kernel window of  $\pm 4\sigma$ . The kernel width was chosen based on the choices made from HAWC’s previous gamma-line study [81] and the observed energy resolution of the NN energy estimator [37]. This differs from HAWC’s previous line study where 30% of HAWC’s energy resolution was used for the kernel [81]. The NN energy estimator’s improved energy resolution

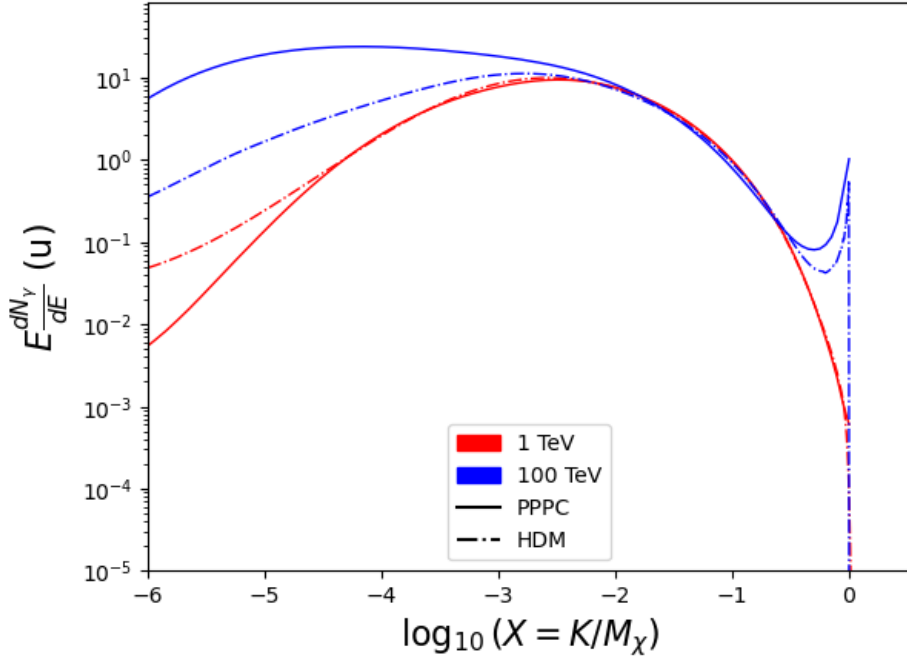


Figure 4.1 Spectral hypotheses from PPPC [58] and HDM [79] for DM annihilation:  $\chi\chi \rightarrow W^-W^+$ . Solid lines are spectral models with EW corrections from the PPPC. Dash-dot lines are spectral models from HDM. Red lines are models for  $M_\chi = 1$  TeV. Blue lines represent models for  $M_\chi = 100$  TeV.

compared to  $f_{\text{hit}}$  at low gamma-ray energy enables narrower kernels [79] and see Section 2.2.4. The annihilation spectra after Gaussian smoothing for  $\chi\chi \rightarrow \gamma\gamma$  and  $ZZ$  spectral hypotheses are shown in Figure 4.2. We did not explore how well we reconstruct injected signal events for various kernels widths. This is a systematic that should be tested before publication in a journal. Spectral models for the remaining annihilation channels are plotted for each  $m_\chi$  in Figure B.1.

### 4.3.2 J Astrophysical Components

The J-factor profiles for each source are imported from Louis Strigari et al. (referred to with  $\mathcal{LS}$ ) [80]. The  $\mathcal{LS}$  catalog fits a Navarro–Frenk–White (NFW) [62] spatial DM distributions to the dSphs which has a DM density of

$$\rho(r) = \frac{\rho_0}{\frac{r}{R_s} \left(1 + \frac{r}{R_s}\right)^2}. \quad (4.1)$$

$\rho_0$  and the scale radius,  $R_s$  are free parameters fit for each dSph.  $r$  is the distance from the center of the dSph.

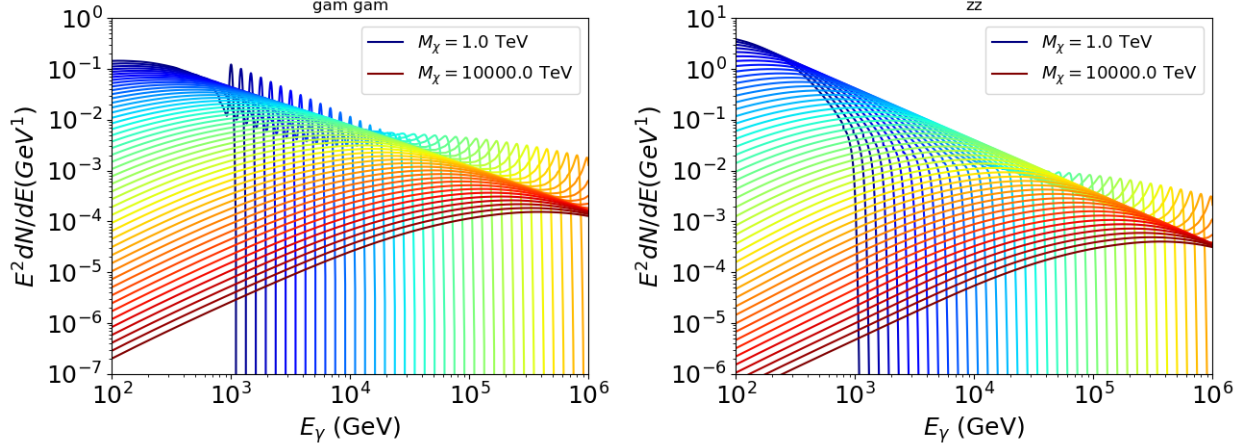


Figure 4.2 Photon spectra for  $\chi\chi \rightarrow \gamma\gamma$  (left) and  $\chi\chi \rightarrow ZZ$  (right) after Gaussian convolution of line features. Both spectra have  $\delta$ -features at photon energies equal to the DM mass. Bluer lines are annihilation spectra with lower DM mass. Redder lines are spectra from larger DM mass. All spectral models are sourced from the Heavy Dark Matter models [79]. Axes are drawn roughly according to the energy sensitivity of HAWC.

Profiles in  $\frac{dJ}{d\Omega}(\theta)$  up to an angular separation  $\theta = 0.5^\circ$  were provided directly by the authors.

Map generation from these profiles were almost identical to Section 3.3.2 except that a higher order trapezoidal integral was used for the normalization of the square, uniformly-spaced map:

$$p^2 \cdot \sum_{i=0}^N \sum_{j=0}^M w_{i,j} \frac{dJ}{d\Omega}(\theta_{i,j}, \phi_{i,j}) \quad (4.2)$$

$p$  is the angular side of one pixel in the map.  $w_{i,j}$  is a weight assigned the following ways:

$w_{i,j} = 1$  if  $(\theta_{i,j}, \phi_{i,j})$  is fully within the region of integration

$w_{i,j} = 1/2$  if  $(\theta_{i,j}, \phi_{i,j})$  is on an edge of the region of integration

$w_{i,j} = 1/4$  if  $(\theta_{i,j}, \phi_{i,j})$  is on a corner of the region of integration

Figure 4.3 shows the median and  $\pm 1\sigma$  maps used as input for this DM annihilation study.

### 4.3.3 Source Selection and Annihilation Channels

HAWC's sources for this multithreaded analysis include Coma Berenices, Segue 1, and Sextans.  $\mathcal{LS}$  estimated the DM distributions of 43 sources in its publication, however only 4 of the best fit profiles within HAWC's field of view were provided at the time this thesis was written. A full description of each source used in this analysis is found in Table 4.1.

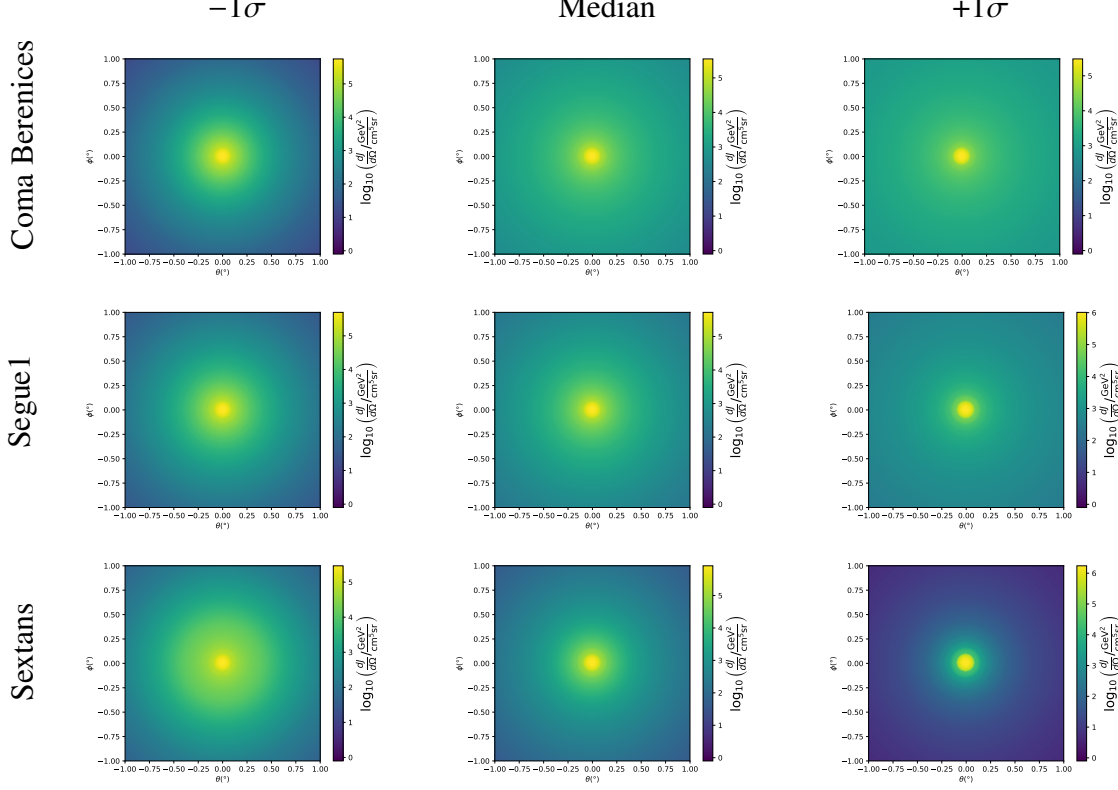


Figure 4.3  $\frac{dJ}{d\Omega}$  maps for Coma Berenices, Segue1, and Sextans. Columns are divided for the  $\pm 1\sigma$  uncertainties in  $dJ/d\Omega$  around the mean value from  $\mathcal{LS}$  [80]. Origin is centered on the specific dwarf spheroidal galaxies (dSph).  $\theta$  and  $\phi$  axes are the angular separation from the center of the dwarf. Profiles are truncated at  $1^\circ$  and flattened beyond.

This analysis improves on chapter 3 in the following ways. Previously, the particle physics model used for gamma-ray spectra from DM annihilation was from the PPPC [58] which missed important considerations relevant for the neutrino sector. HDM is used to account for this shortfall

Name	Distance (kpc)	$l, b$ ( $^\circ$ )	$\log_{10} J$ ( $\mathcal{LS}$ set) $\log_{10}(\text{GeV}^2 \text{cm}^{-5} \text{sr})$
Coma Berenices	44	241.89, 83.61	$19.00^{+0.36}_{-0.35}$
Segue I	23	220.48, 50.43	$19.12^{+0.49}_{-0.58}$
Sextans	86	243.50, 42.27	$17.73^{+0.13}_{-0.12}$

Table 4.1 Summary of the relevant properties of the dSphs used in the present work. Column 1 lists the dSphs. Columns 2 and 3 present their heliocentric distance and galactic coordinates, respectively. Column 4 reports the  $J$ -factors of each source given from the  $\mathcal{LS}$  studies and estimated  $\pm 1\sigma$  uncertainties. The values  $\log_{10} J$  ( $\mathcal{LS}$  set) [80] correspond to the mean  $J$ -factor values for a source extension truncated at  $0.5^\circ$ .

[79]. HDM also models DM to the Planck scale which permits HAWC to probe PeV scale DM. For this study, we sample DM masses: 1 TeV - 10 PeV with 6 mass bins per decade in DM mass. In the case of line spectra ( $\chi\chi \rightarrow \gamma\gamma$ , or  $ZZ$ ), we double the mass binning to 12 DM mass bins per decade in DM mass.

$\mathcal{LS}$  published 25 sources'  $J$ -factors within HAWC's field of view. Additionally, NFW [62] DM distributions have fewer parameters than Zhao [61], so  $\mathcal{LS}$  fits ultra-faint dwarves which expands the number of sources. However, all sources were not provided by the authors in time for the completion of this dissertation. Draco was provided by the authors. However, Draco is not included in this study as the PSF of the bins at its declination were wider than what is reasonable for a point source analysis. Finally, the gamma-ray ray dataset is much larger. The study performed here analyzes 2565 days of data compared to 1017 days analyzed in chapter 3.

#### 4.4 Likelihood Methods

These are identical to Section 3.4.1 and no additional changes are made to the likelihood. Bins in this analysis are expanded to include HAWC's NN energy estimator.

#### 4.5 Computational Methods: Multithreading

Previously, as in Section 3.3, the likelihood was minimized for one model at a time. One model in this case representing a DM annihilation channel (CHAN), DM mass ( $m_\chi$ ), and dSph ((SOURCE)). In an effort to conserve human and CPU time, jobs submitted for high performance computing contained a list of  $m_\chi$  to iterate over for likelihood fitting. Jobs were then trivially parallelized for each permutation of the two lists: CHANS and SOURCES. The lists for CHANS and SOURCES are found in Section 4.3.1 and Table 4.1, respectively. Initially, 11  $m_\chi$  were serially sampled for one job defined by a [CHAN, SOURCE] tuple. Computing the likelihoods would take between 1.5 to 2 hrs, stochastically, for a job. We expect to compute likelihoods for data and 300 Poisson background trials. The estimated CPU time based on the above for all CHAN (N = 17) and SOURCE (M = 25) was estimated to 127,925 jobs. In total, 1,407,175 likelihood fits and profiles would be computed for the 11 mass bins we wished to study. The estimated CPU time ranged between 8k CPU days to 10k CPU days. Human time is more challenging to estimate as job allocation is stochastic and

highly dependent on what other users are submitting. Yet, it is unlikely that all jobs would run simultaneously. Therefore, we can expect human time to be about as long as was seen in chapter 3 which was on the order of months to fully compute on a smaller analysis. A visual aid to describe how jobs were organized is provided in Figure 4.4.

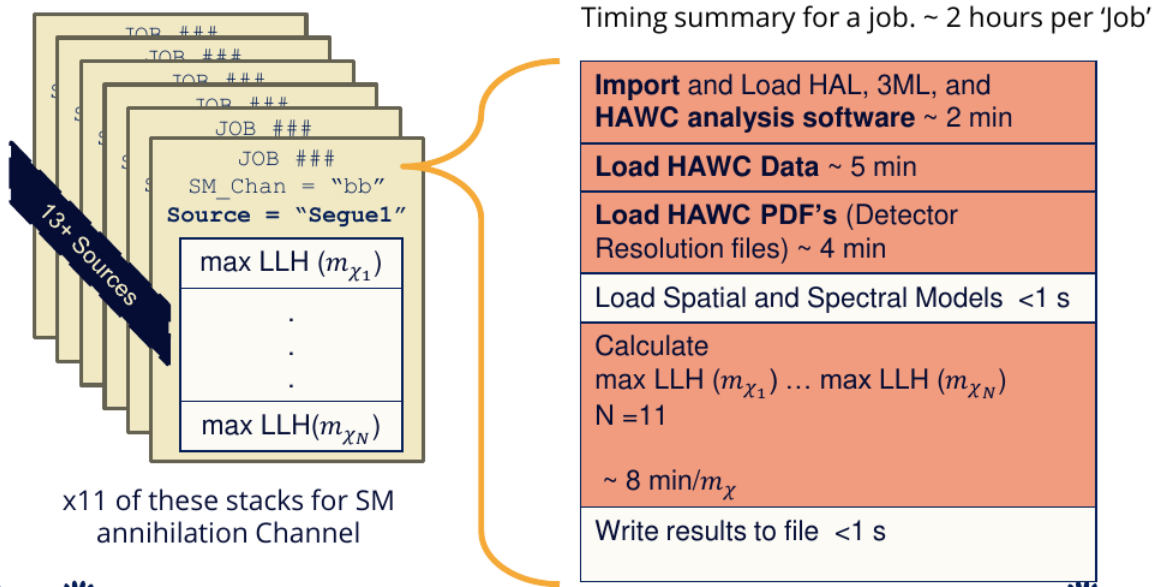


Figure 4.4 Infographic on how jobs and DM computation was organized in Section 3.3. Jobs were built for each permutation of CHANS and SOURCES shown by the left block in the figure. Each job, which took on the order 2 hrs to compute, had the following work flow: 1. Import HAWC analysis software, 2 min to run. 2. Load HAWC count maps, 5 min to run. 3. Load HAWC energy and spatial resolutions, 4 min. 5. Load DM spatial source templates and spectral models, less than 1 s. 6. Perform likelihood fit on data and model, about 8 min per DM mass. 7. Write results to file, less than 1s.

The computational needs for this next generation DM analysis are extreme and is unlike other analyses performed on HAWC. It became clear that there was a lot to gain from optimizing how the likelihoods are computed. This section discusses how multi-threading was applied to solve and reduce HAWC’s computing of likelihoods for large parameter spaces like in DM searches.

#### 4.5.1 Relevant Foundational Information

The profiling of the likelihood for HAWC is done via gradient descent where the normalization of Equation (3.1) (linearly correlated with  $\langle \sigma v \rangle$ ) is rescaled in the descent. Additionally, we sample the likelihood space for a defined list of  $\langle \sigma v \rangle$ ’s described in Section 3.4.2. The time to compute

these values is not predictable or consistent because many variables can change across the full model-space. Comprehensively, these variables are:

- $m_\chi$  : DM rest mass
- CHAN : DM annihilation channel in SM.
- SOURCE : dSph. Involves a spatial template AND coordinate in HAWC data.
- $\langle \sigma v \rangle$ : Proportional to the flux normalization and free parameter in the likelihood fit.

Therefore, we develop an asynchronous, functional-parallel coding pattern. Asynchronous means the instructions within a function are independent and permitted to be out of sync with sibling computations. Functional-parallel means that instructions are the subject of parallelization rather than threading the likelihood computation. This is close to trivial parallelization seen in Figure 4.4 except that we seek to consolidate the loading stages (software, data, and detector resolution loading). Multiple asynchronous threads are expected to reduce total serial processing time and total overhead across the entire project in addition to saving human time.

We need a way to measure and compare the expected speedup and efficiency gain for this asynchronous coding pattern. I pull inspiration for timing measurement from [82] and use *Amdahl's law with hybrid programming*. Hybrid programming meaning that the computation is a mix of distributed and shared memory programming. If we assume the code is fully parallelizable over  $p$  processors and  $c$  threads, the ideal speedup is simply  $pc$ , and ideal run-time is  $T_1/(pc)$ .  $T_1$  is the total time for a parallel program to run if only 1 processor is allocated. However, the coding pattern contains some amount of unavoidable serial computation, as shown in Figure 4.5. In our case, the run time,  $T_{p,c}$ , is estimated to be

$$T_{p,c} = \frac{T_1}{pc} (1 + F_s(c - 1)). \quad (4.3)$$

$F_s$  is the fraction of CPU time dedicated to serial computation. The expected speedup,  $S_{p,c}$ , is

$$S_{p,c} \equiv \frac{T_1}{T_{p,c}} = \frac{pc}{1 + F_s(c - 1)}. \quad (4.4)$$

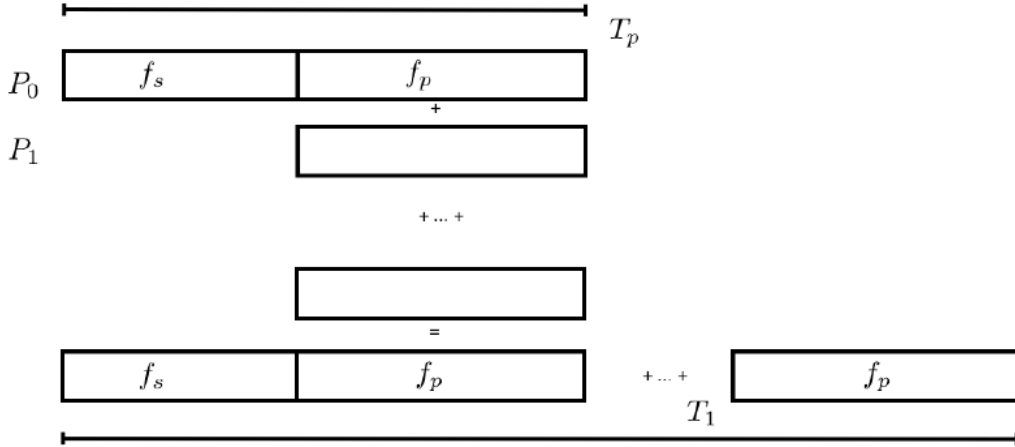


Figure 4.5 Graphic of Gustafson parallel coding pattern.  $f_s$  is the fraction of a program, in time, spent on serial computation.  $f_p$  is the fraction of computing time that is parallelizable.  $T_p$  is the total time for a parallel program to run.  $T_1$  is the total time for a parallel program to run if only 1 processor is allocated.  $P_N$  is the  $N$ -th processor where it's row is the computation the processor performs. The Gustafson pattern is most similar to what is implemented for this analysis. Figure is pulled from [82].

From Equation (4.4), we can see that the speed-up scales with  $p/F_s$ . We are free to minimize  $F_s$  asymptotically by enlarging the total models that are submitted to the thread pool, thereby shrinking the CPU fraction dedicated to serial operation. We are also free to define exactly how many threads and processors we utilize, yet eventually hit a hard cap at the hardware available on our computing cluster. HAWC uses Intel Xeon™processors with 48 cores and 96 threads. We see that a successful code will scale well as the expected speedup is inversely correlated with  $F_s$ . As the total number of models sampled grows, the speedup will also.

#### 4.5.2 Implementation

The multithreaded code was written in Python3 and is documented in the [dark\\_matter\\_hawc repository](#) within the script named `mpu_analysis.py`. A version of the script as of April 25 **TODO: make sure to update on this date** is also provided in Section B.2. It has many dependencies including the HAWC analysis software. Figure 4.6 displays the workflow of a job with 3 threads. Within a job, SOURCE is kept fixed and CHANS remains 17 elements long. More  $m_\chi$  are sampled from 11 bins up to 49 (for  $\gamma\gamma$  and ZZ) and 25 (for remaining CHANS) which amounts to 12 or 6

Timing summary for a multi-threaded job.

<b>Import and Load HAL, 3ML, and HAWC analysis software</b> ~ 2 min		
<b>Load HAWC Data</b> ~ 5 min		
<b>Load HAWC PDF's (Detector Resolution files)</b> ~ 4 min		
Load Spatial Model < 1s		
Load Spectra Models <1 s	Load Spectra Models <1 s	Load Spectra Models <1 s
Calculate max LLH (Chan_0, $m_{\chi_1}$ ) ... max LLH (Chan_?, $m_{\chi_N}$ ) N = TOTAL/N_THREADS  ~ 8 min/Spec_model	Calculate max LLH (Chan_?, $m_{\chi_1}$ ) ... max LLH (Chan_?, $m_{\chi_N}$ ) N = TOTAL/N_THREADS  ~ 8 min/Spec_model	Calculate max LLH (Chan_?, $m_{\chi_1}$ ) ... max LLH (Chan_?, $m_{\chi_N}$ ) N = TOTAL/N_THREADS  ~ 8 min/Spec_model
Write results to file <1 s	Write results to file <1 s	Write results to file <1 s
Join Threads and terminate < 1s		

Figure 4.6 Task chart for one multithreaded job developed for this project. Green blocks indicate a shared resource across the threads AND computation performed serially. Red blocks indicate functional parallel processing within each thread. 3 threads are represented here, yet many more can be employed during the full analysis. Jobs are defined by the SOURCE as these require unique maps to be loaded into the likelihood estimator. The  $m_{\chi}$ , CHAN, and  $\langle \sigma v \rangle$  variables are entered into the thread pool and allocated as evenly as possible across the threads.

mass bins per decade.  $m_{\chi}$  and CHANS are permuted into a 473 element list which is split evenly across N threads where N is [2, 8, 16]. For each  $m_{\chi}$ -CHAN tuple, 1001  $\langle \sigma v \rangle$  values are sampled in the likelihood, and the value of  $\langle \sigma v \rangle$  that maximizes the likelihood is found. Although rare, fits that failed are handled on a case by case basis.

#### 4.5.3 Performance

We see a significant reduction to wall time needed for our dSph analyses to run. Table 4.2 shows the timing summaries for analyses of different sizes and thread counts. Additionally, the efficiency gained when consolidating the serial loading of data is also apparent in our ability to study many more tasks in about the same amount of wall time as a smaller serial computation. Trials represented in the table were run on an AMD Opteron® processor 6344 with 48 cores, 2 threads per core; 2.6 GHz clock. This is not the same architecture used for analysis on the HAWC computing cluster however they are similar enough that results shown here are reasonably representative of

M Tasks	$T_{p,c}$ (hr:min:s)			
	$T_{1,1}$	$T_{1,2}$	$T_{1,8}$	$T_{1,16}$
50	1:40:37.5	0:52:43.7	0:19:13.8	0:13:44.0
74	2:22:30.0	1:15:00.6	0:25:21.3	0:15:49.8
100	(3:07:51.9)	1:40:10.5	0:30:44.4	0:20:01.4
200	(6:02:20.6)	-	1:00:32.0	0:30:35.0
473	(13:58:40.3)	-	2:01:41.4	1:07:53.2

Table 4.2 Timing summaries for analyses for serial and multithreaded processes. M tasks is the number of functional-parallel tasks ran for the computation.  $T_{p,c}$  is a single run time in hours:minutes:seconds for runs utilizing  $p$  nodes and  $c$  threads. Runs are run interactively on the same computer to maximize consistency. Empty entries are indicated with '-'. (·) entries are estimated entries extrapolated from data earlier in the column.

computing on the HAWC computing cluster. I use Tab. 4.2 for the inferences and conclusions in the following paragraphs.

First, we want to find  $T_s$ , the time of serial computation. From Fig. 4.5, the timing for our coding pattern can be written as

$$T_s + Mt_p = T_{1,1}^M. \quad (4.5)$$

$M$  is the number of functional-parallel tasks (represented as column 1 of Tab. 4.2), and  $t_p$  is the average time to complete a single parallel task.  $T_{1,1}^M$  is the total time for a parallel program to run if only 1 processor is allocated for  $M$  parallel task. With two runs of different  $M$  ( $M_1$  and  $M_2$ ), we can use a system of equations to compute

$$T_s = 803.1\text{s} \text{ and } t_p = 104.6\text{s} \quad (4.6)$$

Now, we have specific estimation for the fraction of serial computing time,  $F_s$ :

$$F_s = \frac{803.1}{803.1 + 104.6 \cdot M}. \quad (4.7)$$

The maximum  $M$  for this study is 473 which evaluates to:  $F_s = 0.016$  or 1.6% of computing time. Table 4.3 shows the resulting speedups.

We see a speedup that generally exceeds expectations from Eq. (4.4) for real trail runs. We also see that there are diminishing returns as the number of threads increases. For small jobs with large  $c$ , both the expected and observed speedup are significantly smaller than  $c$ . One thing not considered

M Tasks	$F_s$	$S_{1,2}$	$S_{1,8}$	$S_{1,16}$
50	1.33 E-1	1.90 [1.76]	5.23 [4.14]	6.35 [5.34]
74	9.40 E-2	1.90 [1.83]	5.62 [4.82]	9.00 [6.64]
100	7.13 E-2	1.88 [1.87]	6.11 [5.34]	9.38 [7.73]
200	3.70 E-2	- [1.93]	5.98 [6.36]	11.85 [10.29]
473	1.60 E-2	- [1.97]	6.89 [7.20]	12.35 [12.91]

Table 4.3 Speed up summaries for analyses for serial and multithreaded processes. M tasks is the number of functional-parallel tasks ran for the computation.  $S_{p,c}$  is a single speedup comparison for runs utilizing  $p$  nodes and  $c$  threads. [·] are the estimated speedups calculated from Tab. 4.2, Eq. (4.7), and Eq. (4.4). Empty entries are indicated with '-'.

in Eq. (4.4) is the time incurred via communication latency. Communication latency increases with the number of threads and contributes to diminishing returns. Additionally, these values are for single runs and do not consider the stochastic variation expected in a shared high performance computing resource. Therefor, these results are not strictly conclusive, yet demonstrate the merits of multi-threading. We see very clearly that there is a lot to gain, and this new coding pattern will expand HAWC’s analysis capabilities.

## 4.6 Analysis Results

3 of the 43  $\mathcal{L}S$  dSphs considered for the multithreaded analysis. These dSph are analyzed for emission from DM annihilation according to the likelihood method described in Section 3.4. The three likelihood profiles are then stacked to synthesize a combined limit on the dark matter annihilation cross-section,  $\langle\sigma v\rangle$ . This combination is done each of the 17 SM annihilation channels. Figure 4.7 and Fig. 4.8 show the combined limits for all annihilation channels with HAWC’s observations. Test statistics of the best fit  $\langle\sigma v\rangle$  values for each  $m_\chi$  and CHAN are shown in Fig. 4.9 and Fig. 4.10. We also compare these limits to HAWC’s Glory Duck limits shown in Section 3.5. The comparison to Glory Duck are featured in Fig. 4.11 for all the DM annihilation channels studied for Glory Duck. A full comparison is provided in the appendix in Fig. B.2, Fig. B.3, and Fig. B.4. Here, we show updated limits for  $\chi\chi \rightarrow b\bar{b}$ ,  $e\bar{e}$ ,  $\mu\bar{\mu}$ ,  $\tau\bar{\tau}$ ,  $t\bar{t}$ ,  $W^+W^-$ ,  $\gamma\gamma$  and  $ZZ$ . For the first time ever, we show limits for  $\chi\chi \rightarrow c\bar{c}$ ,  $s\bar{s}$ ,  $u\bar{u}$ ,  $d\bar{d}$ ,  $\nu_e\bar{\nu}_e$ ,  $\nu_\mu\bar{\nu}_\mu$ ,  $\nu_\tau\bar{\nu}_\tau$ ,  $gg$ , and  $hh$ .

No DM was found in HAWC observations. The largest excess found in HAWC data was for DM annihilating to  $W$ -bosons or  $\nu_e\bar{\nu}_e$  for  $m_\chi = 10$  TeV at significance  $2.11\sigma$  and  $2.14\sigma$  respectively.

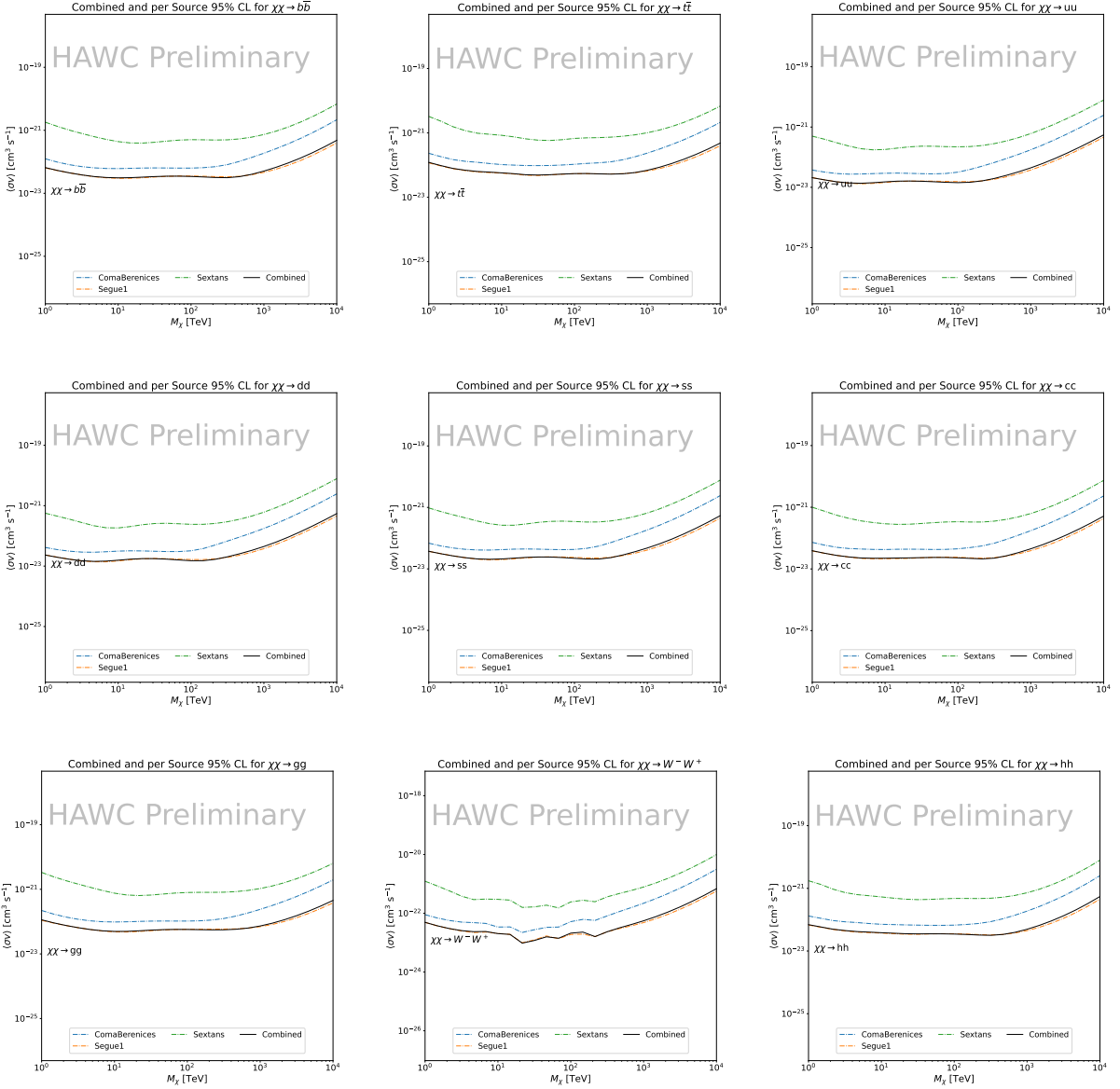


Figure 4.7 HAWC upper limits at 95% confidence level on  $\langle\sigma v\rangle$  versus  $m_\chi$  for  $\chi\chi \rightarrow b\bar{b}$ ,  $t\bar{t}$ ,  $u\bar{u}$ ,  $d\bar{d}$ ,  $s\bar{s}$ ,  $c\bar{c}$ ,  $gg$ ,  $W^-W^+$ , and  $hh$ . Limits are with  $\mathcal{L}\mathcal{S}$   $J$ -factors [80]. The solid line represents the observed combined limit. Dashed lines represent limits from individual dSphs.

HAWC's limits and excesses are dominated by Segue1. Coma Berenices shows excesses at higher DM mass, yet no similar excesses were observed in Segue1 or Sextans. Sextans did not contribute significantly to signal excesses or the combined limit as it is at high zenith. Draco is at a high zenith for HAWC, so the effort required to include it was not justified by the benefits.

We did not generate background trials in time of writing this thesis. These are not shown and

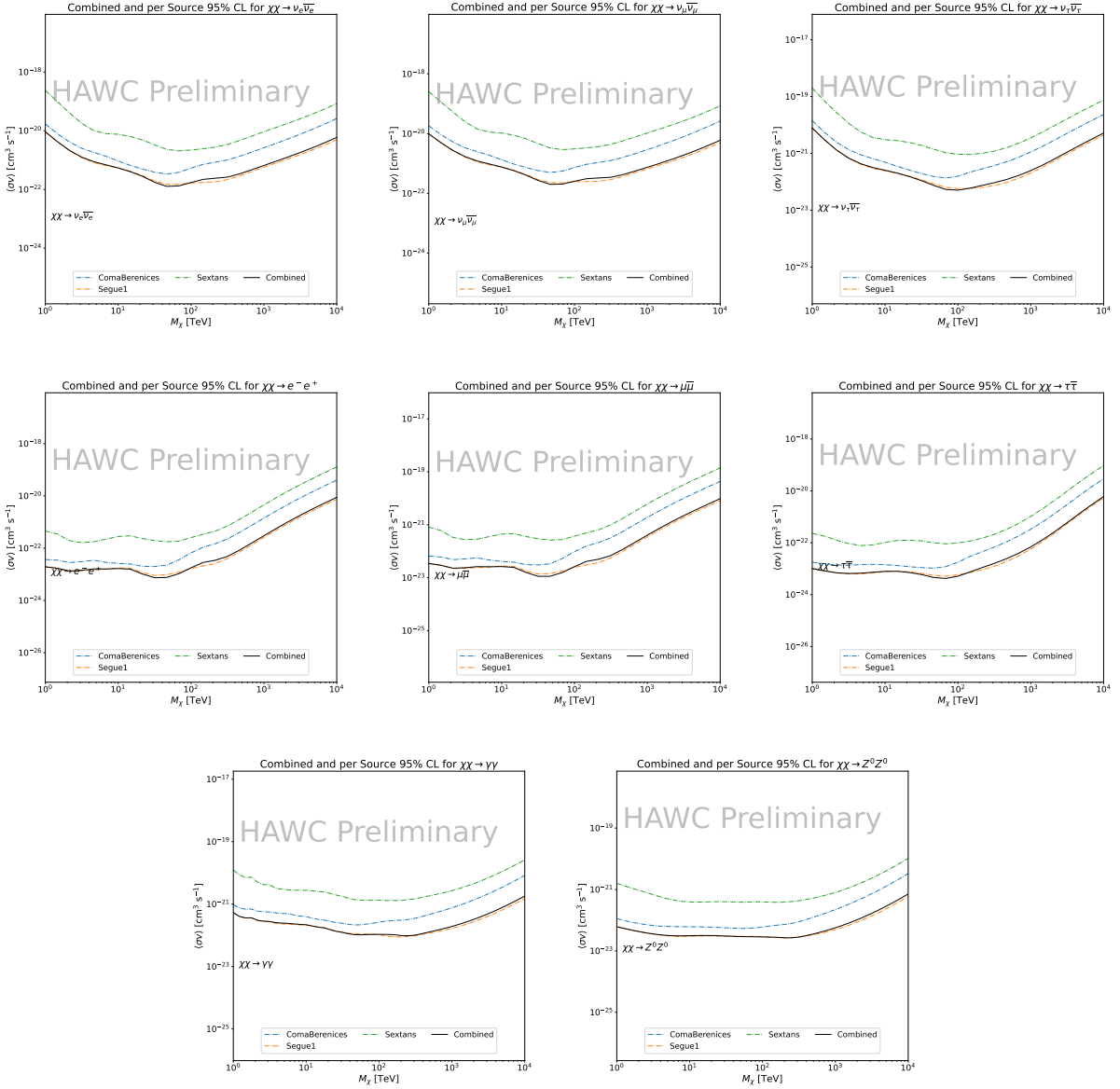


Figure 4.8 HAWC upper limits at 95% confidence level on  $\langle\sigma v\rangle$  versus  $m_\chi$  for  $\chi\chi \rightarrow \nu_e \bar{\nu}_e$ ,  $\nu_\mu \bar{\nu}_\mu$ ,  $\nu_\tau \bar{\nu}_\tau$ ,  $e \bar{e}$ ,  $\mu \bar{\mu}$ ,  $\tau \bar{\tau}$ ,  $\gamma\gamma$  and  $ZZ$ . Limits use  $\mathcal{L}S$   $J$ -factors [80]. The solid line represents the observed combined limit. Dashed lines represent limits from individual dSphs.

are an immediate next step for this analysis before publication.

When comparing these results to Section 3.5, we see an overall decrease in the observed confidence limits on  $\langle\sigma v\rangle$ , therefore improvement to HAWC's expected sensitivity. This improvement is generally stronger than a doubling of data, or a factor  $\sqrt{2}$  decrease. The comparison is somewhat complex and dependent on the dSph and SM annihilation channel. Figure 4.11 shows the com-

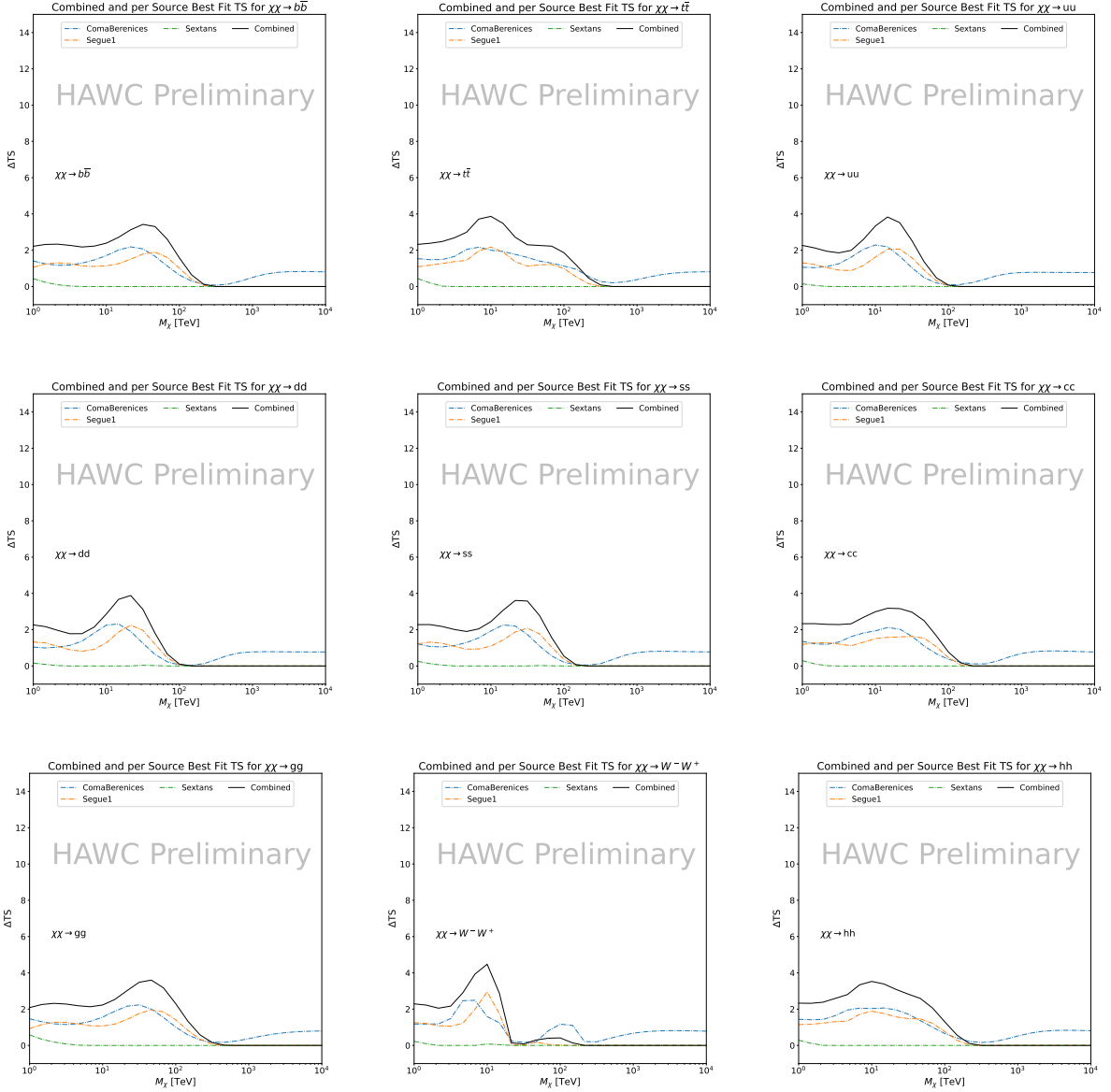


Figure 4.9 HAWC TS values for best fit  $\langle\sigma v\rangle$  versus  $m_\chi$  for SM annihilation channels:  $\chi\chi \rightarrow b\bar{b}$ ,  $t\bar{t}$ ,  $u\bar{u}$ ,  $d\bar{d}$ ,  $s\bar{s}$ ,  $c\bar{c}$ ,  $gg$ ,  $W^-W^+$ , and  $hh$ . Limits use  $\mathcal{LS}$   $J$ -factors. The solid black line shows the combined best fit TS values. The colored, dashed lines are the TS values from each dSph.

parisons of limits calculated for this analysis and Glory Duck (Section 3.5). Segue 1 and Coma Berenices are source at low zenith angles where improvements to HAWC's analysis come almost entirely from energy estimation. Differences between these two are dominantly from their differences in  $J$ -factor, half-light radii of the dSphs, and the particle physics inputs. Substantial gains in HAWC's analysis methods (pass 5.F) were made at high zenith which is important for sources

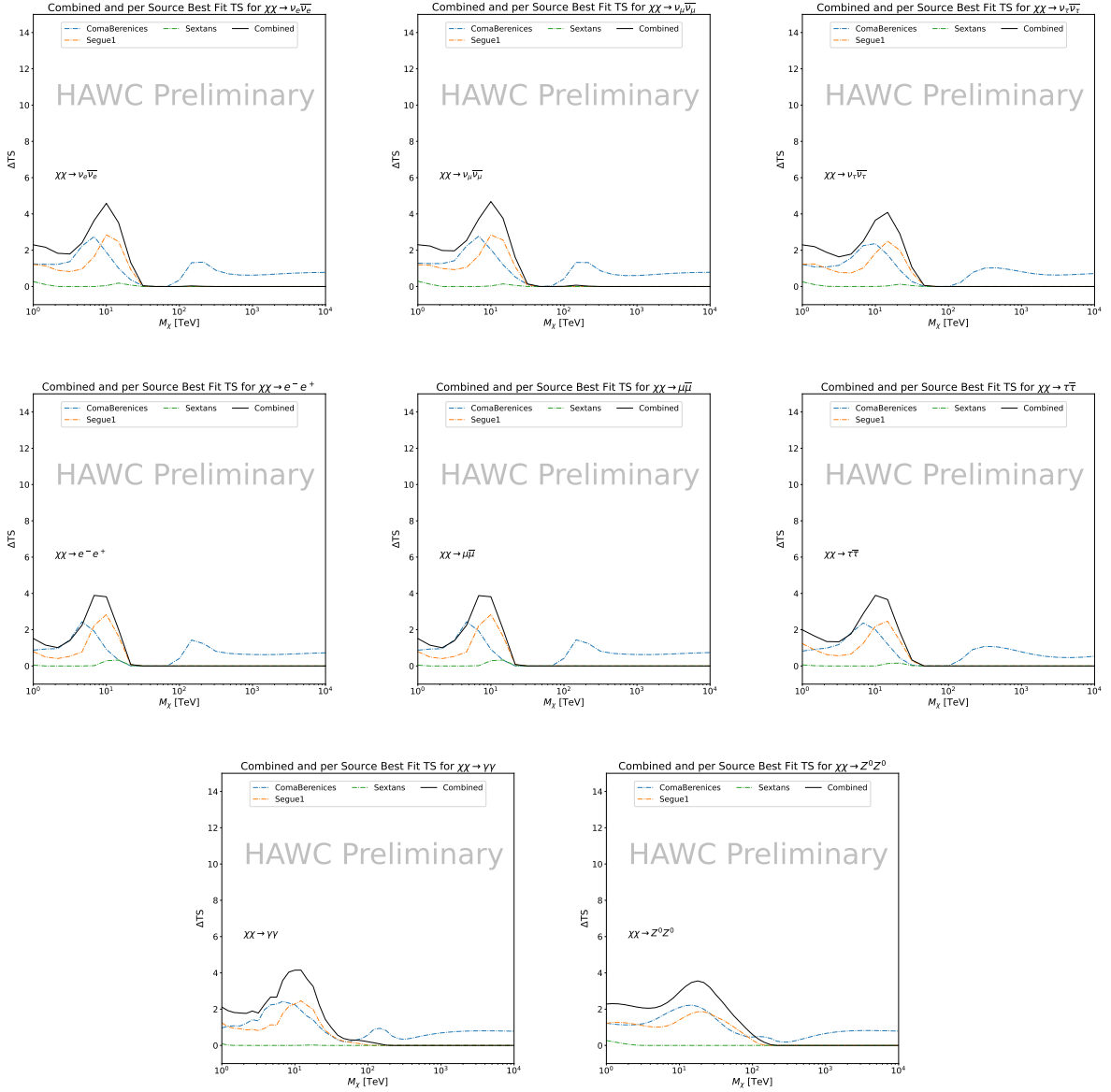


Figure 4.10 HAWC TS values for best fit  $\langle\sigma v\rangle$  versus  $m_\chi$  for SM annihilation channels:  $\chi\chi \rightarrow \nu_e \bar{\nu}_e$ ,  $\nu_\mu \bar{\nu}_\mu$ ,  $\nu_\tau \bar{\nu}_\tau$ ,  $e^- e^+$ ,  $\mu \bar{\mu}$ ,  $\tau \bar{\tau}$ ,  $\gamma\gamma$  and  $ZZ$ . Limits use  $\mathcal{LS}$   $J$ -factors. The solid black line shows the combined best fit TS values. The colored, dashed lines are the TS values from each dSph.

like Sextans. The HDM particle physics model produces almost identical spectra to the PPPC for  $\chi\chi \rightarrow e^- e^+$ . This channel can be used to compare limits between dSph spatial models. Overhead sources see modest improvement to the observed limits on  $\langle\sigma v\rangle$ , while high zenith sources see an order of magnitude improvement for all DM masses. Softer SM annihilation channels see broad improvements to the limit compared to harder channels.

## 4.7 Systematics

Systematics to this analysis are identical to what was performed earlier in Glory Duck, Section 3.7. We are also sensitive to the choice in spatial template, and this was explored in Section 3.7.2 and Section 3.8.2.

## 4.8 Conclusion and Discussion

In this multithreaded analysis, we have used observations of 3 dSphs from HAWC to perform a collective DM annihilation search towards dSphs. The data were combined across sources to significantly increase the sensitivity of the search. Advanced computational techniques were deployed to accelerate wall-time spent analyzing by an order of magnitude. We have observed no significant deviation from the null, no DM hypothesis, and so present our results in terms of upper limits on the velocity-weighted cross-section,  $\langle\sigma v\rangle$ , for seventeen potential DM annihilation channels across four decades of DM mass.

This analysis serves as a proof of concept for multithreaded HAWC analyses with large parameter spaces. Larger datasets with fast techniques will be essential to tackling the DM problem. The models we used for this study include annihilation channels with neutrinos in the final state. Advanced studies could aim to merge our results with those from neutrino observatories with large data sets.

A full HAWC analysis will include systematic studies of the  $J$ -factor distributions. Additionally, because of the timing reduction, the study can be doubled in size to include DM decay. We have not yet received the remaining spatial profiles to the  $\mathcal{LS}$  catalog, and limits can be quickly computed once these are received. Finally, statistical studies with Poisson variation of HAWC’s background are essential to a comprehensive understanding of our observed excesses.

Segue1

Coma Berenices

Sextans

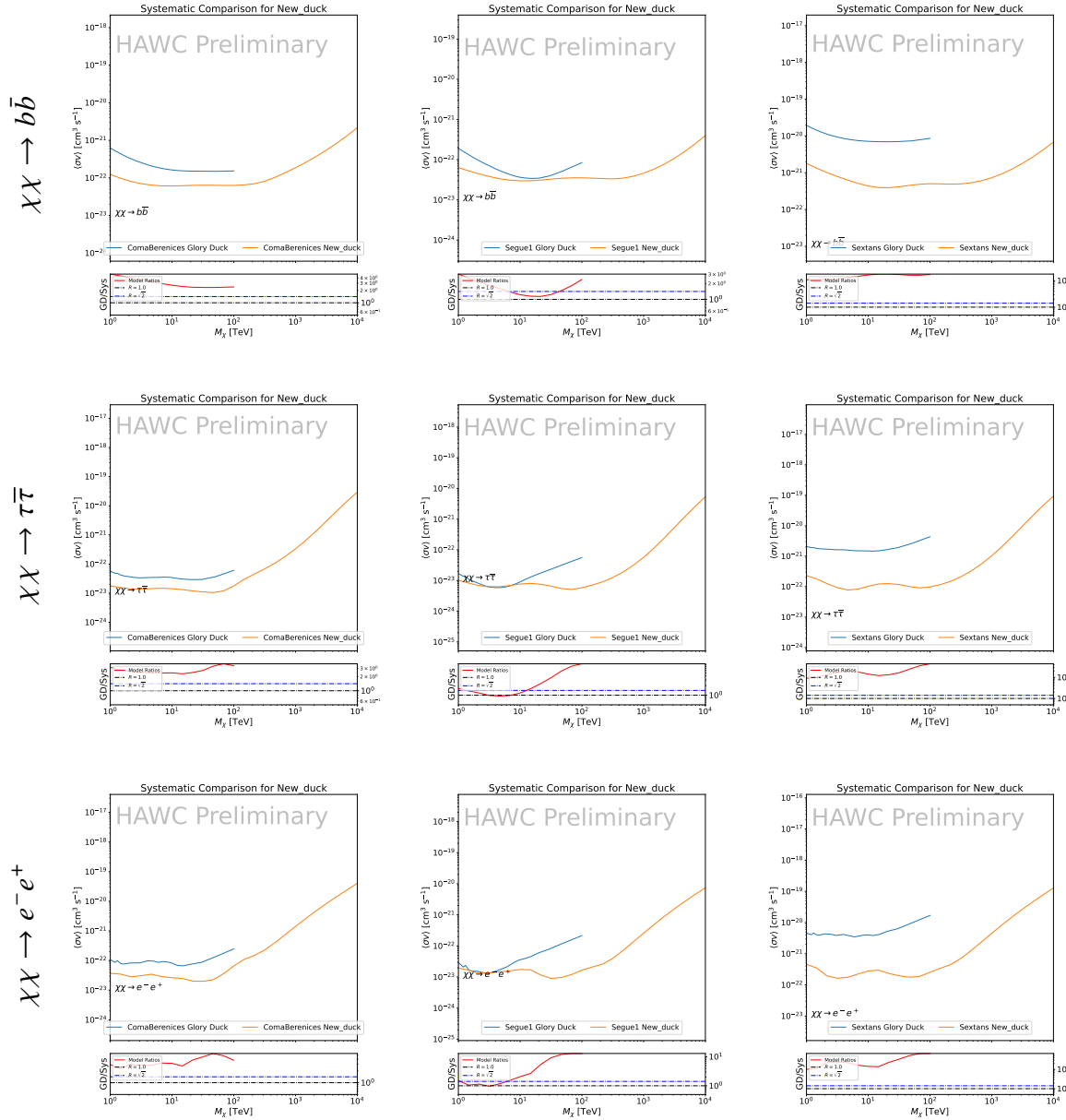


Figure 4.11 Comparison of HAWC limits from this analysis to Glory Duck (Fig. 3.5) for 3 dSphs and 3 DM annihilation channels:  $b\bar{b}$ ,  $\tau\bar{\tau}$ , and  $e\bar{e}$ . Each sector shows the 95% confidence limit from Glory Duck (blue line) and this analysis (orange line) in the top plot. The lower plot features the ratio in log scale of Glory Duck to this analysis in a red solid line. Horizontal dashed lines are for ratios of 1.0 (black) and  $\sqrt{2}$  (blue). Ratios larger than 1.0 are for limits smaller, or stricter, than Glory Duck. Ratios larger than  $\sqrt{2}$  indicates limits are stricter than a simple doubling of the Glory Duck data.

## CHAPTER 5

### ICECUBE NEUTRINO OBSERVATORY



Figure 5.1 IceCube Neutrino observatory and science center at the South Pole. Detector volume is beneath glacial ice. Image from [83].

Located at the South Pole, the IceCube Neutrino Observatory is a pivotal instrument for neutrino astronomy. IceCube's primary function is the detection and analysis of elusive, high-energy neutrinos. These neutrinos carry information from the most energetic and distant cosmic phenomena. The observatory uses thousands of digital optical modules embedded in a cubic kilometer of Antarctic ice to detect Cherenkov radiation. This radiation occurs when neutrinos interact with the ice, revealing their origin and energy.

IceCube is a critical component in the multi-messenger astrophysics toolkit, especially in the search for dark matter and beyond standard model (BSM) astrophysical processes. The observatory's analysis of neutrino signals enhances our understanding of the universe by correlating these signals with other cosmic messengers, including electromagnetic, gravitational waves, and cosmic



Figure 5.2 IceCube Laboratory (ICL) that houses the data acquisition systems. Picture from [83].

rays.

The following sections will discuss the observatory’s design, data acquisition, and event reconstruction methodologies. These details will underscore IceCube’s role in advancing our understanding of the cosmos through data-driven insights.

### 5.1 The Detector

The IceCube Neutrino Observatory is embedded within a cubic kilometer of Antarctic ice at the South Pole. IceCube’s modules are designed to detect neutrinos through Cherenkov radiation emitted after neutrino interactions within the ice. It comprises of 5160 Digital Optical Modules (DOMs), arranged across 86 strings that span depths of 1450 m to 2450 m beneath the surface. This arrangement allows IceCube to capture high-energy neutrinos across a broad neutrino energy spectrum.

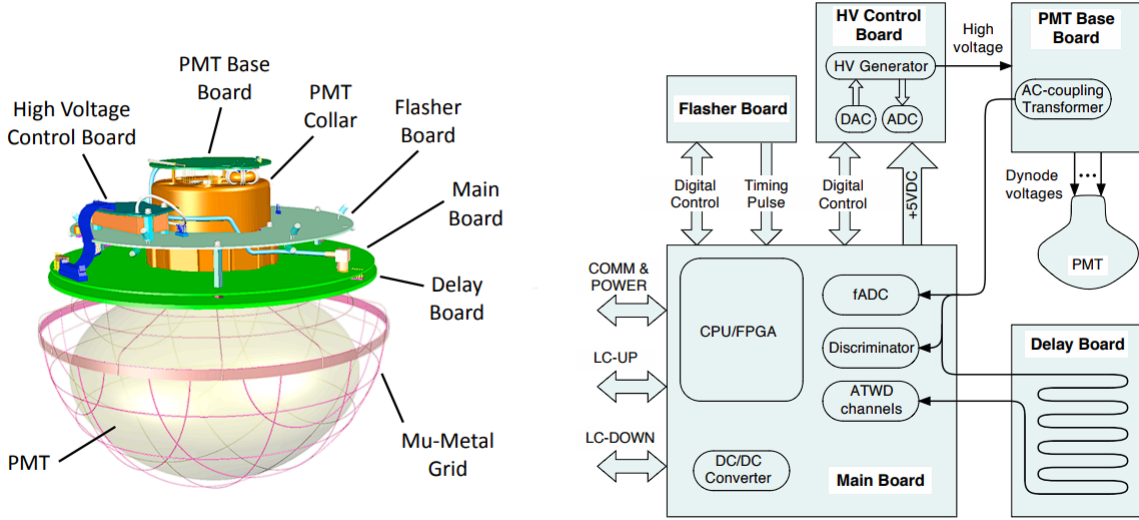


Figure 5.3 Composition of the Digital Optical Module (DOM). Left image is an illustration of the mechanical layout. Right is a flow chart of functional connections. Figure from [84]

### 5.1.1 Hardware and Construction

Digital Optical Modules (DOMs) are at the core of IceCube’s detection technology. Figure 5.3 illustrates the construction and signal flow of a DOM. Each DOM is encased in a glass sphere that can withstand deep-ice pressures. A DOM features a 10-inch PMT for Cherenkov light detection, a high-voltage power supply for the PMT, and a Main Board for signal digitization and timestamping. An LED Flasher Board is included for calibration purposes. They assist in verifying DOM responses and measuring the glacial ice’s optical properties. The DOMs are deployed along cables on strings in a hexagonal grid pattern that spans a cubic kilometer. Strings are placed with 125 m of horizontal spacing, and DOMs are vertically separated by 17 m on each string. This detector geometry optimizes detection of TeV to PeV neutrinos.

DeepCore and IceTop, additional components of IceCube, extend its research capabilities. DeepCore, with its denser array of DOMs, targets lower energy neutrinos for studies such as neutrino oscillations. IceTop, situated at the ice surface, measures cosmic rays, contributing data that complement the neutrino observations from below the ice. Figure 5.4 illustrates the full detector volume and auxiliary systems.

The central hub for IceCube’s operations is the IceCube Laboratory (ICL), situated at the

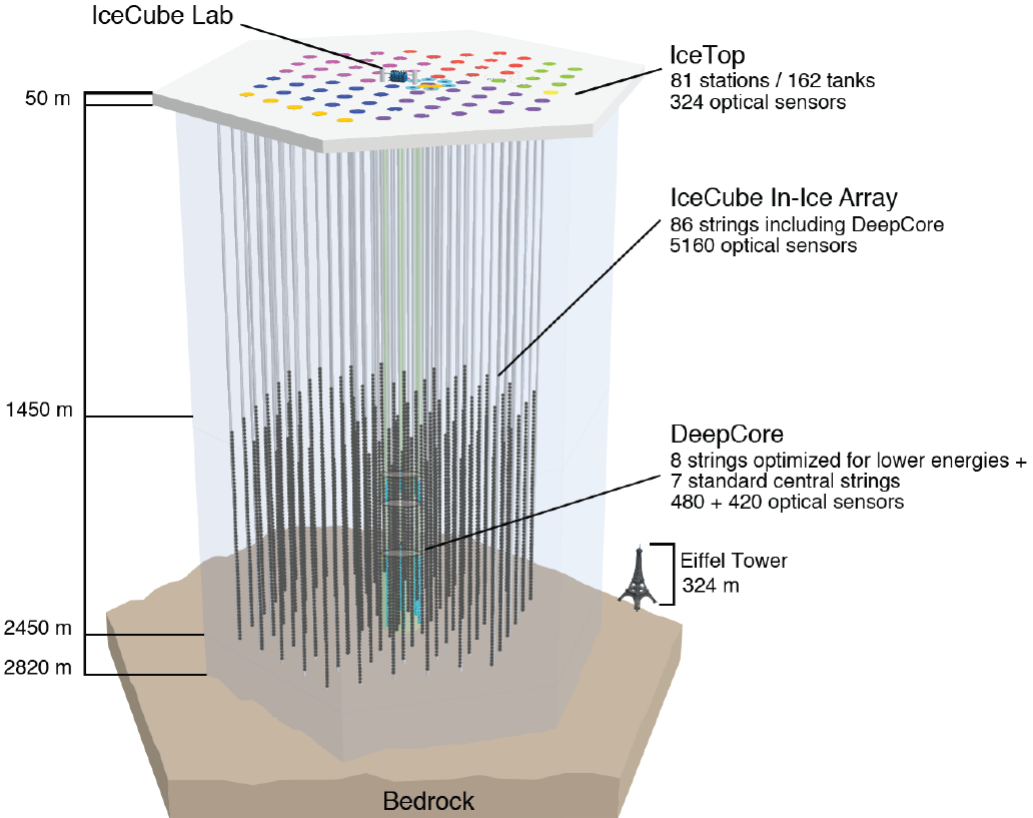


Figure 5.4 Graphic of the full IceCube Neutrino Observatory. In-ice array is made up of 86 strings with a total of 5160 optical sensors. Deepcore is a denser arrangement of optical sensors for sensitivity to lower energy neutrinos. Figure from [83].

surface at the center of the array. This facility houses the servers and computers responsible for data acquisition and online filtering. ICL connects to the DOMs via cables routed up from beneath the ice [84]. The ICL manages the data flow from the ice, ensuring continuous operation and data integrity. It maintains optimal conditions for its electronic equipment, including temperature control and protection against electromagnetic interference [84].

### 5.1.2 Data Acquisition

The data acquisition process in IceCube starts when a PMT within a DOM detects light surpassing a threshold of 0.25 photoelectrons. The importance of the information transmitted to the ICL depends on the detection of hits in neighboring DOMs within a microsecond window. Isolated signals prompt a Soft Local Coincidence (SLC) response, transmitting only a timestamp

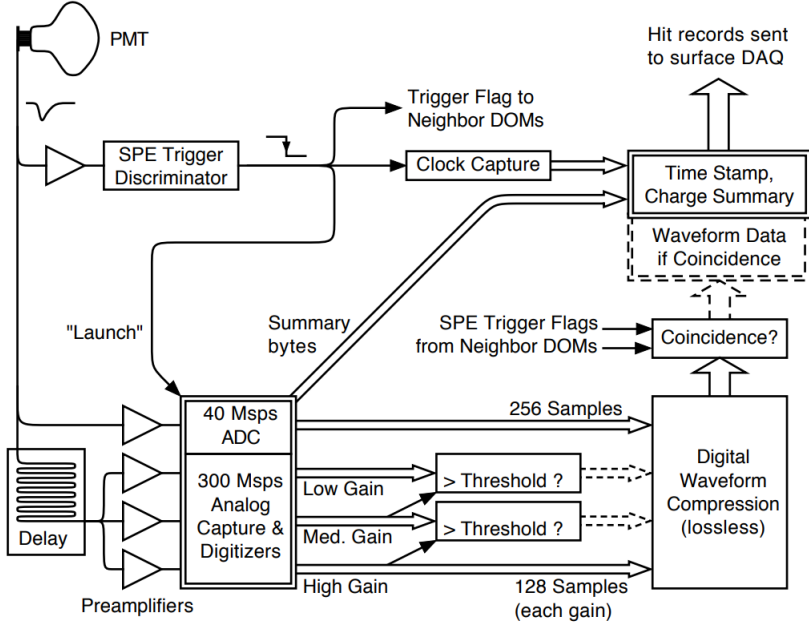


Figure 5.5 Data flow chart PMT waveforms from the DOMs. “Hit Records” are sent to the surface DAQ computers in ICL. Full waveform data, represented with dashed arrows, are included when neighboring DOMs are hit in coincidence above the SPE discriminator threshold.

and a charge summary. In contrast, signals detected by neighboring DOMs initiate a Hard Local Coincidence (HLC). The full waveform is compressed and sent along with the timestamp and charge summary to the ICL [84].

Achieving uniform timing across DOMs is essential for accurate event reconstruction. Each DOM’s independent clock is finely calibrated and synchronized with the ICL’s clocks. Times are translated to Universal Coordinated Time (UTC). This calibration is set by sending continuous pulses between the DOMs and the ICL. The waveforms are adjusted by subtracting the common baseline and applying the gain [84].

Within the ICL, the Data Acquisition (DAQ) system employs various trigger algorithms to discern neutrino events from the vast majority of DOM hits caused by dark noise. One such mechanism, the Simple Multiplicity Trigger (SMT), requires a specific number of HLC hits within a brief timeframe to recognize a series of hits as an event [84].

Further refining the observatory’s data, the Processing and Filtering (PnF) system, also housed within the ICL, applies around 25 different filters after initial event detection. Each filter is designed

for specific physics analyses. The system employs filters such as: The Muon Track Filter to isolate high-quality track events crucial for neutrino source identification; the Shower Event Filter to select events with large energy deposits indicative of neutrino interactions; and the High-Charge Filter to highlight events with extensive photoelectron deposits [84]. These filters ensure that the data prepared for further analysis and transmission to researchers in the Northern Hemisphere contains the most significant scientific insights [84].

The operational control of the observatory, maintained by the LiveControl system within the ICL, oversees the DAQ and PnF systems. It handles the initiation and conclusion of data-taking runs and maintains a database of operational parameters. LiveControl alerts operators to any deviations from expected conditions. It is crucial for ensuring that the observatory operates within its optimal parameters [84].

## 5.2 Event Reconstruction

Event Reconstruction within the IceCube Neutrino Observatory transforms signals captured by DOMs into quantifiable scientific insights. The goal of event reconstruction is to ascertain the origin, trajectory, and energy of interacting neutrinos. This process is pivotal for interpreting signals as either originating from celestial neutrino sources or other phenomena. I will focus mostly one how IceCube reconstructs track-like events as these are the most relevant for this dissertation.

### 5.2.1 Tracks and Cascades

Events in IceCube’s detector volume manifest primarily as either tracks or cascades. The primary cause of the event topology are both the neutrino flavor and the nature of the primary neutrino’s interaction with the ice.

Tracks emerge from charged-current (CC) interactions involving muon neutrinos ( $\nu_\mu$ ). These events are characterized by the production of a high-energy muon ( $\mu$ ). These muons, due to its relatively large mass compared to electrons, can traverse substantial distances through the ice, exceeding kilometers. These long trajectories are obvious from their continuous, distinct, and elongated track of Cherenkov light in the ice. See Fig. 5.8 for a simulated track event. The angular deviation between the incoming  $\nu_\mu$  and the secondary  $\mu$  is notably slight, tapering to near  $0.3^\circ$

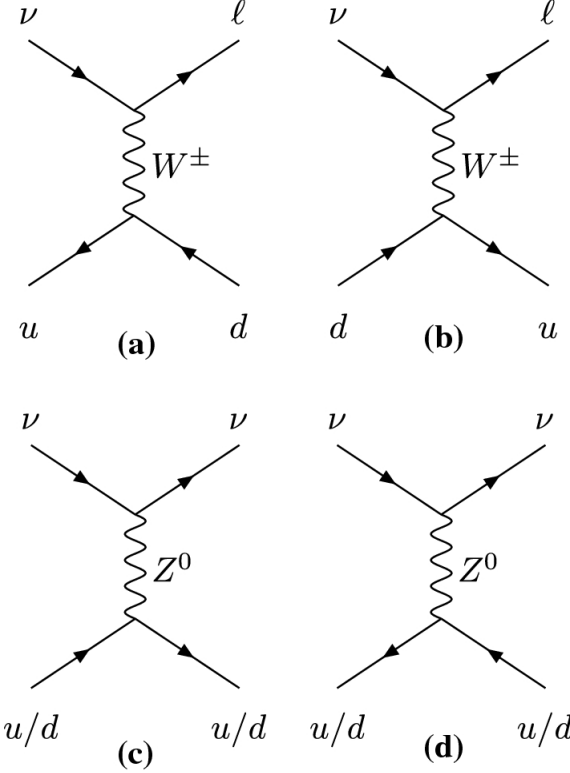


Figure 5.6 Feynman diagrams for W (a/b) and Z (c/d) boson mediated interactions between neutrinos and light quarks. Charged current (CC) interactions are shown in panels a and b. Neutral current (NC) interactions are shown in panels c and d. NC interactions occur between neutrinos and quarks within atomic nuclei in the ice. CC interactions will exchange W bosons and produce a lepton corresponding to the neutrino flavor and a hadronic cascade. NC interactions will exchange a Z boson and produce a hadronic cascade. Figure from [85].

above TeV energies. Therefore,  $\mu$  tracks closely approximate the primary neutrino's path [85, 88]. Such precision affords angular resolutions finer than  $1^\circ$  for TeV neutrinos which facilitates the determination of their cosmic origins [85].

Cascades are products of both neutral-current (NC) interactions across all neutrino flavors and CC interactions involving electron or tau neutrinos,  $\nu_e$  and  $\nu_\tau$  respectively. Unlike tracks, cascades result in a more localized burst of Cherenkov radiation. The burst imprints as a nearly spherical light pattern from the rapid dissipation of energy by the produced particles. This diffusion creates a distinct event signature with good energy estimation, but worse directional clarity compared to track events. The isotropic nature of cascades leads to larger angular uncertainties, typically around  $15^\circ$ . Yet, cascades excel in providing energy measurements, with resolutions reaching as tight as 15% from the contained nature of the energy deposition [85, 88].

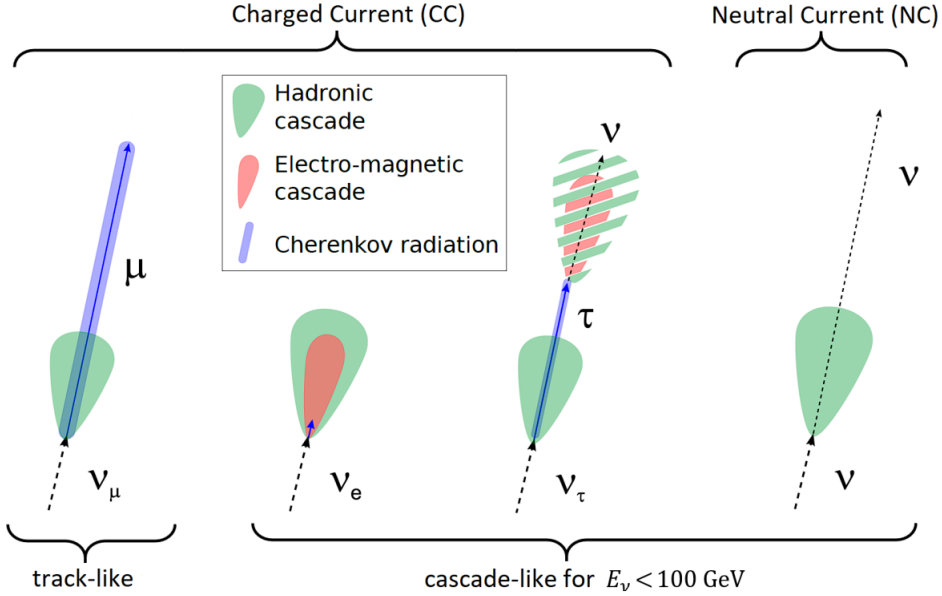


Figure 5.7 Event topologies for high energy NC and CC neutrino interactions with ice. Signatures can be split as either: hadronic and electromagnetic cascades; Cherenkov radiation from a charged, long-lived particle. Cascades from  $\tau$  decays will depend on its decay products. For energies below 1 PeV the double bang of the  $\nu_\tau$  signature overlap and are indistinguishable. Figure from [86].

The double-bang event, posited for  $\nu_\tau$  interacting via CC at energies above 1 PeV, would display as two distinct cascades within the detector. These events start from an initial interaction and subsequent decay of the  $\tau$  lepton over a discernible distance. The double-bang offers a unique marker for high-energy  $\nu_\tau$  detection [85]. Preliminary whispers of double-bang events IceCube have been observed [89]. Yet, efforts are ongoing to isolate such an event.

### 5.2.2 Reconstruction of Track Direction

Angular reconstruction for  $\nu_\mu$  induced tracks in the IceCube detector volume starts with the LineFit algorithm [90]. LineFit estimates the  $\mu$ 's trajectory through the least squares fit to the Cherenkov light hits on the DOMs. LineFit assumes the muon propagates with constant velocity and treats its path as linear in order to simplify the emission patterns of Cherenkov radiation. To improve this approximation, the Huber penalty function [91] is applied which distinguishes between signal and noise by considering the spatial distribution of hits relative to the track [92].

The reconstruction process is refined further by the Single Photoelectron (SPE) likelihood method, which calculates the probability of photon arrival times at the DOMs [91]. It does so by

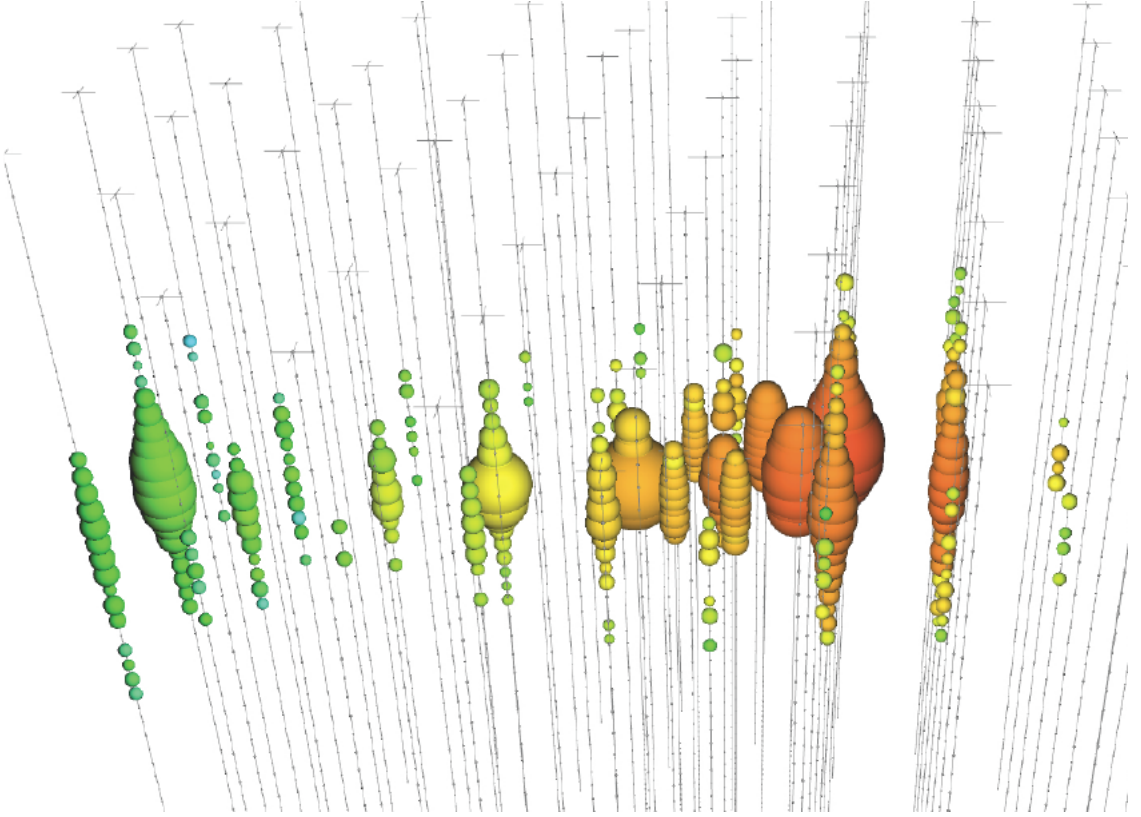


Figure 5.8 A simulation of a track-like event in IceCube. Redder bubbles indicate earlier photon arrival times. Greener bubbles occur later. The size of the DOM bubble illustrate the charge deposition in the DOM. For this event, the CC neutrino interaction occurred by the red hits. There is then a long muon track going to the left. Figure taken from [87].

taking into account the earliest detected photons as they are least likely to have been scattered in the ice:

$$L(\Theta) = \prod_{j=1}^{N_{\text{DOM}}} \prod_{i=1}^{N_{\text{hit}}} p_j(t_i)^{q_i} \quad (5.1)$$

where  $N_{\text{DOM}}$  is the number of DOMs involved in the event.  $N_{\text{hit}}$  is the number of hits registered [90].  $p_j(t_i)$  is the probability density function (PDF) of the photon arrival time. The charge detected by each DOM,  $q_i$ , factors into the probability calculation, assuming that earlier photons provide more reliable directional information.

An alternative to SPE, the Multi-Photoelectron (MPE) likelihood method accounts for all detected photons. MPE uses the total observed charge to weight the significance of each hit:

$$L(\Theta) = \prod_{j=1}^{N_{\text{DOM}}} \left[ p_j(t_1)^{q_1} \cdot (1 - P_j(t_1))^{Q_j - q_1} \right], \quad (5.2)$$

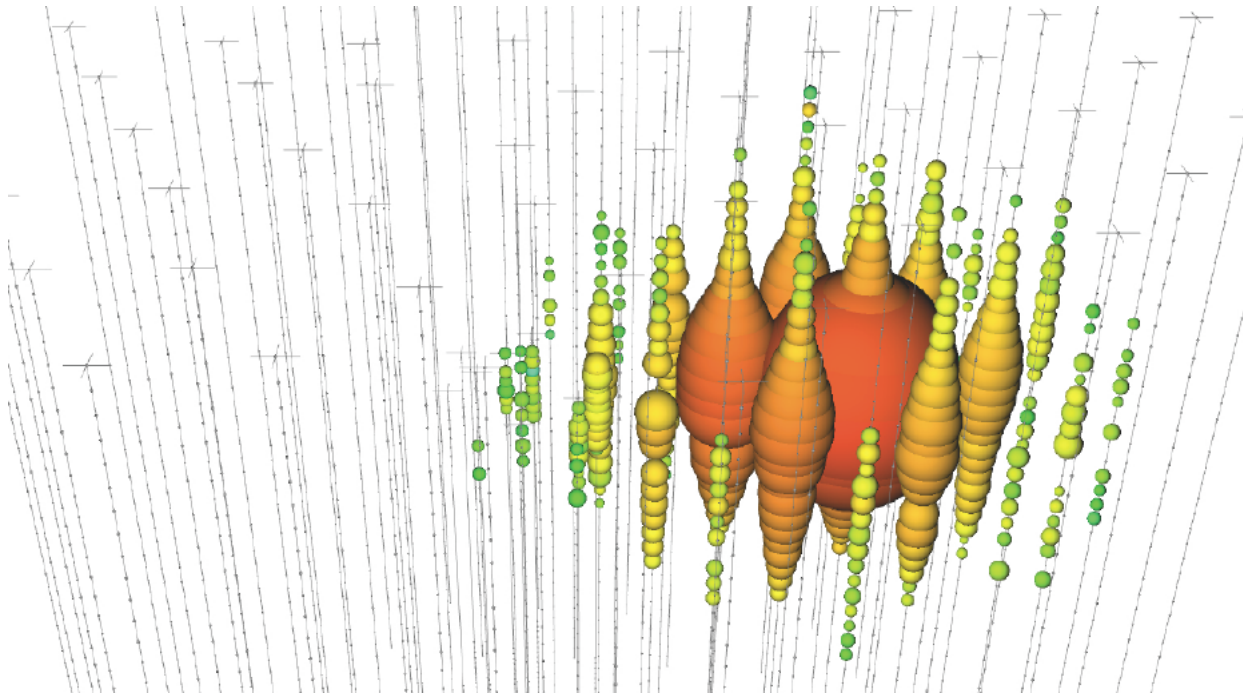


Figure 5.9 Same as Fig. 5.8 but for a cascade-like event. Figure taken from [87].

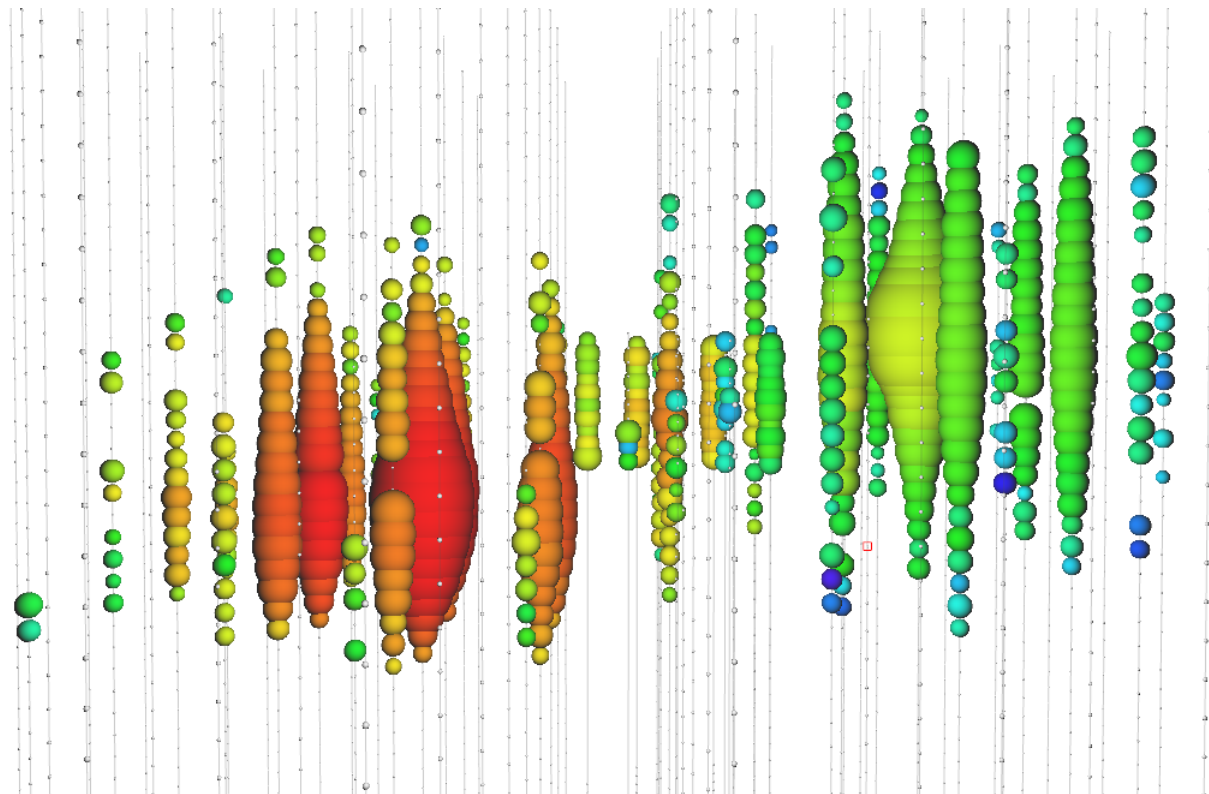


Figure 5.10 Same as Fig. 5.8 but for a double-bang event. Two distinct cascades are visible if the initial neutrino is very high energy. Figure taken from [87].

where  $Q_j$  is the sum of charges observed by the j-th DOM, providing a more detailed picture of the  $\mu$ 's path [90].

SplineMPE, is the final step and employs a spline-based parameterization of the photon arrival times. These spline fits encode a detailed understanding of the ice's optical properties derived from calibration data [90]. This approach yields the following likelihood function for improved angular resolution:

$$L(\vec{r}_0, t_0, \theta, \phi) = \prod_k L_{\text{DOM}_k}(\vec{r}_0, t_0, \theta, \phi), \quad (5.3)$$

where the parameters  $\vec{r}_0$ ,  $t_0$ ,  $\theta$ , and  $\phi$  describe the reconstructed track within IceCube's voluminous array [90].

From the light weight LineFit to the complex SplineMPE, each step incorporates more detailed physics to enhance the reconstruction's accuracy. Each hones in on the  $\mu$  track to reveal the  $\mu$ 's cosmic origin. This nuanced tracking is crucial for IceCube's mission to map the universe through the lens of high-energy neutrino interactions.

### 5.2.3 Energy

After pinpointing the  $\mu$  track's direction, IceCube employs the MuEX algorithm to estimate the energy deposited by the muon inside the detector. The MuEX algorithm uses a Poisson likelihood model, comparing the observed photoelectrons  $k$  to the expected light output,  $\Lambda$ , which is directly related to the deposited energy  $E$ :

$$\ln \mathcal{L} = k \ln(\Lambda E + \rho) - (\Lambda E + \rho) - \ln(k!) \quad (5.4)$$

$\rho$  is the number of expected noise photons, and  $\Lambda$  reflects the light yield per unit energy, taking into account the optical properties of the ice and the detector response. The logarithm of the likelihood is minimized with respect to the energy, resulting in a best-fit estimate [88].

For a more detailed energy reconstruction, the Millipede algorithm unfolds the muon's energy loss along its path by adapting the Poisson likelihood. This approach accounts for the stochastic energy losses due to Bremsstrahlung and pair production, treating the  $\mu$  as a series of electromagnetic

cascades:

$$\vec{k} - \vec{\rho} = \Lambda \cdot \vec{E} \quad (5.5)$$

where  $k$  denotes the observed photons,  $\rho$  the noise,  $E$  the energy losses, and  $\Lambda$  the matrix of predicted light yields throughout the detector. By fitting the muon's position, direction, and the vector of energy losses, Millipede achieves a resolution on total deposited energy along the muon track of approximately 10-15% [88].

IceCube makes some approximations when estimating  $\lambda$  for the reduction of computational time. Two important assumptions IceCube makes are that Cherenkov light from cascades is spherically symmetric along the  $\mu$  track and the Cherenkov emission is uniform [88]. The uncertainties in these approximations is accounted for by convolving  $\lambda$  with a PDF,  $G$ , on the light yield. The likelihood is then rewritten as:

$$\mathcal{L} = \prod_j \int_0^\infty d\lambda_j G(\lambda_i, \lambda_j) \frac{\lambda_j^{k_i} e^{-\lambda_i}}{k_i!}, \quad (5.6)$$

The full description for the PDF,  $G(\lambda_i, \lambda_j)$  is discussed in [88]. After considering the uncertainties, the energy resolution was observed to be in the range of 30%-35% [88].

### 5.3 Background

In IceCube, the primary challenge in detecting astrophysical neutrinos is the background noise from atmospheric neutrinos. These are produced from cosmic rays hitting the Earth's atmosphere, leading to a cascade that includes both neutrinos and muons (see Fig. 2.2). These particles sometimes generate detector signals similar to those from astrophysical sources.

IceCube employs selective criteria to reduce this background. For instance, downward-moving tracks are scrutinized more heavily, as these are more likely to be related to atmospheric events. Upward-moving neutrinos, however, are less likely to be confused with this background because the Earth filters out most other particles, including muons. The detector uses the Earth itself as a filter to increase the purity of potential astrophysical neutrino signals. This differentiation between upgoing and downgoing events helps IceCube focus on the neutrinos that are of most interest for astronomical observations.

## CHAPTER 6

### HEAVY DARK MATTER ANNIHILATION SEARCH WITH ICECUBE'S NORTH SKY TRACK DATA

#### 6.1 Introduction

Neutrinos are another astrophysical messenger than can travel long distances without significant attenuation or deflection. Additionally, Neutrinos come in three flavors which triples the multiplicity of the particles we are searching for. Uniquely, they interact less readily than photons especially above PeV energies. Neutrinos therefore provide another window through which we can perform dark matter searches.

The previous IceCube DM annihilation analysis towards dwarf galaxies was performed in 2013 [93] which, in technical terms, is more than a minute ago. This is in spite of IceCube's crucial sensitivity afforded from neutrino spectral lines [94]. A lot has changed in IceCube since its previous DM annihilation search such as, additional strings, more sophisticated analysis methods, and more accurate theory modeling. It has come time for IceCube to make a DM dSph contribution.

IceCube is sensitive to annihilating DM for DM masses above 1 TeV. Additionally, IceCube's sensitivity is comparable gamma-ray observatories in spectral models that produce hard neutrino features. The goal of this analysis is to perform a DM annihilation search using the Northern Sky Tracks datasets. The search will only be towards dwarf spheroidal galaxies (dSph) for the strengths mentioned in Section 3.3.3. These sources are treated as point sources for IceCube with little loss to sensitivity or model dependence on how the DM is distributed. DM masses from 500 GeV to 100 PeV are considered for this analysis. Several DM annihilation channels available from the HDMspectra [79] are studied in this analysis. This chapter presents the analysis work for IceCube to update our DM searches toward dSphs.

#### 6.2 Dataset and Background

This section enumerates the data and background methods used for IceCube's study of dSphs. Section 6.2.1 and Section 6.2.2 are most useful for fellow IceCube collaborators looking to replicate this analysis.

### 6.2.1 Itemized IceCube files

These files are only available within IceCube’s internal documentation and wikis. They are not meant for public access, and are presented here so that IceCube collaborators can reproduce results accurately.

- Software Environment: CVMFS Py3-v4.1.1
- Data Sample: Northern Tracks NY86v5p1
- Analysis Software: csky ([nu\\_dark\\_matter](#))
- Analysis wiki: [https://wiki.icecube.wisc.edu/index.php/Dark\\_Matter\\_Annihilation\\_Search\\_towards\\_dwarf\\_spheroidals\\_with\\_NST\\_and\\_DNN\\_Cascades](https://wiki.icecube.wisc.edu/index.php/Dark_Matter_Annihilation_Search_towards_dwarf_spheroidals_with_NST_and_DNN_Cascades)
- Project repository

### 6.2.2 Software Tools and Development

This analysis was performed inside IceCube’s CVMFS (3.4.1.1) software environment using csky for likelihood calculations. Csky at first did not come with dark matter spectral models nor could accommodate custom flux models. We developed these capacities for single source and stacked source studies for this analysis. The analysis code is held in a separate repository from csky. The [nu\\_dark\\_matter branch of csky](#) manages the input of custom dark matter spectra and accompanied DM astrophysical source. Csky also enables the use of multithreading which was shown to be crucial for DM searches (see Sec. 4). Csky then calculates likelihoods with a selected data sample. The [IceCube Dark Matter dSph repository](#) manages the generation of spectral models for neutrinos, physics parameter extraction from  $n_{\text{sig}}$ ,  $J$ -factor per source inputs, and bookkeeping for the large parameter space. The project repository required a secondary software environment for neutrino oscillations. How to launch and run those calculations are documented in the project repository and the Docker image is additionally saved in Section C.1.

### 6.2.3 Data Set and Background Description

For this analysis, I use the Northern Sky Tracks (NST) Sample (Version V005-P01). The sample contains up-going track-like events, usually from  $\nu_\mu$  and  $\nu_\tau$ , with a superior angular resolution compared to the cascade dataset. This sample covers 10.4 years of data (IC86\_2011-2021). The accepted neutrino energy range used for the analysis is unique from most other IceCube searches because DM spectra are hard with large contributions close to  $E_\nu = m_\chi$ . Therefore, the sampled energy range is  $1 < \log(E_\nu/\text{GeV}) < 9.51$  with step size 0.125.

The strengths of a dwarf analysis is that there are no additional background considerations beyond nominal, baseline background estimations (see Section 3.2.3). For NST, the nominal contributions come from atmospheric neutrinos and isotropic astrophysical neutrinos. We estimate the background by scrambling NST data along Right Ascension.

## 6.3 Analysis

The expected differential neutrino flux from DM-DM annihilation to standard model particles,  $d\Phi_\nu/dE_\nu$ , over solid angle,  $\Omega$  is described by the familiar equation.

$$\frac{d\Phi_\nu}{dE_\nu} = \frac{\langle\sigma\nu\rangle}{8\pi m_\chi^2} \frac{dN_\nu}{dE_\nu} \times \int_{\text{source}} d\Omega \int_{l.o.s} \rho_\chi^2 dl(r, \theta') \quad (6.1)$$

This is identical to Eq. (3.1) except that there are 3 neutrino flavors, so there are a corresponding 3 flux equations. Section 3.3 has a complete description of each term in Eq. (6.1). Additionally, neutrinos oscillate between flavors which needs to be considered for the expected neutrino flux at Earth. Section 6.3.1 presents the particle physics model and processing for DM annihilation. Section 6.3.2 presents the spatial distributions built for each dSph.

### 6.3.1 $\frac{dN_\nu}{dE_\nu}$ - Particle Physics Component

Neutrino spectra from heavy DM annihilation were generated using HDMspectra [79] and  $\chi$ arov [95]. HDMspectra has tables for the decay and annihilation of heavy DM for different dark DM and SM primary annihilation channels. The simulation includes electroweak or gluon radiative corrections and higher order loop corrections from the  $W$  and  $Z$  bosons ( $WWZ$  and  $WW\gamma$ ). These corrections are especially important for accurately estimating the prompt neutrino flux. This

publication also pushes the simulated DM mass to the Plank scale (1 EeV), however this study will not explore that high.

An important feature in the spectra is that neutrino line channels will be accompanied by a low energy tail [79], see Fig. 6.1. Thus, the Earth will not fully attenuate a heavy neutrino line-like signal from high declination sources where the neutrino flux must first traverse through the Earth. The DM annihilation channels that feature lines include all leptonic channels:  $\nu_{e,\mu,\tau}$ ,  $e$ ,  $\mu$ , and  $\tau$ . We use the `xarov` software to propagate and oscillate the neutrinos from the source to Earth. Because these sources are quite large in absolute terms, and also far (order 10 kpc or more), the resulting flavor spectra are the averages of the transition probabilities [95]:

$$P(\nu_\alpha \rightarrow \nu_\beta) \approx \begin{bmatrix} 0.55 & 0.18 & 0.27 \\ 0.18 & 0.44 & 0.38 \\ 0.27 & 0.38 & 0.35 \end{bmatrix} \quad (6.2)$$

Examples of the spectra before and after propagation are shown in Fig. 6.1.

When calculating the expected contribution to  $n_s$ , only  $\nu_\mu$  and  $\nu_\tau$  are considered as NST's effective area to  $\nu_e$  is negligible [96]. Therefore, the expected composite neutrino spectrum is the sum of the two flavors:  $\frac{dN\nu_\mu}{dE\nu_\mu} + \frac{dN\nu_\tau}{dE\nu_\tau}$ . The spectral tables are then converted to splines to condense information, enable random sampling of the spectra, and reduce computing times. The spectral splines are finally implemented as a DM class in csky.

### 6.3.1.1 Treatment of Neutrino Line Features

All DM annihilation channels into leptons  $\chi\chi \rightarrow [\nu_{e,\mu,\tau}, e, \mu, \tau]$  develop a prominent and narrow spectral line feature. For all neutrino flavors, this line is visible and prominent in all  $m_\chi$  studied in this analysis. For charged leptons, the feature typically manifests at  $m_{chi} > 10$  TeV, yet its prominence varies slightly between the flavors. Examples for lines in the annihilation spectra with neutrinos or charged leptons are provided in Fig. 6.1.

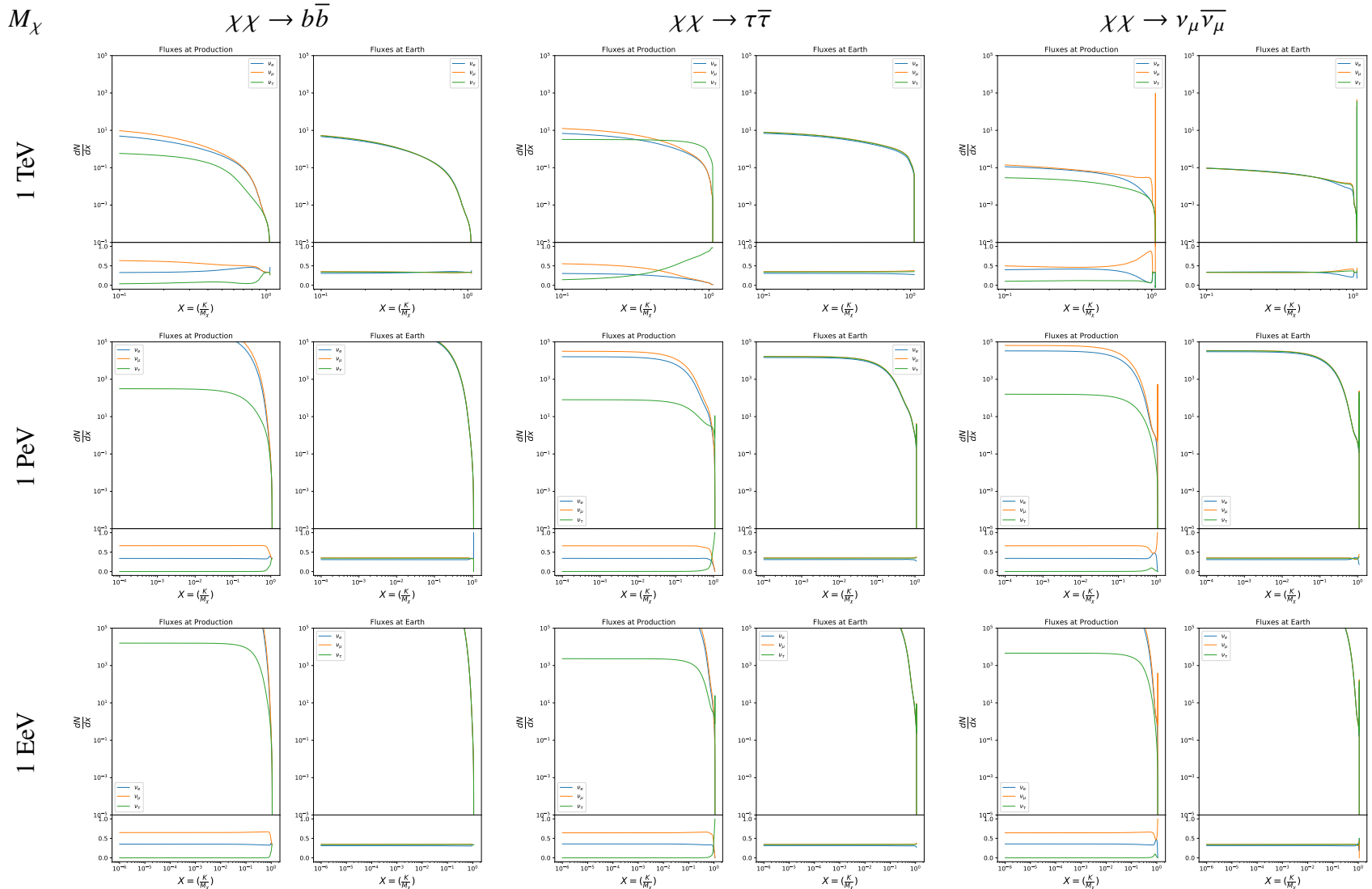


Figure 6.1 Neutrino spectra at production (left panels) and after oscillation at Earth (right panels). Blue, orange, and green lines are the  $\nu_e$ ,  $\nu_\mu$ , and  $\nu_\tau$  spectra respectively. Top panels show the spectra in  $\frac{dN}{dE}$ . Lower panels plot the flavor ratio to  $\nu_e + \nu_\mu + \nu_\tau$ . SM annihilation channels  $b\bar{b}$ ,  $\tau\bar{\tau}$ , and  $\nu_\mu\bar{\nu}_\mu$  are shown for  $M_\chi = 1$  Pev, TeV, and EeV.

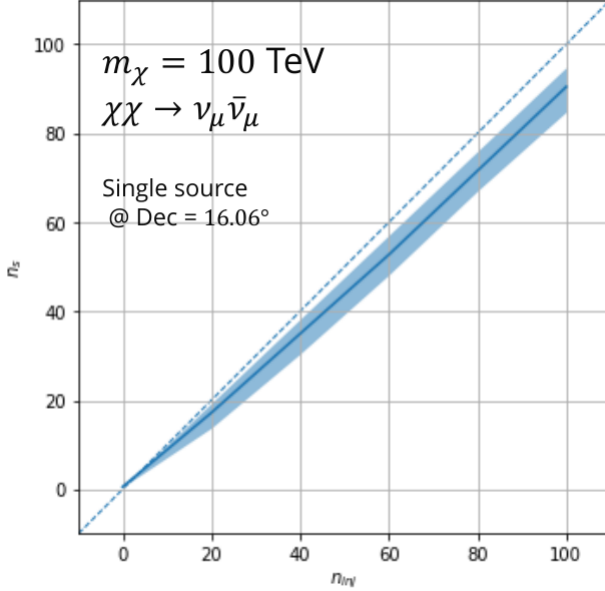


Figure 6.2 Signal recovery for 100 TeV DM annihilation into  $\nu_\mu \bar{\nu}_\mu$  for a source at Dec = 16.06°.  $n_{\text{inj}}$  is the number of injected signal events in simulation.  $n_s$  is the number of reconstructed signal events from the simulation data. Although the uncertainties are small and tight, the reconstructed  $n_s$  are systematically underestimated.

The neutrino line feature is so narrow relative the sampled energy range that the random sampling of the spectra and likelihood fitting rarely capture the line in computation. As a result, often the best fit to simulation of background will always floor to TS = 0 and the signal recovery systematically underestimates the signal (see Fig. 6.2).

To remedy this, we take a similar approach to the IceCube’s decay analysis [97] and the previous gamma-ray study in Section 4.3.1. Two smoothing kernels were tested (Gaussian and uniform) to widen the line feature. The widths were tuned such that the signal recovery approached unity for DM mass 100 TeV to 1 PeV for a source at Segue 1’s declination, 16.06°. Near horizon was chosen in order to isolate loss in signal recovery away from Earth’s attenuation of very high energy neutrinos and atmospheric backgrounds. The kernel convolution needed closely preserve the integrated counts of neutrinos. The optimized kernel parameters for all lines are summarized as:

- Gaussian kernel with  $1\sigma$  width =  $1.75\text{E-}3 \cdot m_\chi$
- Minimum energy included in convolution =  $\text{MIN}[0.995 \cdot m_\chi, E(\nu_{\text{line}}) - 4\sigma]$

- Maximum energy included in convolution =  $\text{MAX}[1.005 \cdot m_\chi, E(\nu_{\text{line}}) + 4\sigma]$

where  $E(\nu_{\text{line}})$  is the neutrino energy where the neutrino line is at the maximum.

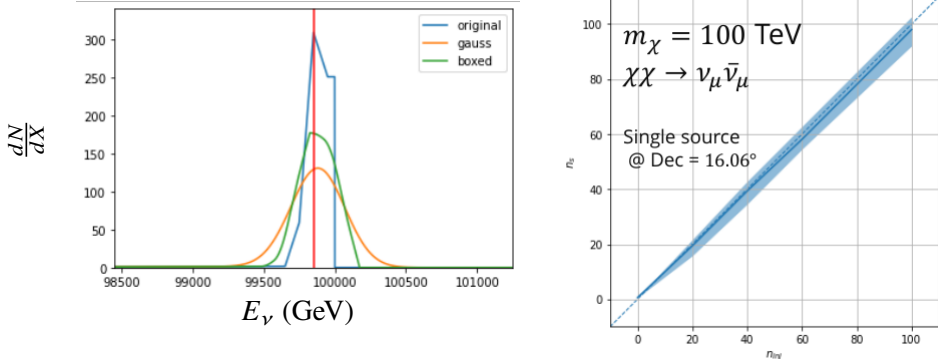


Figure 6.3 Left panel shows the two kernels overlaying the original spectrum from  $\chi\text{aron}\nu$  after propagation to Earth [95]. The vertical red line indicates where the original neutrino line is maximized. Blue line is the output from  $\chi\text{aron}\nu$ . Green line is the spectrum after convolution with a flat kernel. Orange line is the spectrum after Gaussian convolution. Right panel shows the signal recovery of the spectral model using the Gaussian kernel with parameters enumerated above.

These parameters broadly improved the signal recovery of the line spectra. An example is in Fig. 6.3. Analysis level signal recovery studies are expanded upon in Section 6.6.

### 6.3.1.2 Spline Fitting

In an effort to reduce computational work, memory burden, and align with point source methods used for NGC1068 [98], spectral splines were created and adopted for estimating the neutrino flux for the different spectral models. Software was written to generate, book keep, and calculate values on the splines.

When using splines, one has to be careful of the goodness to fit. The spline software used here, Photospline [99], uses the penalized spline technique [100]. Through the penalized technique, poor fits are penalized according to the accuracy of the nominal value, and the smoothness of the first and second derivatives. However, this construction does not penalize on the integral of the fit distribution which is critical in low signal studies, such as DM searches. There are additional caveats when testing the goodness to fit to the MC generated above for all DM annihilation channels.

- The splines must be Log10(\*) in Energy and dN/dX to account for the exponential nature of the flux.
- The fidelity of the fit matters more at  $E_\nu \approx m_\chi$  where the model uncertainties are minimal and physical considerations (like the cut-off) are most important.
- The fidelity of the fit matters less at low  $E_\nu$  as the model uncertainties are large AND IceCube's sensitivity diminishes significantly below 500 GeV.
- Total integrated counts should be well-preserved.

The resulting cost function was built to evaluate the goodness of spline fits to account for the above considerations.

$$e_i = x_i \cdot \left( \frac{dN_i}{dX_i} - 10^{\hat{e}_i} \right) \quad (6.3)$$

Where  $\hat{e}_i$  is the spline estimator's value for  $x_i$ .  $x_i = E_{\nu_i}/m_\chi$ .  $\frac{dN_i}{dX_i}$  is the flux value from MC. I then take the RMS of the error distribution and the resulting value, err, is used to evaluate the fidelity of the spectral spline.

$$\text{err} = \sqrt{\frac{1}{x_{\max} - x_{\min}} \int_{x_{\min}}^{x_{\max}} e^2 dx} \quad (6.4)$$

$x_{\min}$  and  $x_{\max}$  are the scope of the error evaluation and are provided in Tab. 6.1.

Each SM channel had unique tolerances for 'err'. Channels with very hard cut-offs had looser tolerance for err because a significant error would be generated from single counts over/underestimated at the cut-off. Soft channels do not share this issue, so the tolerance is much stricter. All annihilation channels from HDM are modeled well below IceCube's NST sensitivity which falls off substantially below 100 GeV [96]. We do not think it is necessary to evaluate the spline fits below 100 GeV and use this value as the default lower cut-off. Yet, HDM's model uncertainties at  $E_\nu < 10^{-6} \cdot m_\chi$  span an order of magnitude [79]. We also choose not to evaluate the splines below this critical value if it is within IceCube's sensitivity. Finally, the smoothing of the spectral lines in leptonic annihilation channels are ignored for evaluating the fit. We used the lower limit of

$\chi\chi \rightarrow$	GOOD	OK	FAIL	Limits of err calc [ $X_{min}, X_{max}$ ]
$Z^0 Z^0, W^+ W^-$	1.0E-3	1.0E-3, 1.0E-2	1.0E-2	MAX[100GeV/ $m_\chi$ , $10^{-6}$ ], 1.0
$t\bar{t}, hh$	1.0E-5	1.0E-5, 1.0E-4	1.0E-4	MAX[100GeV/ $m_\chi$ , $10^{-6}$ ], 1.0
$b\bar{b}, d\bar{d}, u\bar{u}$	9.0E-7	9.0E-7, 9.0E-6	9.0E-6	MAX[100GeV/ $m_\chi$ , $10^{-6}$ ], 1.0
$\nu\bar{\nu}_{e,\mu,\tau}$	1.0E-3	1.0E-3, 1.0E-2	1.0E-2	MAX[100GeV/ $m_\chi$ , $10^{-6}$ ], MIN[0.995, ( $E_n(\nu_{line}) - 4\sigma$ )/ $M_\chi$ ]
$e\bar{e}, \mu\bar{\mu}, \tau\bar{\tau}$	1.0E-3	1.0E-3, 1.0E-2	1.0E-2	MAX[100GeV/ $m_\chi$ , $10^{-6}$ ], MIN[0.995, ( $E_n(\nu_{line}) - 4\sigma$ )/ $M_\chi$ ]

Table 6.1 Spline err tolerances used for input in particle physics component to Eq. (3.1). Column 1 is the DM annihilation channel being fit. Columns 2, 3, and 4 are the tolerances for "GOOD" (pass), "OK" requires inspection, and "FAIL" (tune and refit) respectively. Column 5 has the X ranges over which the error is evaluated. MAX/MIN [·, ·] takes the maximum or minimum of the two enclosed values.

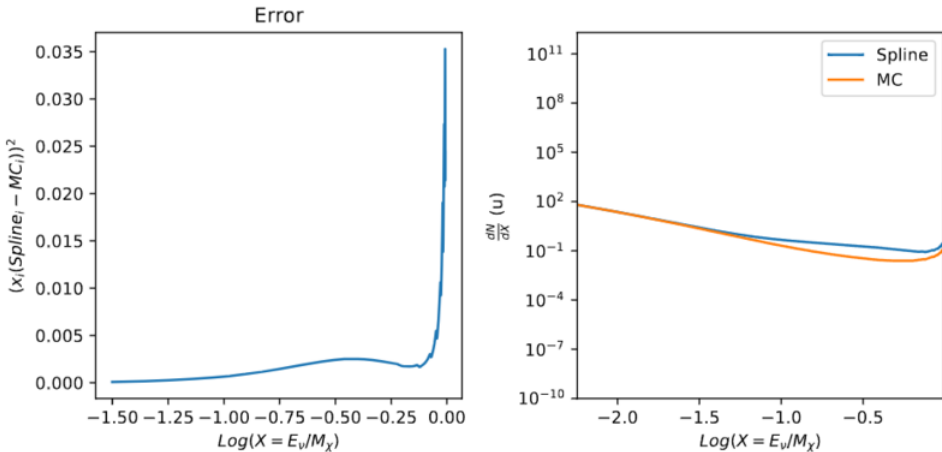


Figure 6.4 Example spline that failed the fit. Failed splines are corrected on a case by case basis unless the SM channel has a systematic problem fitting the splines. In this case, I made a bookkeeping error and loaded the incorrect spectral model

the kernel mask as the upper limit of evaluation. Table 6.1 summarizes the tolerances for the DM annihilation channels used for this analysis.

The errors are then assessed in two ways. First, FAIL and OK are directly plotted with  $e_i$  as a function of  $x$  with the full spline and MC. An example of a single failure is provided in Fig. 6.4. Second, a summary plot of all the splines is plotted and colors coded. Figure C.1 are the spline summaries as of writing this thesis. The goal broadly is to eliminate all red and inspect yellow statuses.

The  $\nu_e$  spectra at Earth are not considered in this analysis, so no work was done to refine the

spline fits for this flavor. Finally, I perform a visual inspection of the splines to verify that the spline fitting did not introduce spurious features that would corrupt the likelihood fitting.

### 6.3.1.3 Composite Neutrino Spectra

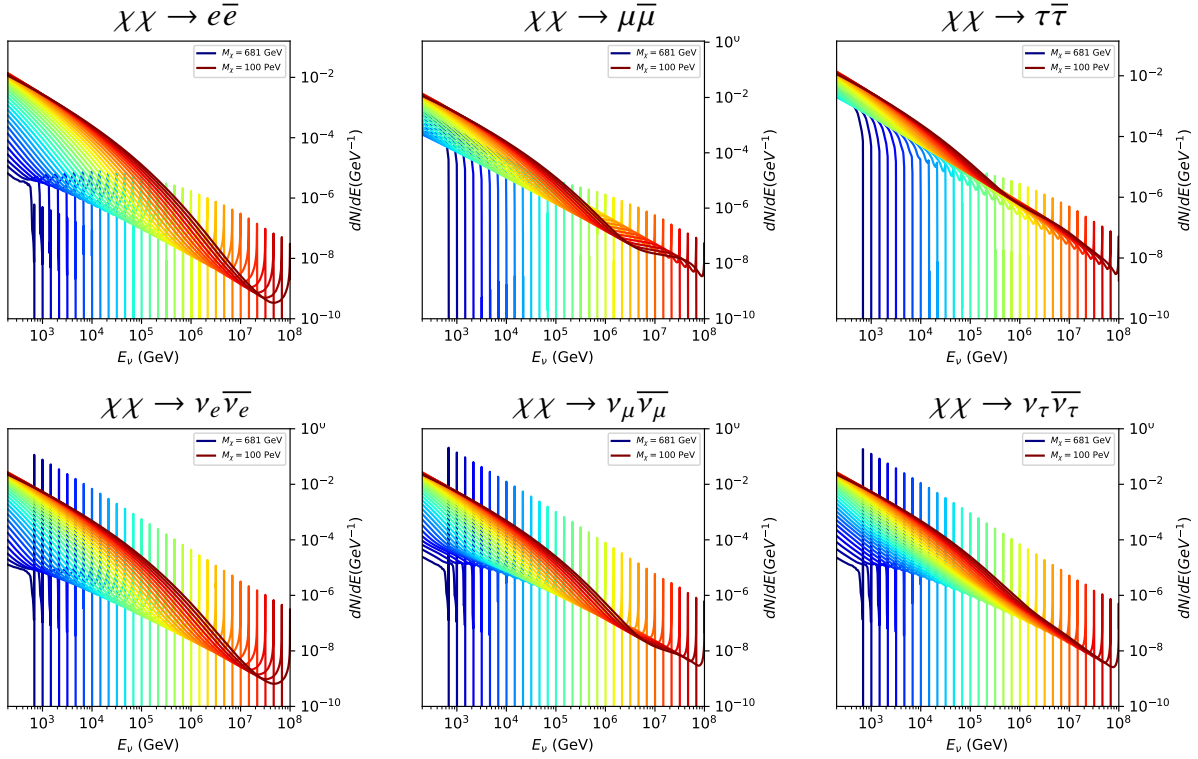


Figure 6.5 Summary of input spectral models that were smoothed with Gaussian kernels. Spectral models are for  $\chi\chi \rightarrow e\bar{e}$ ,  $\mu\bar{\mu}, \tau\bar{\tau}$ ,  $\nu_e\bar{\nu}_e$ ,  $\nu_\mu\bar{\nu}_\mu$ , and  $\nu_\tau\bar{\nu}_\tau$ . These spectra are the composite ( $\nu_\mu + \nu_\tau$ ) of neutrino flavors. Every spectral model used for this analysis is featured as a colored solid line. Bluer lines are for low  $m_\chi$  models.  $m_\chi$  ranges from 681 GeV to 100 PeV. HDM [79],  $\chi$ arov [95], and Photospline [99] are used to generate these spectra. Energy (x-axis) was chosen to roughly represent the energy sensitivity of NST.

With all the previously mentioned pieces, we are ready to fully assemble a comprehensive description of the particle physics term  $dN/dE$  in Eq. (6.1).

$$\frac{dN_\nu}{dE_{\nu \oplus}} = \left( \frac{dN_{\nu_e}}{dE_{\nu_e}} + \frac{dN_{\nu_\mu}}{dE_{\nu_\mu}} + \frac{dN_{\nu_\tau}}{dE_{\nu_\tau}} \right)_{\text{src}} \cdot \mathbf{P}(\nu_\alpha \rightarrow \nu_\beta) \quad (6.5)$$

Figure 6.5 shows the spectral models that required Gaussian smoothing, the leptonic annihilation channels. The remaining models where the only processing were spline fitting and neutrino oscillation are documented in Section C.3. Notice that the different neutrino flavors are unique,

especially in their low energy tails. Therefore, this analysis will be sensitive to DM annihilating to the distinct neutrino flavors.

### 6.3.2 *J*- Astrophysical Component

For this analysis, we re-adopt the  $\mathcal{GS}$  model [59] used in Sec. 3 for dSphs. These models are based on a modified Navarro-Frenk-White (NFW) profile where the indices of the NFW (traditionally 1,3,1) are allowed to float. The angular width of these sources is much smaller than the angular resolution of IceCube NST [98]. We therefore treat these sources as point sources in this analysis, and forgo generating maps. These sources and the  $\mathcal{GS}$  model have already been discussed at length in Section 3.3.2 and is not repeated here. IceCube uses identical sources to Tab. 3.1 except we analyze source with declinations above  $0.0^\circ$ .

### 6.3.3 Source Selection and Annihilation Channels

We use all the dSphs presented in IceCube’s previous dSph DM search [93] and expand beyond it. IceCube’s sources for this analysis studies include Boötes I, Canes Venatici I, Canes Venatici II, Coma Berenices, Draco, Hercules, Leo I, Leo II, Leo V, Leo T, Segue 1, Segue 2, Ursa Major I, Ursa Major II, and Ursa Minor. A full description of all sources used is in Table 3.1. Sources with declinations less than  $0.0$  are excluded from this analysis.

This analysis improves on the previous IceCube dSph paper [93] in the following ways. Previously, the IceCube detector was not yet completed to the 86 string configuration. Many more dSphs will be observed, from 4 to 15. Previously, the particle physics model used for neutrino spectra from DM annihilation did not have EW corrections where they are now included [79]. The spectral models also predict substantial differences between the neutrino flavors, so this analysis will be the first DM dwarf analysis to discriminate between primary neutrino flavors. The study performed here studies 10.4 years of data.

The SM annihilation channels probed for this study include  $\chi\chi \rightarrow$

$$b\bar{b}, t\bar{t}, u\bar{u}, d\bar{d}, e\bar{e}, \mu\bar{\mu}, \tau\bar{\tau}, ZZ, W^+W^-, \nu_e\bar{\nu}_e, \nu_\mu\bar{\nu}_\mu, \text{ and } \nu_\tau\bar{\nu}_\tau$$

## 6.4 Likelihood Methods

I use the Point-Source search likelihood which is widely used in IceCube analyses. The likelihood function is defined as the following:

$$L(n_s) = \prod_{i=1}^N \left[ \frac{n_s}{N} S_i + \left(1 - \frac{n_s}{N}\right) B_i \right] \quad (6.6)$$

where  $i$  is an event index,  $S$  and  $B$  are the signal PDF and background PDF respectively. For a joint analysis where the sources are stacked the likelihood is expanded in the simplified way:

$$L(n_s) = \prod_{i=1}^{N_{\text{sources}}} L_i(n_s) \quad (6.7)$$

Where  $L_i$  is the likelihood from the  $i$ -th source in the stacked analysis. The Test Statistic (TS) definition remains the same as Eq. (3.7)

## 6.5 Background Simulation

Before we look at data, we must first analyze background and signal injection to validate our analysis. We set out to characterize the TS distributions for each source, annihilation channel, and  $m_\chi$ . Previous IceCube DM searches [97, 101] showed TS distributions that did not behave according to a  $\chi^2$  distribution with 1 degree of freedom. TS distributions can also vary significantly between DM mass and annihilation models. Therefore, Wilk's theorem may not be applicable to the analysis. Instead, a critical value is defined from many background trials. We study the TS distributions first for each source, then for the stacked analysis. The following sections show the results of the likelihood fitting for a suite of background trials.

I assume that TS values are physical:  $TS \geq 0$ .  $\epsilon[x]$  indicate the fraction of events where  $TS < x$ . For TS plots shown here, the decimal values of  $x$  are 1.0e-2 and 1.0e-3. Each subplot represents a simulation of 100,000 data-scrambled background trials. Section 6.5.1 show the background TS distributions obtained from Segue 1, a source with little Earth attenuation and large  $J$ -factor, and Ursa Major II, which has similarly large  $J$ -factor but significantly more Earth attenuation, assuming DM annihilation into  $b\bar{b}$ ,  $\tau\bar{\tau}$ , and  $\nu_\mu\bar{\nu}_\mu$ . I show the TS distributions of a stacked study of 15 sources for all DM annihilation channels.

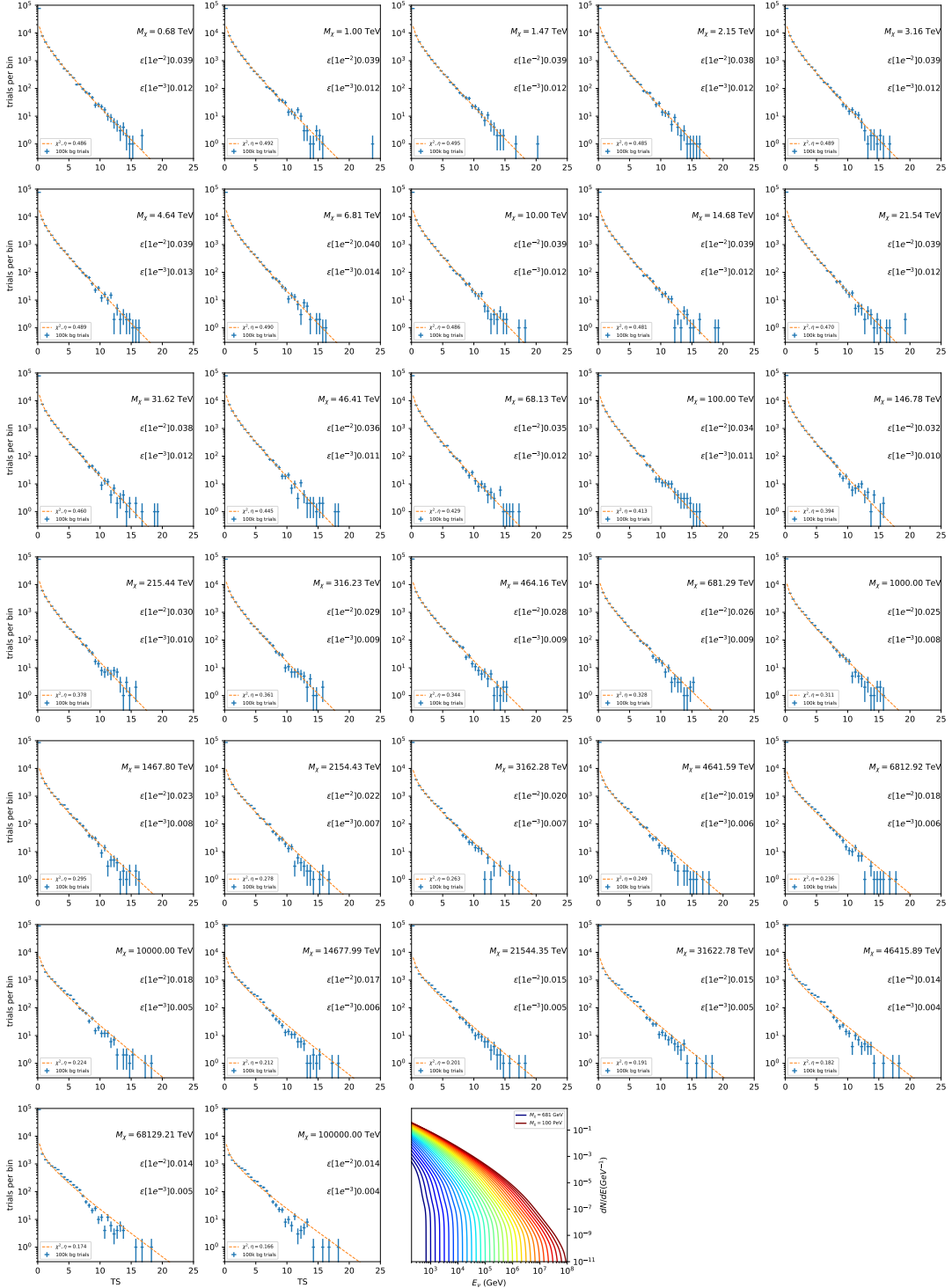


Figure 6.6 Test statistic (TS) distributions for Segue 1 and  $\chi\chi \rightarrow b\bar{b}$ . Each subplot, except the final, is the TS distribution for a specific DM mass listed in the subplot. Orange dashed lines are the traces for a  $\chi^2$  distribution with 1 degree of freedom.  $\epsilon[\cdot]$  is the fraction of trials smaller than the bracketed value. The final subplot features the all DM spectral models, similar to Fig. 6.5, used as input for the TS distributions.

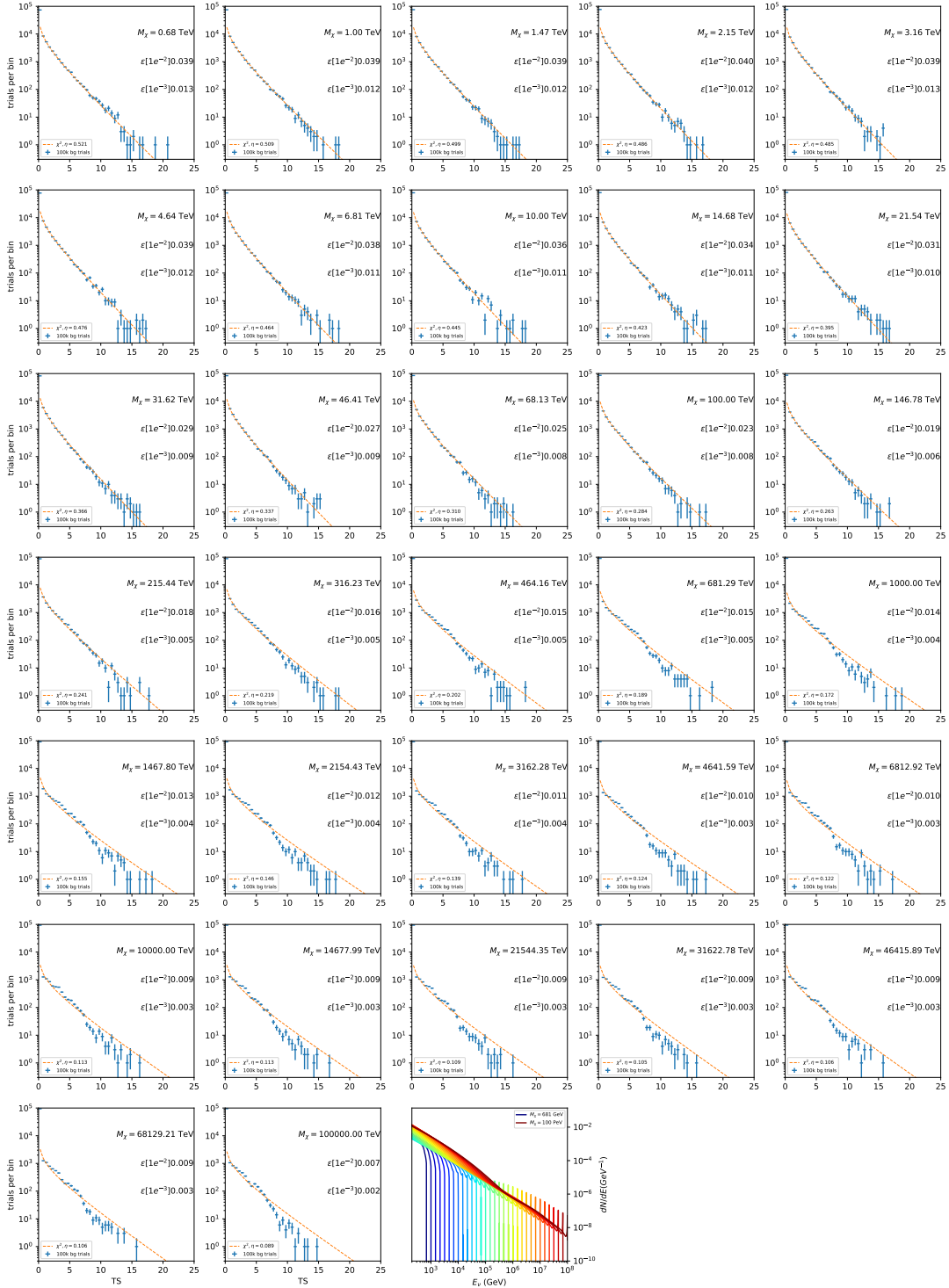


Figure 6.7 Same as Fig. 6.6 for Segue 1  $\chi\chi \rightarrow \tau\bar{\tau}$ .

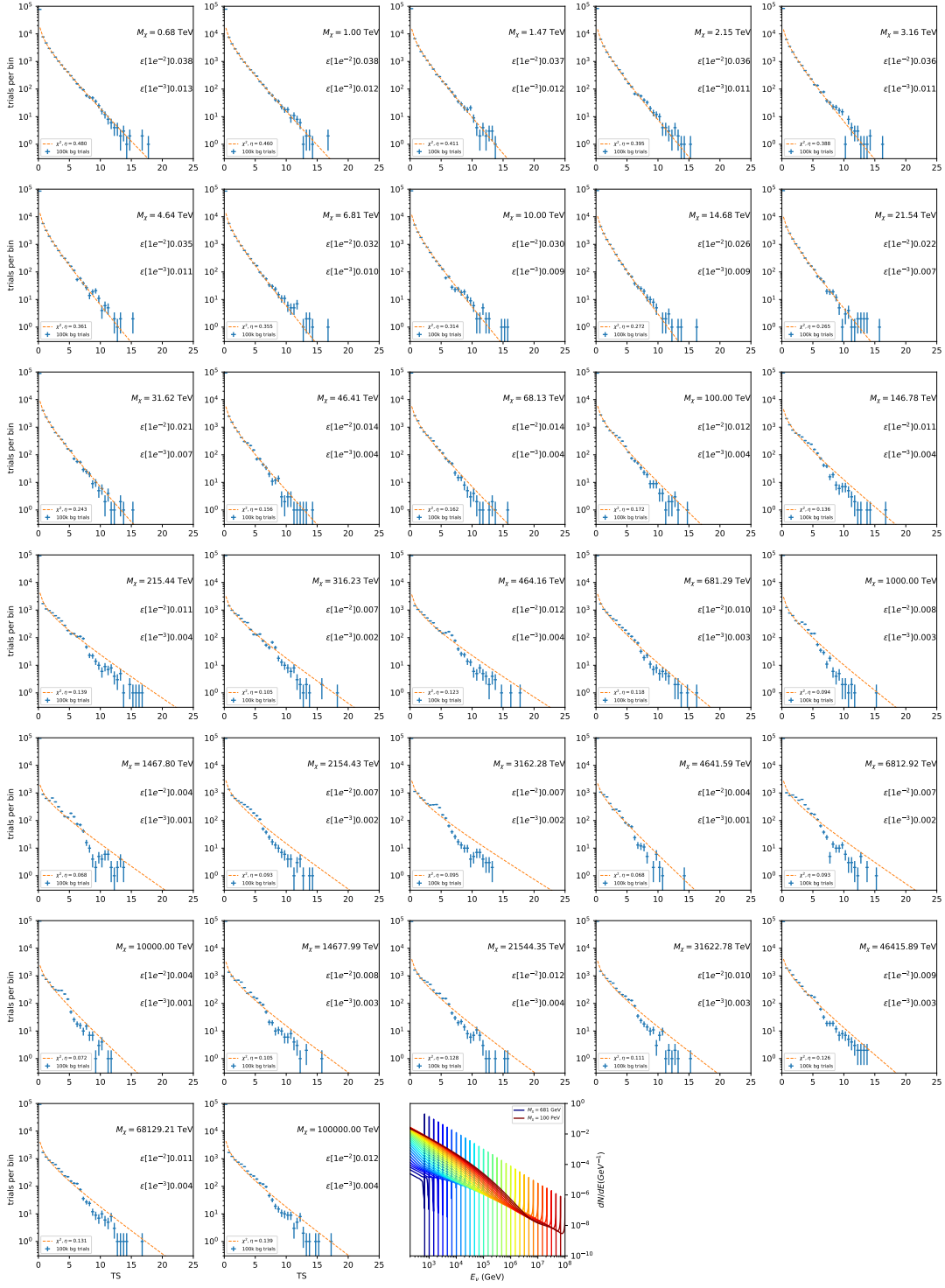


Figure 6.8 Same as Fig. 6.6 for Segue 1  $\chi\chi \rightarrow \nu_\mu \bar{\nu}_\mu$ .

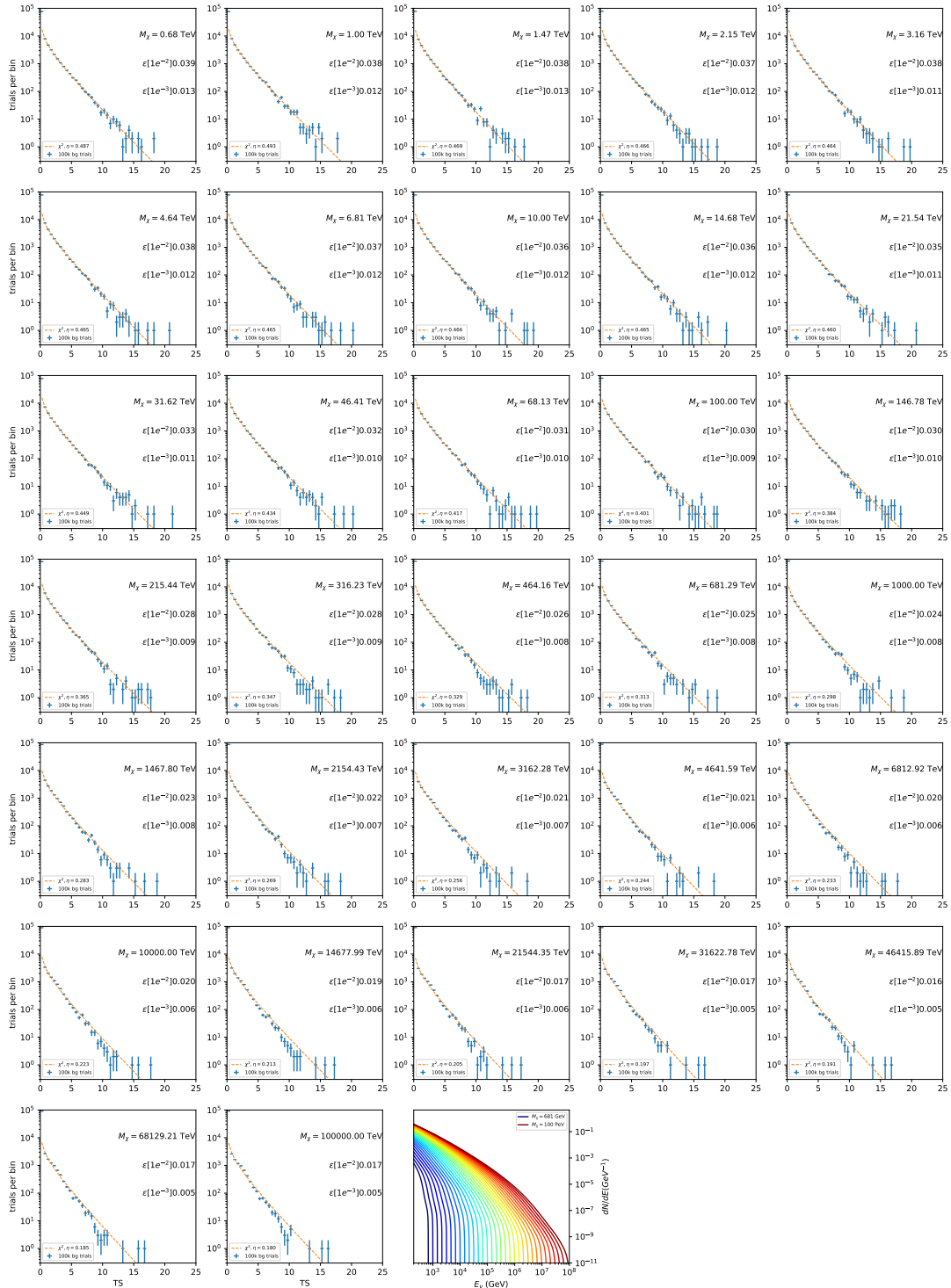


Figure 6.9 Same as Fig. 6.6 for Ursa Major II 1  $\chi\chi \rightarrow b\bar{b}$ .

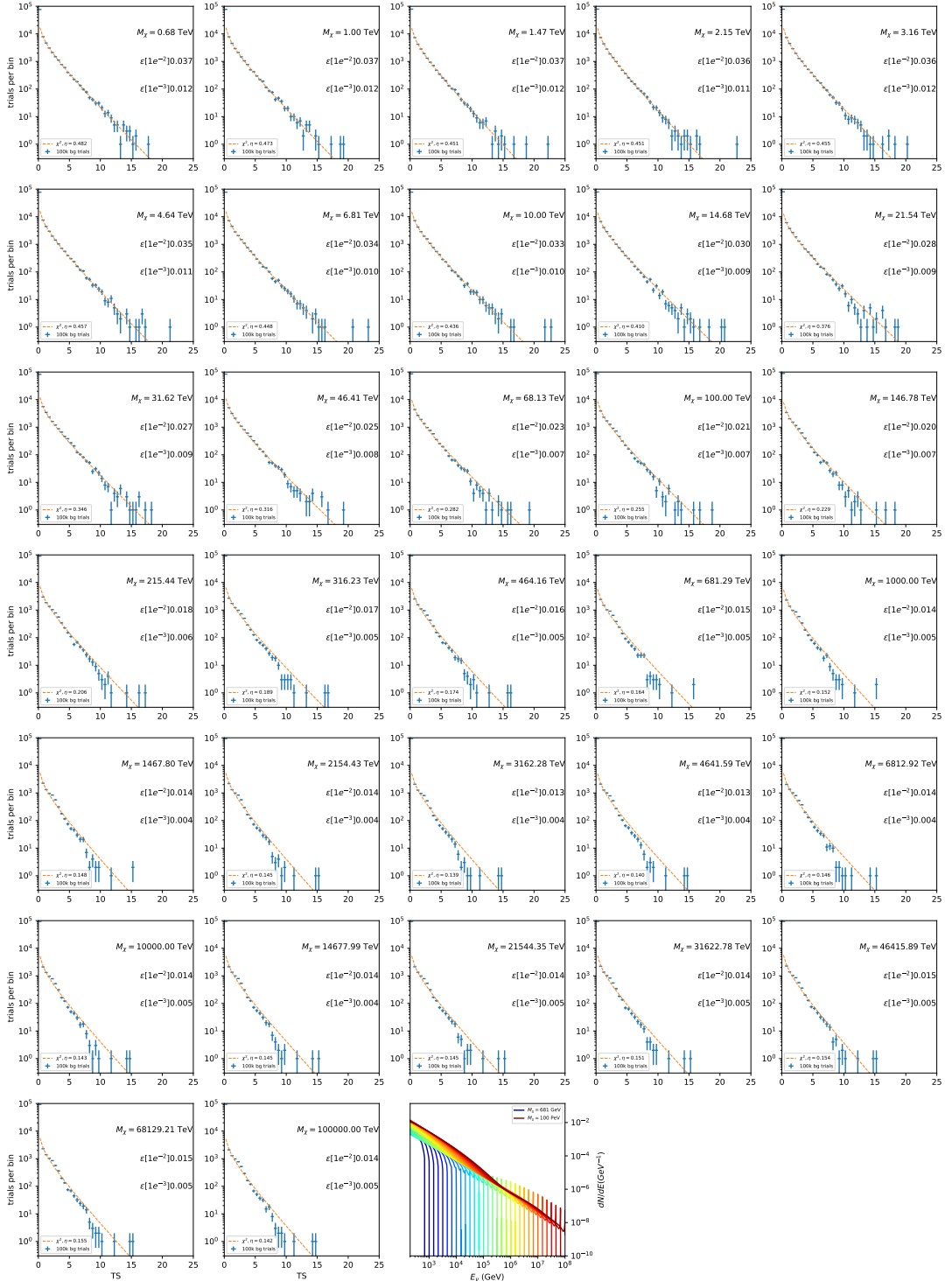


Figure 6.10 Same as Fig. 6.6 for Ursa Major II 1  $\chi\chi \rightarrow \tau\bar{\tau}$ .

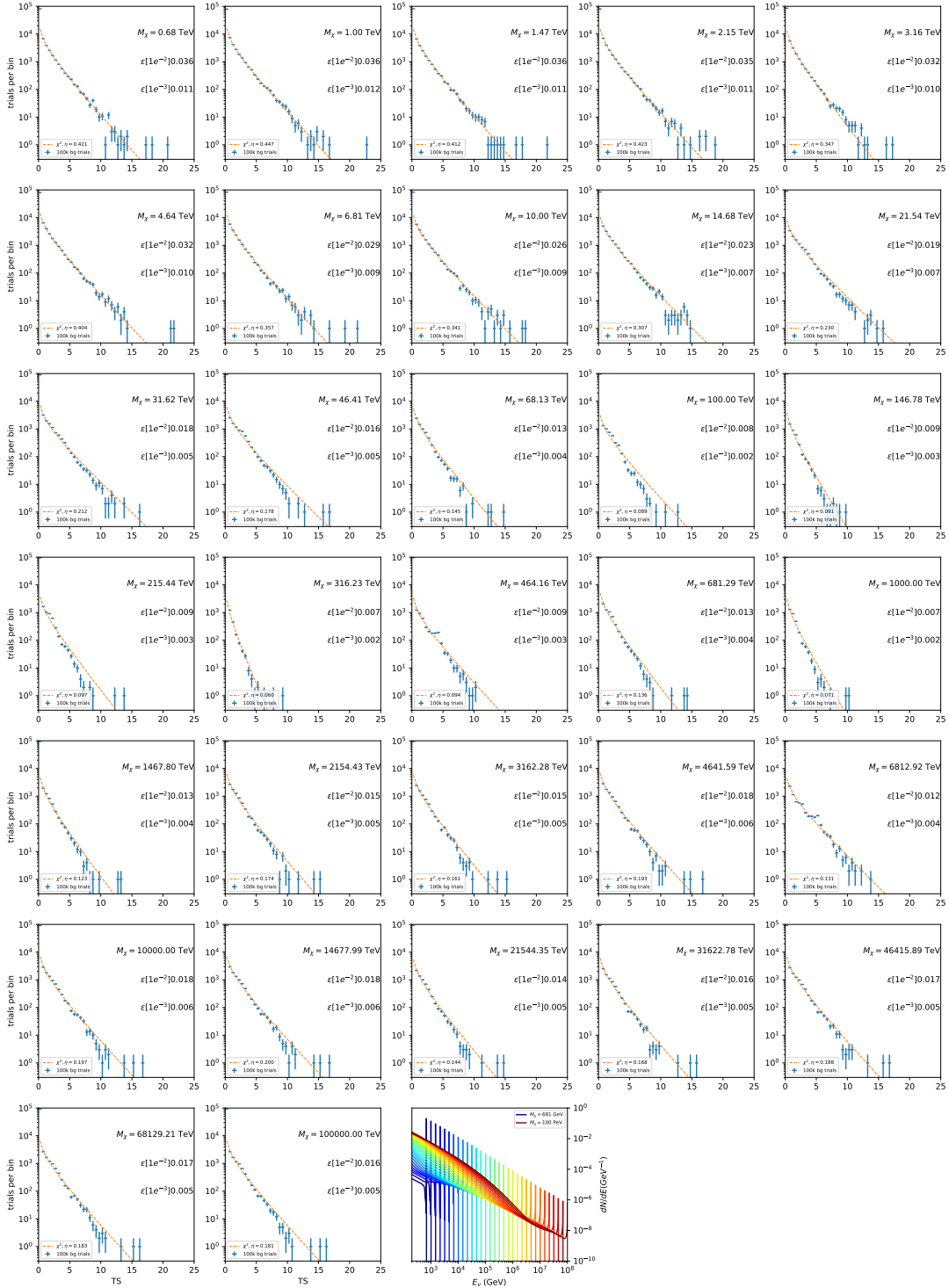


Figure 6.11 Same as Fig. 6.6 for Ursa Major II 1  $\chi\chi \rightarrow \nu_\mu\bar{\nu}_\mu$ .

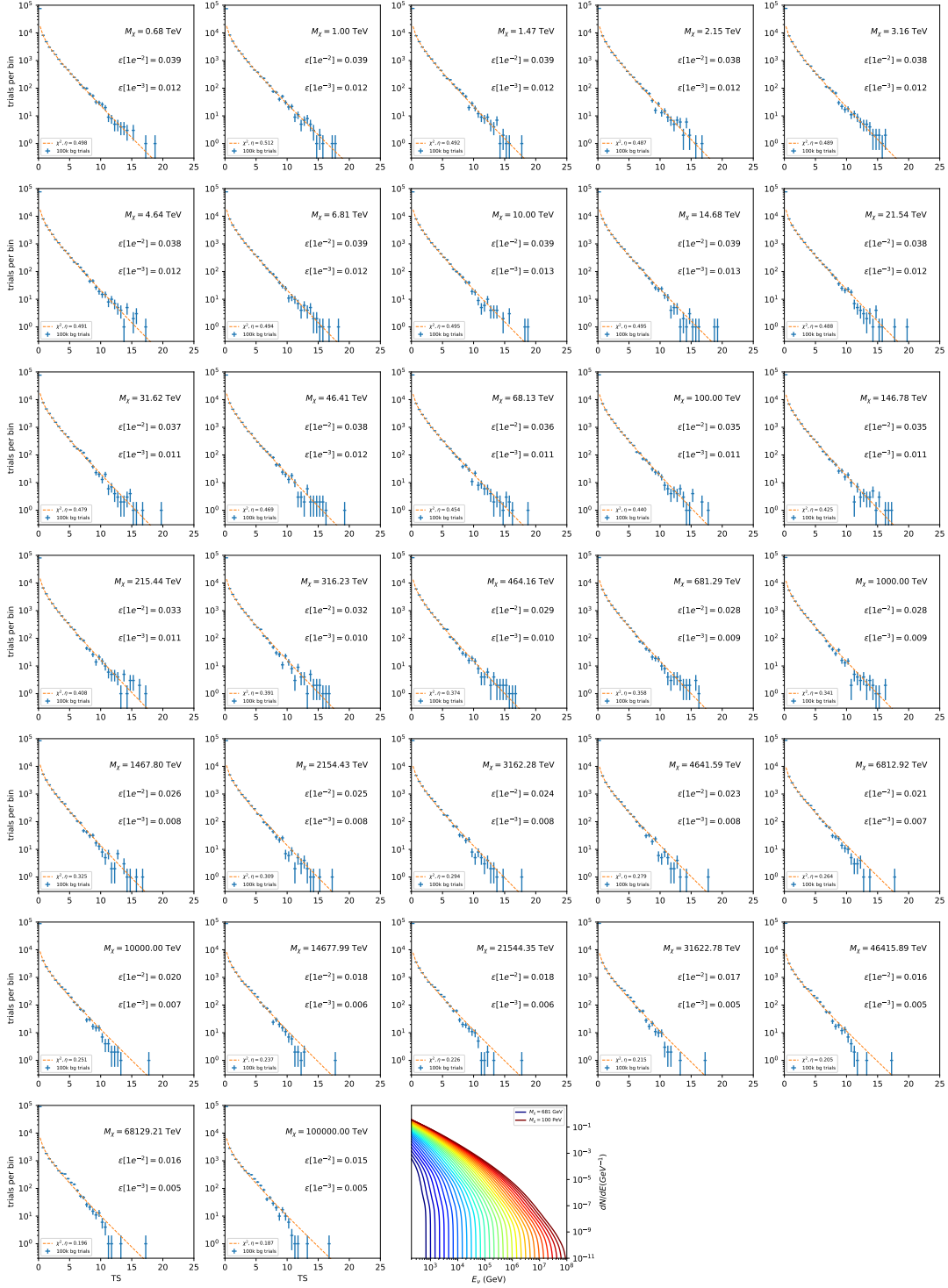


Figure 6.12 Same as Fig. 6.6 for 15,  $\mathcal{GS}$   $J$ -factor, stacked sources and  $\chi\chi \rightarrow b\bar{b}$ .

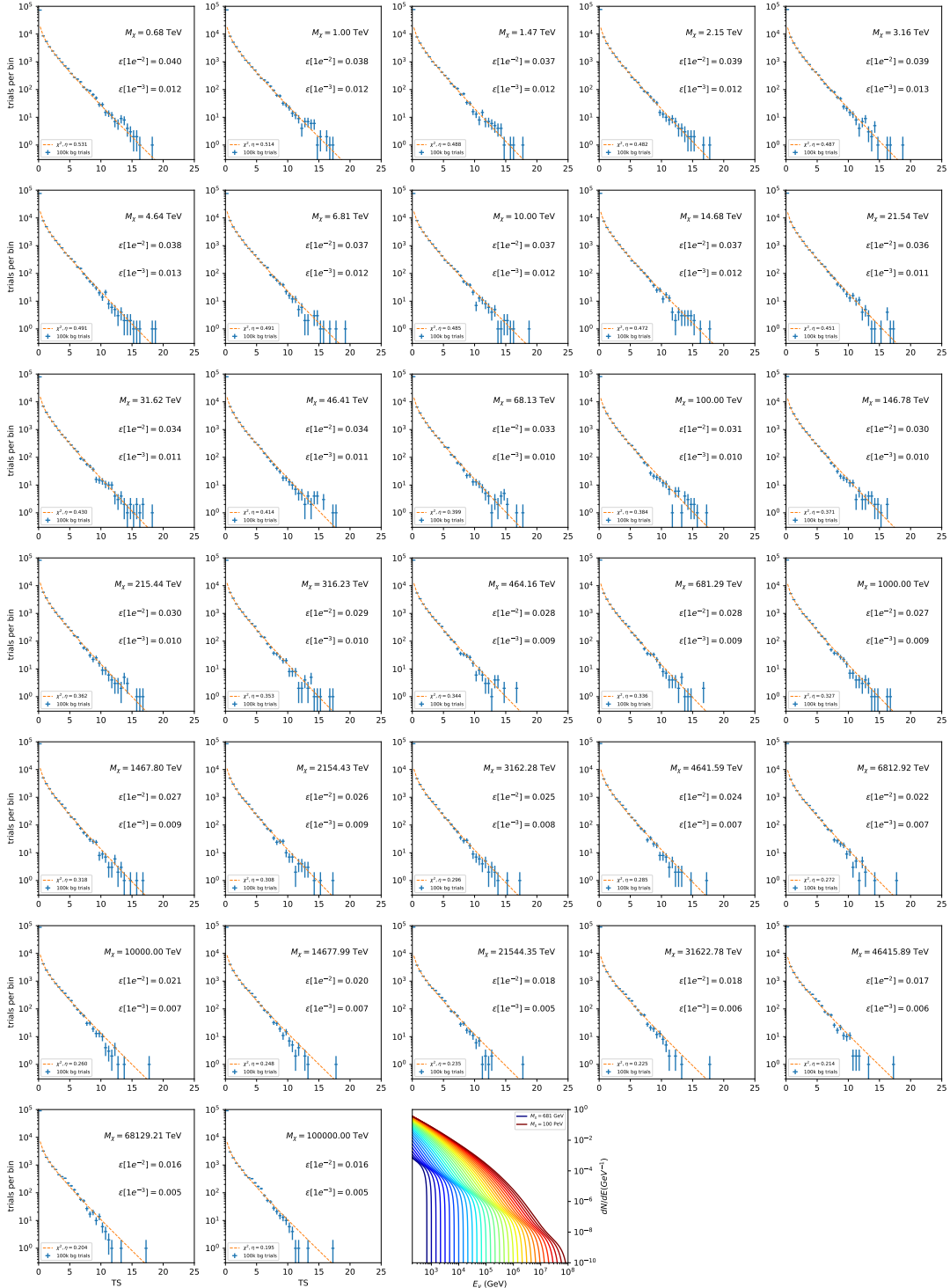


Figure 6.13 Same as Fig. 6.6 for 15,  $\mathcal{GS}$   $J$ -factor, stacked sources and  $\chi\chi \rightarrow t\bar{t}$ .

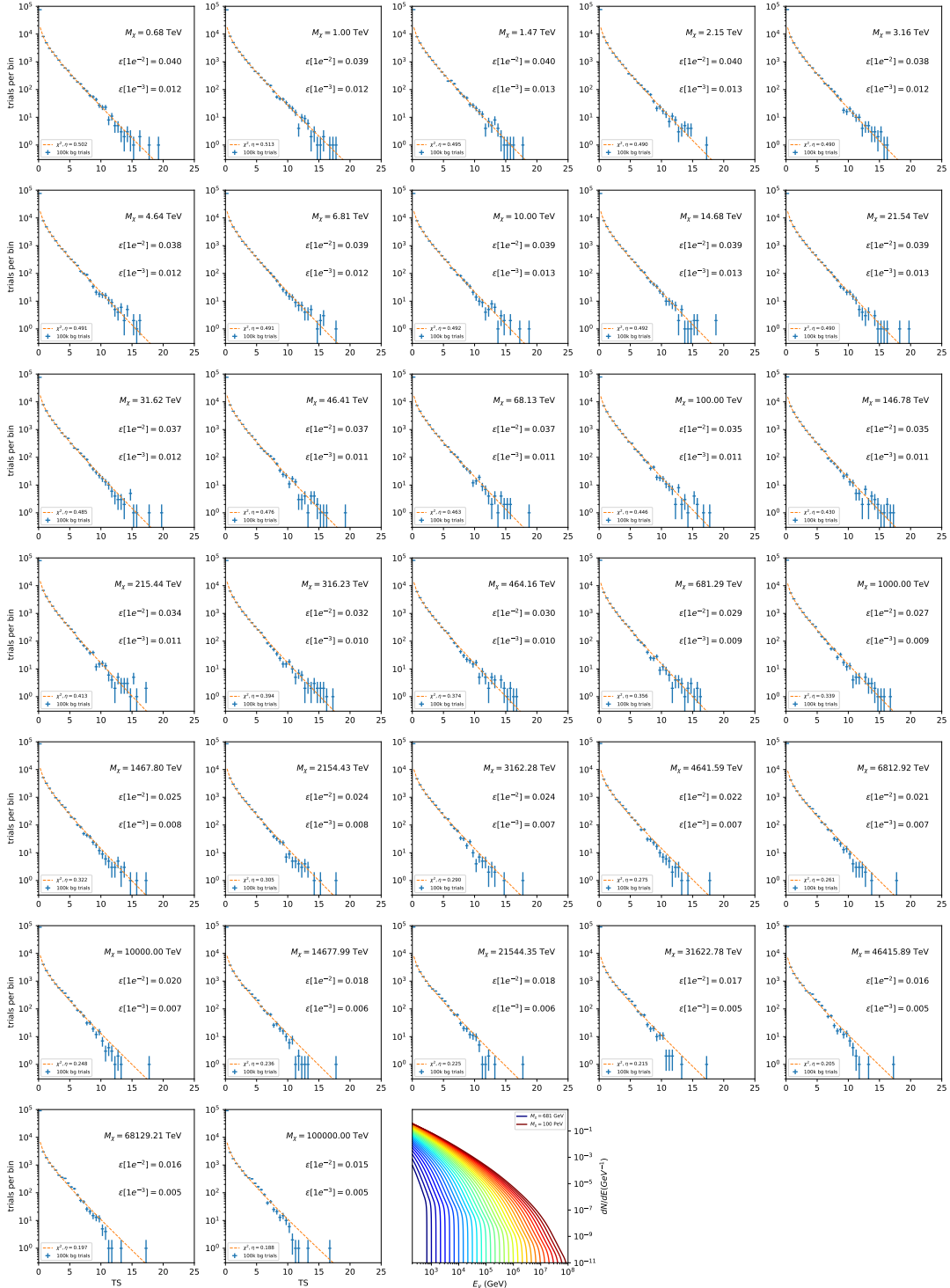


Figure 6.14 Same as Fig. 6.6 for 15,  $\mathcal{GS}$   $J$ -factor, stacked sources and  $\chi\chi \rightarrow u\bar{u}$ .

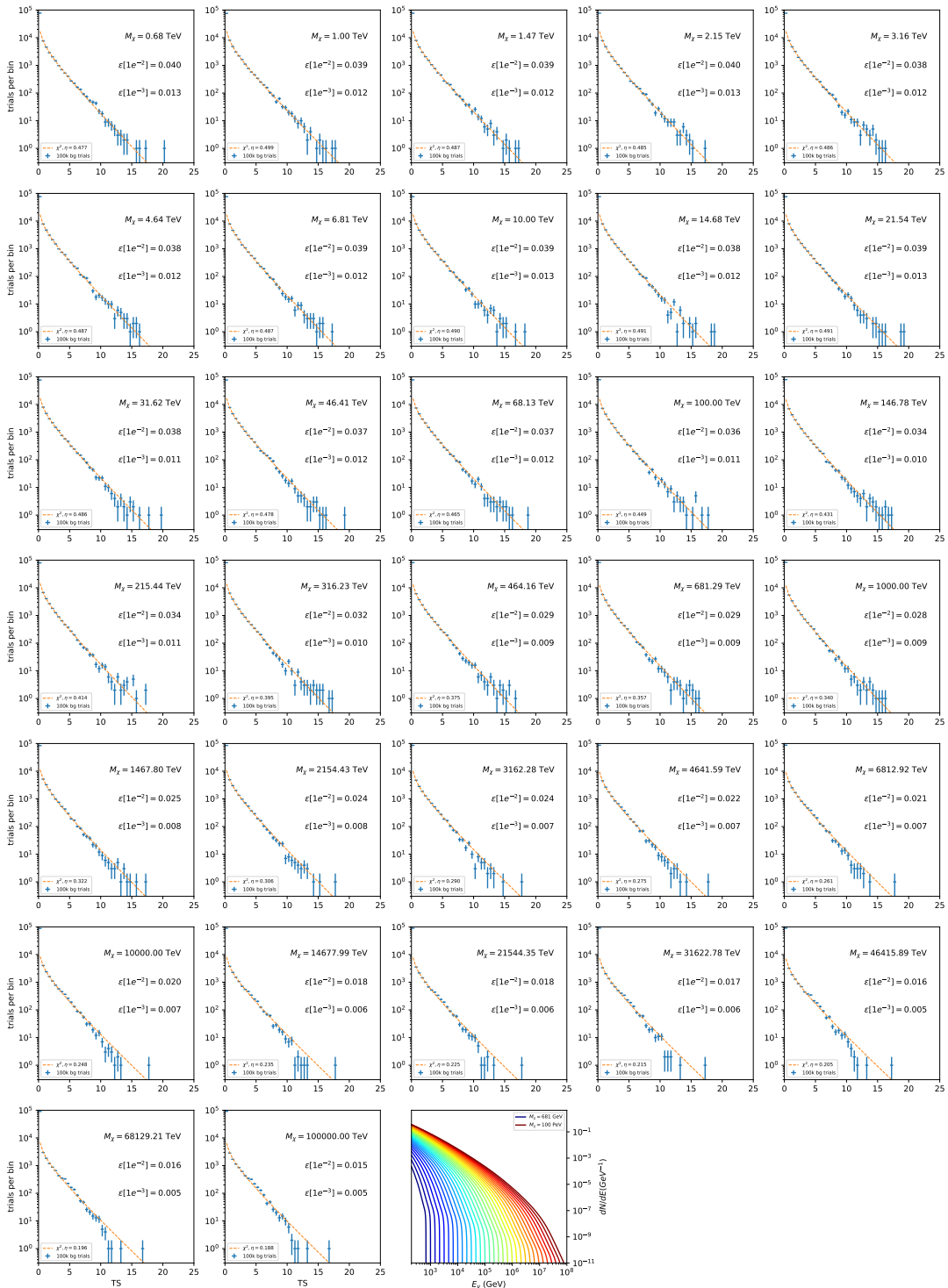


Figure 6.15 Same as Fig. 6.6 for 15,  $\mathcal{GS}$  J-factor, stacked sources and  $\chi\chi \rightarrow d\bar{d}$ .

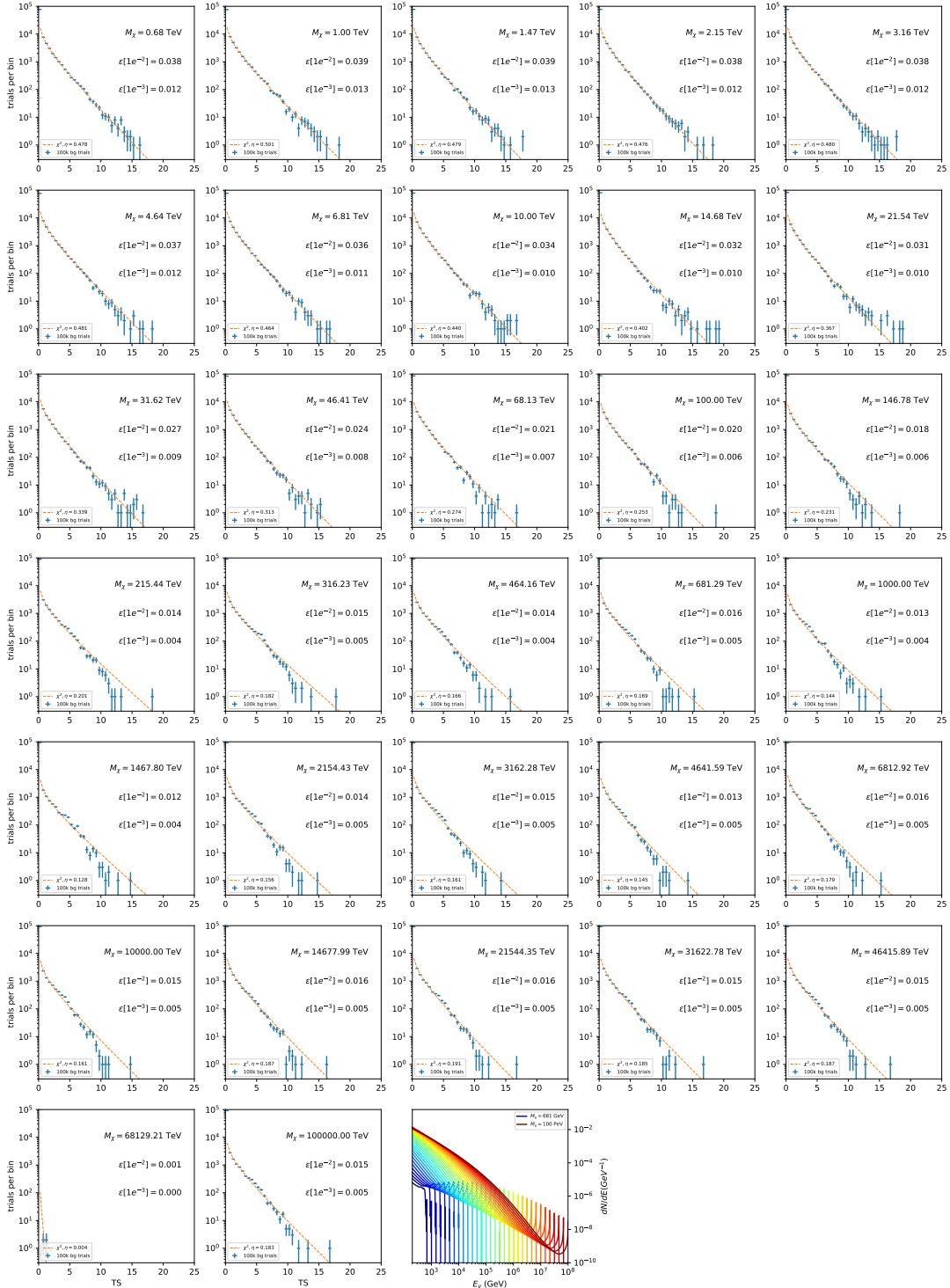


Figure 6.16 Same as Fig. 6.6 for 15,  $\mathcal{G}\mathcal{S}$  J-factor, stacked sources and  $\chi\chi \rightarrow e\bar{e}$ .

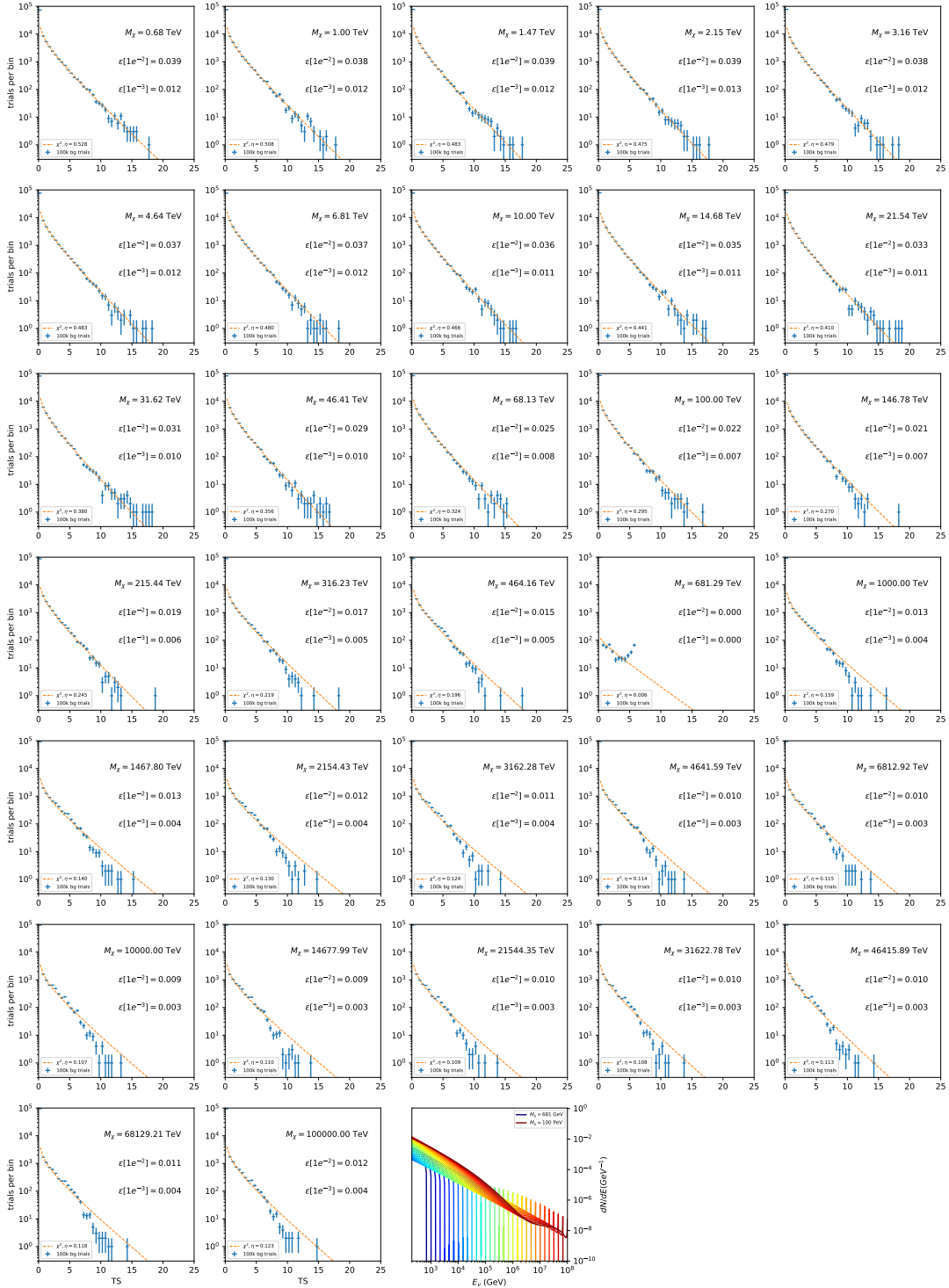


Figure 6.17 Same as Fig. 6.6 for 15,  $\mathcal{GS}$   $J$ -factor, stacked sources and  $\chi\chi \rightarrow \mu\bar{\mu}$ .

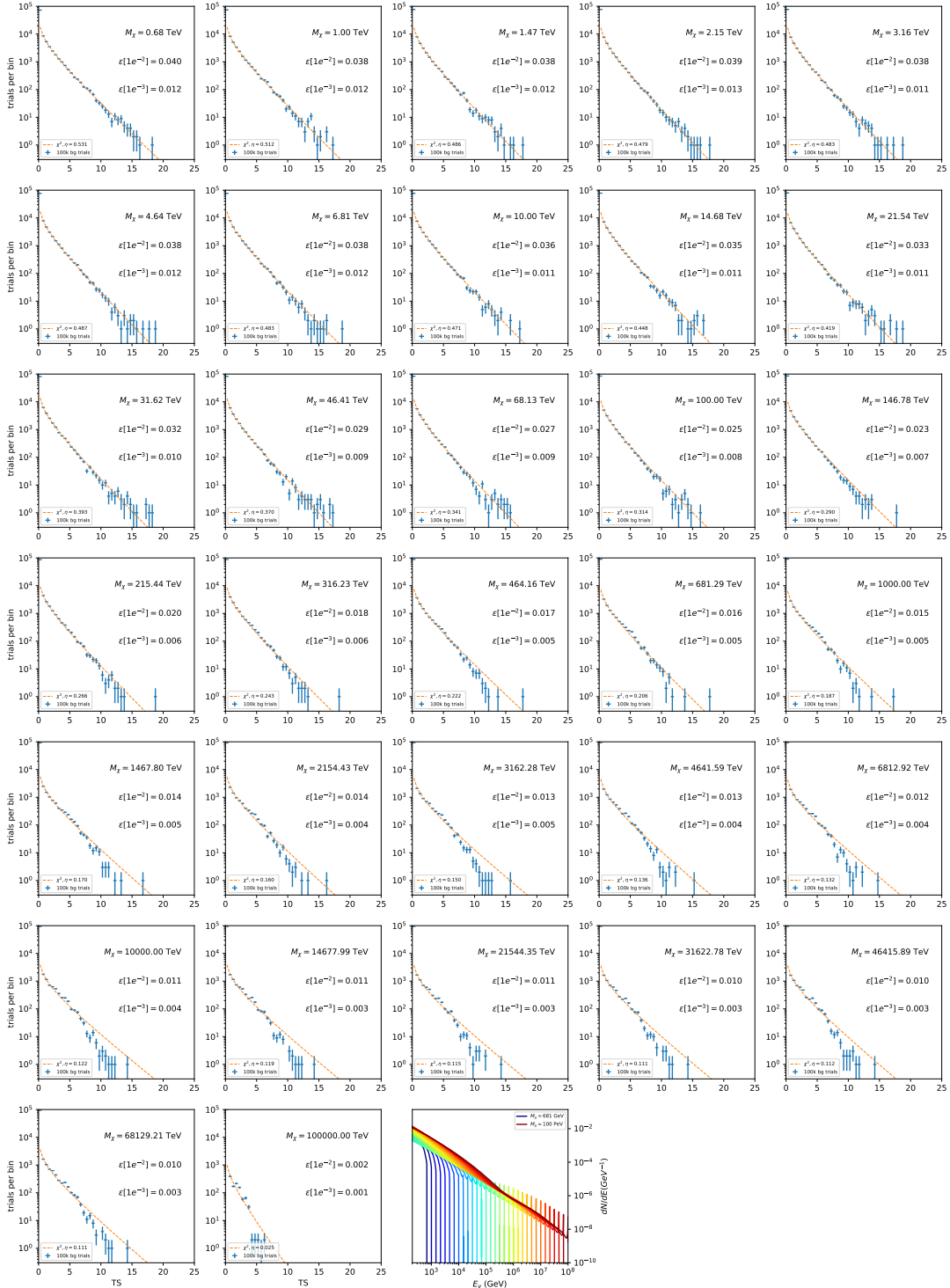


Figure 6.18 Same as Fig. 6.6 for 15,  $\mathcal{GS}$   $J$ -factor, stacked sources and  $\chi\chi \rightarrow \tau\bar{\tau}$ .

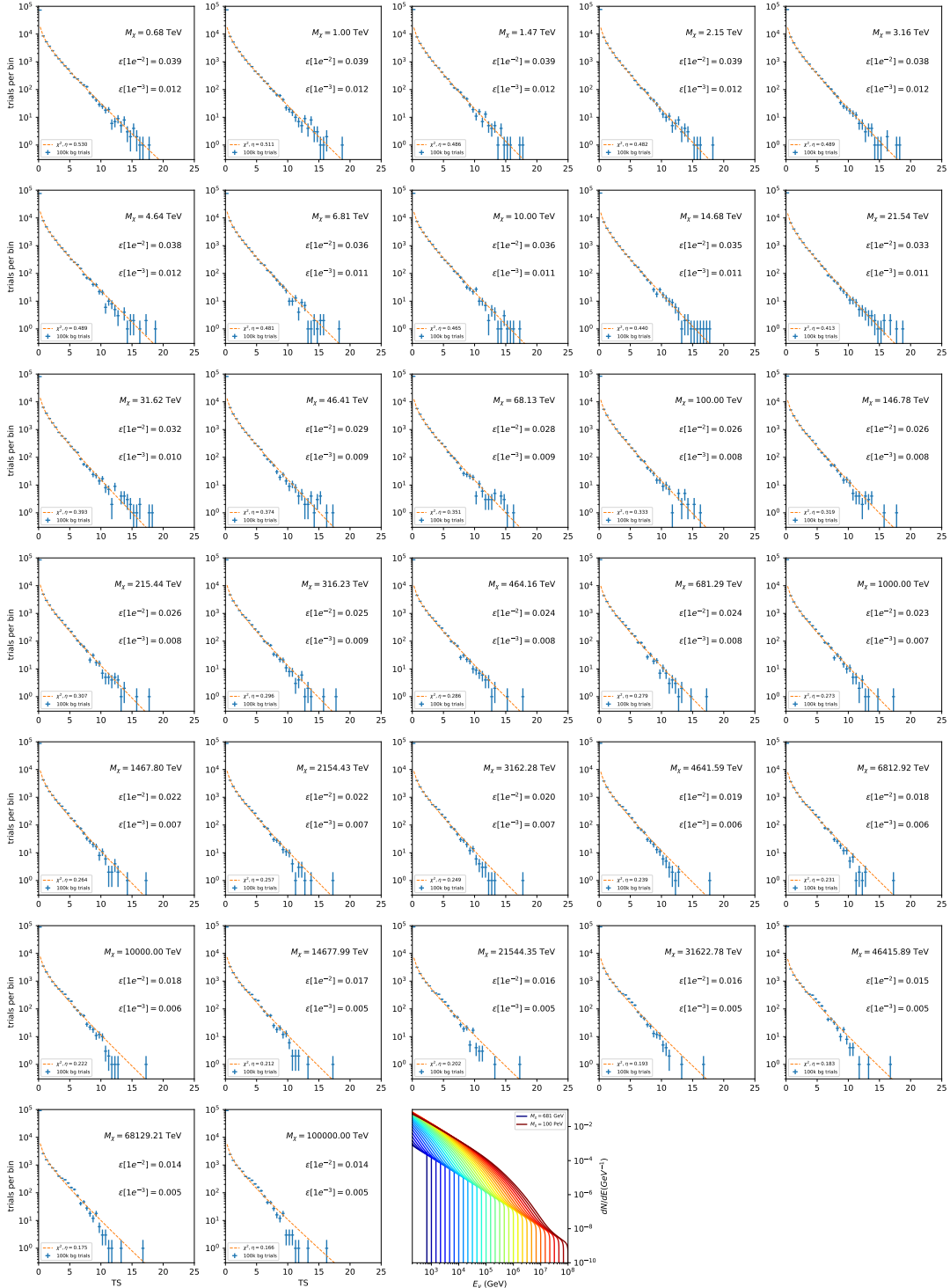


Figure 6.19 Same as Fig. 6.6 for 15, GS J-factor, stacked sources and  $\chi\chi \rightarrow W^+W^-$ .

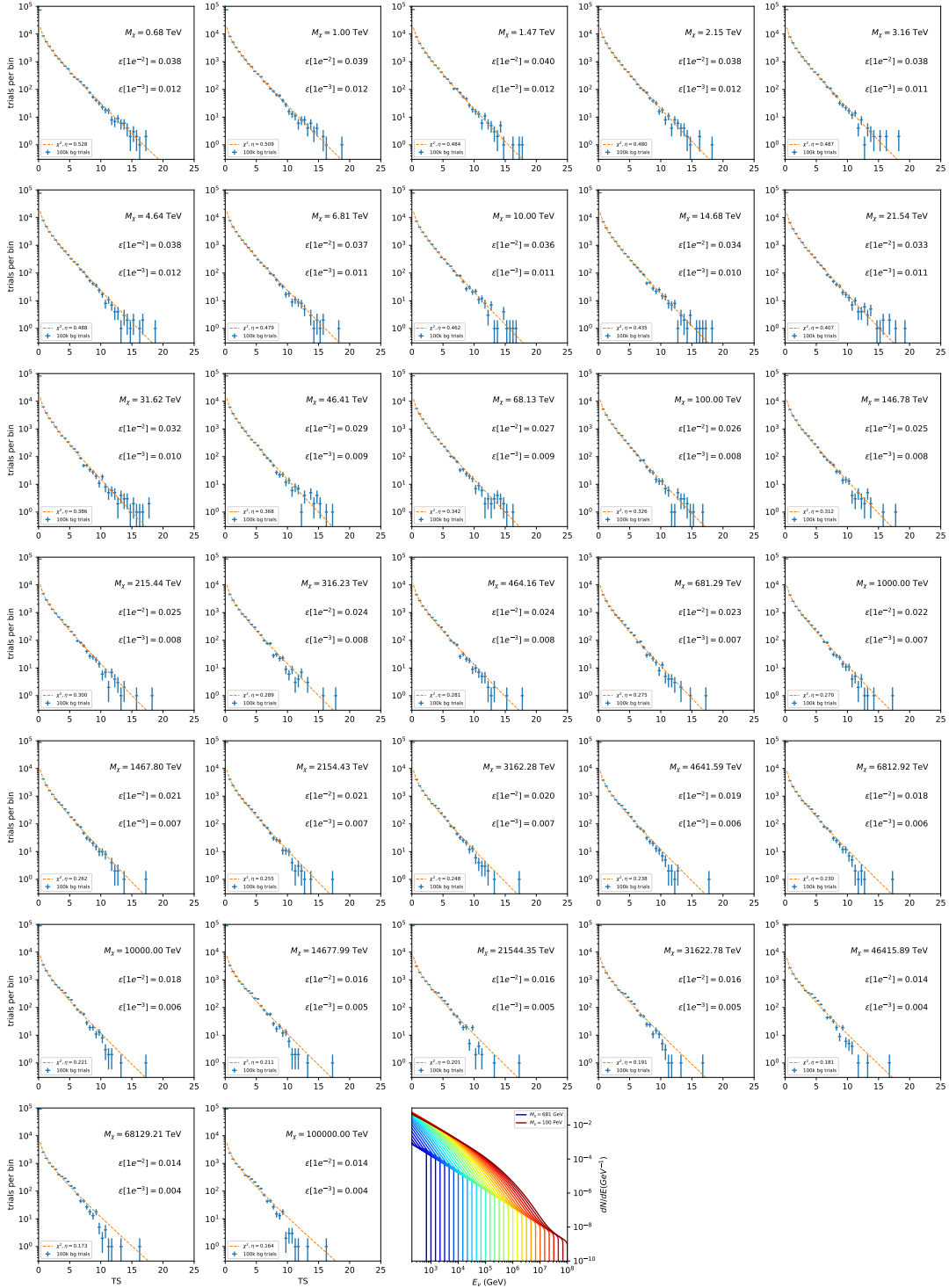


Figure 6.20 Same as Fig. 6.6 for 15,  $\mathcal{GS}$  J-factor, stacked sources and  $\chi\chi \rightarrow ZZ$ .

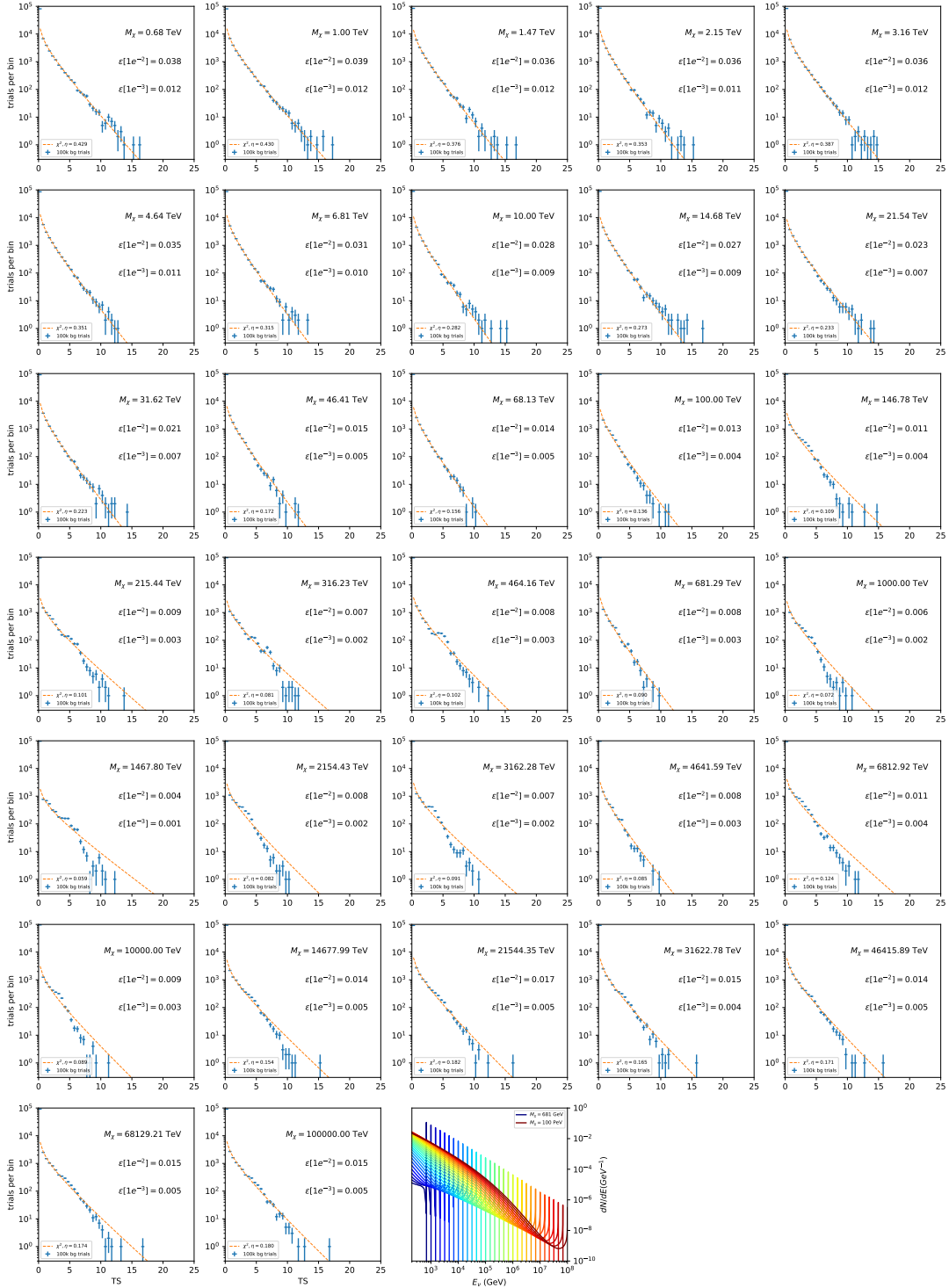


Figure 6.21 Same as Fig. 6.6 for 15, GS J-factor, stacked sources and  $\chi\chi \rightarrow \nu_e \bar{\nu}_e$ .

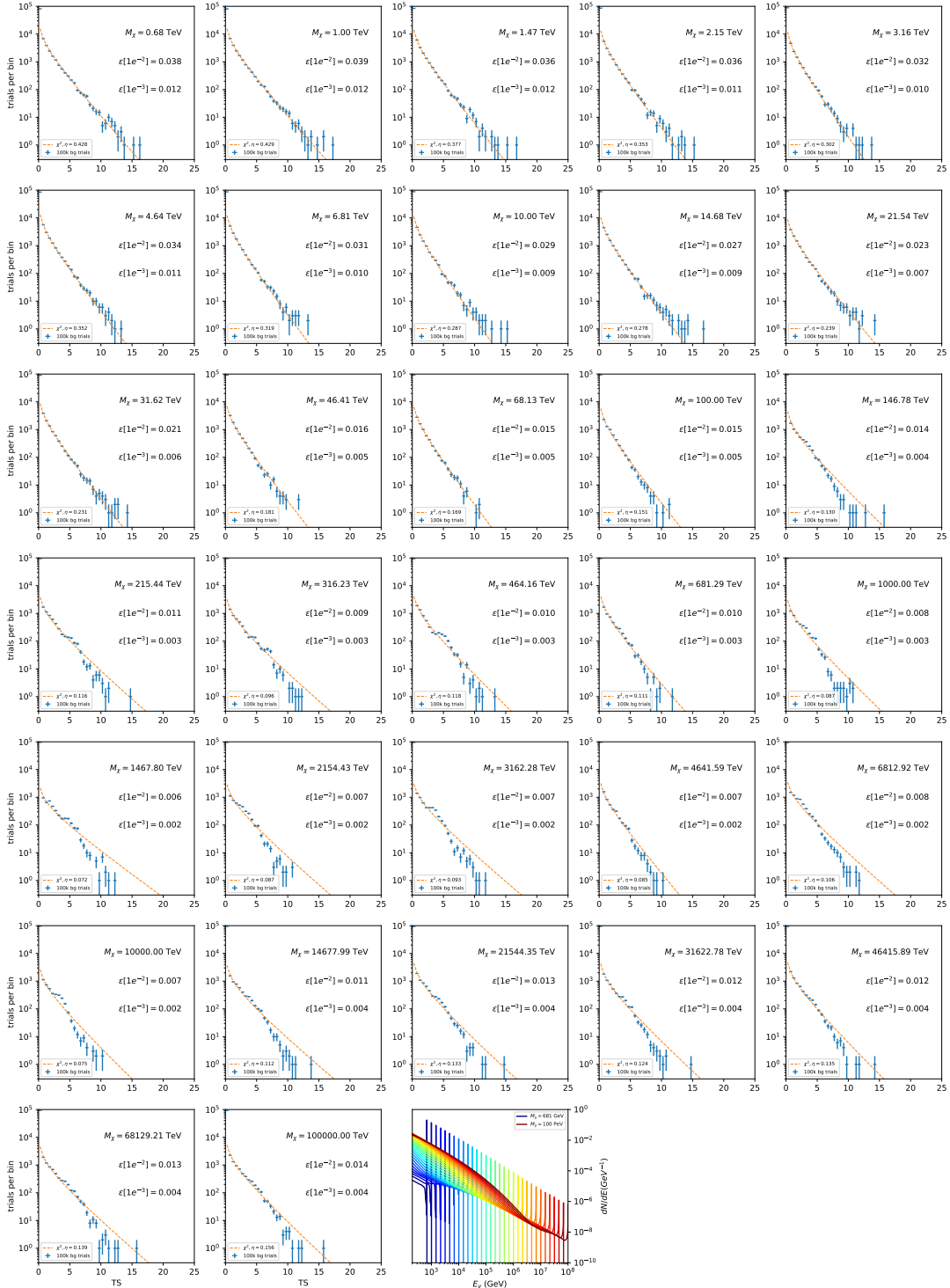


Figure 6.22 Same as Fig. 6.6 for 15, GS J-factor, stacked sources and  $\chi\chi \rightarrow \nu_\mu \bar{\nu}_\mu$ .

### 6.5.1 TS per Source

Figure 6.6 to Figure 6.11 present the TS distributions for Segue 1 and Ursa Major II for 100,000 trials. More studies for all annihilation channels and remaining 13 sources were also performed and are documented in IceCube’s internal wiki.

Almost every distribution produced follows a  $\chi^2$  distribution with 1 degree of freedom. This is more true for low  $m_\chi$  than high  $m_\chi$  models. These observations are important for future assumptions made in Sec. 7 and may justify statistical calculations assuming our test statistics follow a  $\chi^2$  with 1 degree of freedom.

### 6.5.2 Stacked TS

Figure 6.12 to Figure 6.22 present the TS distributions for a stacked study of 15 sources with  $GS$   $J$ -factors on 100,000 trials. The presentation of these plots are identical to the single source distributions in Section 6.5.1. We see similar behaviour in the stacked TS distributions compared to the single source studies.

## 6.6 Signal Recovery

We also wish to understand how well the analysis is able to reconstruct signal neutrinos. In order to test this, we inject neutrinos from our spectral models randomly then attempt to discern the number of signal neutrinos in the simulated data. Figure 6.23 and Figure 6.24 show this study for  $\chi\chi \rightarrow b\bar{b}$ ,  $t\bar{t}$ , and  $\nu_\mu\bar{\nu}_\mu$  for a stacked analysis of 15 sources. Figure C.3 to Figure C.8 show identical studies for Segue 1 and Ursa Major II. We see that the analysis is conservative at smaller  $m_\chi$ , yet improves at larger  $m_\chi$ . We also see that the uncertainty is small for the neutrino annihilation spectra, and the uncertainty is larger for softer channels like  $b\bar{b}$ .

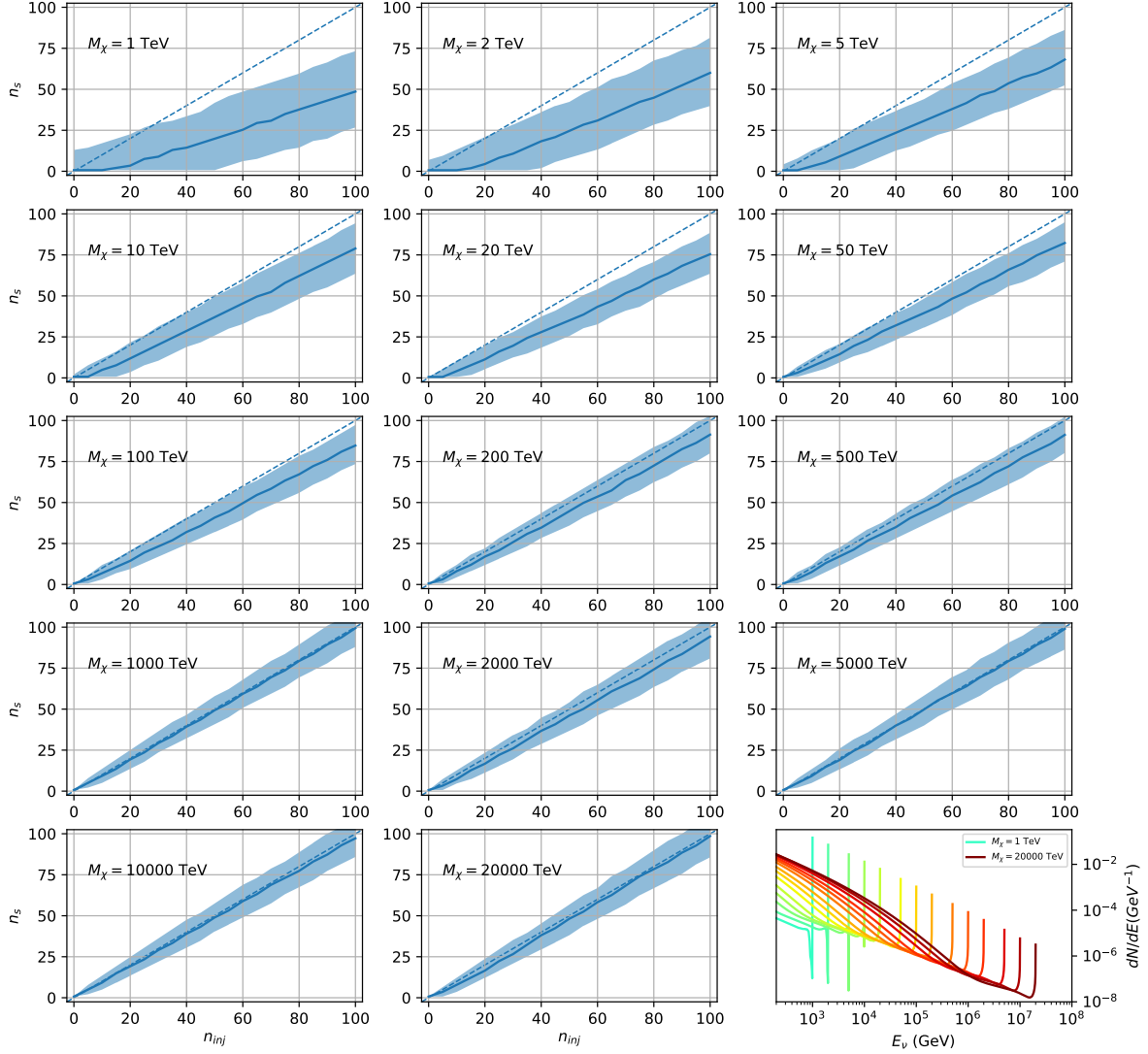


Figure 6.23 Signal Recovery study for an analysis with 15 stacked sources using the  $\mathcal{GS}$   $J$ -factors [59]. Above shows 14 studies for DM mass ranging between 1 TeV and 20 PeV for  $\chi\chi \rightarrow \mu_\mu\bar{\mu}_\mu$ . The bottom right subplot features every spectral model used as input for the remaining subplots. The remaining subplots show  $n_{inj}$  as the number of signal events injected into background simulation. Whereas,  $n_s$  is the number of signal events recovered from analyzing the injected simulation. Blue line represents the median values of 100 simulations. Light blue bands show the  $1\sigma$  statistical uncertainty around the median.

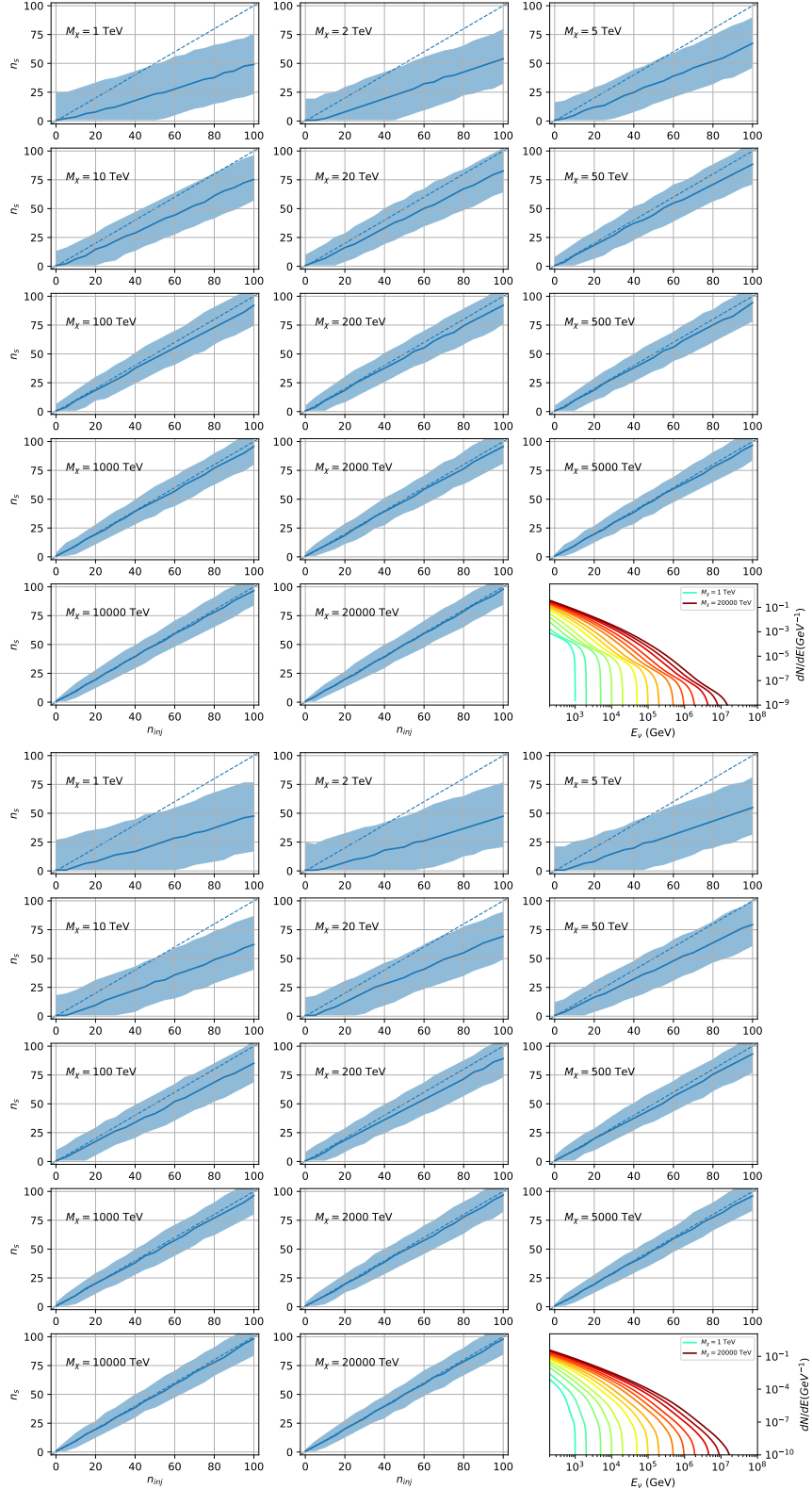


Figure 6.24 Same as Fig. 6.23 but for  $\chi\chi \rightarrow t\bar{t}$  (top) and  $b\bar{b}$  (bottom).

### 6.6.1 Sensitivities

In IceCube, we usually define the 90% confidence level (CL), as the minimum number of signal events ( $n_s$ ) required to have a Type I error rate smaller than 0.5 and Type II error rate of 0.1. We compute  $n_s$  from the following equation

$$n_s = T_{\text{live}} \int_0^{\Delta\Omega} d\Omega \int_{E_{\min}}^{E_{\max}} dE_\nu A_{\text{eff}}(\hat{n}, E_\nu) \frac{d\Phi_\nu}{d\Omega dE_\nu}(\hat{n}, E_\nu), \quad (6.8)$$

to extract the sensitivity on the dark matter velocity-weighted annihilation cross-section,  $\langle\sigma v\rangle$ .  $T_{\text{live}}$  is the detector live time,  $A_{\text{eff}}$  is the effective area of the detector, and  $E_{\min}$ ,  $E_{\max}$  are the minimum, maximum energies of the expected neutrinos, respectively.

Sensitivities are calculated for each source individually as if they were the only source and as a stack over 1000 trials. From Eq. (6.8) and Eq. (6.1) we can compute the  $\langle\sigma v\rangle$  at a 90% confidence level. Figure 6.26 and Fig. 6.25 show the sensitivities for some DM annihilation channels. Not all channels computed successfully in time for the writing of this dissertation. Among channels missing include the charged leptons:  $e$  and  $\tau$ .

## 6.7 Systematics

The current analysis plan is to compare these sensitivities to another  $J$ -factor catalog such as  $\mathcal{LS}$  [80] although this was not completed in time for this dissertation. Additionally, we set out to perform a standard suite of IceCube systematic studies which include: DOM efficiency, Hole ice, ice absorption, and photon scattering. We do study Earth attenuation, and Section 6.7.1 enumerates the impact of the Earth on our hardest neutrino spectra.

### 6.7.1 Earth Effects

We look to quantify the impact of the Earth on our sensitivity to  $\chi\chi \rightarrow \nu_\mu \bar{\nu}_\mu$ . This channel is expected to be among the significantly impacted annihilation channels because it has a significant contribution at PeV energies for  $m_\chi \geq 1\text{PeV}$ . The Earth is expected to attenuate these higher energy neutrinos. However, these neutrino spectra have significant low energy contributions, so we do not expect to entirely lose our sensitivity. This motivated a study examining our  $\langle\sigma v\rangle$  sensitivity over all DM masses sampled for a selection of declinations.

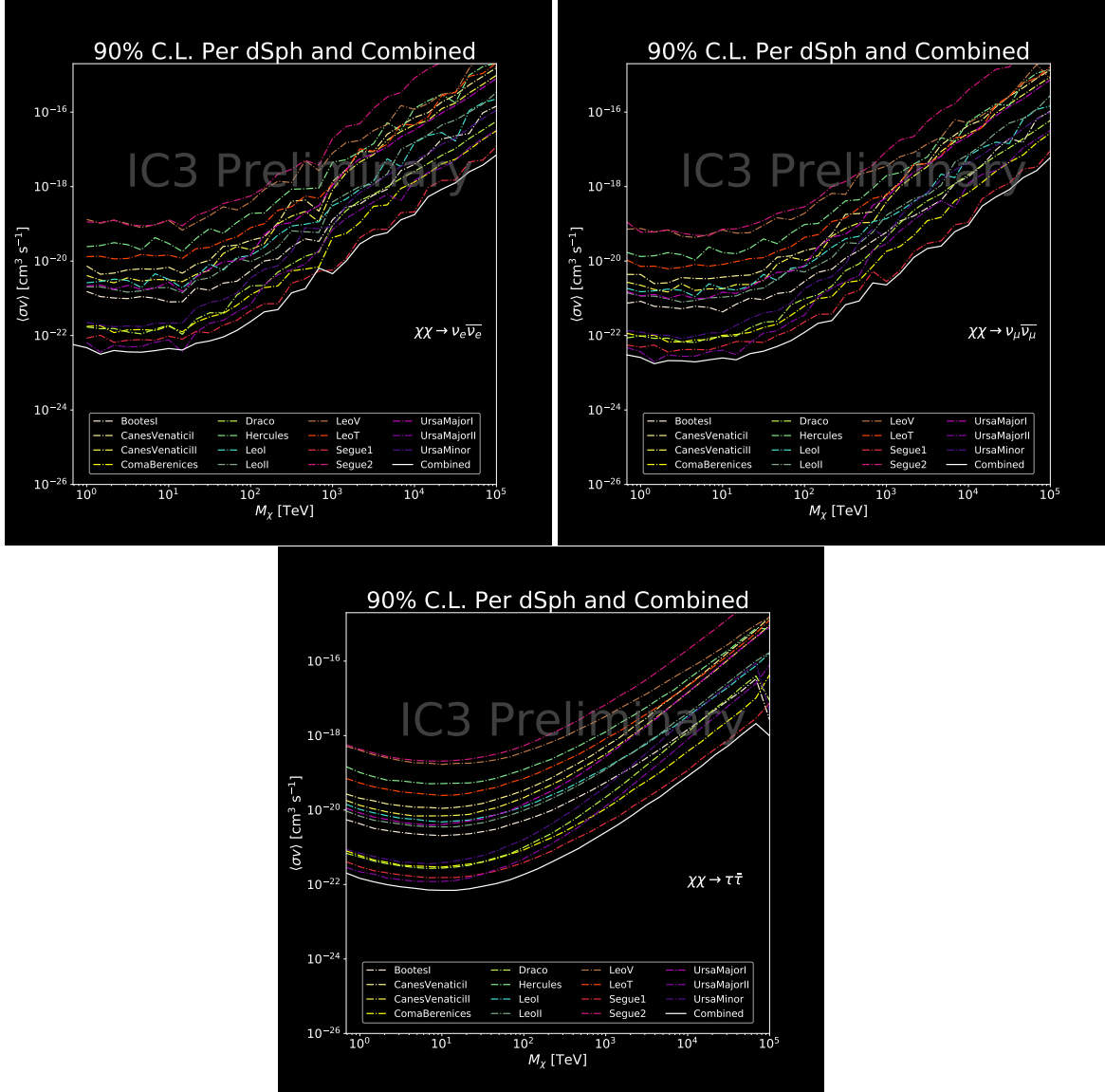


Figure 6.25 IceCube North Sky Track Sensitivities. Each panel shows sensitivity curves for various DM annihilation channels. Sensitivities are for the velocity-weighted cross-section  $\langle\sigma v\rangle$  versus  $m_\chi$ . Dotted, colored lines are sensitivities for individual sources. Solid white lines are for the combined sensitivity of all 15  $\mathcal{GS}$  sources used in this study.

For this systematic study, I sample 6 DM masses per decade from 681 GeV to 100 PeV. I select declinations that are shared with sources in the  $\mathcal{GS}$  catalog: Boötes I, Canes Venatici II, Leo V, Ursa Major I, and Ursa Minor. I study a fake source who's  $J$ -factor is shared with Ursa Major II, but who's coordinates belong to the aforementioned list. The sensitivity studies performed for each source (Fig. 6.25 and Section C.5) provided  $n_s$  for 1000 trials which we extracted from Eq. (6.8). We derive  $\langle\sigma v\rangle$  using  $\log_{10} J = 19.42 \log_{10}(\text{GeV}^2 \text{cm}^{-5})$ . Figure 6.28 shows the results.

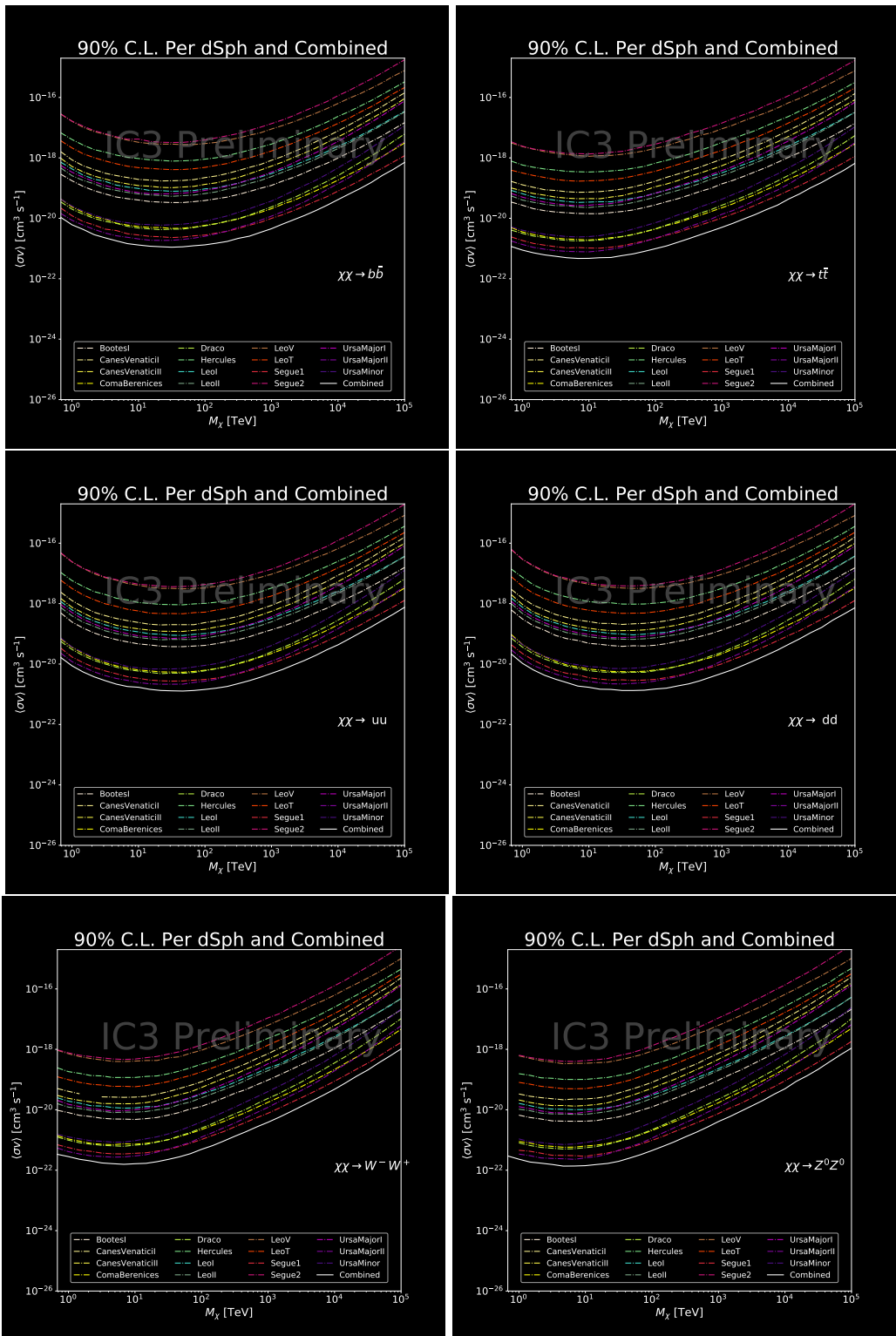


Figure 6.26 Same as Fig. 6.25 for three additional DM annihilation channels.

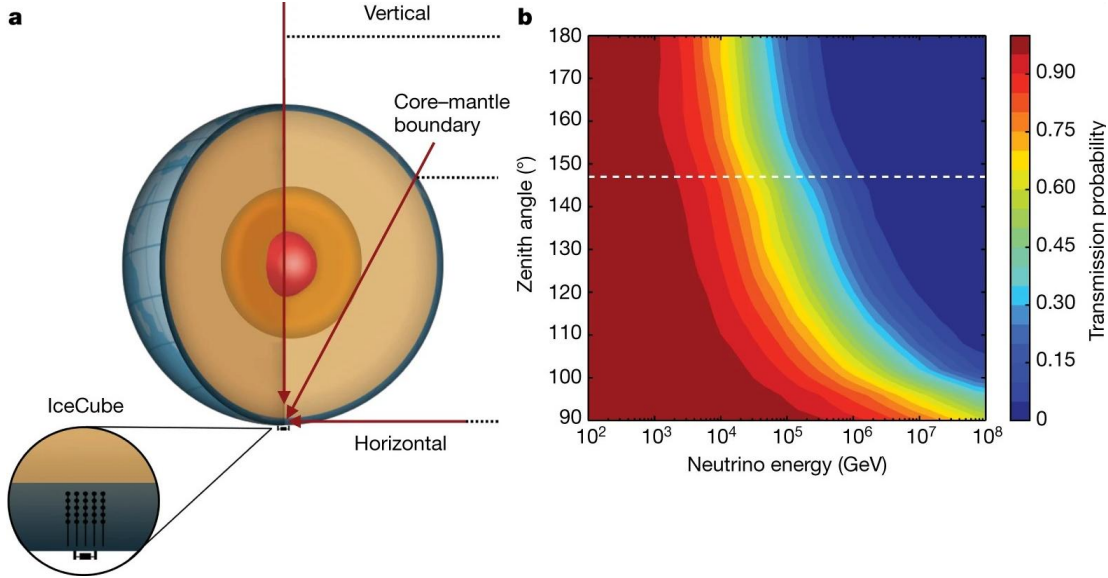


Figure 6.27 Panel A: Neutrino's from the Northern sky and incident on the IceCube detector will travel through the Earth. How much of the Earth these neutrinos travels is a function of zenith from the vertical axis. Panel B: SM prediction of neutrino transmission probabilities for neutrinos arriving at  $90^\circ - 180^\circ$  zenith and with 100 GeV to 100 PeV energies. High-energy neutrinos traversing the whole Earth are completely absorbed, whereas low-energy neutrinos pass through unimpeded. Neutrinos coming from above the horizon will arrive unimpeded for all neutrino energies. Figure pulled from [102].

Figure 6.28 shows that we have significant but diminishing sensitivity to sources at high declination. We see in the worse case, the sensitivity at high declination is up to an order of magnitude worse than at low declination. However, for  $m_\chi < 1$  PeV, the sensitivities are very similar. The comparable sensitivities imply that a stacking analysis with IceCube is most powerful in the 500 GeV to 1 PeV region. Above 1 PeV, our limits and sensitivities are dominated by sources near the horizon. When we additionally consider the  $J$ -factors, we expect Segue 1 to dominate contributions to sensitivity and limits where  $m_\chi > 1$  PeV.

## 6.8 Conclusions

We utilized advanced computing techniques like parallel programming and spline fitting of particle physics Monte Carlo to greatly expand and refine IceCube's sensitivity to DM annihilation from dSphs. Furthermore, we imported updated astrophysical and particle physics models that better represent what we believe neutrino signals from DM annihilation should look like. We, for the first time, build an analysis that is sensitive to PeV DM annihilation.

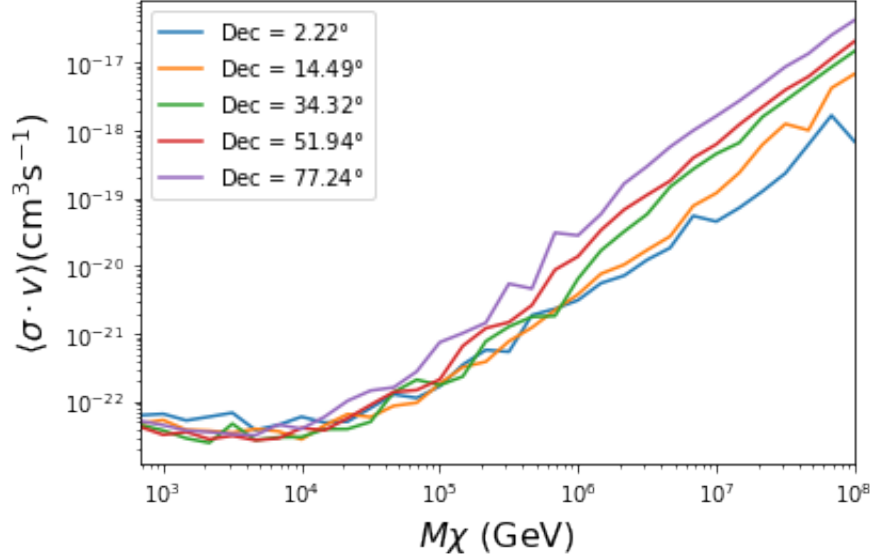


Figure 6.28  $\langle \sigma v \rangle$  sensitivities for 5 imaginary sources with  $\log_{10} J = 19.42$   $\log_{10}(\text{GeV}^2 \text{cm}^{-5})$ . Each imaginary source shares a declination with a source in Tab. 3.1

When we compare to previous IceCube publications of dSphs [93], we see an order of magnitude improvement to our sensitivity. This analysis has been working group approved within IceCube and is currently under collaboration review before unblinding. These processes did not complete in time for this dissertation. Therefore we do not show data for this thesis and is the clear next step.

The test statistic distributions in this analysis also demonstrate more characteristic behavior compared to previous DM analyses [97, 101]. With a 10-year dataset, we finally have enough statistics to almost trivially combine with other photon observatories, such as HAWC. The first groundwork for a multi-messenger DM search is provided with concluding remarks in chapter 7.

## CHAPTER 7

### NU DUCK: CONCLUSIONS AND FUTURE DIRECTIONS

#### 7.1 Conclusions

This dissertation, "Leveraging Multi-Messenger Astrophysics for Dark Matter Searches," advances our quest to understand dark matter. We used gamma-ray and neutrino observatories alongside advanced computational techniques. Our goal was to enhance the search for dark matter within the universe.

The Glory Duck project was a key part of this work. It involved a multi-instrument analysis using gamma-ray telescopes. These included Fermi-LAT, H.E.S.S., MAGIC, VERITAS, and HAWC. They focused on 20 dwarf spheroidal galaxies (dSphs). The aim was to detect dark matter annihilation signals. Although we found no significant deviations from the null hypothesis, we greatly improved search sensitivity. We set stringent upper limits on the annihilation cross-section for dark matter candidates. This effort represents a major advance, offering the most comprehensive constraints for WIMP dark matter search to date.

Our exploration of multithreading techniques in HAWC analyses showed the benefits of computational methods. By accelerating analysis time, we enhanced the efficiency of dark matter searches. This approach has set the stage for more ambitious studies. It highlights the importance of computational innovation in addressing astrophysical challenges.

Furthermore, our work with IceCube's North Sky Track Data has broken new ground. It aimed at detecting heavy dark matter annihilation. We used parallel programming and spline fitting to improve IceCube's sensitivity. This analysis is a step towards probing dark matter annihilation up to the PeV scale. It demonstrates a significant sensitivity improvement compared to previous efforts. The groundwork laid here is a strong foundation for future discoveries.

This dissertation highlights the potential of multi-messenger astrophysics and computational innovation in dark matter searches. Each analysis has contributed to our understanding and capabilities. Together, they showcase a progressive approach to astrophysical research. By integrating observations and using the latest computational techniques, we have expanded our capabilities. We

have also charted a path for future dark matter searches.

Looking back, it's clear that our journey through the dark universe is far from complete. The methods developed and findings reported here significantly contribute to the astrophysical community. They set the stage for future multi-messenger observations and analyses. In this pursuit, the challenges we face and the questions we seek to answer drive us forward. They fuel the continuous evolution of our search for dark matter.

## 7.2 Future Directions: Multi-Messenger Dark Matter Search

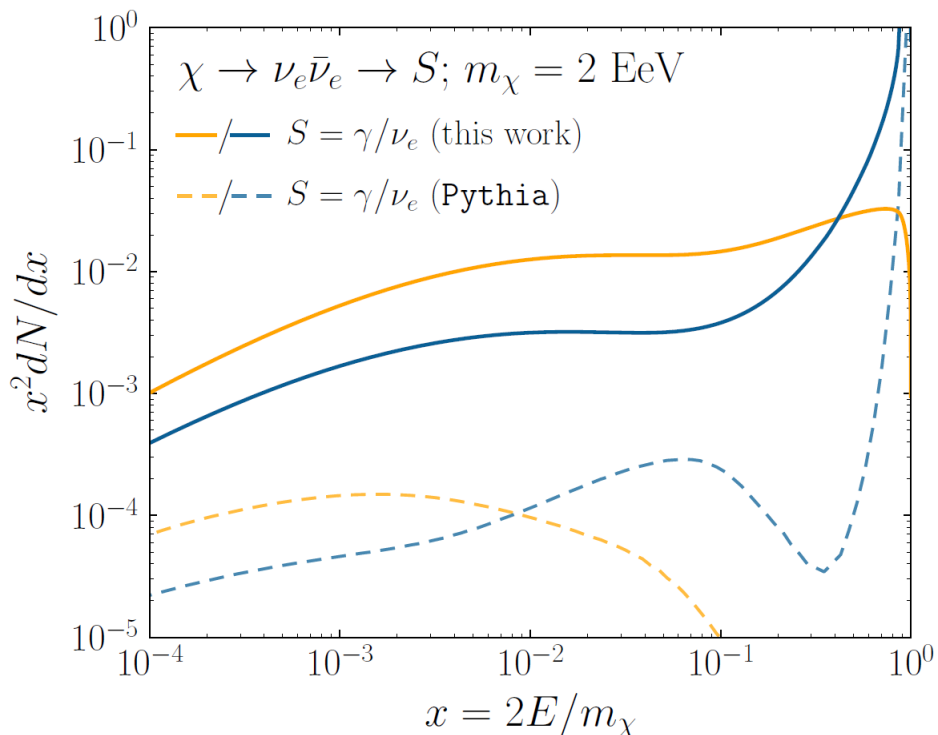


Figure 7.1 The prompt electron neutrino and photon spectrum resulting from the decay of a 2EeV DM particle to  $\nu_e\bar{\nu}_e$ , as currently being searched for at IceCube [5]. Solid curves represent the results of this work, and predict orders of magnitude more flux at certain energies than the dashed results of Pythia 8.2, one of the only existing methods to generate spectra at these masses. In both cases energy conservation is satisfied: there is a considerable contribution to a  $\delta$ -function at  $x = 1$ , associated with events where an initial W or Z was never emitted and thus no subsequent shower developed. Large disagreements are generically observed at these masses for electroweak dominated channels, while the agreement is better for colored initial SM states.

As I have shown previously in Sec. 3 and Sec. 4, we can build a fast and robust analysis that shares tools with the field. The hope being that IceCube can eventually combine data with

gamma-ray observatories.



Figure 7.2 TODO: neutrino and bb plot with nu Sensitivities[NEEDS A SOURCE][FACT CHECK THIS]

## APPENDIX A

### MULTI-EXPERIMENT SUPPLEMENTARY FIGURES

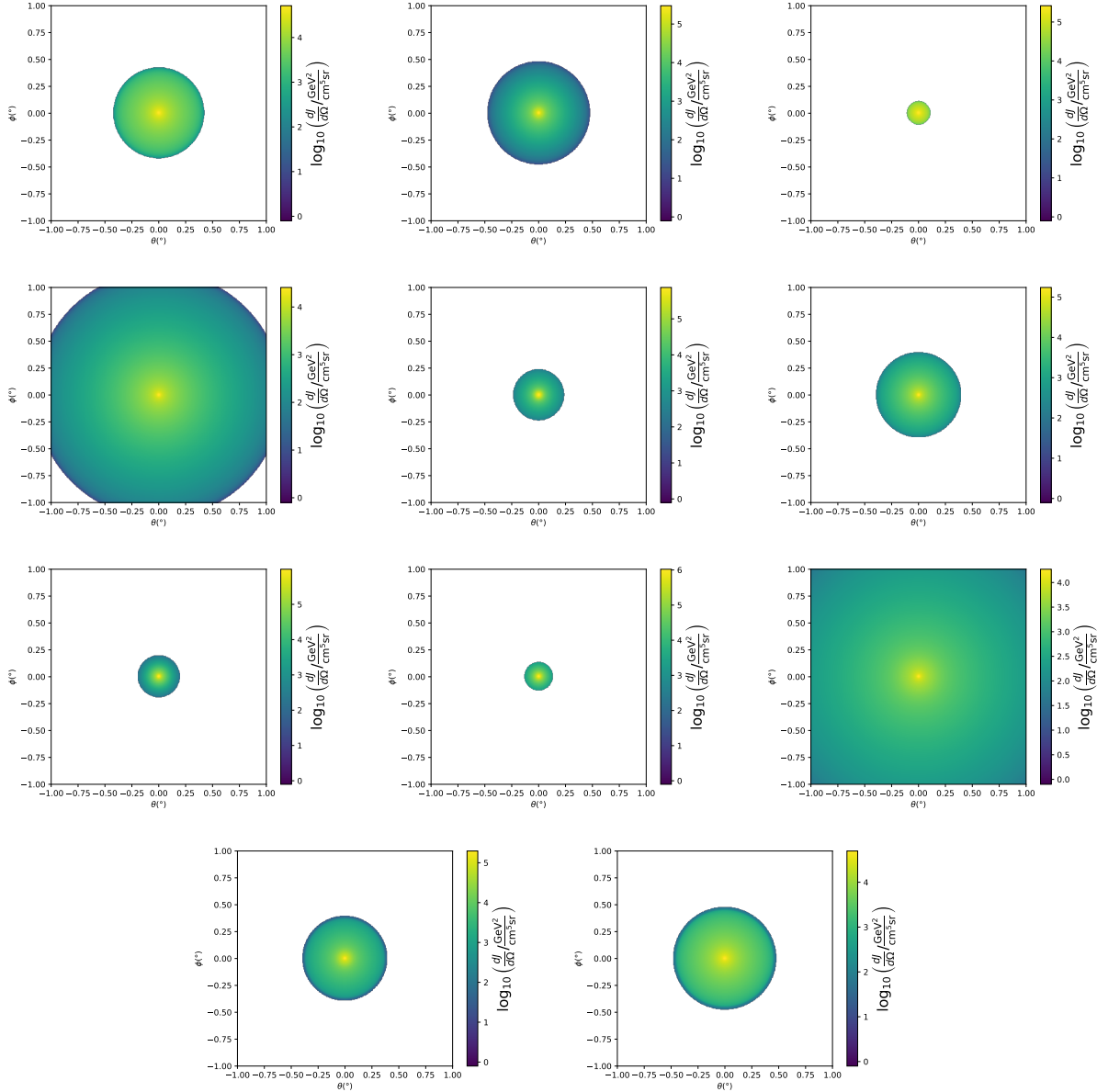


Figure A.1 Sister figure to Figure 3.3. Sources in the first row from left to right: Bootes I, Canes Venatici I, II. In second row: Draco, Hercules, Leo I. In the first row: Leo II, Leo IV, Sextans. In the final row: Ursa Major I, Ursa Major II.

## APPENDIX B

### MULTITHREADING DARK MATTER ANALYSES SUPPLEMENTARY MATERIAL

#### B.1 Remaining Spectral Models

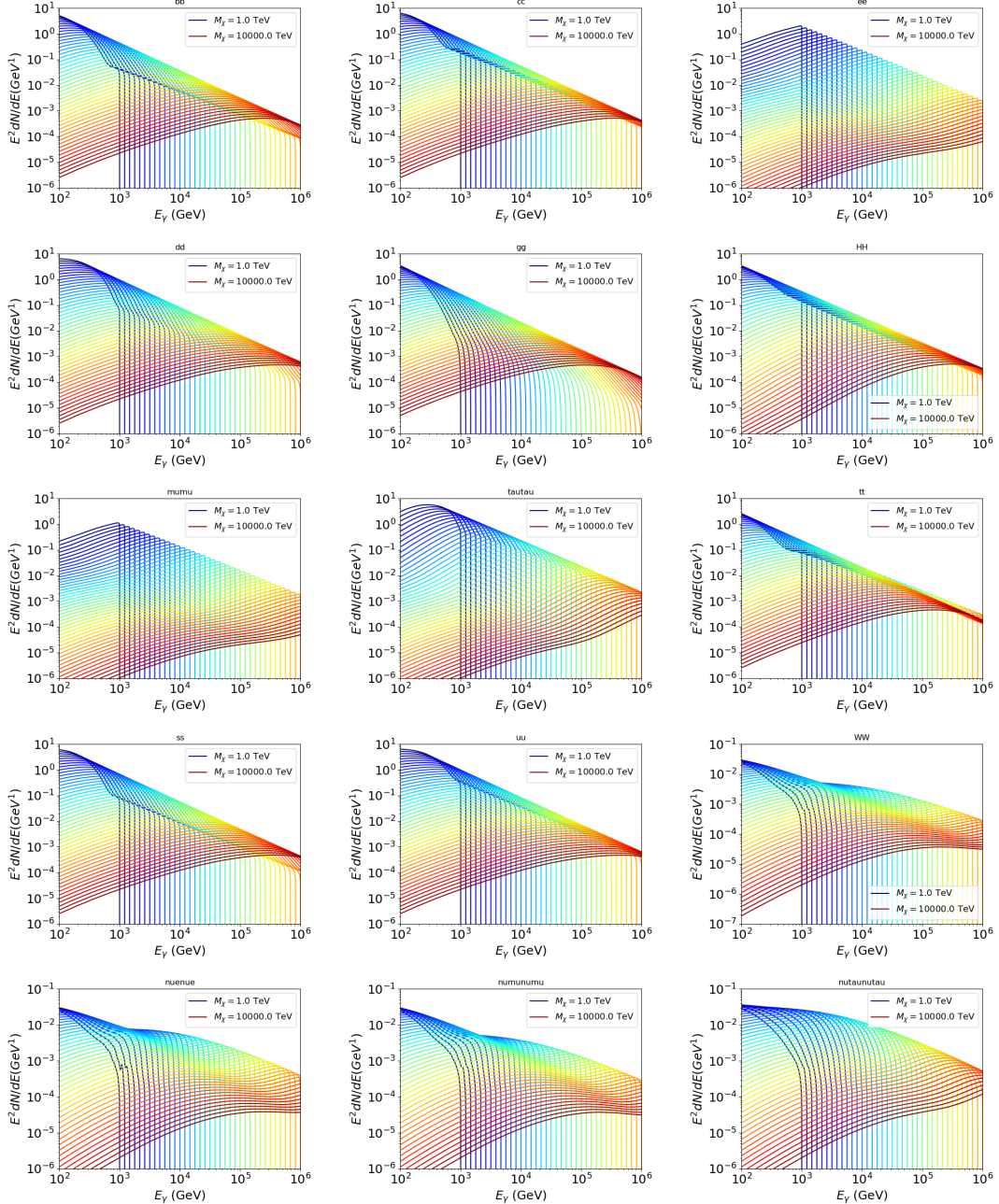


Figure B.1 Sister figure to Figure 4.2 for remaining SM primary annihilation channels studied for this thesis. These did not require any post generation smoothing and so are directly pulled from [79] with a binning scheme most helpful for a HAWC analysis.

## B.2 mpu\_analysis.py

```
1 import warnings
2 with warnings.catch_warnings():
3     warnings.simplefilter("ignore")
4 # Python base libraries
5 import os
6 import sys
7 import time
8 # Import general libraries with namespace
9 import matplotlib
10 # Necessary for computing on cluster
11 matplotlib.use("agg")
12 import numpy as np
13 import multiprocessing as mp
14 # Import HAWC software
15 sys.path.insert(1, os.path.join(os.environ['HOME'], 'hawc_software', 'threeML-
    analysis-scripts', 'fitModel'))
16 from analysis_modules import *
17 from threeML import *
18 from hawc_hal import HAL, HealpixConeROI
19 from threeML.minimizer.minimization import FitFailed
20 # Import Dark Matter HAWC Libraries
21 import analysis_utils as au
22 import spectra as spec
23 import sources as srcs
24
25 #* READ ONLY PATHS This block will change eventually
26 MASS_LIST = './plotting/studies/nd/masses.txt'
27 CHAN_LIST = './plotting/studies/nd/chans.txt'
28
29 #* WRITE PATHS, default location is to scratch
30 OUT_PATH = os.path.join(os.environ["SCRATCH"], os.environ["USER"], 'New_duck')
```

```

31 print('Our out path is going to be {}'.format(OUT_PATH))
32
33 # Define parallel Function. Can also be run serially
34 def some_mass_fit(sigVs, datalist, shape, dSph, jfactor, mass_chan,
35                     progress=None, log_file='', queue=None, i_job=0):
36
37     if progress is None:
38         progress = [0]
39     else: # Create log files for each thread
40         log_file = log_file.replace('.log', '_ThreadNo_')
41         log_file = log_file + str(i_job) + ".log"
42         sys.stdout = open(log_file, "w")
43
44     fits = []
45
46     try:
47         for m_c in mass_chan:
48             print(f'Mass chan tuple: {m_c}')
49             mass = int(m_c[0])
50             ch = m_c[1]
51             # Build path to output files
52             outPath = os.path.join(OUT_PATH, ch, dSph)
53             au.ut.ensure_dir(outPath)
54
55             if progress[i_job] < 0:
56                 # If the master gets a Keyboard interrupt, commit suicide.
57                 break
58
59             ### Start Model Building for DM mass and SM channel #####
60             spectrum = spec.DM_models.HDMSpectra()
61             spectrum.set_channel(ch)
62
63             myDwarf = ExtendedSource(dSph, spatial_shape=shape,

```

```

64                     spectral_shape=spectrum)

65

66 spectrum.J = jfactor * u.GeV**2 / u.cm**5
67 spectrum.sigmav = 1e-24 * u.cm**3 / u.s
68 spectrum.set_dm_mass(mass * u.GeV)

69

70 spectrum.sigmav.bounds = (1e-30,1e-12)
71 model = Model(myDwarf)
72 ##### End model Building #####
73
74 jl = JointLikelihood(model,datalist,verbose=False)
75
76 try:
77     result, lhdf = jl.fit(compute_covariance=False)
78     ts = -2.* (jl.minus_log_like_profile(1e-30) - jl.
79     _current_minimum)
80
81     # Also profile the LLH vs sv
82     ll = jl.get_contours(spectrum.sigmav, sigVs[0],
83                           sigVs[-1], len(sigVs),
84                           progress=False, log=['False'])
85
86     sigv_ll = au.ut.calc_95_from_profile(ll[0], ll[2])
87
88     # Write results to file
89     outFileLL = outPath+f"/LL_{dSph}_{ch}_mass{int(mass)}_GD.txt"
90     np.savetxt(outFileLL, (sigVs, ll[2]),
91                delimiter='\t', header='sigV\tLL\n')
92
93     with open(outPath+f"/results_{dSph}_{ch}_mass{int(mass)}_GD.
94     txt", "w") as results_file:
95         results_file.write("mDM [GeV]\tsigV_95\tsigV_B.F.\n")
96
97         results_file.write("%i\t%.5E\t%.5E\t%.5E"%(mass, sigv_ll,
98                               ts, result.value[0]))

```

```

95         # End write to file
96
97     except FitFailed: # Don't kill all threads if a fit fails
98         print("Fit failed. Go back and calculate this spectral model
99             later")
100
101
102     fits.append((ch, mass, -1, -1))
103
104     with open(log_file+'.fail', 'w') as f_file:
105         f_file.write(f'{ch}, {mass}\n')
106
107     progress[i_job] += 1
108
109     matplotlib.pyplot.close() # Prevent leaky memory
110
111
112     fits.append((ch, mass, result.value[0], ts))
113     progress[i_job] += 1
114
115     matplotlib.pyplot.close()
116
117 except KeyboardInterrupt:
118     progress[i_job] = -1
119
120
121     fits = np.array(fits)
122
123     if queue is None:
124
125         return fits
126
127     else:
128
129         queue.put((i_job, fits))
130
131
132 def main(args):
133
134     masses = np.loadtxt(MASS_LIST, dtype=int)
135
136     chans = np.loadtxt(CHAN_LIST, delimiter=',', dtype=str)
137
138     mass_chan = au.ut.permute_lists(chans, masses)
139
140
141     print(f"DM masses for this study are: {masses}")
142     print(f"SM Channels for this study are XX -> {chans}")
143     print(mass_chan)
144
145
146     # extract information from input argument

```

```

127 dSph = args.dSph
128 data_mngr = au.ut.Data_Selector('P5_NN_2D')
129 dm_profile = srcts.Spatial_DM(args.catalog, dSph, args.sigma, args.decay)
130
131     ### Extract Source Information ####
132 if dm_profile.get_dec() < -22.0 or dm_profile.get_dec() > 62.0:
133     raise ValueError("HAWC can't see this source D: Exitting now...")
134
135 print(f'{dSph} information')
136 print(f'jfacc: {dm_profile.get_factor()}\tRA: {dm_profile.get_ra()}\tDec: {dm_profile.get_dec()}\n')
137
138 shape = SpatialTemplate_2D(fits_file=dm_profile.get_src_fits())
139     ### Finish Extract Source Information ####
140
141     ### LOAD HAWC DATA ####
142 roi = HealpixConeROI(data_radius=2.0, model_radius=8.0,
143                         ra=dm_profile.get_ra(), dec=dm_profile.get_dec())
144 bins = choose_bins.analysis_bins(args, dec=dm_profile.get_dec())
145
146 hawc = HAL(dSph, data_mngr.get_datmap(), data_mngr.get_detres(), roi)
147 hawc.set_active_measurements(bin_list=bins)
148 datalist = DataList(hawc)
149     ### FINISH LOAD HAWC DATA ####
150
151 # set up SigV sampling. This sample is somewhat standardized
152 sigVs = np.logspace(-28,-18, 1001, endpoint=True) # NOTE This will change
153 whith HDM
154
155 if args.n_threads == 1:
156     # No need to start || programming just iterate over the masses
157     kw_arg = dict(sigVs=sigVs, datalist=datalist, shape=shape, dSph=dSph,
158                   jfactor=dm_profile.get_factor(), mass_chan=mass_chan,

```

```

158                 log_file=args.log)
159             some_mass_fit(**kw_arg)
160         else:
161             # I Really want to suppress TQMD output
162             from tqdm import tqdm
163             from functools import partialmethod
164             tqdm.__init__ = partialmethod(tqdm.__init__, disable=True)
165
166             x = np.array_split(mass_chan, args.n_threads)
167             n_jobs = len(x)
168
169             print("Thread jobs summary by mass and SM channel")
170             for xi in x:
171                 print(f'{xi}')
172
173             queue = mp.Queue()
174             progress = mp.Array('i', np.zeros(n_jobs, dtype=int))
175
176             # Define task pool that will be split amongsts threads
177             kw_args = [dict(sigVs=sigVs, datalist=datalist, shape=shape,
178                             dSph=dSph, jfactor=dm_profile.get_factor(),
179                             mass_chan=mass_chan, progress=progress,
180                             queue=queue, i_job=i, log_file=args.log)
181                         for i, mass_chan in enumerate(x)]
182
183             # Define each process
184             procs = [mp.Process(target=some_mass_fit, kwargs=kw_args[i]) \
185                     for i in range(n_jobs)]
186
187             ### Start MASTER Thread only code block ###
188             # Begin running all child threads
189             for proc in procs: proc.start()
190

```

```

191     try:
192
193         # In this case, the master does nothing except monitor progress of
194         # the threads
195
196         # In an ideal world, the master thread also does some computation.
197         n_complete = np.sum(progress)
198
199         while_count = 0
200
201
202         while n_complete < len(mass_chan):
203
204             if np.any(np.asarray(progress) < 0):
205
206                 # This was no threads are stranded when killing the script
207                 raise KeyboardInterrupt()
208
209             if while_count%1000 == 0:
210
211                 print(f'{np.sum(progress)} of {len(mass_chan)} finished')
212
213             n_complete = np.sum(progress)
214
215             time.sleep(.25)
216
217             while_count += 1
218
219
220         except KeyboardInterrupt:
221
222             # signal to jobs that it's time to stop
223
224             for i in range(n_jobs):
225
226                 progress[i] = -2
227
228                 print('\nKeyboardInterrupt: terminating early.')
229
230             ### End MASTER Thread only code block ###
231
232
233             fitss = [queue.get() for proc in procs]
234
235             print(fitss)
236
237             print(f'Thread statuses: {progress[:]}')
238
239
240             # putting results in a file
241
242
243             print("QUACK! All Done!")

```

```

223
224
225 if __name__ == '__main__':
226     import argparse
227
228     p = argparse.ArgumentParser(description="Run a DM annihilation analysis on
229         a dwarf spheroidal for a specific SM channel for DM masses [1 TeV to 10
230         PeV]")
231
232     # Dwarf spatial modeling arguements
233     p.add_argument("-ds", "--dSph", type=str,
234                   help="dwarf spheroidal galaxy to be studied", required=
235             True)
236
237     p.add_argument("-cat", "--catalog", type=str, choices=['GS15', 'LS20'],
238                   default='LS20', help="source catalog used")
239
240     p.add_argument("-sig", "--sigma", type=int, choices=[-1, 0, 1], default=0,
241                   help="Spatial model uncertainty. 0 corresponds to the
242             median. +/-1 correspond to the +/-1sigma uncertainty respectively.")
243
244     # Arguements for the energy estimators
245     p.add_argument("-e", "--estimator", type=str,
246                   choices=['P5_NHIT', 'P5_NN_2D'],
247                   default="P5_NN_2D", required=False,
248                   help="The energy estimator choice. Options are: P5_NHIT,
249             P5_NN_2D. GP not supported (yet).")
250
251     p.add_argument("--use-bins", default=None, nargs="*",
252                   help="Bins to use for the analysis", dest="use_bins")
253
254     p.add_argument('--select_bins_by_energy', default=None, nargs="*",
255                   help="Does nothing. May fill in later once better
256             understood")
257
258     p.add_argument('--select_bins_by_fhit', default=None, nargs="*",
259                   help="Also does nothing see above")
260
261     p.add_argument( '-ex', "--exclude", default=None, nargs="*",

```

```

250             help="Exclude Bins", dest="exclude")
251
252     # Computing and logging arguements.
253     p.add_argument('-nt', '--n_threads', type=int, default=1,
254                     help='Maximum number of threads spawned by script. Default
255                     is 4')
256     p.add_argument('-log', '--log', type=str, required=True,
257                     help='Name for log files. Especially needed for threads')
258
259     p.add_argument('--decay', action="store_true",
260                     help='Set spectral DM hypothesis to decay')
261
262     args = p.parse_args()
263     print(args.decay)
264     if args.exclude is None: # default exclude bins 0 and 1
265         args.exclude = ['B0C0Ea', 'B0C0Eb', 'B0C0Ec', 'B0C0Ed', 'B0C0Ee']
266
267     if args.decay: OUT_PATH += '_dec'
268     else: OUT_PATH += '_ann'
269
270     OUT_PATH = OUT_PATH + '_' + args.catalog
271     if args.sigma != 0: OUT_PATH += f'_{args.sigma}sig'
272
273     main(args)

```

### B.3 Comparison with Glory Duck

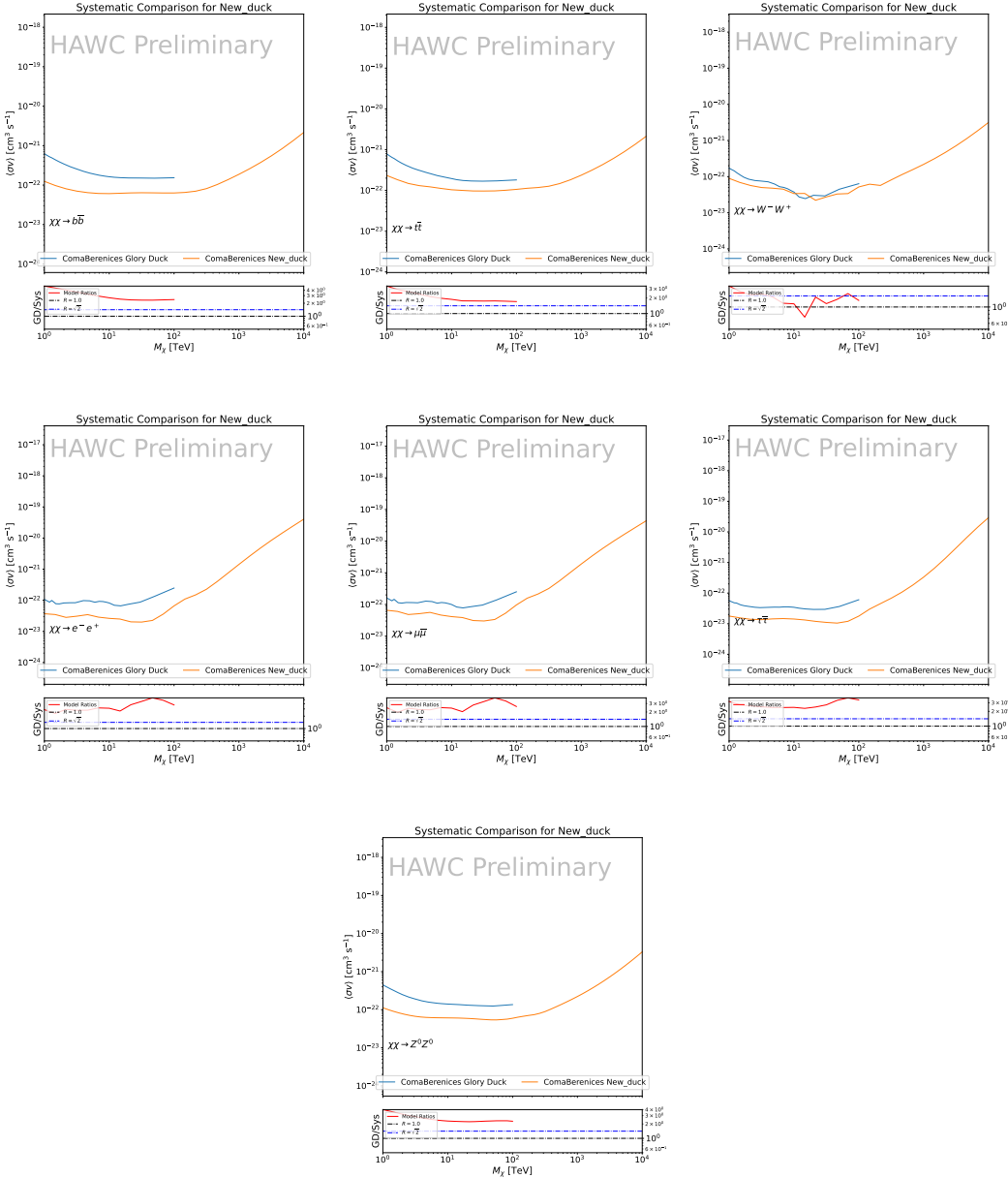


Figure B.2 Comparison of HAWC limits from this analysis to Glory Duck (Fig. 3.5) for Coma Berenices and 7 DM annihilation channels.

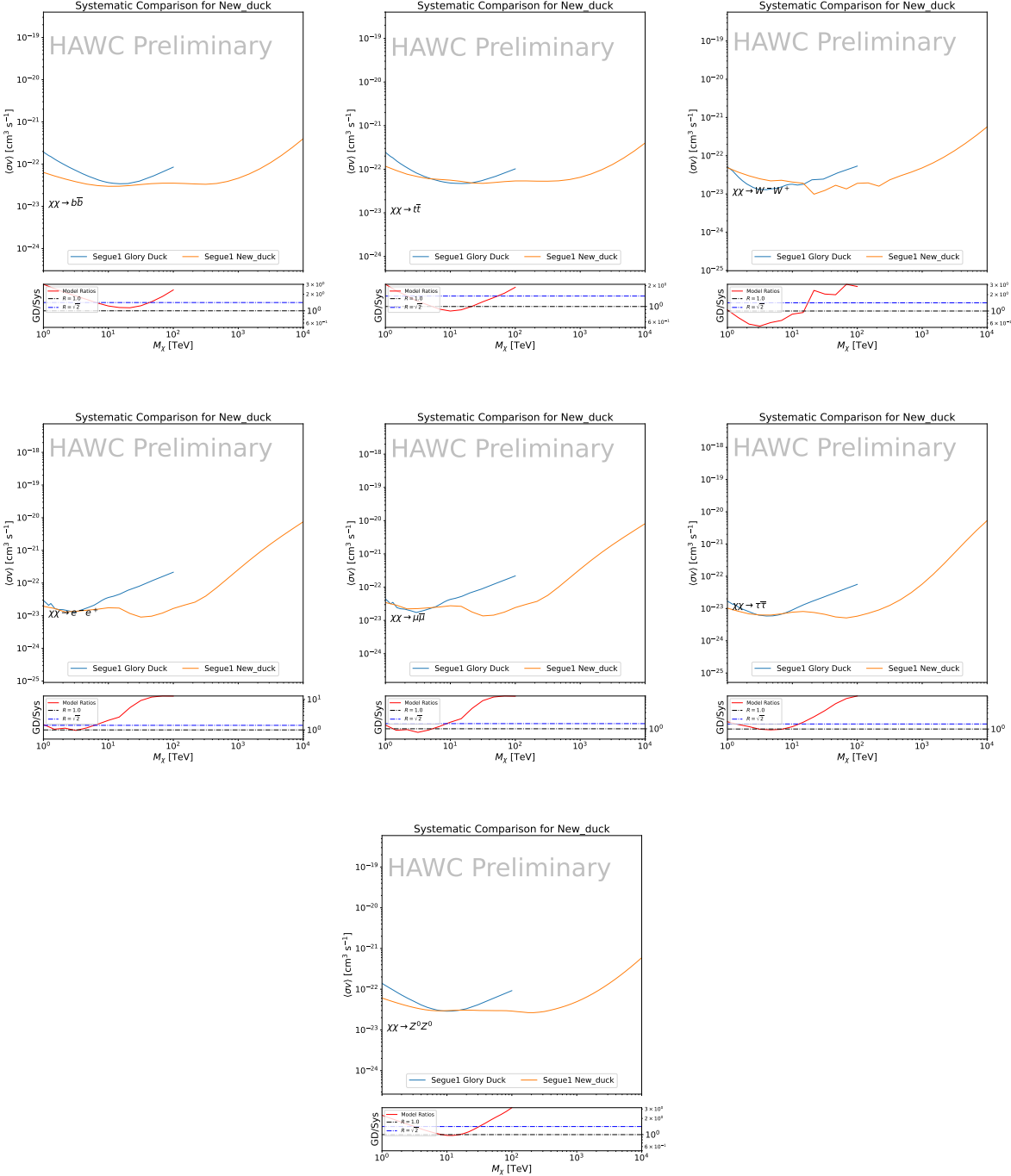


Figure B.3 Same as Fig. B.2 but for Segue 1.

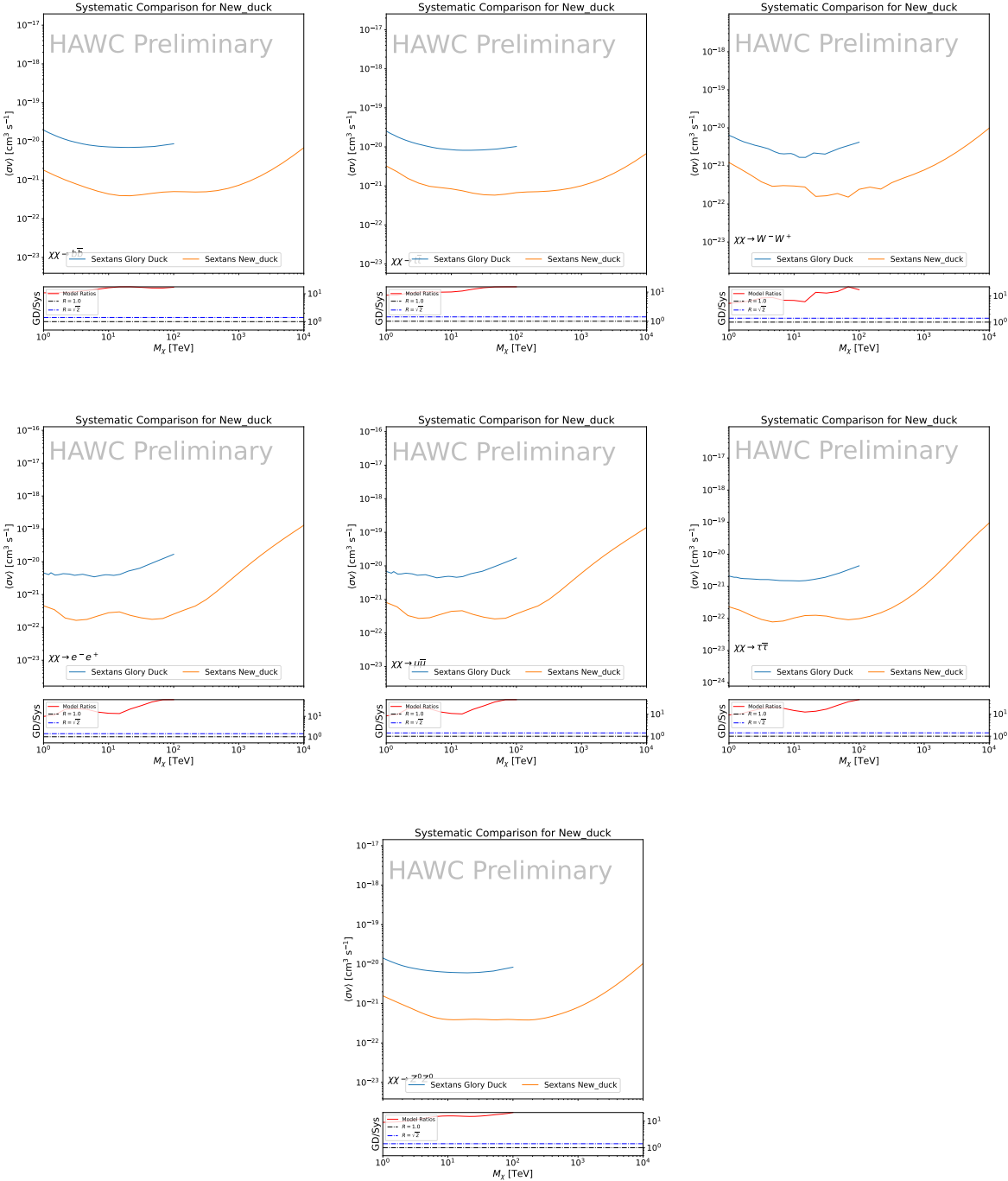


Figure B.4 Same as Fig. B.2 but for Sextans.

## APPENDIX C

### ICECUBE HEAVY DARK MATTER ANALYSIS SUPPLEMENTARY MATERIAL

#### C.1 Docker Image for Oscillating Neutrino Spectra

```
1 FROM ubuntu:18.04
2
3 # Execute commands to install software packages
4 RUN apt -y update
5
6 # Install utility programs
7 RUN apt -y install vim wget git cmake
8
9 ARG DEBIAN_FRONTEND=noninteractive
10
11 # Install python
12 RUN apt -y install python python-dev python-pip libjpeg-dev zlib1g-dev
13
14 # We need Python2 for installing Charon.
15 RUN apt -y install python-numpy python-sympy python-matplotlib \
16             python-sympy python-h5py python-astropy python-ipython
17
18 # Install dependencies of Charon : SQuIDS, NuSQuIDS
19 RUN apt -y install libgsl-dev libgslcblas0 libgsl23 gsl-bin pkg-config
20 # Install SQuIDS
21 RUN mkdir /home/SQuIDS /home/SQuIDS_install
22 WORKDIR /home/SQuIDS
23 RUN git clone https://github.com/j salvado/SQuIDS.git
24 WORKDIR /home/SQuIDS/SQuIDS
25 RUN git checkout 7ad9ba7c6ad06d1f0fa8418f937ebf1a403fef90
26 # Before executing "make install" an environmental variable has to be set.
27 ENV PKG_CONFIG_PATH=/home/SQuIDS/SQuIDS/lib
28 RUN ./configure --prefix=../SQuIDS_install \
```

```

29   && make
30 RUN make install
31
32 # Set up an environmental variable that is required to install nuSQuIDS..
33 ENV SQuIDS=/home/SQuIDS/SQuIDS
34 ENV LD_LIBRARY_PATH=$SQuIDS/lib:$LD_LIBRARY_PATH
35
36 # Install NuSQuIDS
37 RUN mkdir /home/nuSQuIDS
38 WORKDIR /home/nuSQuIDS
39 RUN git clone https://github.com/qrliu/nuSQuIDS.git
40 WORKDIR /home/nuSQuIDS/nuSQuIDS
41 RUN git checkout 072d8ef740e2fc7330f1fabaea94f0f4540c46f9
42 RUN apt -y install libhdf5-dev hdf5-tools
43 RUN apt -y install libboost1.65-all-dev
44 RUN ./configure --with-squids=$SQuIDS --with-python-bindings --prefix=../
        nuSQuIDS_install \
45   && make \
46   && make install
47
48 # Set up an environmental variable for nuSQuIDS.
49 ENV nuSQuIDS=/home/nuSQuIDS/nuSQuIDS
50 ENV LD_LIBRARY_PATH=$nuSQuIDS/lib:$LD_LIBRARY_PATH
51
52 # Build the python bindings
53 WORKDIR /home/nuSQuIDS/nuSQuIDS/resources/python/src
54 RUN make
55
56 # Set up an environmental variable for the python bindings.
57 ENV PYTHONPATH=$nuSQuIDS/resources/python/bindings/:$PYTHONPATH
58
59 # Install Charon in the /home/Charon/charon directory.
60 RUN mkdir /home/Charon

```

```
61 WORKDIR /home/Charon
62 RUN git clone https://github.com/icecube/charon.git \
63   && apt -y install unzip python-scipy
64 WORKDIR charon
65 RUN git checkout c531efe4e01dc364a60d1c83f950f04526ccd771
66 RUN unzip ./charon/xsec/xsec.zip -d charon/xsec/ \
67
68 # Download neutrino spectra tables in the /home/Charon/charon/data directory
69 .
70 && mkdir ./charon/data
71 WORKDIR ./charon/data
72 RUN wget --no-check-certificate https://icecube.wisc.edu/~qliu/charon/
73   SpectraEW.hdf5 \
74 && wget --no-check-certificate https://icecube.wisc.edu/~qliu/charon/
75   Spectra_PYTHIA.hdf5 \
76 && wget --no-check-certificate https://icecube.wisc.edu/~qliu/charon/
77   Spectra_noEW.hdf5
78
79 WORKDIR ../..
80 RUN python setup.py install
81 WORKDIR /home
```

## C.2 Spline Fitting Statuses

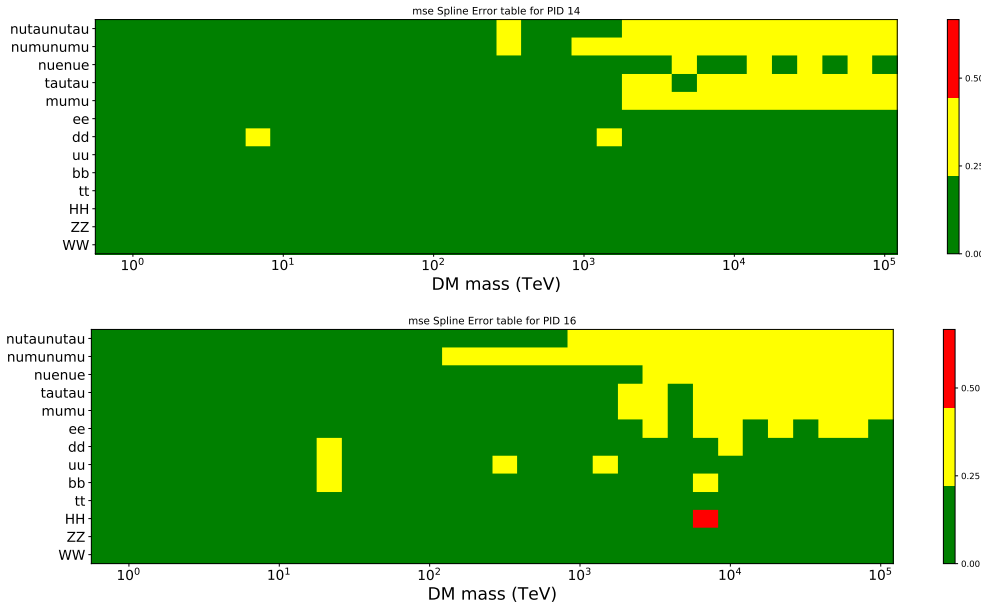


Figure C.1 Current status of spline tables according to constraints defined by Tab. 6.1. Green splines are splines that passed under the GOOD tolerance. Yellow are splines that are OK. Red are splines that FAIL. All yellow splines were inspected individually before running the analysis. Splines were made for the  $\mu$  (PID 14; top panel) flavor and  $\tau$  (PID 16; bottom panel) neutrino flavors.

### C.3 Neutrino Composite Spectra

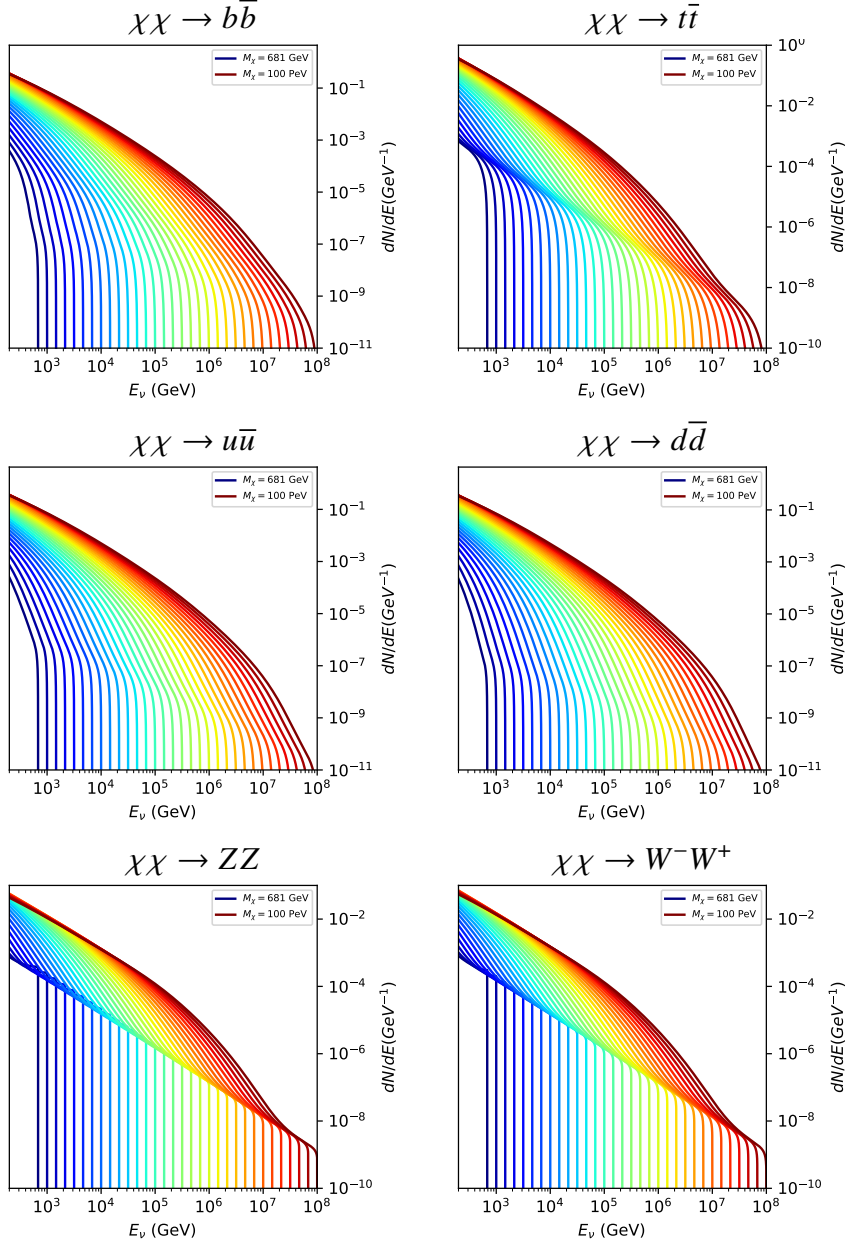


Figure C.2 Sister figure to Fig. 6.5 for annihilation channels that did not require kernel smoothing. These spectra are the composite ( $\nu_\mu + \nu_\tau$ ) of neutrino flavors. Every spectral model used for this analysis is featured as a colored solid line. Bluer lines are for lower DM mass spectral models. DM masses range from 681 GeV to 100 PeV.

#### C.4 Segue 1 And Ursa Major II Signal Recovery

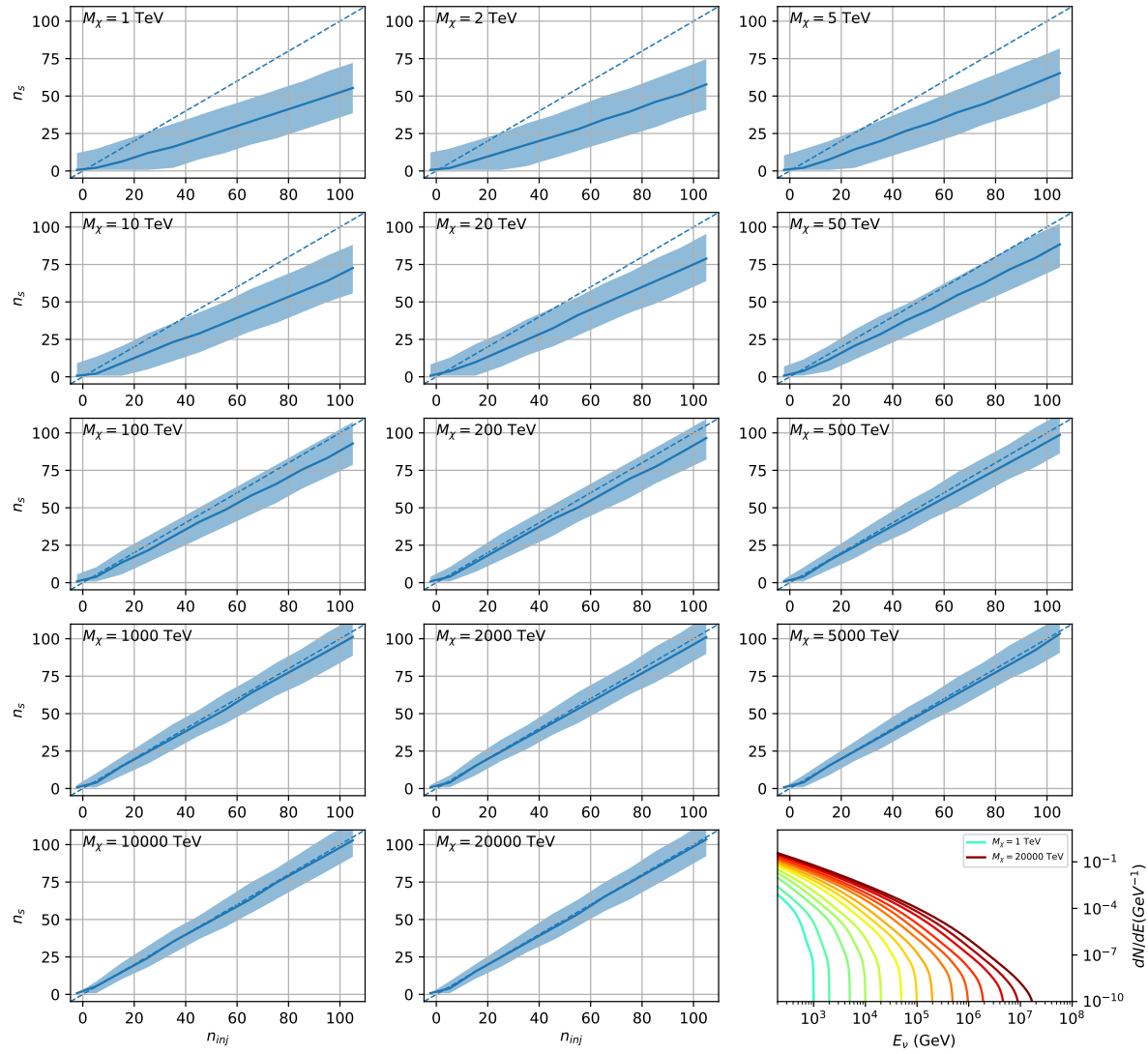


Figure C.3 Same as Fig. 6.23 but for Segue 1 and  $\chi\chi \rightarrow b\bar{b}$ .

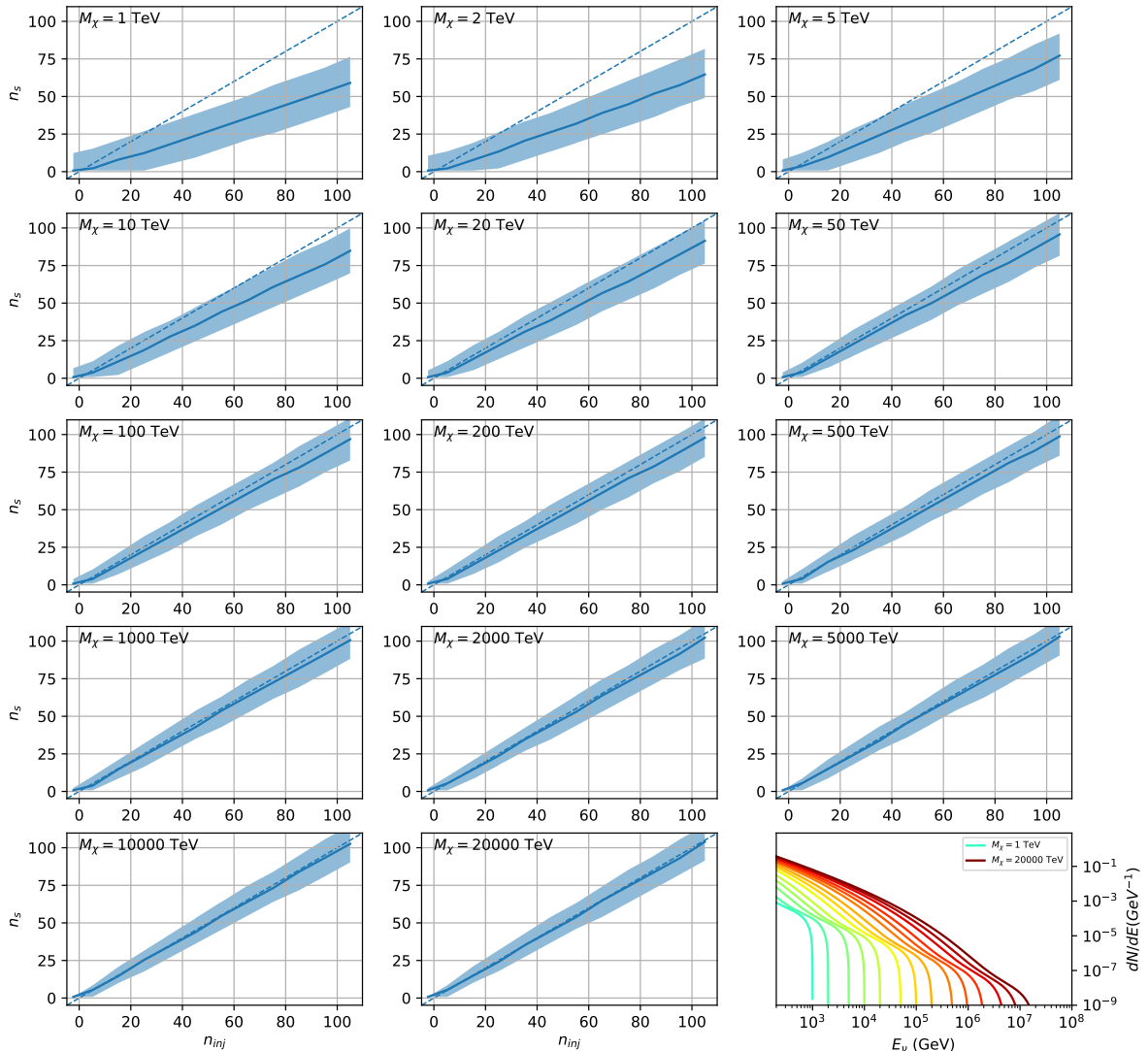


Figure C.4 Same as Fig. 6.23 but for Segue 1 and  $\chi\chi \rightarrow t\bar{t}$ .

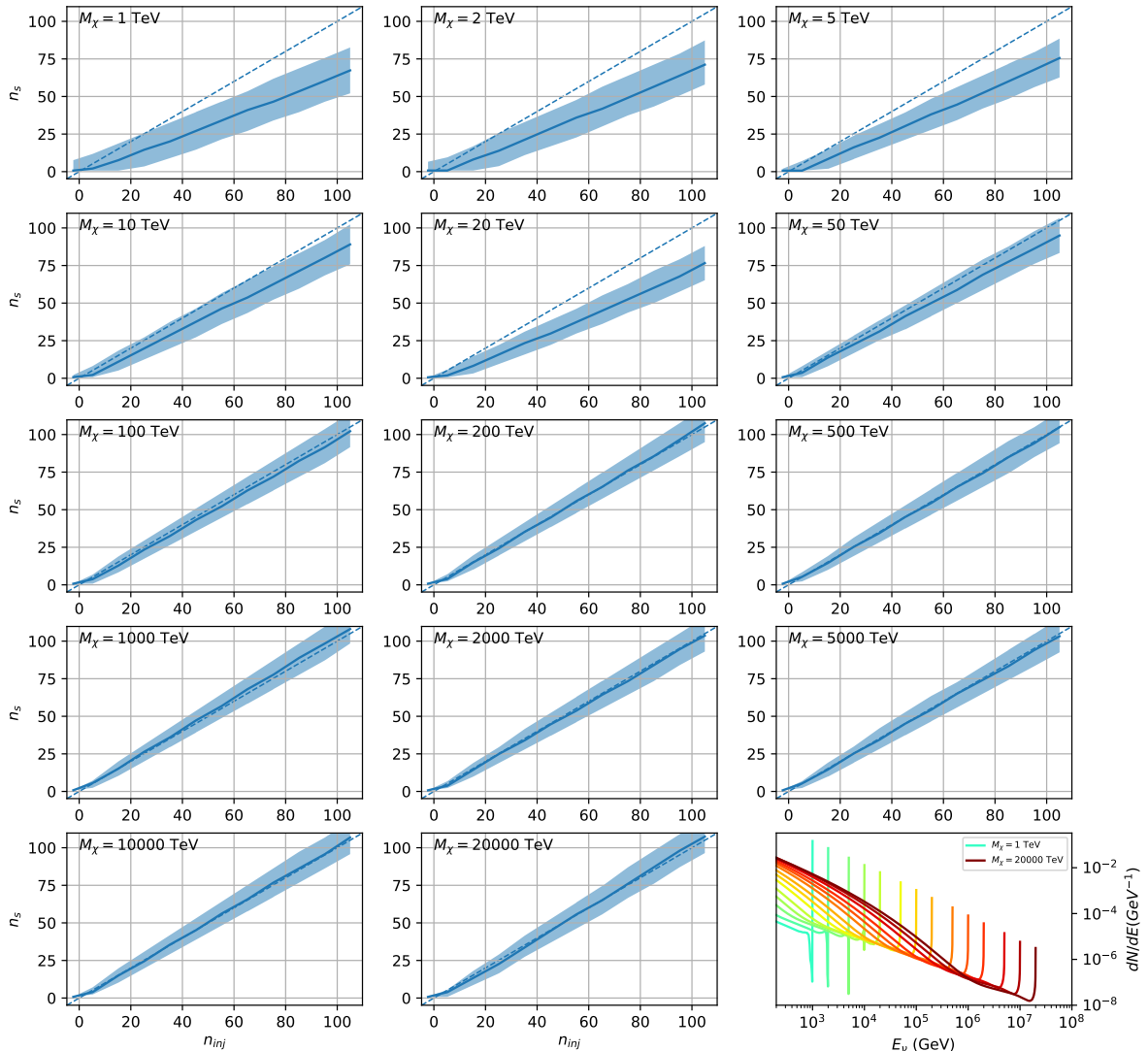


Figure C.5 Same as Fig. 6.23 but for Segue 1 and  $\chi\chi \rightarrow \nu_\mu \bar{\nu}_\mu$ .

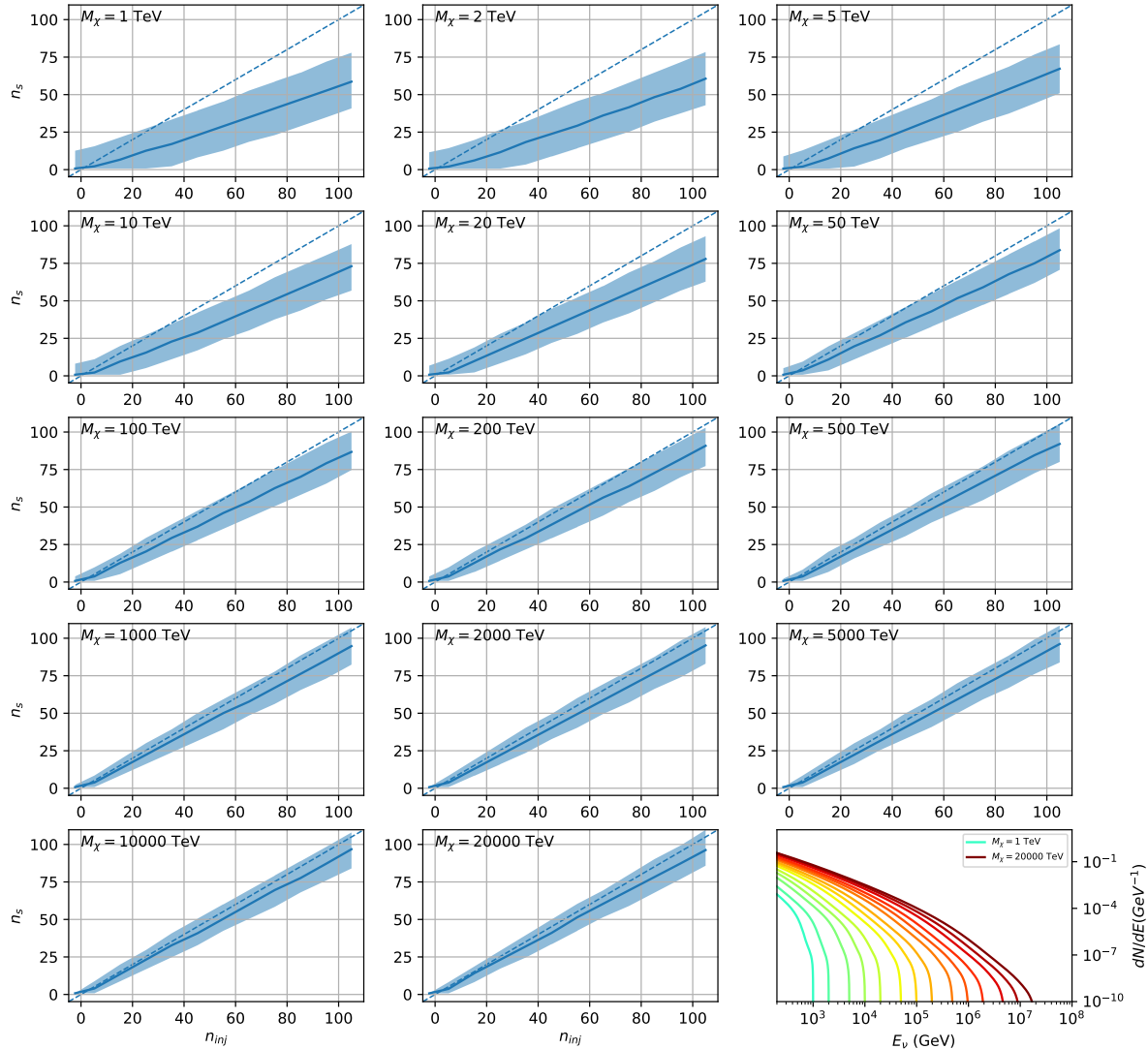


Figure C.6 Same as Fig. 6.23 but for Ursa Major II and  $\chi\chi \rightarrow b\bar{b}$ .

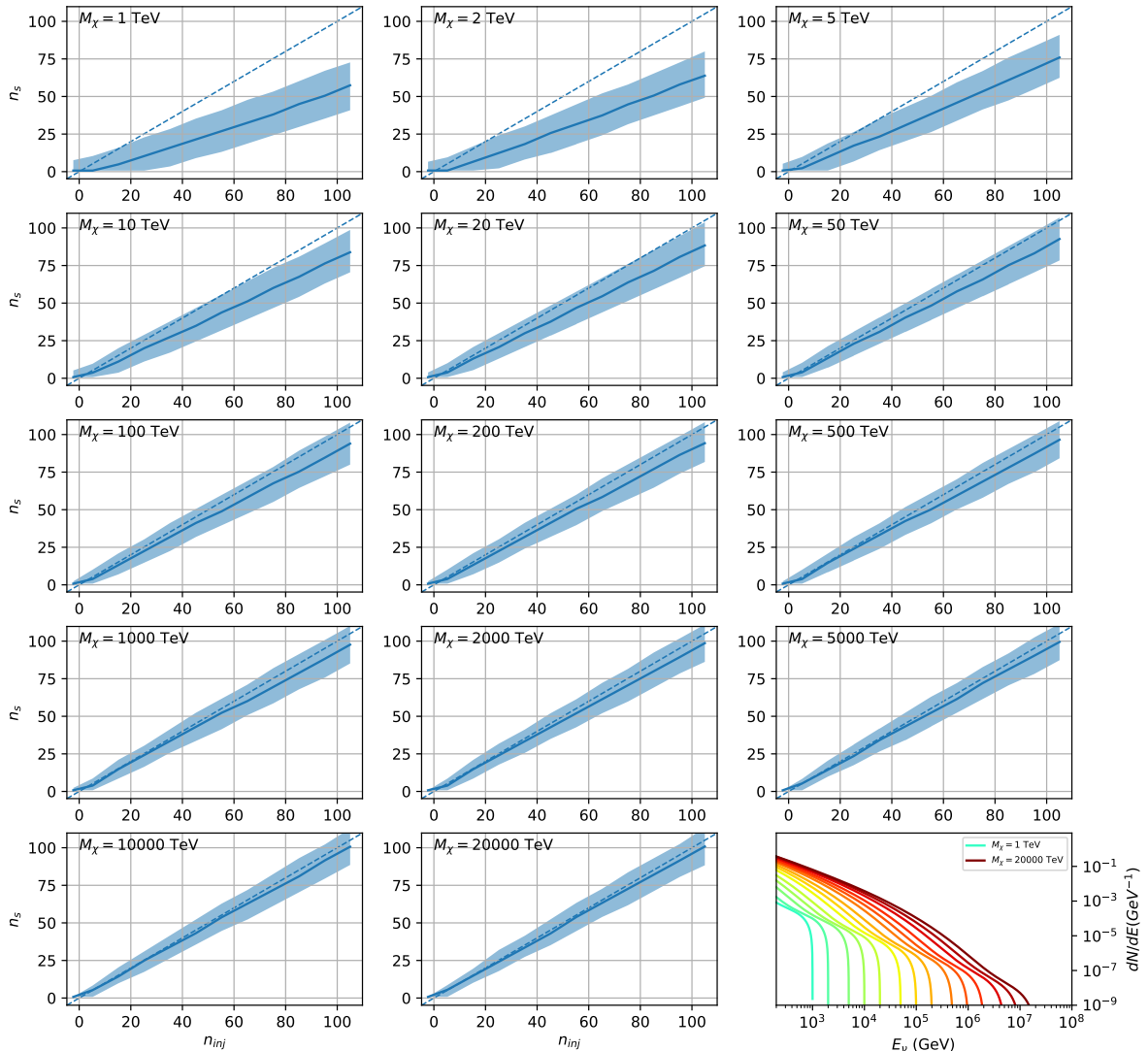


Figure C.7 Same as Fig. 6.23 but for Ursa Major II and  $\chi\chi \rightarrow t\bar{t}$ .

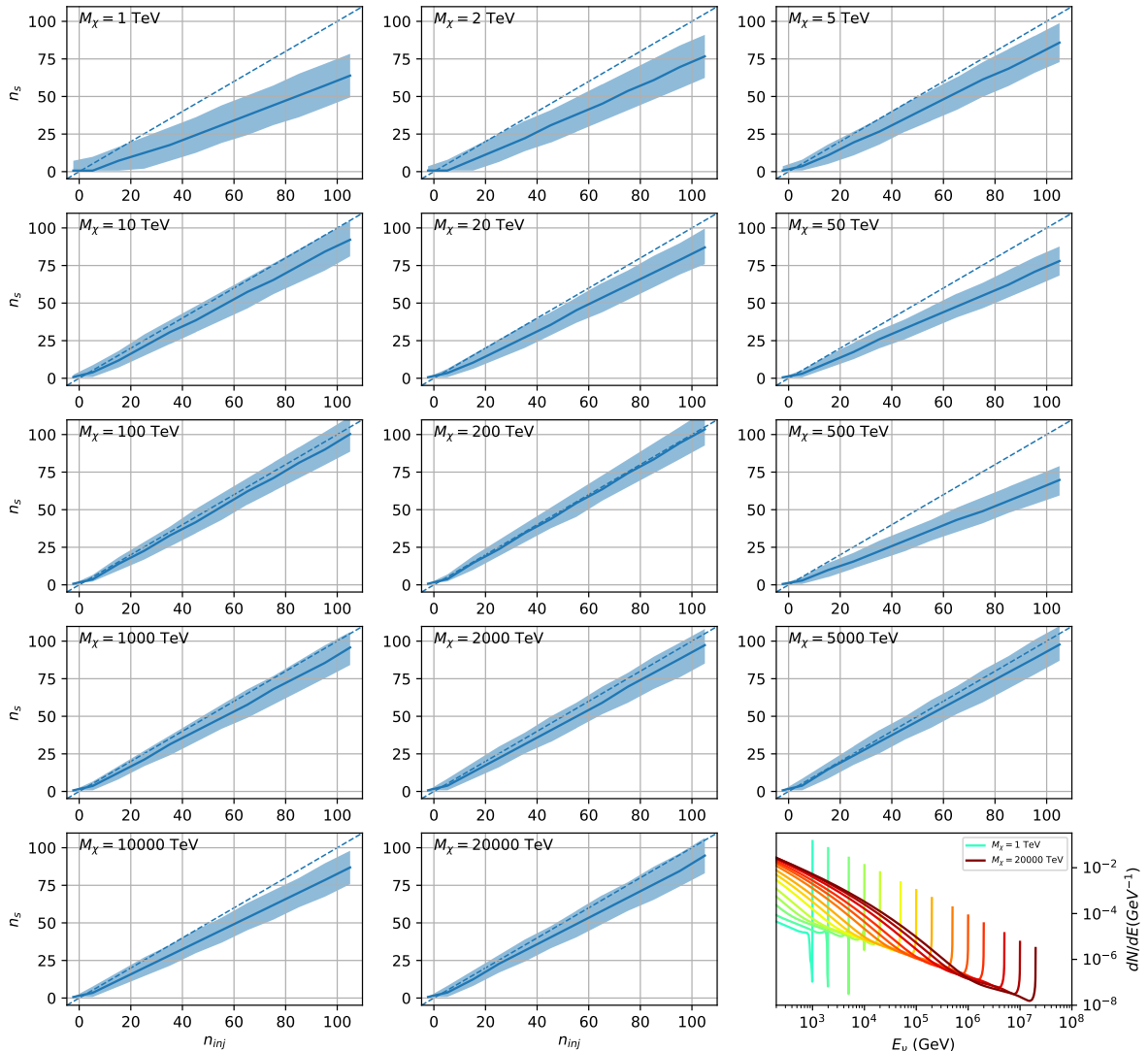


Figure C.8 Same as Fig. 6.23 but for Ursa Major II and  $\chi\chi \rightarrow \nu_\mu \bar{\nu}_\mu$ .

## C.5 $n_s$ Sensitivities

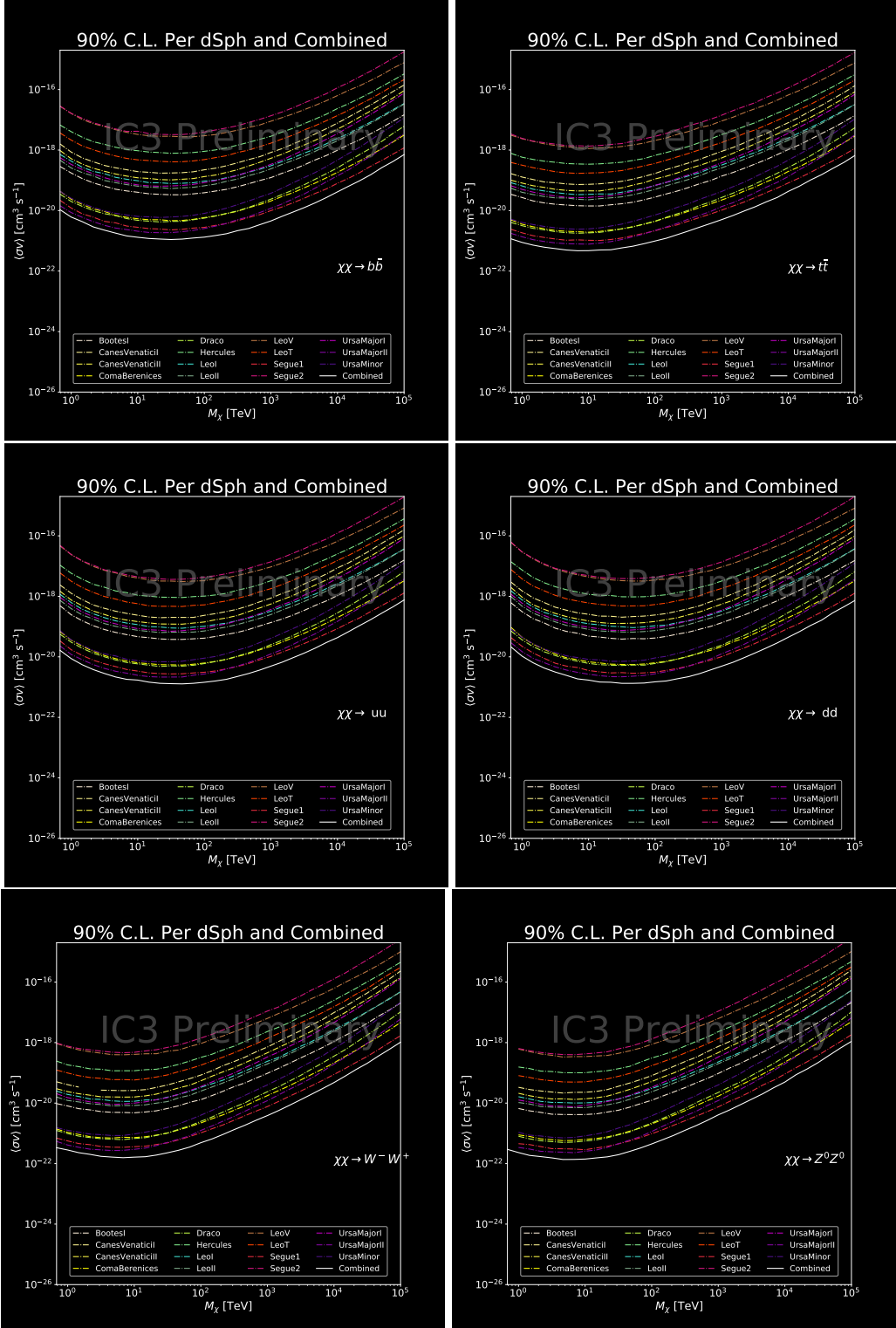


Figure C.9 IceCube North Sky Track Sensitivities for  $n_s/\langle N \rangle$ .  $n_s$  values are the counts fed into Eq. (6.8) to produce Fig. 6.26 and Fig. 6.25.

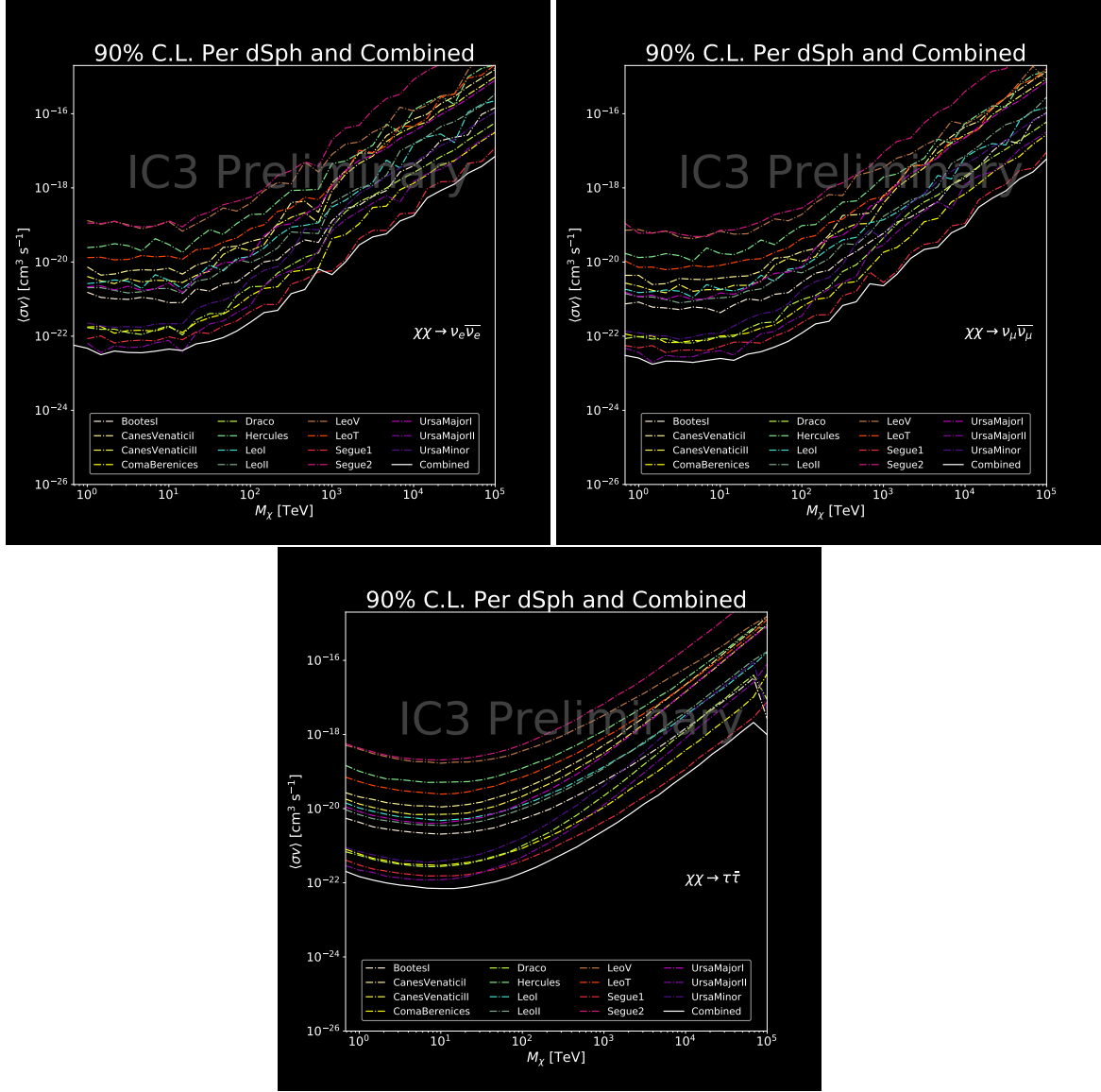


Figure C.10 Same as Fig. C.9 for three additional DM annihilation channels.

## BIBLIOGRAPHY

- [1] Anne M. Green. “Dark matter in astrophysics/cosmology”. In: *SciPost Phys. Lect. Notes* (2022), p. 37. doi: [10.21468/SciPostPhysLectNotes.37](https://doi.org/10.21468/SciPostPhysLectNotes.37). URL: <https://scipost.org/10.21468/SciPostPhysLectNotes.37>.
- [2] Bing-Lin Young. “A survey of dark matter and related topics in cosmology”. In: *Frontiers of Physics* 12 (Oct. 2016). doi: <https://doi.org/10.1007/s11467-016-0583-4>. URL: <https://doi.org/10.1007/s11467-016-0583-4>.
- [3] Gianfranco Bertone, Dan Hooper, and Joseph Silk. “Particle dark matter: evidence, candidates and constraints”. In: *Physics Reports* 405.5 (2005), pp. 279–390. ISSN: 0370-1573. doi: <https://doi.org/10.1016/j.physrep.2004.08.031>. URL: <https://www.sciencedirect.com/science/article/pii/S0370157304003515>.
- [4] Gianfranco Bertone and Dan Hooper. “History of dark matter”. In: *Rev. Mod. Phys.* 90 (4 Aug. 2018), p. 045002. doi: [10.1103/RevModPhys.90.045002](https://doi.org/10.1103/RevModPhys.90.045002). URL: <https://link.aps.org/doi/10.1103/RevModPhys.90.045002>.
- [5] Fritz Zwicky. “The Redshift of Extragalactic Nebulae”. In: *Helvetica Physica Acta* 6. (1933), pp. 110–127. doi: [10.5169/seals-110267](https://doi.org/10.5169/seals-110267).
- [6] Vera C. Rubin and Jr. Ford W. Kent. “Rotation of the Andromeda Nebula from a Spectroscopic Survey of Emission Regions”. In: *ApJ* 159 (Feb. 1970), p. 379. doi: [10.1086/150317](https://doi.org/10.1086/150317).
- [7] K. G. Begeman, A. H. Broeils, and R. H. Sanders. “Extended rotation curves of spiral galaxies: dark haloes and modified dynamics”. In: *Monthly Notices of the Royal Astronomical Society* 249.3 (Apr. 1991), pp. 523–537. ISSN: 0035-8711. doi: [10.1093/mnras/249.3.523](https://doi.org/10.1093/mnras/249.3.523). eprint: <https://academic.oup.com/mnras/article-pdf/249/3/523/18160929/mnras249-0523.pdf>. URL: <https://doi.org/10.1093/mnras/249.3.523>.
- [8] *Different types of gravitational lenses*. website. Feb. 2004. URL: <https://esahubble.org/images/heic0404b/>.
- [9] Douglas Clowe et al. “A Direct Empirical Proof of the Existence of Dark Matter”. In: *apjl* 648.2 (Sept. 2006), pp. L109–L113. doi: [10.1086/508162](https://doi.org/10.1086/508162). arXiv: [astro-ph/0608407 \[astro-ph\]](https://arxiv.org/abs/astro-ph/0608407).
- [10] Planck Collaboration and N. et. al. Aghanim. “Planck 2018 results I. Overview and the cosmological legacy of Planck”. In: *A&A* 641 (2020). doi: [10.1051/0004-6361/201833880](https://doi.org/10.1051/0004-6361/201833880). URL: <https://doi.org/10.1051/0004-6361/201833880>.
- [11] Wayne Hu. *Matter Density Animation*. web. 2024. URL: <http://background.uchicago.edu/~hu/density.html>

[o.edu/~whu/animbut/anim2.html](http://o.edu/~whu/animbut/anim2.html).

- [12] Wenlong Yuan et al. “A First Look at Cepheids in a Type Ia Supernova Host with JWST”. In: *The Astrophysical Journal Letters* 940.1 (Nov. 2022). doi: [10.3847/2041-8213/ac9b27](https://doi.org/10.3847/2041-8213/ac9b27). URL: <https://dx.doi.org/10.3847/2041-8213/ac9b27>.
- [13] Wendy L. Freedman. “Measurements of the Hubble Constant: Tensions in Perspective”. In: *The Astrophysical Journal* 919.1 (Sept. 2021), p. 16. doi: [10.3847/1538-4357/ac0e95](https://doi.org/10.3847/1538-4357/ac0e95). URL: <https://dx.doi.org/10.3847/1538-4357/ac0e95>.
- [14] Jodi Cooley. “Dark Matter direct detection of classical WIMPs”. In: *SciPost Phys. Lect. Notes* (2022), p. 55. doi: [10.21468/SciPostPhysLectNotes.55](https://doi.org/10.21468/SciPostPhysLectNotes.55). URL: <https://scipost.org/10.21468/SciPostPhysLectNotes.55>.
- [15] “Search for new phenomena in events with an energetic jet and missing transverse momentum in  $pp$  collisions at  $\sqrt{s} = 13$  TeV with the ATLAS detector”. In: *Phys. Rev. D* 103 (11 July 2021), p. 112006. doi: [10.1103/PhysRevD.103.112006](https://doi.org/10.1103/PhysRevD.103.112006). URL: <https://link.aps.org/doi/10.1103/PhysRevD.103.112006>.
- [16] *Jetting into the dark side: a precision search for dark matter*. website. July 2020. URL: <https://atlas.cern/updates/briefing/precision-search-dark-matter>.
- [17] Celine Armand et. al. “Combined dark matter searches towards dwarf spheroidal galaxies with Fermi-LAT, HAWC, H.E.S.S., MAGIC, and VERITAS”. in: *Proceedings of Science*. Vol. 395. Mar. 2022. doi: <https://doi.org/10.22323/1.395.0528>.
- [18] Tracy R. Slatyer. “Les Houches Lectures on Indirect Detection of Dark Matter”. In: *SciPost Phys. Lect. Notes* (2022), p. 53. doi: [10.21468/SciPostPhysLectNotes.53](https://doi.org/10.21468/SciPostPhysLectNotes.53). URL: <https://scipost.org/10.21468/SciPostPhysLectNotes.53>.
- [19] Christian W Bauer, Nicholas L. Rodd, and Bryan R. Webber. “Dark matter spectra from the electroweak to the Planck scale”. In: *Journal of High Energy Physics* 2021.1029-8479 (June 2021). doi: [https://doi.org/10.1007/JHEP06\(2021\)121](https://doi.org/10.1007/JHEP06(2021)121).
- [20] Riccardo Catena and Piero Ullio. “A novel determination of the local dark matter density”. In: *Journal of Cosmology and Astroparticle Physics* 2010.08 (Aug. 2010), p. 004. doi: [10.1088/1475-7516/2010/08/004](https://doi.org/10.1088/1475-7516/2010/08/004). URL: <https://dx.doi.org/10.1088/1475-7516/2010/08/004>.
- [21] B. P. Abbott et al. “Observation of Gravitational Waves from a Binary Black Hole Merger”. In: *Phys. Rev. Lett.* 116 (6 Feb. 2016), p. 061102. doi: [10.1103/PhysRevLett.116.061102](https://doi.org/10.1103/PhysRevLett.116.061102). URL: <https://link.aps.org/doi/10.1103/PhysRevLett.116.061102>.
- [22] R. Abbasi et. al. “Observation of high-energy neutrinos from the Galactic plane”. In: *Science* 380.6652 (June 2023), pp. 1338–1343.

- [23] NASA Goddard Space Flight Center. *Fermi's 12-year view of the gamma-ray sky*. website. 2022. URL: <https://svs.gsfc.nasa.gov/14090>.
- [24] Marco Cirelli et al. “PPPC 4 DM ID: a poor particle physicist cookbook for dark matter indirect detection”. In: *Journal of Cosmology and Astroparticle Physics* 2011.03 (Mar. 2011), p. 051. doi: [10.1088/1475-7516/2011/03/051](https://doi.org/10.1088/1475-7516/2011/03/051). URL: <https://dx.doi.org/10.1088/1475-7516/2011/03/051>.
- [25] The HAWC Collaboration. “The High-Altitude Water Cherenkov (HAWC) observatory in México: The primary detector”. In: *Nuclear Instruments and Methods in Physics Research Section A: Accelerators, Spectrometers, Detectors and Associated Equipment* 1052 (2023), p. 168253. ISSN: 0168-9002. doi: <https://doi.org/10.1016/j.nima.2023.168253>. URL: <https://www.sciencedirect.com/science/article/pii/S0168900223002437>.
- [26] Alicia Lopez Oramas. “Multi-year Campaign of the Gamma-Ray Binary LS I +61° 303 and Search for VHE Emission from Gamma-Ray Binary Candidates with the MAGIC Telescopes”. PhD thesis. Instituto de Astrofísica de Canarias, 2014. doi: <http://dx.doi.org/10.13140/RG.2.1.4140.4969>.
- [27] A.U. Abeysekara et. al. “The High-Altitude Water Cherenkov (HAWC) observatory in México: The primary detector”. In: *Nuclear Instruments and Methods in Physics Research Section A: Accelerators, Spectrometers, Detectors and Associated Equipment* 1052 (2023), p. 168253. ISSN: 0168-9002. doi: <https://doi.org/10.1016/j.nima.2023.168253>. URL: <https://www.sciencedirect.com/science/article/pii/S0168900223002437>.
- [28] Hamamatsu Photonics KK. *Large Photocathode Area Photomultiplier Tubes*. 2019. URL: [https://www.hamamatsu.com/content/dam/hamamatsu-photonics/sites/documents/99\\_SALES\\_LIBRARY/etd/LARGE\\_AREA\\_PMT TPMH1376E.pdf](https://www.hamamatsu.com/content/dam/hamamatsu-photonics/sites/documents/99_SALES_LIBRARY/etd/LARGE_AREA_PMT TPMH1376E.pdf).
- [29] The HAWC Collaboration. “Data acquisition architecture and online processing system for the HAWC gamma-ray observatory”. In: *Nuclear Instruments and Methods in Physics Research Section A: Accelerators, Spectrometers, Detectors and Associated Equipment* 888 (2018), pp. 138–146. ISSN: 0168-9002. doi: <https://doi.org/10.1016/j.nima.2018.01.051>. URL: <https://www.sciencedirect.com/science/article/pii/S0168900218300688>.
- [30] The Milagro Collaboratio. “Milagrito, a TeV air-shower array”. In: *Nuclear Instruments and Methods in Physics Research Section A: Accelerators, Spectrometers, Detectors and Associated Equipment* 449.3 (2000), pp. 478–499. ISSN: 0168-9002. doi: [https://doi.org/10.1016/S0168-9002\(00\)00146-7](https://doi.org/10.1016/S0168-9002(00)00146-7). URL: <https://www.sciencedirect.com/science/article/pii/S0168900200001467>.
- [31] Ian Gabriel Wisher. “Real-time Transient Monitoring With the HAWC Detector: Design

and Performance”. PhD thesis. The University of Wisconsin - Madison, 2016.

- [32] The ZeroMQ authors. “ZeroMQ An open-source universal messaging library”. In: (2021). URL: <https://zeromq.org>.
- [33] Zigmund Hampel-Archisman. “Cosmic Ray Observations at the TeV Scale with the HAWC Observatory”. PhD thesis. University of Wisconsin-Madison, 2017.
- [34] A. U. Abeysekara et al. “Observation of the Crab Nebula with the HAWC Gamma-Ray Observatory”. In: *The Astrophysical Journal* 843.1 (June 2017), p. 39. doi: [10.3847/1538-4357/aa7555](https://doi.org/10.3847/1538-4357/aa7555). URL: <https://doi.org/10.3847/1538-4357/aa7555>.
- [35] Kenneth Greisen. “Cosmic Ray Showers”. In: *ANNUAL REVIEW OF NUCLEAR AND PARTICLE SCIENCE* 10 (1960), pp. 63–108.
- [36] The HAWC Collaboration. “Sensitivity of the high altitude water Cherenkov detector to sources of multi-TeV gamma rays”. In: *Astroparticle Physics* 50-52 (2013), pp. 26–32. ISSN: 0927-6505. doi: <https://doi.org/10.1016/j.astropartphys.2013.08.002>. URL: <https://www.sciencedirect.com/science/article/pii/S0927650513001230>.
- [37] The HAWC Collaboration. “Measurement of the Crab Nebula Spectrum Past 100 TeV with HAWC”. in: *The Astrophysical Journal* 881.2 (Aug. 2019), p. 134. doi: [10.3847/1538-4357/ab2f7d](https://doi.org/10.3847/1538-4357/ab2f7d). URL: <https://dx.doi.org/10.3847/1538-4357/ab2f7d>.
- [38] Samuel Miranelli. “CONSTRAINTS ON LORENTZ-INVARIANCE VIOLATION WITH THE HAWC OBSERVATORY”. PhD thesis. Michigan State University, 2019.
- [39] A. A. Abdo et al. “OBSERVATION AND SPECTRAL MEASUREMENTS OF THE CRAB NEBULA WITH MILAGRO”. in: *The Astrophysical Journal* 750.1 (Apr. 2012), p. 63. doi: [10.1088/0004-637X/750/1/63](https://doi.org/10.1088/0004-637X/750/1/63). URL: <https://dx.doi.org/10.1088/0004-637X/750/1/63>.
- [40] Javier Rico. “Gamma-Ray Dark Matter Searches in Milky Way Satellites—A Comparative Review of Data Analysis Methods and Current Results”. In: *Galaxies* 8.1 (Mar. 2020), p. 25. doi: [10.3390/galaxies8010025](https://doi.org/10.3390/galaxies8010025). arXiv: [2003.13482 \[astro-ph.HE\]](https://arxiv.org/abs/2003.13482).
- [41] W. B. Atwood et al. “The Large Area Telescope on the Fermi Gamma-Ray Space Telescope Mission”. In: *apj* 697.2 (June 2009), pp. 1071–1102. doi: [10.1088/0004-637X/697/2/1071](https://doi.org/10.1088/0004-637X/697/2/1071). arXiv: [0902.1089 \[astro-ph.IM\]](https://arxiv.org/abs/0902.1089).
- [42] M. Ackermann et al. “Searching for Dark Matter Annihilation from Milky Way Dwarf Spheroidal Galaxies with Six Years of Fermi Large Area Telescope Data”. In: *prl* 115.23, 231301 (Dec. 2015), p. 231301. doi: [10.1103/PhysRevLett.115.231301](https://doi.org/10.1103/PhysRevLett.115.231301). arXiv: [1503.02641 \[astro-ph.HE\]](https://arxiv.org/abs/1503.02641).

- [43] Mattia Di Mauro, Martin Stref, and Francesca Calore. “Investigating the effect of Milky Way dwarf spheroidal galaxies extension on dark matter searches with Fermi-LAT data”. In: *Phys. Rev. D* 106 (12 Dec. 2022), p. 123032. doi: [10.1103/PhysRevD.106.123032](https://doi.org/10.1103/PhysRevD.106.123032). URL: <https://link.aps.org/doi/10.1103/PhysRevD.106.123032>.
- [44] F. et al. Aharonian. “Observations of the Crab Nebula with H.E.S.S.”. In: *Astron. Astrophys.* 457 (2006), pp. 899–915. doi: [10.1051/0004-6361:20065351](https://doi.org/10.1051/0004-6361:20065351). arXiv: [astro-ph/0607333](https://arxiv.org/abs/astro-ph/0607333).
- [45] J. Albert et al. “VHE  $\gamma$ -Ray Observation of the Crab Nebula and its Pulsar with the MAGIC Telescope”. In: *The Astrophysical Journal* 674.2 (Feb. 2008), p. 1037. doi: [10.1086/525270](https://doi.org/10.1086/525270). URL: <https://dx.doi.org/10.1086/525270>.
- [46] N. Park. “Performance of the VERITAS experiment”. In: *Proceedings, 34th International Cosmic Ray Conference (ICRC2015): The Hague, The Netherlands, July, 30th July - 6th August*. Vol. 34. 2015, p. 771. arXiv: [1508.07070 \[astro-ph.IM\]](https://arxiv.org/abs/1508.07070).
- [47] A. Abramowski et al. “H.E.S.S. constraints on Dark Matter annihilations towards the Sculptor and Carina Dwarf Galaxies”. In: *Astropart. Phys.* 34 (2011), pp. 608–616. doi: [10.1016/j.astropartphys.2010.12.006](https://doi.org/10.1016/j.astropartphys.2010.12.006). arXiv: [1012.5602 \[astro-ph.HE\]](https://arxiv.org/abs/1012.5602).
- [48] A. Abramowski et al. “Search for dark matter annihilation signatures in H.E.S.S. observations of Dwarf Spheroidal Galaxies”. In: *Phys. Rev. D* 90 (2014), p. 112012. doi: [10.1103/PhysRevD.90.112012](https://doi.org/10.1103/PhysRevD.90.112012). arXiv: [1410.2589 \[astro-ph.HE\]](https://arxiv.org/abs/1410.2589).
- [49] H. Abdalla et al. “Searches for gamma-ray lines and ‘pure WIMP’ spectra from Dark Matter annihilations in dwarf galaxies with H.E.S.S”. in: *JCAP* 11 (2018), p. 037. doi: [10.1088/1475-7516/2018/11/037](https://doi.org/10.1088/1475-7516/2018/11/037). arXiv: [1810.00995 \[astro-ph.HE\]](https://arxiv.org/abs/1810.00995).
- [50] J. Aleksić et al. “Optimized dark matter searches in deep observations of Segue 1 with MAGIC”. in: *JCAP* 1402 (2014), p. 008. doi: [10.1088/1475-7516/2014/02/008](https://doi.org/10.1088/1475-7516/2014/02/008). arXiv: [1312.1535 \[hep-ph\]](https://arxiv.org/abs/1312.1535).
- [51] V.A. Acciari et al. “Combined searches for dark matter in dwarf spheroidal galaxies observed with the MAGIC telescopes, including new data from Coma Berenices and Draco”. In: *Physics of the Dark Universe* (2021), p. 100912. ISSN: 2212-6864. doi: <https://doi.org/10.1016/j.dark.2021.100912>. URL: <https://www.sciencedirect.com/science/article/pii/S2212686421001370>.
- [52] M. L. Ahnen et al. “Indirect dark matter searches in the dwarf satellite galaxy Ursa Major II with the MAGIC Telescopes”. In: *JCAP* 1803.03 (2018), p. 009. doi: [10.1088/1475-7516/2018/03/009](https://doi.org/10.1088/1475-7516/2018/03/009). arXiv: [1712.03095 \[astro-ph.HE\]](https://arxiv.org/abs/1712.03095).
- [53] S. et al. Archambault. “Dark matter constraints from a joint analysis of dwarf Spheroidal galaxy observations with VERITAS”. in: *prd* 95.8 (Apr. 2017). doi: [10.1103/PhysRevD.95.083008](https://doi.org/10.1103/PhysRevD.95.083008).

.95.082001. arXiv: 1703.04937 [astro-ph.HE].

- [54] Louise Oakes et al. “Combined Dark Matter searches towards dwarf spheroidal galaxies with Fermi-LAT, HAWC, HESS, MAGIC and VERITAS”. in: *Proceedings of Science*. 2019.
- [55] Celine Armand et al. on behalf of the Fermi-LAT, HAWC, HESS, MAGIC, VERITAS. “Combined Dark Matter searches towards dwarf spheroidal galaxies with Fermi-LAT, HAWC, HESS, MAGIC and VERITAS”. in: *Proceedings of Science*. 2021.
- [56] Daniel Kerszberg et al. on behalf of the Fermi-LAT, HAWC, HESS, MAGIC, and VERITAS collaborations. “Search for dark matter annihilation with a combined analysis of dwarf spheroidal galaxies from Fermi-LAT, HAWC, H.E.S.S., MAGIC and VERITAS”. in: *Proceedings of Science*. 2023.
- [57] Giacomo Vianello et al. *The Multi-Mission Maximum Likelihood framework (3ML)*. 2015. arXiv: 1507.08343 [astro-ph.HE].
- [58] Marco Cirelli et al. “PPPC 4 DM ID: a poor particle physicist cookbook for dark matter indirect detection”. In: *Journal of Cosmology and Astroparticle Physics* 2011.03 (Mar. 2011). ISSN: 1475-7516. doi: [10.1088/1475-7516/2011/03/051](https://doi.org/10.1088/1475-7516/2011/03/051). URL: <http://dx.doi.org/10.1088/1475-7516/2011/03/051>.
- [59] Alex Geringer-Sameth, Savvas M. Koushiappas, and Matthew Walker. “DWARF GALAXY ANNIHILATION AND DECAY EMISSION PROFILES FOR DARK MATTER EXPERIMENTS”. in: *The Astrophysical Journal* 801.2 (Mar. 2015), p. 74. ISSN: 1538-4357. doi: [10.1088/0004-637x/801/2/74](https://doi.org/10.1088/0004-637x/801/2/74). URL: <http://dx.doi.org/10.1088/0004-637X/801/2/74>.
- [60] A. Albert et al. “Dark Matter Limits from Dwarf Spheroidal Galaxies with the HAWC Gamma-Ray Observatory”. In: *The Astrophysical Journal* 853.2 (Feb. 2018), p. 154. ISSN: 1538-4357. doi: [10.3847/1538-4357/aaa6d8](https://doi.org/10.3847/1538-4357/aaa6d8). URL: <http://dx.doi.org/10.3847/1538-4357/aaa6d8>.
- [61] HongSheng Zhao. “Analytical models for galactic nuclei”. In: *Mon. Not. Roy. Astron. Soc.* 278 (1996), pp. 488–496. doi: [10.1093/mnras/278.2.488](https://doi.org/10.1093/mnras/278.2.488). arXiv: astro-ph/9509122 [astro-ph].
- [62] Julio F. Navarro, Carlos S. Frenk, and Simon D. M. White. “The Structure of Cold Dark Matter Halos”. In: *ApJ* 462 (May 1996), p. 563. doi: [10.1086/177173](https://doi.org/10.1086/177173). eprint: astro-ph/9508025 (astro-ph).
- [63] V. Bonnivard et al. “Spherical Jeans analysis for dark matter indirect detection in dwarf spheroidal galaxies - Impact of physical parameters and triaxiality”. In: *Mon. Not. Roy. Astron. Soc.* 446 (2015), pp. 3002–3021. doi: [10.1093/mnras/stu2296](https://doi.org/10.1093/mnras/stu2296). arXiv:

[1407.7822 \[astro-ph.HE\]](#).

- [64] M. Ackermann et al. “Searching for Dark Matter Annihilation from Milky Way Dwarf Spheroidal Galaxies with Six Years of Fermi Large Area Telescope Data”. In: *prl* 115.23, 231301 (Dec. 2015), p. 231301. doi: [10.1103/PhysRevLett.115.231301](https://doi.org/10.1103/PhysRevLett.115.231301). arXiv: [1503.02641 \[astro-ph.HE\]](#).
- [65] M. L. Ahnen et al. “Limits to Dark Matter Annihilation Cross-Section from a Combined Analysis of MAGIC and Fermi-LAT Observations of Dwarf Satellite Galaxies”. In: *JCAP* 1602.02 (2016), p. 039. doi: [10.1088/1475-7516/2016/02/039](https://doi.org/10.1088/1475-7516/2016/02/039). arXiv: [1601.06590 \[astro-ph.HE\]](#).
- [66] Javier Rico et al. *gLike: numerical maximization of heterogeneous joint likelihood functions of a common free parameter plus nuisance parameters*. <https://doi.org/10.5281/zenodo.4601451>. Version v00.09.03. Mar. 2021. doi: [10.5281/zenodo.4601451](#). URL: <https://doi.org/10.5281/zenodo.4601451>.
- [67] Tjark Miener and Daniel Nieto. *LklCom: Combining likelihoods from different experiments*. <https://doi.org/10.5281/zenodo.4597500>. Version v0.5.3. Mar. 2021. doi: [10.5281/zenodo.4597500](#). URL: <https://doi.org/10.5281/zenodo.4597500>.
- [68] T. Miener et al. “Open-source Analysis Tools for Multi-instrument Dark Matter Searches”. In: *arXiv e-prints*, arXiv:2112.01818 (Dec. 2021), arXiv:2112.01818. arXiv: [2112.01818 \[astro-ph.IM\]](#).
- [69] Alex Geringer-Sameth and Matthew Koushiappas Savvas M. and Walker. “Dwarf galaxy annihilation and decay emission profiles for dark matter experiments”. In: *Astrophys. J.* 801.2 (2015), p. 74. doi: [10.1088/0004-637X/801/2/74](https://doi.org/10.1088/0004-637X/801/2/74). arXiv: [1408.0002 \[astro-ph.CO\]](#).
- [70] Gianfranco Bertone, Dan Hooper, and Joseph Silk. “Particle dark matter: evidence, candidates and constraints”. In: *Physics Reports* 405.5-6 (Jan. 2005), pp. 279–390. ISSN: 0370-1573. doi: [10.1016/j.physrep.2004.08.031](https://doi.org/10.1016/j.physrep.2004.08.031). URL: <http://dx.doi.org/10.1016/j.physrep.2004.08.031>.
- [71] V. Bonnivard et al. “Dark matter annihilation and decay in dwarf spheroidal galaxies: The classical and ultrafaint dSphs”. In: *Mon. Not. Roy. Astron. Soc.* 453.1 (2015), pp. 849–867. doi: [10.1093/mnras/stv1601](https://doi.org/10.1093/mnras/stv1601). arXiv: [1504.02048 \[astro-ph.HE\]](#).
- [72] A. et al. Albert. “Searching for Dark Matter Annihilation in Recently Discovered Milky Way Satellites with Fermi-LAT”. in: *Astrophys. J.* 834.2 (2017), p. 110. doi: [10.3847/1538-4357/834/2/110](https://doi.org/10.3847/1538-4357/834/2/110). arXiv: [1611.03184 \[astro-ph.HE\]](#).
- [73] Mattia Di Mauro and Martin Wolfgang Winkler. “Multimessenger constraints on the dark matter interpretation of the Fermi-LAT Galactic Center excess”. In: *prd* 103.12, 123005

(June 2021), p. 123005. doi: [10.1103/PhysRevD.103.123005](https://doi.org/10.1103/PhysRevD.103.123005). arXiv: [2101.11027](https://arxiv.org/abs/2101.11027) [astro-ph.HE].

- [74] H. C. Plummer. “On the Problem of Distribution in Globular Star Clusters: (Plate 8.)” In: *Monthly Notices of the Royal Astronomical Society* 71.5 (Mar. 1911), pp. 460–470. ISSN: 0035-8711. doi: [10.1093/mnras/71.5.460](https://doi.org/10.1093/mnras/71.5.460). eprint: <https://academic.oup.com/mnras/article-pdf/71/5/460/2937497/mnras71-0460.pdf>. URL: <https://doi.org/10.1093/mnras/71.5.460>.
- [75] Daniel R. Hunter. “Derivation of the anisotropy profile, constraints on the local velocity dispersion, and implications for direct detection”. In: *JCAP* 02 (2014), p. 023. doi: [10.1088/1475-7516/2014/02/023](https://doi.org/10.1088/1475-7516/2014/02/023). arXiv: [1311.0256](https://arxiv.org/abs/1311.0256) [astro-ph.CO].
- [76] Barun Kumar Dhar and Liliya L. R. Williams. “Surface mass density of the Einasto family of dark matter haloes: are they Sersic-like?” In: *Mon. Not. Roy. Astron. Soc.* (2010). doi: [10.1111/j.1365-2966.2010.16446.x](https://doi.org/10.1111/j.1365-2966.2010.16446.x).
- [77] M. Baes and E. Van Hese. “Dynamical models with a general anisotropy profile”. In: *Astron. Astrophys.* 471 (2007), p. 419. doi: [10.1051/0004-6361:20077672](https://doi.org/10.1051/0004-6361:20077672). arXiv: [0705.4109](https://arxiv.org/abs/0705.4109) [astro-ph].
- [78] Matthew G. Walker, Edward W. Olszewski, and Mario Mateo. “Bayesian analysis of resolved stellar spectra: application to MMT/Hectochelle observations of the Draco dwarf spheroidal”. In: *mnras* 448.3 (Apr. 2015), pp. 2717–2732. doi: [10.1093/mnras/stv099](https://doi.org/10.1093/mnras/stv099). arXiv: [1503.02589](https://arxiv.org/abs/1503.02589) [astro-ph.GA].
- [79] Nicholas L. Rodd et al. “Dark matter spectra from the electroweak to the Planck scale”. In: *J. High Energy Physics* 121.10.1007 (June 2021).
- [80] Pace, Andrew B and Strigari, Louis E. “Scaling relations for dark matter annihilation and decay profiles in dwarf spheroidal galaxies”. In: *Monthly Notices of the Royal Astronomical Society* 482.3 (Oct. 2018), pp. 3480–3496. ISSN: 0035-8711. doi: [10.1093/mnras/sty2839](https://doi.org/10.1093/mnras/sty2839).
- [81] Albert, A. et al. “Search for gamma-ray spectral lines from dark matter annihilation in dwarf galaxies with the High-Altitude Water Cherenkov observatory”. In: *Phys. Rev. D* 101 (10 May 2020), p. 103001. doi: [10.1103/PhysRevD.101.103001](https://doi.org/10.1103/PhysRevD.101.103001). URL: <https://link.aps.org/doi/10.1103/PhysRevD.101.103001>.
- [82] Victor Eijkhout and Edmund Show and Robert van de Geijn. *The Science of Computing. The Art of High Performance Computing*. Vol. 3. Open Copy published under CC-BY 4.0 license, 2023, pp. 63–66.
- [83] IceCube Gallery. 2019. URL: [https://gallery.icecube.wisc.edu/internal/v/SPIImages/weekly/winteroverweeklyphotos2019/icl.JPG.html?g2\\_imageView](https://gallery.icecube.wisc.edu/internal/v/SPIImages/weekly/winteroverweeklyphotos2019/icl.JPG.html?g2_imageView)

**sIndex=1.**

- [84] The IceCube Collaboration. “The IceCube Neutrino Observatory: instrumentation and online systems”. In: *Journal of Instrumentation* 12.03 (Mar. 2017), P03012. doi: [10.1088/1748-0221/12/03/P03012](https://doi.org/10.1088/1748-0221/12/03/P03012). URL: <https://dx.doi.org/10.1088/1748-0221/12/03/P03012>.
- [85] Ahlers, Markus and Helbing, Klaus and Pérez de los Heros, Carlos. “Probing particle physics with IceCube”. In: *The European Physical Journal C* 78.11 (Nov. 2018). ISSN: 1434-6052. doi: [10.1140/epjc/s10052-018-6369-9](https://doi.org/10.1140/epjc/s10052-018-6369-9). URL: <http://dx.doi.org/10.1140/epjc/s10052-018-6369-9>.
- [86] Rene Reimann. “Search for the Sources of the Astrophysical High-Energy Muon-Neutrino Flux with the IceCube Neutrino Observatory”. PhD thesis. Aachen University in Erlangen, 2019.
- [87] IceCube Collaboration. *Detecting Neutrinos*. Web. 2024.
- [88] IceCube Collaboration. “Energy reconstruction methods in the IceCube neutrino telescope”. In: *Journal of Instrumentation* 9.03 (Mar. 2014), P03009. doi: [10.1088/1748-0221/9/03/P03009](https://doi.org/10.1088/1748-0221/9/03/P03009). URL: <https://dx.doi.org/10.1088/1748-0221/9/03/P03009>.
- [89] The IceCube Collaboration. “Detection of astrophysical tau neutrino candidates in IceCube”. In: *The European Physical Journal C* 82.11 (Nov. 2022). ISSN: 1434-6052. doi: [10.1140/epjc/s10052-022-10795-y](https://doi.org/10.1140/epjc/s10052-022-10795-y). URL: <http://dx.doi.org/10.1140/epjc/s10052-022-10795-y>.
- [90] J. Ahrens et al. “Muon track reconstruction and data selection techniques in AMANDA”. in: *Nuclear Instruments and Methods in Physics Research Section A: Accelerators, Spectrometers, Detectors and Associated Equipment* 524.1 (2004), pp. 169–194. ISSN: 0168-9002. doi: <https://doi.org/10.1016/j.nima.2004.01.065>. URL: <https://www.sciencedirect.com/science/article/pii/S0168900204001871>.
- [91] Peter J. Huber. “Robust Estimation of a Location Parameter”. In: *The Annals of Mathematical Statistics* 35.1 (1964), pp. 73–101. doi: [10.1214/aoms/1177703732](https://doi.org/10.1214/aoms/1177703732). URL: <https://doi.org/10.1214/aoms/1177703732>.
- [92] IceCube Collaboration. “Calibration and characterization of the IceCube photomultiplier tube”. In: *Nuclear Instruments and Methods in Physics Research Section A: Accelerators, Spectrometers, Detectors and Associated Equipment* 618.1 (2010), pp. 139–152. ISSN: 0168-9002. doi: <https://doi.org/10.1016/j.nima.2010.03.102>. URL: <https://www.sciencedirect.com/science/article/pii/S0168900210006662>.
- [93] Aartsen, M. et al. “IceCube search for dark matter annihilation in nearby galaxies and galaxy

- clusters”. In: *Phys. Rev. D* 88 (12 Dec. 2013), p. 122001. doi: [10.1103/PhysRevD.88.122001](https://doi.org/10.1103/PhysRevD.88.122001). URL: <https://link.aps.org/doi/10.1103/PhysRevD.88.122001>.
- [94] Pearl Sandick et al. “Sensitivity of the IceCube neutrino detector to dark matter annihilating in dwarf galaxies”. In: *Phys. Rev. D* 81 (8 Apr. 2010), p. 083506. doi: [10.1103/PhysRevD.81.083506](https://doi.org/10.1103/PhysRevD.81.083506). URL: <https://link.aps.org/doi/10.1103/PhysRevD.81.083506>.
- [95] Qinrui Liu and Jeffrey Lazar and Carlos A. Argüelles and Ali Kheirandish. “ $\chi$ aro: a tool for neutrino flux generation from WIMPs”. In: *Journal of Cosmology and Astroparticle Physics* 2020.10 (Oct. 2020), p. 043. doi: [10.1088/1475-7516/2020/10/043](https://doi.org/10.1088/1475-7516/2020/10/043). URL: <https://dx.doi.org/10.1088/1475-7516/2020/10/043>.
- [96] Tessa Cerver. “Time Integrated searches for Astrophysical Neutrino Sources using the IceCube Detector and Gender in Physics studies for the Genera Project”. PhD thesis. UNIVERSITE DE GEN ´ EVE, 2019, pp. 57–64.
- [97] Minjin Jeong on behalf of the IceCube Collaboration. “Search for Dark Matter Decay in Nearby Galaxy Clusters and Galaxies with IceCube”. In: *Proceedings of Science* 444.38 (2023).
- [98] IceCube Collaboration. “Evidence for neutrino emission from the nearby active galaxy NGC 1068”. In: *Science* 378.6619 (2022).
- [99] Nathan Whitehorn and Jakob van Santen. *Photospline*. IceCube: GitHub.
- [100] Paul H. C. Eilers and Brian D. Marx. “Flexible smoothing with B-splines and penalties”. In: *Statistical Science* 11.2 (1996), pp. 89–121. doi: [10.1214/ss/1038425655](https://doi.org/10.1214/ss/1038425655). URL: <https://doi.org/10.1214/ss/1038425655>.
- [101] The IceCube Collaboration. *Search for neutrino lines from dark matter annihilation and decay with IceCube*. 2023. arXiv: [2303.13663 \[astro-ph.HE\]](https://arxiv.org/abs/2303.13663).
- [102] The IceCube Collaboration. “Measurement of the multi-TeV neutrino interaction cross-section with IceCube using Earth absorption”. In: *Nature* 551 (2017).